2019

Design of a solid-state array detector prototype for small-field dosimetry in megavoltage photon beams

Giordano Biasi
University of Wollongong, giordano_biasi@uow.edu.au

UNIVERSITY OF WOLLONGONG AUSTRALIA

Design of a solid-state array detector prototype for small-field dosimetry in megavoltage photon beams

Giordano Biasi

This thesis is presented as part of the requirement for the conferral of the degree:
Doctor of Philosophy

Supervisors:
Dist. Prof. Anatoly B. Rosenfeld
Prof. Tomas Kron, OAM
A/Prof. Marco Petasecca
A/Prof. Susanna Guatelli

Centre for Medical Radiation Physics, School of Physics,
Faculty of Engineering and Information Sciences, The University of Wollongong

January 2019

Table of contents

Acknowledgements

I would like to acknowledge the Gross Foundation (Melbourne, Australia) for financial support. I would like to thank, in alphabetical order:

David Bolst[1], Martin Carolan[1,2], Trent Causer[1], Stephanie Corde-Tehei[1,3], Jeremy A. Davis[1], Martin A. Ebert[4,5], Garry Grogan[4], Susanna Guatelli[1], Nicholas Hardcastle[6], Benjamin Hug[4,5], Tomas Kron[1,6,7], Jonathan Lane[4], Marco Petasecca[1], Anatoly B. Rosenfeld[1], Nauljun Stansook[8], Kananan Utitsarn[9], Dean Wilkinson[2]

[1] Centre for Medical Radiation Physics, University of Wollongong, Wollongong, Australia
[2] Illawarra Cancer Care Centre, Wollongong, Australia
[3] Prince of Wales Hospital, Randwick, Sydney, Australia
[4] Sir Charles Gairdner Hospital, Nedlands, Australia
[5] School of Physics and Astrophysics, University of Western Australia, Australia
[6] Peter MacCallum Cancer Care Centre, Melbourne, Australia
[7] Sir Peter MacCallum Cancer Institute, University of Melbourne, Parkville, Australia
[8] Department of Radiology, Faculty of Medicine, Mahidol University, Bangkok, Thailand
[9] Department of Medical Services, Lopburi Cancer Hospital, Lopburi, Thailand

Certification

I, Giordano Biasi, declare that this thesis submitted in fulfilment of the requirements for the conferral of the degree Doctor of Philosophy from the University of Wollongong, is wholly my own work unless otherwise referenced or acknowledged. This document has not been submitted for qualifications at any other academic institution.

_____

Giordano Biasi

January 2019

List of figures

List of tables

List of acronyms, portmanteaus & abbreviations

A, a

AAPM - American Association of Physicists in Medicine

ACPSEM - Australasian College of Physical Scientists and Engineers in Medicine

ADC - Analogue-to-Digital Converter

AFE - Analog Front End

B, b

C, c

CAX - Central AXis

CCE - Charge Collection Efficiency

CMRP - Centre for Medical Radiation Physics (University of Wollongong, Australia)

CoP - Code of Practice

COR - Centre Of Rotation

CPE - Charged Particle Equilibrium

CVD - Chemical Vapour Deposition

D, d

DAQ - Data Acquisition system

DMG - Dose Magnifying Glass

DP - Dose Profile (also referred to as OAR Off-Axis Ratio)

DPP - Dose Per Pulse

E, e

EBRT - External Beam Radiation Therapy

ED - Energy Deposition

EPSM - Engineering and the Physical Sciences in Medicine

ESTRO - European SocieTy for Radiotherapy & Oncology

F, f

FB - Flattened Beam

FEA - Finite Element Analysis

FFF - Flattening-Filter Free

FPGA - Field Programmable Gate Array

FWHM - Full-Width Half-Maximum

G, g

Geant4 - GEometry ANd Tracking 4

G-R - Generation-Recombination centres

GUI - Graphical User Interface

H, h

I, i

IAEA - International Atomic Energy Agency (Vienna, Austria)

IC - Ionization Chamber

ICCC - Illawarra Cancer Care Centre (Wollongong, NSW, Australia)

ICRU - International Commission on Radiation Units and measurements

IEEE - Institute of Electrical and Electronics Engineers

IMRT - Intensity-Modulated Radiation Therapy

J, j

K, k

L, l

LET - Linear Energy Transfer

linac - LInear Accelerator

M, m

MC - Monte Carlo

MIP - Minimum Ionising Particle

MLC - Multi-Leaf Collimator

MOSFET - Metal-Oxide-Semiconductor Field-Effect Transistor

MP512 - MagicPlate 512

MU - Monitor Unit

MV - Mega Voltage

N, n

O, o

OAR - Off-Axis Ratio (also referred to as DP - Dose Profile)

OF - Output Factor

OSLD - Optically Stimulated Luminescent Detector

P, p

PCB - Printed Circuit Board

PDD - Percentage Depth Dose

PHSP - PHase SPace file

PMCC - Peter MacCallum Cancer Centre (Melbourne, Australia)

PMMA - Polymethylmethacrylate

Q, q

QA - Quality Assurance

R, r

RTI - Relative Temperature Instability

S, s

SABR - Stereotactic Ablative Radiation Therapy

SBRT - Stereotactic Body Radiation Therapy

SCGH - Sir Charles Gairdner Hospital (Nedlands, WA, Australia)

SDD - Source-to-Detector Distance

SFD - Stereotactic Field Diode (SFD Diode, IBA Dosimetry, Germany)

SSE - Sentaurus Structure Editor

SRH - Shockley–Read–Hall

SRS - Stereotactic Radio Surgery

SRT - Stereotactic Radiation Therapy

SSD - Source-to-Surface Distance

SV - Sensitive Volume

T, t

TCAD - Technology Computer-Aided Design

TLD - ThermoLuminescent Dosimeter

TMR - Tissue Maximum Ratio

TPR - Tissue Phantom Ratio

TPS - Treatment-Planning System

U, u

USB - Universal Serial Bus

V, v

VMAT - Volumetric Modulated Arc Therapy

W, w

Y, y

Z, z

List of publications

G. Biasi *et al.*, (2018) A novel high-resolution 2D silicon array detector for small field dosimetry with FFF photon beams, *Physica Medica*, 45, 117–126 (DOI: 10.1016/j.ejmp.2017.12.010)

G. Biasi *et al.*, (2019) Today's monolithic silicon array detector for small field dosimetry: the Octa, *Journal of Physics: Conference series* 1154 012002 (DOI: 10.1088/1742-6596/1154/1/012002)

G. Biasi *et al.*, (2018) CyberKnife® fixed cone and Iris™ defined small radiation fields: assessment with a high-resolution solid-state detector array, *Journal of Applied Clinical Medical Physics*, 19 (5), 547-557 (DOI: 10.1002/acm2.12414)

G. Biasi *et al.*, (2018) On monolithic silicon array detectors for small-field photon beam dosimetry, *IEEE Transaction on Nuclear Science*, 65 (9), 2640-2649 (DOI: 10.1109/TNS.2018.2860625)

G. Biasi *et al.*, (2019) On the instantaneous dose rate and angular dependence of monolithic silicon array detectors, *IEEE Transaction on Nuclear Science*, 66 (1), 519-527 (DOI: 10.1109/TNS.2018.2885017)

L. T. Tran, D. Bolst, S. Guatelli, **G. Biasi** *et al.*, (2018) High spatial resolution microdosimetry with monolithic ΔE-E detector on 12C beam: Monte Carlo simulations and experiment, *Nuclear Instruments and Methods in Physics Research, Section A*, 887, 70-80 (DOI: 10.1016/j.nima.2017.12.079)

S. Alhujaili, **G. Biasi** *et al.*, (2018) Quality assurance of CyberKnife® robotic stereotactic radiosurgery using an angularly-independent silicon detector, *Journal of Applied Clinical Medical Physics*, 20 (1), 76-88 (DOI: 10.1002/acm2.12496)

N. Stansook, **G. Biasi** *et al.*, (2019) 2D monolithic silicon-diode array detectors in megavoltage photon beams: does the fabrication technology matter? A medical physicist's perspective,

Australasian Physical & Engineering Sciences in Medicine (DOI: 10.1007/s13246-019-00736-7)

K. Utitsarn, **G. Biasi** *et al.*, (2018) 2D solid-state array detectors: a technique for in-vivo dose verification in a variable effective area, *Journal of Applied Clinical Medical Physics* (submitted for publication, pending)

N. Stansook, **G. Biasi** *et al.*, (2018) IMRT and VMAT quality assurance in heterogeneous media: first experience with a 2D solid-state detector prototype, *Australasian Physical & Engineering Sciences in Medicine* (submitted for publication, pending)

List of conference abstracts & presentations

G. Biasi *et al.*, (2017) - Geant4 User Workshop 2017, Wollongong, Australia - A Geant4 study on air gap optimization for a correction-free silicon diode array detector

G. Biasi *et al.*, (2018) - ESTRO 37, Barcelona, Spain - EP-1720 A silicon diode array detector for small field dosimetry with flattening filter free beams, *Radiotherapy and Oncology*, *127* (1)

S. Alhujaili, **G. Biasi** *et al.*, (2018) - ESTRO 37, Barcelona, Spain - EP-1725 Quality assurance of Robotic SRS (CyberKnife®) by an innovative angular independent silicon detector, *Radiotherapy and Oncology*, *127* (1)

G. Biasi *et al.*, (2018) - AAPM 60, Nashville, USA - E620 Small Static Fields: Real-Time Assessment of the Accuracy of a Treatment Planning System Calculated Dose with a Step-And-Shoot Method, *Medical Physics*, 45 (6)

G. Biasi *et al.*, (2018) - IEEE NISS-MIC 2018, Sydney, Australia - On monolithic silicon diode array detectors for small-field photon beam dosimetry

G. Biasi *et al.*, (2018) - IEEE NISS-MIC 2018, Sydney, Australia - On monolithic silicon diode array detectors for flattening filter free photon beam dosimetry

G. Biasi *et al.*, (2018) - EPSM 2018, Adelaide, Australia - Quality assurance for a CyberKnife®: The power couple

G. Biasi *et al.*, (2018) - HIAS 2018, Canberra, Australia - Numerical characterization of a novel ΔE-E telescope microdosimeter on 12C beam lines

F. Matar, J. A. Davis, D. Wilkinson, T. Causer, I. Fuduli, **G. Biasi** *et al.*, (2018) - ESTRO meets Asia, Singapore - PV-125 Evaluation of a high-resolution silicon detector for quality assurance of VMAT

G. Biasi *et al.*, (2019) - ESTRO 38, Milano, Italy - High-resolution assessment of dose calculations in small MV photon beams on and off central axis

G. Biasi *et al.*, (2019) - ESTRO 38, Milano, Italy - 2D solid-state array detectors a technique for in-vivo dose verification at varying effective area

G. Biasi *et al.*, (2019) - ESTRO 38, Milano, Italy – IMRT/VMAT QA in heterogeneous media first experience with a 2D solid-state detector prototype

Abstract

Recent developments in imaging techniques, medical linear accelerator (linac) design and treatment modalities in megavoltage photon-beam radiotherapy have been aimed at optimizing the delivery of highly conformal dose distributions, leading to an escalation in the use of small radiation fields.

Modern radiotherapy delivered with small fields has more stringent requirements, in terms of quality assurance (QA), than conventional radiotherapy with broad fields. Additionally, accurate dosimetry, paramount for the safe and efficient use of radiation, becomes challenging in this context. Accidents, near misses and discrepancies between the results of different investigators confirm that dosimetry in small fields is complex.

The factors contributing to this are broadly summarized as an absorbed dose distribution characterized by a lack of charged particle equilibrium (CPE) over most of the treatment target, partial source occlusion by the collimation system of the linac, and a measurement of absorbed dose which is highly dependent on radiation detector design and the perturbations it introduces to particles fluence.

Starting from the currently available knowledge on the physics of small radiation fields, the aim of the research in the present dissertation was the design and test of a novel radiation detector prototype with the potential to address the shortcomings of currently available dosimeters.

A 2D monolithic silicon-diode array detector 'Octa', with its associated read-out system, was designed and fabricated. The Octa was experimentally characterized for QA of linacs in a wide range of small radiation fields produced by various beam qualities and collimator systems. It was modelled in Monte Carlo with a Geant4 (GEometry ANd Tracking 4) application and with a TCAD (Technology Computer-Aided Design) software to scrutinize its limitations and put forward recommendations for the development of the next generation of monolithic silicon-based array detectors.

The Octa was demonstrated to be, in the context of currently available small-field-dedicated dosimeters and specifically of arrays, a significant step forward in terms of offered temporal resolution and spatial resolution. Its clever design would provide the medical physicist working in the clinic with an innovative tool for acquiring 2D dose distributions pulse-by-pulse in real time with sub-millimetre accuracy, streamlining QA procedures.

1 Introduction

1.1 Background

A range of radiations has long been routinely employed for medical applications, such as x-rays, gamma rays, neutrons, protons and, more recently, heavy ions. The radiation of choice is ultimately a matter of radiobiology, treatment cost, facilities being available and educated medical considerations. Even so, more than 100 years after their discovery, x-rays produced with a medical linear accelerator (linac) are still by far the most common source for radiotherapy treatments, owing mainly to their cost-effectiveness, robustness and wide availability of the machines that produce them.

Recent advances in megavoltage (MV) photon-beam radiotherapy have been focussed on improving the accuracy of radiation delivery, maximizing dose conformity to the target while still allowing for ever faster treatments. These processes have led to an escalation in the use of small radiation fields in a range of radiotherapy treatments, such as stereotactic radiotherapy (SRT) and intensity modulated radiotherapy (IMRT), at a time when their dosimetry and its implications for quality assurance (QA) procedures was still being discussed. As a result, code of practice (CoP) which were only available for conventional radiotherapy with broad photon beams have been misused, and accidents have occurred in some clinics.

To ensure that the dose that is delivered is the dose that is prescribed, accurate dosimetry following an internationally accepted CoP is paramount. Failure to do so may result in treatment delivery not being as effective as intended or to radiation-induced complications. Two guidance documents dedicated to small-field dosimetry have been published in the second half of 2017: the IAEA-TRS-483 – *Dosimetry of Small Static Fields Used in External Beam Radiotherapy* [1], a CoP for reference and relative dose determination, and the ICRU Report 91 – *Prescribing, Recording and Reporting of Stereotactic Treatments with Small Photon beams* [2]. These documents, addressed to the medical physicists' community which uses or consider the use of small radiation fields in MV photon beams, are meant to outline standardized guidance for dosimetry procedures and selection of detectors.

A selection process that, in the context of small-field relative dosimetry, should be based on the size and material of the sensitive volume (SV) and its packaging, and the response characteristics in terms of energy dependence, dose and dose rate linearity, angular dependence (also referred to as directional dependence) etc. Ultimately, any detector will perturb to some extent the particles fluence in the medium, and appropriate correction factors will be required

to account for this. Yet, since these are often impractical to use and prone to error, the design of a device should seek to minimize the corrections that are needed to convert its readings to dose. All commercial detectors dedicated to small-field dosimetry currently available have disadvantages, and none is sufficiently close to an ideal one. It is prudent and recommended to perform measurements in small fields with different detectors and cross-check for consistency of results.

1.2 Project aim

The aim of the present project was to work towards the design of an ideal dosimeter dedicated to small-field dosimetry. To this end, two goals were pursued:

- a review of the current understanding of the physics of small-field dosimetry and its QA requirements, followed by a review of the currently commercially available small-field-dedicated dosimeters, their advantages and limitations (Table 1).

Table 1. Commercially available dosimeters (selected) used in small radiation fields.

Dosimeter	Type	Characteristics	Selected references
microdiamond 60019 (PTW, Germany)	Synthetic diamond	Single SV disk of 2.2 mm diameter, point dose measurement; over-response in very small fields; expensive	[3]–[5]
SFD diode (IBA Dosimetry, Germany)	Unshielded diode	Single SV disk of 0.6 mm diameter, point dose measurement; reproducibility and long-term stability issues; over-response in small fields; superseded by the Razor	[6], [7]
Razor (IBA Dosimetry, Germany)	Unshielded diode	Single SV disk of 0.6 mm diameter, point dose measurements; over-response in small fields	[8], [9]
SRS diode 60018 (PTW, Germany)	Unshielded diode	Single SV disk of 1.12 mm diameter; over-response in small fields	[3]
Gafchromic EBT3 films (Ashland Inc., USA)	Film dosimetry	2D dose measurement, high resolution; tissue equivalent; complicated to use, not real-time, uncertainties due to scanning and handling procedures	[10]–[12]

SRS Profiler (Sun Nuclear, USA)	Array of 125 single diodes, pitch of 4 mm	2D dose measurement; limited spatial resolution	[13]
MapCHECK3 (Sun Nuclear, USA)	Array of 1527 single diodes, effective pitch of 7.07 mm	2D dose measurement; limited spatial resolution	N/A[1]
Octavius 1000SRS (PTW, Germany)	Array of 977 single ionization chambers, minimum pitch of 2.5 mm	2D dose measurement; limited spatial resolution, volume averaging	[13], [14]

- the design of a novel 2D monolithic silicon-diode array detector prototype dedicated to small-field dosimetry. Its experimental and numerical characterization, as well as benchmarking against commercially available detectors, performed in the context of QA procedures for linacs as outlined by internationally-accepted CoP for small-field dosimetry. The investigation of its potential and limitations. The scope for further improvements.

1.3 Thesis structure

The present dissertation is mostly based on work that has been published or has been submitted for publication. Including the present *Introduction*, it is organized in 11 Chapters:

- Chapter 2 starts with *Modern radiotherapy* (page 6), an overview of modern megavoltage photon-beam radiotherapy, its techniques and prescriptions. This includes a summary of fundamental radiation dosimetry concepts and quantities which are used throughout this dissertation. In *Small-field dosimetry* (page 15) a special attention is dedicated to small-field relative dosimetry for megavoltage photon beams, the physics behind and its requirements in the context of linac QA. An overview of the currently available offer of dedicated dosimeters (*Available suitable small-field dosimeters (or lack thereof)*, page 23), their potential and their shortcomings, is presented.
- Chapter 3 (*A review of silicon-based dosimeters*, page 28) focusses on silicon-based dosimetry and, in particular, small-field dosimetry: *Why silicon?* (page 28) aims at

[1] https://www.sunnuclear.com/solutions/patientqa/mapcheck-3

presenting the reasons for choosing this material for a detector's sensitive volume. However, this choice comes with limitations, as described in *Limitations of silicon detectors* (page 30). The following section is on the *Use of silicon diodes for small-field dosimetry* (page 34) and ends with a presentation of the work carried out within the Centre for Medical Radiation Physics (CMRP) over the last decade towards the development of silicon-based dosimeters for use in radiotherapy (*The CMRP and the quest for the ideal diode-array detector*, page 40).

The present literature review was based on scientific articles published in internationally-recognized peer-reviewed journals, master and doctoral thesis dissertations and textbooks. Example of keywords used in the searching process were "small-field dosimetry", "silicon radiation detector", "diode detector", "diode", "epitaxial substrate", "stereotactic radiotherapy", "CyberKnife quality assurance". Only material published in the English language was considered.

- Chapter 4 (page 43) introduces the 'Octa', a novel 2D monolithic silicon-diode array detector prototype dedicated to small-field dosimetry. Its concept and design, manufacturing process and read-out system are described. Its modelling for numerical investigations using the Geant4 (GEometry ANd Tracking 4) Monte Carlo application and a TCAD (Technology Computer-Aided Design) software is introduced in *A touch of Monte Carlo*, page 51 and in *A touch of TCAD*, page 54, respectively.
- Chapter 5 (page 59) reports on the first experimental characterization of the Octa for dosimetry in small static fields produced with flattened and flattening-filter free (FFF) photon beams, which highlighted some shortcomings related to its manufacturing-related characteristics and pushed through some changes.
- Chapter 6 (page 69) reports on the experimental characterization of the Octa for dosimetry in small static fields with flattened and FFF photon beams produced by Varian (Varian Medical Systems, Palo Alto, USA) linacs. This chapter is based on results in **G. Biasi** *et al*, (2018) A novel high-resolution 2D silicon array detector for small field dosimetry with FFF photon beams, *Physica Medica*, 45, 117–126 [15].
- Chapter 7 (page 87) reports on the experimental characterization of the Octa for dosimetry in small static fields produced by stereotactic-dedicated conical collimators mounted on Elekta Axesse™ (Elekta AB, Stockholm, Sweden) linacs. This chapter is based on results in **G. Biasi** *et al*, (2019) Today's monolithic silicon array detector for small field dosimetry: the Octa, *Journal of Physics: Conference series* [16].

- Chapter 8 (page 97) reports on the experimental and numerical characterizations of the Octa for QA of CyberKnife® system (Accuray, Palo Alto, USA). This chapter is mostly based on results published in **G. Biasi** *et al*, (2018) CyberKnife® fixed cone and Iris™ defined small radiation fields: assessment with a high-resolution solid-state detector array, *Journal of Applied Clinical Medical Physics*, 19 (5), 547-557 [17].
- Chapter 9 (page 124) and Chapter 10 (page 149) discuss potential and limitations of the current detector technology on which the Octa is based, and the scope for improvements. These chapters are based on results published in **G. Biasi** *et al*, (2018) On monolithic silicon array detectors for small-field photon beam dosimetry, *IEEE Transaction on Nuclear Science*, 65 (9), 2640-2649 [18] and on results in **G. Biasi** *et al*, (2019) On the instantaneous dose rate and angular dependence of monolithic silicon array detectors, *IEEE Transaction on Nuclear Science,* 66 (1), 519-527 [19].
- Chapter 11 (page 165) has final remarks: a summary of contributions (*The Octa prototype: design and test*, page 165 and *The Octa prototype: results*, page 166) and recommendations (page 167).

2 Theoretical background for dosimetry

2.1 Modern radiotherapy

Medical linear accelerators (linacs, Figure 1 and Figure 2) are the most used machine to deliver radiotherapy treatments with ionizing radiation. Electrons, produced by an electron gun, are accelerated using microwave radiofrequency fields in the range from 10^3 to 10^4 MHz. Upon exiting the waveguide, megavoltage electrons are focused by bending magnets onto a target, usually made of tungsten. Slowing down through it, electrons emit Bremsstrahlung x-ray radiation [20].

The x-ray beam profile has traditionally been flattened by a flattening filter. Recently, a growing interest in the rapid delivery of heterogeneous dose distributions has revived the use of flattening-filter free (FFF) beams [21]. The removal of the flattening filter changes not only the x-ray beam profile, but also its dosimetry characteristics [22], with an increased available dose rate and a lower peripheral dose which could benefit treatment delivery [23].

Downstream the target, a fixed primary collimation system defines the maximum photon-beam field size. The optional flattening filter resides beneath it, after which a secondary movable collimator system (the jaws) is used to shape different square or rectangular fields. Ever more often, a third collimator system is used to shape arbitrary irregular fields, if a multi-leaf collimator (MLC, mounted either upstream or downstream the jaws, shown in the lower panel of Figure 1, in Figure 2 and in Figure 3) is used, or circular fields, if a conical collimator (be it fixed, Figure 4, or with a variable aperture such as the Iris™) is used. The purpose of this latter beam collimation stage is to achieve maximum conformity of the radiation beam to the patient-specific target [20].

Compared to a not-so-distant past, there currently is an availability of tertiary collimators, exquisite image-guidance techniques, linacs with improved mechanical accuracy and increased stability and dosimetry control. Additionally, novel specialized treatment machines, such as robotic non-isocentric linacs delivering radiation fields to arbitrary locations in the body (the Accuray CyberKnife® system is such an example) and dedicated gantry-based isocentric linacs such as the Varian TrueBeam™ STx (Figure 1) and the Elekta Axesse™, all have facilitated an escalation in the use of small fields in modern radiotherapy [2].

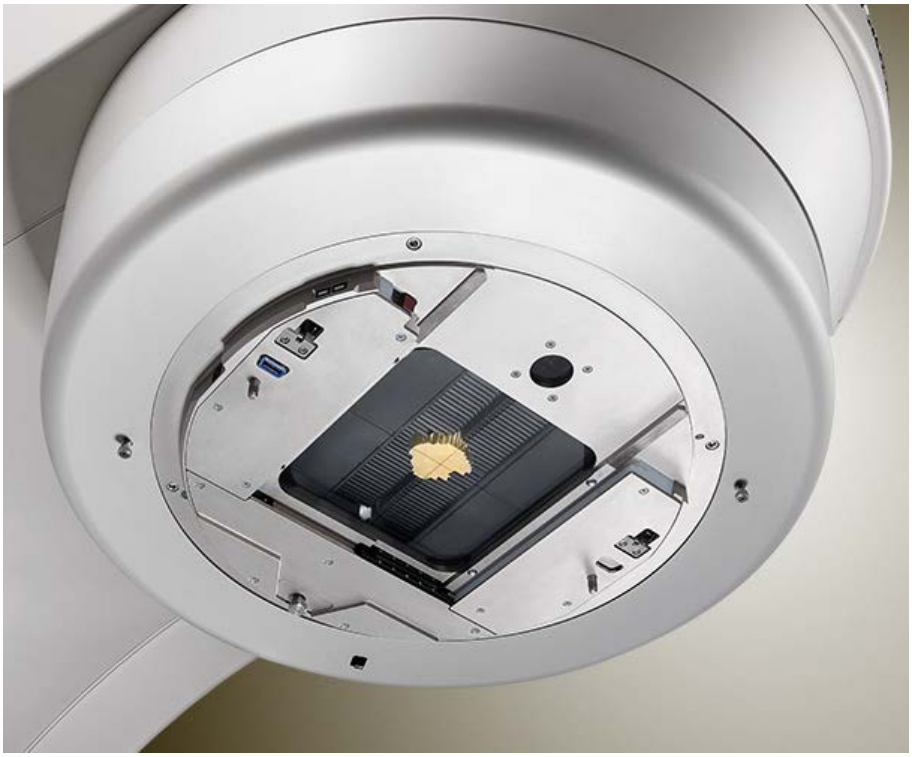

Figure 1. Upper panel: a Varian TrueBeam™ STx medical linear accelerator (Varian Medical Systems, Palo Alto, CA, USA).

Left panel: detail of the treatment head of a Varian TrueBeam™ STx medical linear accelerator mounting its tertiary collimator system (multi-leaf collimator, MLC).

Images courtesy of Varian Medical Systems [2].

[2] varian.com

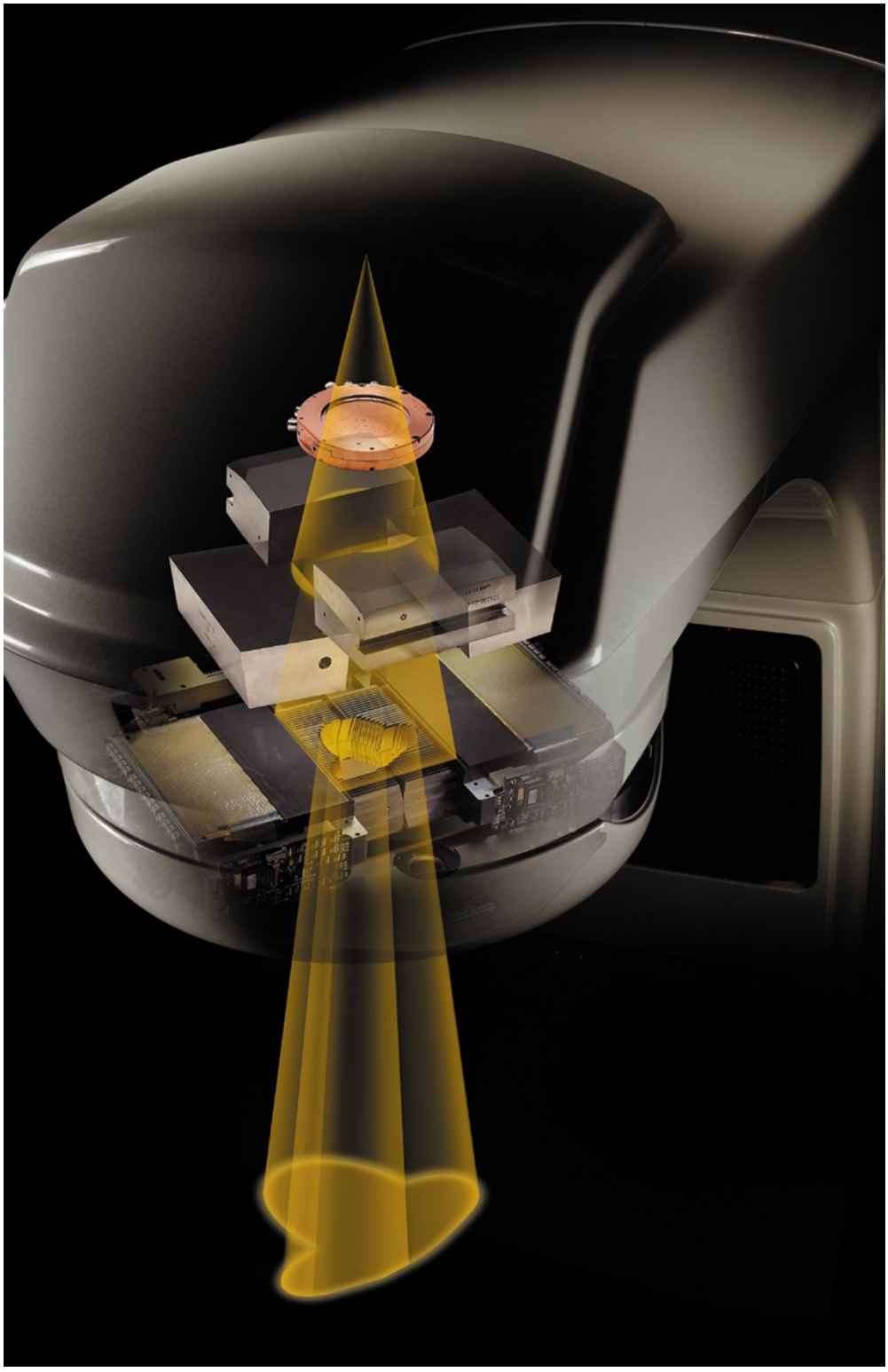

Figure 2. Radiation field shaping in a medical linac using secondary collimators (jaws) and tertiary collimators (MLC). Images courtesy of Varian Medical Systems [3].

[3] varian.com

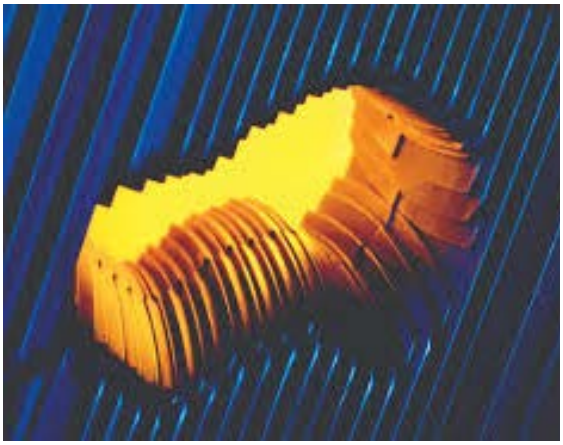

Figure 3. A multi-leaf collimator (MLC) mounted upstream of the exit of a linac's treatment head to shape arbitrary irregular fields.

Figure 4. Fixed conical collimators of various diameters mounted upstream of the exit of a linac's treatment head to shape circular fields.

Stereotactic radiation therapy (SRT) techniques are a specialised form of x-ray external-beam radiation therapy (EBRT) making extensive use of small fields. Traditionally performed only for brain tumours, with the evolution of in-treatment-room imaging systems, and patient motion management, SRT today is used to deliver treatments to extra-cranial targets and includes techniques such as stereotactic radio surgery (SRS), stereotactic body radiation therapy (SBRT) and stereotactic ablative radiation therapy (SABR).

In SRT, the focus is on the delivery of highly conformal dose distributions with steep dose fall-off, thus ensuring optimal dose in the target volume combined with superior non-target dose avoidance. This is achieved by using multiple small (sometimes < 1 cm across), often non-coplanar beams and delivering the treatment in a few high-dose fractions [2], [24], [25]. It is anticipated that future advancements in screening and diagnostic techniques will lead to ever earlier tumour identification, further increasing the use of SRT [2].

Small radiation fields are of interest also to intensity-modulated radiation therapy (IMRT) techniques. By subdividing the beam into multiple and irregular small segments, and modulating the dose rate in each segment by the MLC[4], IMRT achieves dose homogeneity similar to conventional radiotherapy, but with superior target conformality [2]. Today, modern radiotherapy may combine the principle of IMRT (varying the fluence) and SRT (the use of arcs, the use of multiple small beams). The result is the delivery of highly conformal dose distributions with modulated high-doses in just a few fractions [2].

[4] It is the photon fluence (photons per unit area) and not the photon intensity (photon per unit time) that is modulated. The modulation is achieved by varying the time for which photons pass through an area [30].

In small radiation fields, dosimetry is complex and prone to errors, and their use command special care in prescribing, recording and reporting treatments [1], [2], [26].

2.1.1 A hint of radiation dosimetry

Modern radiotherapy relies on radiation dosimetry for accurate and reliable measurement of the effects of the interaction of ionizing radiation with matter, in particular for measurement of the deposited and absorbed dose in a given medium (a phantom or a patient's tissue) [27].

The megavoltage photons used in EBRT interact with a patient's tissue predominantly by Compton interactions [1], [28]. That is, photons striking orbital electrons with enough energy to cause them to be ejected from their own atoms. Removed electrons travel through the medium and deposit part of their energy via ionisation and excitation of other orbital electrons. The result is cell killing either via direct interactions (DNA molecules being directly ionised by electrons) or indirect interactions (the electrons ionise molecules within the tissue. These produce free radicals which subsequently interact with DNA molecules causing cell death) [29]. While stochastic in nature, radiation interactions are, for most applications, well approximated by non-stochastic descriptions thanks to the large number of interactions that take place in the spatial and temporal dimensions of interest [30].

A measure of the effects of the interaction of radiation with a medium enclosed in a volume dV is the ratio of the average energy deposited dE per unit mass dm, the absorbed dose D (units $\mathrm{Gy} = \frac{\mathrm{J}}{\mathrm{kg}}$):

$$\mathrm{D} = \frac{\mathrm{dE}}{\mathrm{dm}} \tag{2.1}$$

The dose delivered to the target by a linac is calibrated by a process called reference dosimetry performed using a detector in water, which is representative of a patient's tissue. The radiation causes ionisation in the detector and the resulting charge is measured and related to the absorbed dose. Reference dosimetry measures the absorbed dose at a point in a fixed geometry (field size, distance, depth) under reference conditions (temperature, pressure, humidity) [20]; the detector to be used in this case is a calibrated ionization chamber. These chambers are the standard for all dosimetry and allow traceability to a primary laboratory and an accurate value [31]. On the other hand, relative dosimetry allows for the evaluation of the dose at any point of interest under any irradiation conditions, relative to the dose at a reference point under reference irradiation conditions.

In this dissertation we will only deal with relative dosimetry.

2.1.2 Fundamental quantities

This section is adapted from P. Andreo et al., *Fundamentals of ionizing radiation dosimetry*) [30].

Let's consider a sphere of infinitesimal volume dV with a cross-sectional area dA. Let N be the average number of particles striking the sphere. The particle fluence Φ (units m^{-2}) through the sphere is defined as:

$$\Phi = \frac{dN}{dA} \tag{2.2}$$

Let R to be the mean value of the energies (excluding rest energy) of the particles striking the sphere. The energy fluence Ψ (units Jm^{-2}) is defined as:

$$\Psi = \frac{dR}{dA} \tag{2.3}$$

The distribution of the particles fluence Φ with respect to energy is known as fluence spectrum Φ_E:

$$\Phi_E = \frac{d\Phi}{dE} \tag{2.4}$$

The energy fluence spectrum Ψ_E (units $Jm^{-2}keV^{-1}$) is defined as:

$$\Psi_E = E\Phi_E \tag{2.5}$$

Let's consider N_0 photons (uncharged particles) incident perpendicularly on a material of thickness dx. The number of photons N passing through it without interacting is given by the exponential attenuation law as:

$$N = N_0 e^{-\mu dx} \tag{2.6}$$

The coefficient μ (units m^{-1}) is called linear attenuation coefficient and expresses the probability of interaction per unit length dx. To remove its strong dependence on the density ρ of the material, it is possible to define the mass attenuation coefficient μ/ρ (units of m^2kg^{-1}).

Photons interacting with matter transfer their energy to secondary charged particles. Let E_{tr} be the average energy transferred to kinetic energy of secondaries by interactions of photons of incident energy E while travelling the distance dx in a material. Then the mass energy transfer coefficient μ_{tr}/ρ is:

$$\frac{\mu_{tr}}{\rho} = \frac{\mu}{\rho dx}\frac{E_{tr}}{E} \tag{2.7}$$

The fraction of the photon energy E that, upon interaction, is transferred as kinetic energy to the charged particles and then lost through collisional losses is represented by the mass

energy absorption coefficient μ_{en}/ρ. It is a fraction of the mass transfer coefficient μ_{tr}/ρ and the two can be linked by:

$$\frac{\mu_{en}}{\rho} = \frac{\mu_{tr}}{\rho}(1 - g) \tag{2.8}$$

where g is the radiative fraction and represents the average fraction of energy lost by charged particles via radiative losses.

For charged particles, the linear stopping power S (units Jm^{-1}) is defined as the average energy loss dE per unit length dl:

$$S = \frac{dE}{dl} \tag{2.9}$$

To remove its dependence on the density ρ of the material, it is possible to define the mass stopping power (units $Jm^{-2}kg^{-1}$):

$$\frac{S}{\rho} = \frac{1}{\rho}\frac{dE}{dl} \tag{2.10}$$

The mass stopping power can be subdivided into different contributions according to the type of energy loss:

$$\frac{S}{\rho} = \frac{S_{el}}{\rho} + \frac{S_{rad}}{\rho} + \frac{S_{nuc}}{\rho} \tag{2.11}$$

S_{el}/ρ is the mass electronic stopping power (or mass collision stopping power) due to interactions with atomic electrons resulting in ionization or excitation, S_{rad}/ρ is the mass radiative stopping power due to bremsstrahlung emission, S_{nucl}/ρ is the mass nuclear stopping power due to elastic Coulomb interactions in which recoil energy is imparted to atoms.

Let's consider dE_{tr} as the mean sum of the initial kinetic energies of all the charged particles liberated in a mass dm of a material of volume dV by the uncharged particles incident on the volume dV i.e. the expectation volume of the energy transferred in dV, a non-stochastic quantity. Then the kerma K (which stands for kinetic energy released per unit mass, units $Gy = J/kg$) is defined as:

$$K = \frac{dE_{tr}}{dm} \tag{2.12}$$

It is possible to define the electronic kerma including only that component of the kerma that results in local energy deposition and not any energy that goes into radiative losses:

$$K_{el} = K(1 - g) = \frac{dE_{tr}^{net}}{dm} \tag{2.13}$$

where g is the radiative fraction and dE_{tr}^{net} the expectation value of the net energy transferred in dm.

2.1.3 Charged particle equilibrium and Bragg-Gray cavity theory

This section is adapted from P. Andreo et al., *Fundamentals of ionizing radiation dosimetry* (2017) [30].

A charged particle equilibrium (CPE) is said to exist for the volume dV if each charged particle of a given type and energy leaving dV is balanced by a particle of the same type and energy entering dV, in terms of expectation values. In other words, the energy imparted outside of dV will be on average replaced by an equal amount of energy imparted by another charged particle generated outside dV, and entering it.

It is possible to show that, under CPE conditions the average energy E imparted by a particle generated within dV equals the average net energy transferred E_{tr}^{net} to charged particles within dV. Therefore:

$$D_{med} = K_{el,med} \tag{2.14}$$

The above relationship states that, under CPE conditions, at a point in a medium, the measurable quantity absorbed dose D_{med} is equal to the calculable quantity electronic kerma K_{el} there.

If CPE is verified, for monoenergetic photons of energy E, the absorbed dose in the medium D_{med} is related to the photon fluence Φ_{med} through:

$$D_{med} = K_{el,med} = \Phi_{med} E \left(\frac{\mu_{en}(E)}{\rho}\right)_{med} \tag{2.15}$$

where

$$\left(\frac{\mu_{en}(E)}{\rho}\right)_{med} \tag{2.16}$$

is the mass-energy absorption coefficient for the medium. For a photon energy fluence spectrum, this becomes:

$$D_{med} = K_{el,med} = \int_0^{E_{max}} \Phi(E)_{med} E \left(\frac{\mu_{en}(E)}{\rho}\right)_{med} dE \tag{2.17}$$

For charged particles of kinetic energy E, this becomes:

$$D_{med} = \Phi_{med} \left(\frac{S_{el}(E)}{\rho}\right)_{med}$$

where

$$\left(\frac{S_{el}(E)}{\rho}\right)_{med} \tag{2.18}$$

is the electron mass stopping power for the medium. Analogously:

$$D_{med} = \int_0^{E_{max}} \Phi(E)_{med} \left(\frac{S_{el}(E)}{\rho}\right)_{med} dE \tag{2.19}$$

Where the stopping power considered is an electronic (or collision) stopping power rather than a total, as bremsstrahlung energy losses are assumed to escape from the region of interest.

For a detector to be useful as a dosimeter, the signal must be proportional to the mean absorbed dose in its sensitive volume (SV). The detector can be considered as a cavity inserted into the medium of interest. The theory that relates the mean absorbed dose D_{cav} in the detector SV to the absorbed dose D_{med} at the reference point in the undisturbed medium is known as cavity theory.

Consider a situation for which:

- the cavity must be small compared to the electron ranges or the material of the cavity must be of very similar atomic composition to the medium such that the cavity perturbation of the charged-particle fluence that would exist in the medium in the absence of the cavity is negligible;
- the absorbed dose in the cavity is deposited entirely by the charged particles entering it.

The two conditions above are known as Bragg-Gray conditions.

If a detector is small relative to the electron ranges, the majority of charge particle tracks (mainly, secondary electrons) crossing it will be originating in the surrounding medium. Only a negligible proportion of them will originate in the detector itself. In this case, the electron fluence in the detector will be a good approximation of the one which would exist in the unperturbed medium. Under these assumptions:

$$\frac{\Phi(E)_{med}}{\Phi(E)_{cav}} \approx 1 \tag{2.20}$$

therefore:

$$\frac{D_{med}}{D_{cav}} = \frac{\Phi(E)_{med}}{\Phi(E)_{cav}} \frac{\left(\frac{S_{el}(E)}{\rho}\right)_{med}}{\left(\frac{S_{el}(E)}{\rho}\right)_{cav}} \approx \frac{\left(\frac{S_{en}(E)}{\rho}\right)_{med}}{\left(\frac{S_{en}(E)}{\rho}\right)_{cav}} = S_{med,cav} \tag{2.21}$$

The secondary electrons in a photon irradiated medium will always be characterized by an energy distribution. Therefore, the above ratio would be more rigorously evaluated as the ratio of the integrals over the respective electron fluence spectrum.

Thanks to Bragg-Gray theory, it is possible to calculate the dose to water (medium) by measuring the dose to the detector (cavity) within the water and multiplying this value by the mass stopping power ratio of water to the detector.

In practice, however, a non-water cavity will always perturb the electron fluence. For relative dosimetry to be performed as a simple measurement ratio, all the Bragg-Gray cavity theory conditions and/or their small deviations must be identical in both the reference field size and the clinical field size of interest [32].

2.2 Small-field dosimetry

The accuracy of the dose delivered to a patient by a medical linac is limited by the accuracy of the dose calculation algorithm implemented into a treatment planning system (TPS) [2]. Other than basic geometric information relative to the linac's treatment head, the commissioning and verification of a TPS requires measured beam data as an input [2]. There exists guidelines for TPS commissioning and verification [33]–[35]. These are general and not specific for small radiation fields [2]. It is a responsibility of the medical physicist in the clinic to ensure that the beam model used by a TPS reproduces the characteristics of the actual beam, and this assumes accurate dosimetry. The overall accuracy of a TPS in predicting dose distributions is significantly limited by uncertainties in underlying dosimetry data [24], [36].

The relative (and reference) dosimetry of broad fields is today a well-standardized procedure [2], [26]. The introduction of small fields had initially seriously compromised dosimetry accuracy due to [1]:

- reference conditions recommended by conventional Codes of Practice (CoP) for broad fields no longer being realizable for some novel linacs;
- measurement procedures for determination of absorbed dose to water in small and composite, irregular fields not being standardized, weakening the traceability of clinical dosimetry to reference dosimetry.

Dosimetry errors were considerably larger than for broad-beam dosimetry [37], and accidents occurred due to the use of methods and procedures appropriate for broad fields but not for small fields [38], [39]. This lead to the realization that dosimetry in small fields is complex and prone to errors [40], [41].

The problems pertaining to small-field dosimetry have been extensively discussed in the literature for many years [28], [37], [50], [42]–[49]. However, only recently have CoP for small

photon-beam dosimetry been outlined by the ICRU Report 91 – *Prescribing, Recording and Reporting of Stereotactic Treatments with Small Photon beams* [2] and by the international CoP IAEA-TRS-483 – *Dosimetry of Small Static Fields Used in External Beam Radiotherapy* [1]. Both documents are based on the same formalism and standards of absorbed dose to water. Their intent was to outline internationally acceptable recommendations regarding:

- quantities and units of ionizing radiation and radioactivity;
- procedures suitable for the measurement and application of these quantities in clinical radiology and radiobiology;
- physical data needed in the application of these procedures, to ensure uniformity in reporting.

2.2.1 The physics behind

Most of the current formulations for converting dose to the detector D_{cav} into dose to water D_{med} rely on CPE-based approximations, as does the conventional stopping-power ratio medium-to-detector, $S_{med,cav}$ which uses the approximation of constant electron fluences, $\phi_{med} \approx \phi_{cav}$ [26]. Under the assumptions that both the stopping-power ratios water-to-detector medium and the perturbation correction factors are field-size independent, perturbation effects are usually neglected in the relative dosimetry of broad photon beams [51].

However, for most detectors in small radiation fields there are important perturbation effects caused by differences in electron fluence in the detector and in the otherwise homogeneous medium. As a result, $\phi_{med} \neq \phi_{cav}$, and the perturbation correction factors are field-size dependent. This is explained by the energy dependence of the stopping-power ratio of a detector SV- and surrounding packaging material-to-water. The energy dependence is governed solely by the mean excitation energy (I-value) of the material for low electron energies, and by the combined effect of the I-value and the electron density n_e ($n_e \propto \rho Z/A$) for electron energies above a few hundred keV. Both parameters enter the so-called 'material perturbation factor' (or density-effect) of the mass electronic stopping power. The result of the fluence inside the detector being substantially different from the fluence in the undisturbed medium is that the condition for CPE is violated and Bragg-Gray cavity theory is no longer valid [26].

As a rule of thumb, CPE fails when the photon beam radius becomes small in comparison to the maximum range of the secondary electrons depositing the dose [26]. Since their range depends on their energy, the beam radius at which CPE fails increases as the beam energy

increases [2]. The parameter r_{CPE} can be used as a measure of the range of laterally scattered electrons. It represents the smallest field dimension for which, past the build-up region, the absorbed dose D and collision kerma K_{el} become proportional as a function of field radius [2]. In other words, it defines the minimum beam radius for which the CPE assumption is verified, and can be expressed as a function of the photon beam quality $TPR_{20,10}$[5] [1], [26]:

$$r_{CPE} = 8.369 \times TPR_{20,10} - 4.382 \quad (2.22)$$

r_{CPE} expressed in units of cm. A measurement in a given beam quality is said to be performed in a small field if the distance from the detector outer boundary, including its SV and packaging, to the radiation field edge is smaller than r_{CPE} [26].

As the radiation field size decreases, there are also changes in the energy spectrum of the photon fluence owing to a reduction in the scattering occurring in the linac head and in the phantom (or patient), because the irradiated volume is smaller. This results in a filtration of the low photon energies and an increase in the mean energy of the photon spectrum [2], [26]. The secondary electron fluence distribution mostly follows the trend of the photon energy distribution, but the effect is compounded in the case of a lack of CPE on the central axis (CAX) [2]. That is because, when the distance to the field boundary is less than the range of secondary electrons, the average energy of the electrons increases at the CAX of the field as lower-energy electrons are under-represented there [2].

In medical linacs, small fields are obtained by collimation jaws, MLCs, conical collimators. The collimation produces a partial occlusion of the primary photon source at the exit plane of the bremsstrahlung target for x-rays (also known as the focal spot size), with a drastic reduction in output fluence rate [2], [52]. The radiation source becomes relatively large compared to the radiation field, and a larger percentage of the field is made up by penumbra, making volume averaging within the detector problematic [2]. In other words, contrary to the case of broad beams, in small beams the size determined by the full-width half-maximum (FWHM) of a radiation field at a typical depth in a phantom, normalized to the beam CAX, usually does not coincide with the indication of the machine collimators, because of the apparent widening of the field [26].

[5] $TPR_{20,10}$ is tissue phantom ratio in water at the depths of 20 and 10 g/cm^2, for a field size of 10 cm $\times$ 10 cm defined at a surface-to-detector-distance (SDD) of 100 cm.

Also the size of the detector used to characterize the radiation field is of relevance in small-field measurements, as a detector with a cross-sectional dimension larger than the one suitable for the field size at the depth of measurement may result in volume averaging effects [2], [26].

In summary, the dosimetry of small photon beams is defined by an absorbed-dose distribution characterized by [2], [26]*:*

- a lack of CPE;
- occlusion of part of the source;
- relation between the size of the radiation field and the dimensions of the detector.

2.2.2 Quality assurance

A comprehensive and dedicated QA program, i.e. procedures that ensure that the prescribed absorbed-dose distribution is delivered to the intended target, must be in place. It would have to encompass all aspects of radiation treatment ranging from linac commissioning to delivery and be performed by a specialized and dedicated team. Failure to meet these requirements may lead to dosimetry inaccuracies and, as a consequence, to poor outcomes for patients [2], [24]. As an example, the output of a TPS is substantially affected by the choice of using measurement procedures and techniques suited to broad fields, as opposed to small-field-specific ones [53], [54].

An essential part of a small-field-specific QA protocol aimed at ensuring dosimetry accuracy is the selection and use of appropriate small-field dedicated detectors [53]. As a starting point, it is good practice to assume that a detector suitable for measurements in broad fields will not be appropriate for measurements in small fields, unless proved otherwise [1].

Ideally, dosimeters would have to be point-like to avoid any volume averaging effects, allow for high positioning accuracy and high spatial and temporal resolution (pulse-by-pulse real-time acquisition), be water equivalent with limited particles fluence perturbation due to SV and packaging, exhibit a response stable and linear with dose and dose rate, ensure a good signal-to-noise ratio, be affected by limited directional dependence [1], [2], [55] (Table 2).

Table 2. Characteristics of detectors for relative small-field dosimetry. Adapted from [41].

Property	Guideline	Notes
Stability	better than 0.1% for a total accumulated dose of many hundreds of kGy, from multiple exposures	Corrections can be made provided the effect is consistent and recalibration is not frequently required
Linearity with dose	better than 0.1% over a dose range of at least 3 orders of magnitude	
Independence of instantaneous dose rate (dose per pulse)	better than 0.1% over the range of interest, typically from 0.2 mGy to 2.0 mGy per pulse	
Energy dependence	minimized in the energy range of interest, typically ^{60}Co to 10 MV	Ideally, energy independent with interaction coefficients (μ_{en}/ρ for photons, S/ρ for electrons) having a constant ratio to those of water
Spatial resolution	trade-off between a high signal-to-noise ratio and a small SV	requirement is set by the dose gradients in the radiation field of interest
Size of SV	Correction for volume averaging better than 5%	
Directional dependence (angular dependence)	better than 0.5% for angles $< 60°$ between the beam axis and the detector axis	Corrections can be made to minimize the effect, or beam incidence can be kept fixed
Background signal (leakage signal)	at least 3 orders of magnitude lower than the detector response	
Environmental factors (temperature, …)	corrections can reduce any influence to better than 0.3% over the full range of working conditions	

None of the detectors currently available is ideal for small-field dosimetry [2]. As a consequence, it has been common practice to perform measurements with at least two types of dosimeters to cross-check the consistency of results [6], as recently recommended by an ICRU report [2]. For example, it was suggested the use of a combination of detectors with perturbation correction factors above and below unity (so that the product of these factors is close to one), such as a micro-ionization chamber, radiochromic films and a solid-state detector (either silicon- or diamond-based) [1]. Type of detectors and their characteristics will be discussed in section 2.3 (page 23)

2.2.3 Radiation quality characterization

Relative dosimetry of small fields for clinical use, e.g. for beam modelling for TPS commissioning and verification, involves the determination of field output factors (OFs), of CAX percentage depth dose (PDD) distributions, tissue phantom ratios (TPR) or tissue maximum ratios (TMR), and lateral beam profiles or off-axis ratios (OAR), all as a function of field size and shape [1], [2].

The OF is a ratio of the absorbed dose D in a clinical field of interest f_{clin} to that in a reference field f_{ref} (usually the 10 cm side square field), at a given depth z. For broad beams, the OF is simply taken as the ratio of the detector readings M [26]:

$$OF_z(f_{clin}) = \frac{D(z, f_{clin})}{D(z, f_{ref})} \approx \frac{M(z, f_{clin})}{M(z, f_{ref})} \tag{2.23}$$

The approximation is justified by the practical constancy of stopping-power ratios and perturbation factors with field size, for a given photon beam quality [26]. In small field dosimetry, these assumptions are no longer valid [56], [57]. Therefore, it is then necessary to calculate the OF as [1], [26]:

$$OF^{f_{clin},f_{ref}}_{Q_{clin},Q_{ref}} = \frac{D^{f_{clin}}_{Q_{clin}}}{D^{f_{ref}}_{Q_{ref}}} = \frac{M^{f_{clin}}_{Q_{clin}}}{M^{f_{ref}}_{Q_{ref}}} \times k^{f_{clin},f_{ref}}_{Q_{clin},Q_{ref}} \tag{2.24}$$

Q a given beam quality and the factor

$$k^{f_{clin},f_{ref}}_{Q_{clin},Q_{ref}} \tag{2.25}$$

a multiplier called “field output correction factor”. It is used to convert the detector readings ratio into dose-to-water ratio and depends on detector design (SV and extra-cameral[6]

[6] In the present work, packaging and extra-cameral components are used interchangeably

components), treatment head design, beam quality, radiation field size and measurement conditions [1], [2].

The field output correction factor can be determined using Monte Carlo simulations or via experimental comparisons with the response of an ideal detector taken as reference [56], [58]–[62]. If determined by Monte Carlo, it requires knowledge of the detector construction and deficiencies in information provided by vendors, or manufacturing variability, will lead to inaccurate results [63].

A preferable solution would be to design a 'correction-free' detector, or one maintaining a correction factor close to unity. This has been shown to be possible with the addition of low density media to the high density detector components [64]. However, it would still be necessary to verify that these modifications are appropriate under all beam quality and measurement conditions [65].

For OFs measurements, the volume averaging effect may be a limiting factor, therefore a detector size must be such that the radiation fluence is uniform over the detector area [1] and the minimum field size recommended for measurements with any given detector is such that the detector-specific correction factor is not greater than $\pm 5\%$ for a given machine [1].

For any given clinical field size f_{clin} of interest, PDD, TMR and OAR are defined as [20]:

$$\mathrm{PDD}(z, f_{clin}, SSD) = \frac{D(z, f_{clin}, SSD)}{D(z_{max}, f_{clin}, SSD)} \tag{2.26}$$

$$\mathrm{TMR}(z, f_{clin}) = \frac{D(z, f_{clin})}{D(z_{max}, f_{clin})} \tag{2.27}$$

$$\mathrm{OAR}(r, z, f_{clin}) = \frac{D(0, z, f_{clin})}{D(r, z, f_{clin})} \tag{2.28}$$

z the depth of measurement, z_{max} the depth of maximum dose, r the distance from the CAX and SSD the source-to-surface distance.

The ability of different dosimeters to correctly measure these quantities in water for small field should be individually assessed [61]. As in the discussion of OFs measurements, the same precautions in terms of dosimeters and their performance apply, and the assumption that the detector correction factors are independent of field size is not valid [2]. In these cases, though, even if correction factors may be calculated or defined, they are inconvenient to use in practice because of the multi-dimensional factor-dependencies (radiation field size, measurement depth and distance from CAX) [59].

The PDD distribution is measured for a fixed phantom arrangement i.e. at a given SSD by moving the detector to different depths. The field size and the energy spectrum changes with depth. The photon spectrum becomes harder with depth, but whereas in broad fields this effect is offset by an increasing amount of scattered radiation, which, depending on the field size, might lead to the photon spectrum effectively becoming softer, this is not true in small fields. As such, detectors that have a strong energy-dependent response are not well suited for PDD measurements in small fields and require the application of field size and depth dependent correction factors [2].

Some TPSs require the measurement of a TMR instead of PDD. The TMR is measured for a fixed source-to-detector distance (SDD) by changing the height of water over the detector. The motivation for measuring A TMR measurement is potentially more accurate than a PDD measurement because the accurate detector positioning on the CAX is performed only once. In addition, the field size at the detector location does not change, therefore there might be fewer corrections to apply or might, for instance for volume averaging effect, cancel. A TMR measurement does not avoid issues related to the change in beam spectrum altogether, though, as the amount of attenuating material in front of the detector changes [2].

Beam modelling typically involves the acquisition of dose profiles in both directions (in-plane and cross-plane) at a variety of depths [2]. The photon spectrum at a given depth as a function of off-axis distance varies much less in small fields than it does in broad fields. Thus, in small fields, for off-axis measurements a detector with a modest energy dependence can be still be used [2].

The TMR discussion regarding the necessity for a correct mounting and precise alignment of the detector on the CAX at all depths applies also to dose profile measurements.

It is advised that a detector allows for high spatial resolution measurements [1]. The use of a detector with a small SV is extremely important to avoid volume averaging effects and significant penumbra blurring of the steep lateral penumbra of the profile [1], [2],

A detector reading dependence on dose-rate or dose-per-pulse changes would have to be verified and corrected for [1], [2]. Instantaneous dose-rate dependence may manifest itself by an overestimation of the absorbed dose by some percentage in part of the profile at distance from the CAX. In this case, a correction is to be made. This is especially relevant for FFF beams, where dose per pulse values are higher than for flattened beams and may affect a detector performance [1].

2.3 Available suitable small-field dosimeters (or lack thereof)

2.3.1 Classes and types

In small-field dosimetry, it is expected that the choice of the most appropriate detector is made according to the parameter (OFs, PDD, TMR, OAR) being measured [1]. Many types of dosimeters (Table 3) have been proposed and tested, but, as previously mentioned, no single system has, at the time of writing, characteristics sufficiently close to an ideal one [1], [2].

In the present section we will present a brief outline of the most common systems. The reader may benefit from reading recent and more comprehensive reviews which have discussed available dosimeters in the context of modern radiotherapy [27], [66]. There exists also more specific ones dedicated to small-field applications [1], [2].

Ionization chambers (IC) are the recognized standard for broad-field dosimetry, but traditional ones are impaired by volume-averaging effects in small radiation fields [1], [27]. These effects are mostly avoided by using micro-ionization chambers (SV of $0.002-0.01\ cm^3$), which have however a reduced sensitivity. Their signal leakage can be significant, particularly in low-dose regions [1]. Even micro-chambers, though, are deemed not suitable for small-field dosimetry [53]. The effective point of measurement is generally not well-known [2], leading to significant uncertainties in the case of PDD measurements where the radiation field size changes with depth. They are also not recommended for measurements of OARs [61].

Plastic scintillators [67]–[69] can be manufactured of very small SVs and are relatively inexpensive. They are usually tissue-equivalent [70]–[72]. They have a wide dynamic range and no directional dependence [72]. When used in megavoltage photon beams, generation of Cherenkov radiation creates a signal not directly related to dose [73]. Corrections [74] are possible and required [75] but of complex application in small radiation fields [27]. Recent developments have been aimed at tackling this problem [67], [76].

Radiochromic films, despite their relatively high cost, are considered attractive thanks to the easy set-up required [27], superior 2D spatial resolution and nearly tissue equivalence [10], [77] and little energy dependence [1] which manifests in an over-response at low dose-to-water levels outside the field owing to their increased sensitivity to low-energy photons [1]. They have to be used with caution as they are known for their limited absorbed dose range dependence [1]. A radiochromic film is really a complex detector system composed of film proper, read-out device (scanner) and analysis software, and handling procedures and

techniques. As such, limitations and potentials are to be discussed with respect to the whole system and not just to the film proper [27]. For instance, careful control of film processing and read-out procedures is essential for accurate dosimetry. The read-out procedure, which is not real-time, requires accurate absorbed dose-to-water calibration, including careful investigation of spatial non-uniformity of film response, scanner response and dependence of signal on film orientation [1].

Gel dosimeters [78] are today mostly based on polymers [79]. They are tissue equivalent and have found extensive use in brachytherapy [79], [80] but not in EBRT [27]. Their spatial resolution is only limited by the evaluation technique in use [27]. They allow for inhomogeneities [81] and deformation [82]. Poor performance has been reported when delivered dose exceeded the range of doses considered in the calibration procedure [83]. Production and standardization of homogenous 3D gel is challenging and less advanced than for film dosimetry [27]. As for film dosimetry, gel dosimeters need to be seen as a complex detector system which includes their read-out and analysis procedures [27].

Dosimetry in small radiation fields calls for relatively small SVs. Not surprisingly, solid-state dosimeters play in this context an important role [27]. They can be made sufficiently small while remaining relatively sensitive. Their sensitivity is much higher than that of ICs of the same volume due to a higher density and an ionization energy that is smaller than for gas [84]. Their potential is for a high-spatial resolution performance comparable to that of radiochromic films, but with a real-time read-out. They have good mechanical stability and it is possible operation with and without external bias [84], [85].

Traditionally, diodes [86], in particular unshielded diodes, have been used. A common choice still today, they will be discussed in more detail in the next section (chapter 3, page 28).

Synthetic diamonds are an alternative [87]. They have a response almost energy-independent thanks to the relatively constant ratio of stopping-power and mass energy absorption coefficients of diamond to water. Commercially available diamond detectors, based on artificial chemical vapour deposition (CVD) diamonds, are used without external bias. Their directional response is uniform. They have been considered for a long time as attractive detectors for small-field dosimetry [60]. However, they require correction factors for measurements in radiation fields < 1 cm across [1]. Albeit more uniform in their response characteristics and more affordable [88], [89] than once-used natural diamond detectors, correction factors vary in the literature and appears to be different between different copies [90]. Synthetic diamonds are still relatively expensive and as such not widely employed.

Table 3. Detectors and their use for small-field dosimetry. Adapted from [2] and [30].

Class	Type	Advantages	Disadvantages	Selected references
Ionization chambers	Air-filled	Broad dose range, multiple configurations, reproducibility; uniform directional response, independent of dose rate	Low sensitivity per unit volume, stem and cable effects to be corrected for, polarity effect to be corrected for; volume averaging in small fields	[91]–[94]
	Liquid-filled	Small SV, small perturbation, energy independent, nearly water equivalent	Dose-rate dependence, temperature dependence, stem and cable effects to be corrected for, long-term stability issues	[95]–[98]
Scintillating detectors	Fiber	Small SV, tissue equivalence for photons	Cerenkov correction, LET dependence	[67]–[69]
Chemical detectors	Radiochromic film	Nearly energy independent, density of detection material close to unity, high resolution, 2D dosimeter	Measurement protocol involved, elaborate processing; non-linear response, reproducibility for low doses is limited	[10], [77]
	Gel dosimeter	3D dosimeter	Non-trivial protocol for processing, involved instrumentation, reproducibility for point type measurements	[79], [80]
Solid-state detectors	Diode	Small SV, ease of use, cost-effective, mature fabrication technology; can be arranged in arrays to form a 2D dosimeter	Energy dependence, accumulated dose and dose rate dependence, directional dependence, temperature dependence; perturbations caused by the substrate	[64], [99]–[101]
	MOSFET	Small SV, cost-effective, generally used for *in-vivo* dosimetry	Energy dependence, directional dependence, poor signal to noise ratio, inadequate reproducibility, perturbations caused by the substrate	[84], [102]
	Diamond	Small SV, tissue equivalence for photons, uniform directional response	Dose rate dependence, effect of mass density compared to water	[28], [60], [90], [103], [104]
	TLD, OSLD	No cables or connectors; generally used for audit programmes	High density, non-trivial protocol for processing, variable tissue equivalence for photons	[105]–[107]

2.3.2 Point detectors and array detectors

It is worth discussing available detectors also distinguishing between point-like detectors and arrays. Point-like detectors have long been the typical choice for broad-beam radiation dosimetry, as the dose was typically assessed in points of interest [27]. In small-field dosimetry, when used with various scanning techniques to measure 2D dose distributions, they remain the only commercially available option able to satisfy the sub-millimetre spatial resolution requirement [2].

However, a logical step in the development of devices for QA is to combine point-like detectors into arrays.

1D arrays have been used for commissioning and QA procedures [108]. Arrays have advantages for routine QA: increased time efficiency with the acquisition of multiple data at once. Along with commonly characterized QA parameters, such as OFs, PDD, TMR and OAR, thanks to their fixed geometry, these devices would allow for easier accurate and repeatable machine-specific QA: examples would include the positional accuracy verification of the movable parts of a linac, such as the leaves of an MLC and the aperture of dynamic circular collimators (Iris™). They would also allow for a more accurate alignment with respect to the beam CAX, as opposed to point-like detectors, which remain affected from positioning and alignment-related inaccuracies [1].

There are also other reasons for introducing arrays, and specifically of real-time ones. The use of point-like detectors in patient-specific QA has limitations in the context of complex dose distributions used in modern MV EBRT [27]. Temporal beam-modulation requires integrating dosimeters and the scanning technique cannot be used to measure dose distributions in dynamic fields. The use of real-time arrays was investigated in dynamic wedge deliveries [109] and in IMRT [110]. Their ability to resolve individual beam pulses was used for research purposes [111], and they have been proposed for on-line transit portal dosimetry [112], for measurements in electron-beam radiotherapy [113] and in mixed electron-photon fields [114].

In the case of arrays, care must be taken to ensure that the pitch between SVs is suitable for the size of the radiation field of interest and for accurately assessing its dose gradients.

A preferable alternative to 1D arrays would be 2D arrays. In particular, 2D monolithic silicon-diode arrays can be fabricated of relatively large area while optimizing the spatial resolution with small SVs [115]–[118].

Diodes and ICs are a common choice for arrays, but scintillator-based arrays have also been proposed [69], [119]. The Octavius 1000SRS (Figure 5) is an example of a 2D array of 977 ICs. SVs have a pitch of 2.5 mm in the square central area of 5 cm side, and a 5 mm pitch outside. In small fields, the performance of the 1000SRS was found to be comparable to EBT3 films in terms of accuracy and sensitivity, but more user-friendly [13]. Array of diodes will be discussed in section 3.3.3 (page 36).

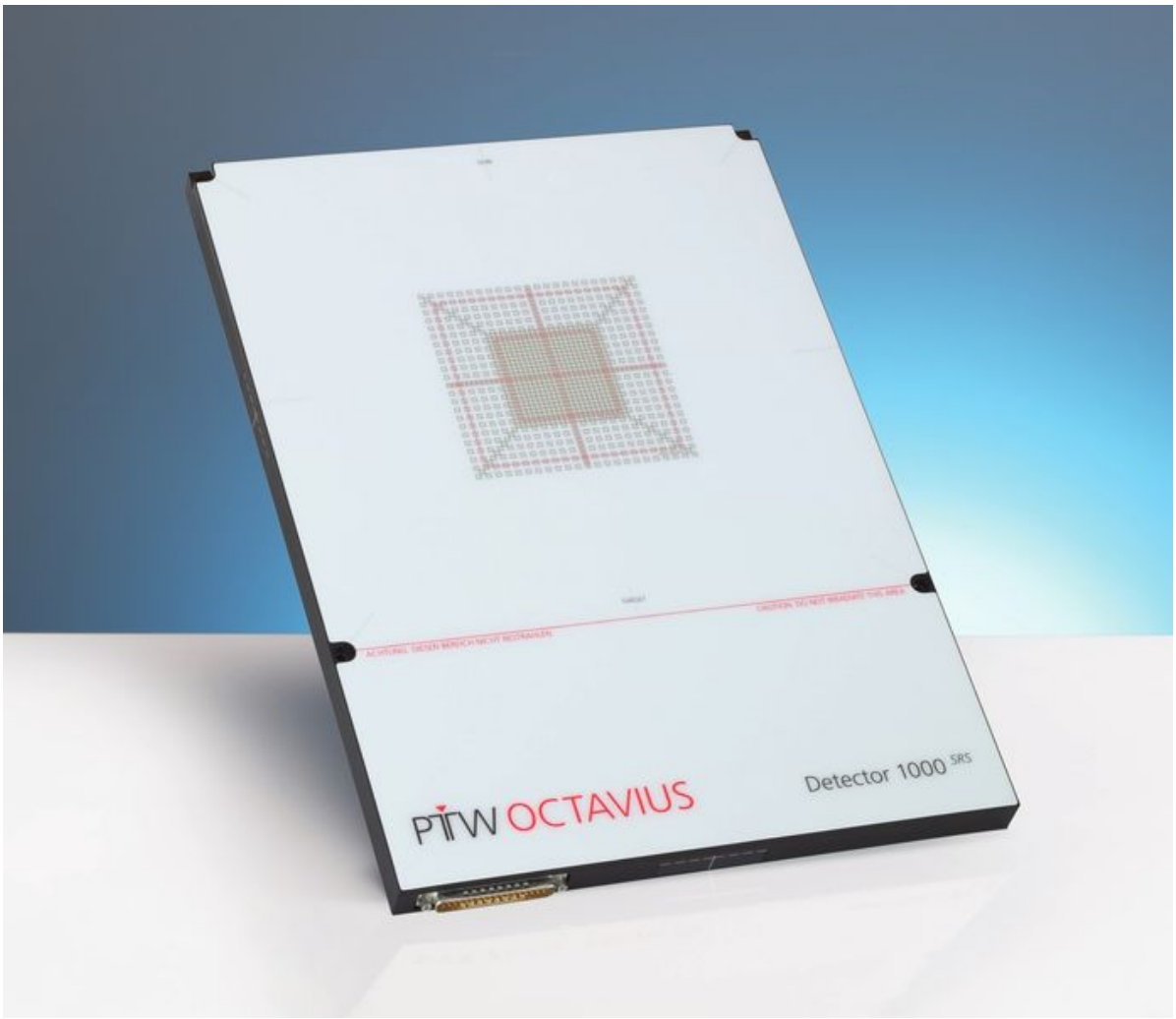

Figure 5. The Octavius 1000SRS is a 2D array of 977 liquid-filled ionization chambers. Image courtesy of PTW, Germany[7].

[7] https://www.ptw.de/2287.html

3 A review of silicon-based dosimeters

3.1 Why silicon?

The operation of a silicon-based detector is simple [120]: it is based on the existence of an electric field across a volume dV where there is a low concentration of free charge carriers. When incident ionizing radiation deposits energy E in dV, N of these carriers, i.e. electron–hole pairs are created:

$$N = \frac{E}{w} \tag{3.1}$$

w the mean energy required to produce free charge carriers. Owing to the existing electric field, free charge carriers are swept across dV and are available for collection by electrodes. The collected charge is directly proportional to the dose deposited in the silicon.

Silicon-based dosimeters, which can be operated both in passive (i.e. no external bias applied) and in active mode, offer key features such as high signal-to-noise ratio explained by a relatively small energy band gap ($E_g = 1.12$ eV at 300 K), the possibility of manufacturing compact SVs in the order of $\sim\mu m$ while still retaining a relatively high sensitivity (a sensitivity per unit volume 18000 times greater for silicon than for air used for ICs), fast signal collection in the order of $\sim ns$, a response which is stable and linear with accumulated dose [66], [120].

Silicon-based dosimeters have wide application for integral dosimetry of reference and relative absorbed dose in electron- [121] and photon-based radiotherapy techniques, such as brachytherapy [122] and both kilovoltage [123] and megavoltage [27] x-ray EBRT. They are used for commissioning and machine-specific QA of linacs, for commissioning and verification of dose calculations with algorithms implemented into a TPS, and for pre-treatment or patient-specific QA.

At present, the silicon structure most commonly used for dosimetry is the diode. It can be manufactured starting from a pure silicon (group IV) substrate, doped by adding phosphorous (group V) with concentrations of 10^{14} to 10^{16} $1/cm^3$, or boron (group III) with concentrations of 10^{15} to 10^{17} $1/cm^3$. In the first case, valence electrons are donated resulting in a n-type base, while in the second case holes are created in the crystal lattice resulting in a p-type base. Commercial diode dosimeters are typically created starting with a lightly doped p- or n-type base, and then heavily doping the surface region with a concentration of more than two orders of magnitude than that of the substrate with impurities of the opposite type to form a junction.

Joining together n- and p-type, electrons diffuse from the former to the latter and holes in the opposite direction until a depletion region w (Figure 6) is created where an electric field of the order of 10^3 V/cm prevents further diffusion. Under unbiased conditions the region is < 1 μm for typical doping concentrations used for commercial diode dosimeters. It is worth noting that the region can also be extended by applying a reverse bias, essential for using diodes in spectroscopy applications.

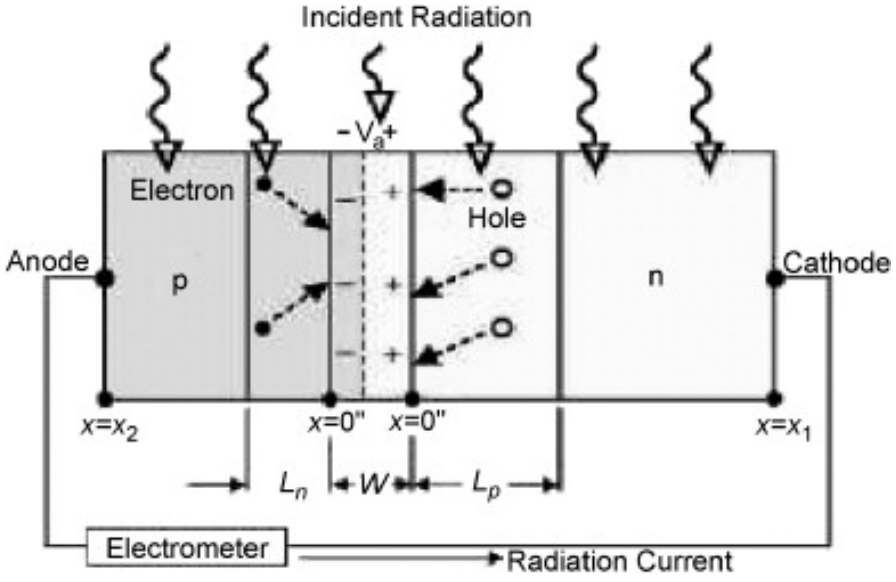

Figure 6. p-n junction. Incident ionizing radiation generates excess minority charge carriers (electrons, holes). These, if within one diffusion length (L_n, L_p) from the junction, are swept through it and are collected by electrodes. Collected radiation-induced current is proportional to dose rate. Image courtesy of [124].

Considering the mean electron-energy required to produce electron–hole pairs, it is possible to show that the generation constant for silicon under ionizing radiation is [125]:

$$g = 4.2 \times 10^{13}\ \text{electron} - \text{hole pairs/cGy/cm}^3 \qquad (3.2)$$

Medical linacs deliver dose in pulses with a duration in the range from 2 μs to 6 μs and with a repetition frequency in the range from 180 Hz to 400 Hz. The dose in a single pulse $\dot{D}$ (or instantaneous dose rate to water, of the order of 10^2 Gy/s) determines Q, the rate of excess minority charge carriers (Δn in a p-type diode, Δp in an n-type diode) generated in silicon per cm^3 [124]:

$$Q = g\dot{D} \qquad (3.3)$$

Excess minority charge carriers diffuse toward the junction and, if the device is operating in unbiased conditions, are swept across by the built-in potential. Only excess minority charge carriers within one diffusion length, L_n for electrons on the p-side and L_p for holes on the n-side (Figure 6) reach the junction and are eventually collected by electrodes. L_n (L_p) is a function of the diffusion coefficient constant of minority charge carriers D_n (D_p), a constant

which only depends on silicon resistivity and temperature, and of the mean lifetime of minority charge carriers τ_n (τ_p) [124], [126], a function of defects concentration, intrinsic or radiation-induced. For a p-type diode [8]:

$$L_n = \sqrt{D_n \tau_n} \tag{3.4}$$

τ_n (τ_p) can be written as [124], [127]:

$$\tau_n = \frac{1}{\sigma_e v_{th} N_t} \tag{3.5}$$

v_{th} the thermal velocity of electrons, σ_e the cross section of minority charge carrier capture for generation-recombination (G-R) centres and N_t their concentration. It is worth mentioning that there may be also other processes, distinct from G-R centres, involved in the recombination of minority charge carriers [99], [128], [129].

The sensitivity S of a diode, in terms of charge collected by electrometers, is proportional to the product of Q and the dimensions of the SV of the diode in terms of its cross-sectional area A and the minority charge carrier diffusion length. For a p-type diode [124]:

$$S \propto QAL_n \tag{3.6}$$

using expressions (2.31), (2.32) and (2.34):

$$S \propto g\dot{D}A\sqrt{D_n \tau_n} \tag{3.7}$$

3.2 Limitations of silicon detectors

The response of a diode to incident ionizing radiation, as can be partially inferred from relationship (2.35), depends on accumulated dose D (responsible for radiation damage) [130], instantaneous dose rate $\dot{D}$ (also referred to as dose per pulse, DPP, dependence) [128] and temperature T (also referred to as relative temperature instability RTI) [131]. It also has a directional dependence [101], [132] and a radiation field-size dependence in megavoltage photon beams [26]. These limitations are introduced in the present section and further discussed in chapter 9 (page 124) and chapter 10 (page 149).

3.2.1 Accumulated dose dependence

The concentration of radiation-induced defects increases with accumulated dose, and τ_n (τ_p) decreases accordingly, causing a gradual decrease in S:

[8] under the assumption of low-injection conditions, i.e. a condition for which the excess minority charge carriers concentration Δn is relatively small compared to the equilibrium majority charge carriers concentration p_0 ($\Delta n / p_0 \ll 1$), for a p-type diode

$$\Delta\frac{1}{\tau_n}\sim\Phi \tag{3.8}$$

Φ the incident radiation fluence [117], [133]. The dependence of S on accumulated dose is not linear, with steeper gradients at lower doses up to approximately 4 kGy [117]. Degradation of S with accumulated dose is a function of beam quality (energy, particle type) and of previous irradiations.

A degradation of 25% after an accumulated dose of 6 kGy (18 MV photon beam) and of 20% after an accumulated dose of 10 kGy (6 MV photon beam) were reported for n-type diodes [134]. Higher photon energies cause increased radiation damage owing to the presence of neutrons generated by photonuclear reactions. A comparable reduction in S in the range from 20% to 25% was reported for p-type diodes for accumulated doses > 10 kGy (electron and photon beams) [135]. Degradation of S with accumulated dose is typically less pronounced for a p-type diode [136], explained by dominant defects produced by electron radiation in silicon having a capture cross-section for holes higher than that for electrons [124].

Stabilization of S has historically been addressed with pre-irradiation, taking advantage of the saturating behaviour of τ with accumulated dose. Usually pre-irradiation electron dose is of the order of 10^4 Gy. To counter the subsequent increase of leakage currents the device can be operated in passive mode.

More recently, it was shown that it is possible to achieve an S almost independent of accumulated dose by fixing the dimensions of the SV in two directions: laterally, by using guard-rings, and in depth, by growing onto a highly conductive substrate an epitaxial layer whose thickness is shorter than the expected L_n (L_p) in the operative dose range. For a p-type epitaxial device with a thickness of 50 μm grown on a Czochralski (Cz) substrate, if:

$$L_n \geq W, r \tag{3.9}$$

W the epitaxial layer thickness and r the guard ring-SV distance, S was found to be stable even at the highest accumulated dose [117].

3.2.2 Instantaneous dose rate dependence

The fraction of excess minority charge carriers Δn (Δp), generated in a single beam pulse produced with a medical linac, that recombine with majority charge carriers is a function of N_t (relationship 2.32), which can be considered constant for successive pulses [129]. However, it also depends on Δn itself, i.e. on the injection level [117], [129]. This is because while at low instantaneous dose rate the G-R centres are mostly empty, and a fraction of the excess minority

charge carrier is captured and recombines, as the instantaneous dose rate increases the centres are filled. Eventually, as they approach saturation, the fraction of excess minority charge carriers recombining decreases and a larger fraction is available for collection by the electrode [124], [129].

In the case of radiation delivered by a linac, intermediate injection levels during each pulse apply, the excessive minority charge carrier concentration being of the same order of the majority charge carrier concentration (10^{16}– 10^{17} $1/\mathrm{cm}^3$). For small-deviations from a low-injection condition, the time-scale on which recombination happens is written as [117], [124], for a p-type diode:

$$\tau \approx \tau_n \left(1 + \frac{(\tau_p + \tau_n)}{\tau_n} \frac{\Delta n}{p_0}\right) \tag{3.10}$$

By recalling expression (2.34), it is apparent the origin of the dependence of S on instantaneous dose rate.

Experiments with p-type and n-type diodes demonstrated large differences in the dependence of S on instantaneous dose rate [124], [129], [130], [137]. These are explained by initial characteristics of the diode base in terms of initial resistivity and defects concentration, both intrinsic and deliberately introduced.

N-type diodes have shown an increase in the instantaneous dose rate dependence after pre-irradiation within 4%, whereas pre-irradiated p-type diodes have shown an increase within 1% in the range 1×10^4 cGy/s to 4×10^4 cGy/s [131]. For n-type diodes the instantaneous dose rate dependence was shown to increase with accumulated dose. Detailed analysis [124] demonstrated that, owing to the physics of G-R centres, the instantaneous dose rate dependence is stronger in n-type diodes than in p-type diodes.

Considering expression (2.38), it is also apparent that it is possible to reduce the instantaneous dose rate dependence by decreasing the resistivity of the substrate (p_0 is inversely proportional to the resistivity) [137], or reducing the minority charge carrier lifetime (τ_n, in this case) [117], [128].

3.2.3 Temperature dependence

The RTI of S can be explained by considering:

$$\frac{dS}{dT}\frac{1}{S} = \frac{d\ln S}{dT} \propto \frac{d\ln \tau}{dT} \tag{3.11}$$

The variation of S with temperature T depends on the irradiation history of the diode as well as on its material and packaging. This is supported by investigations of commercially available

diodes. RTI in the range 0.29% to 0.36% per °C was first reported [131]. Other studies reported a variation of S with temperature in the range 0.02 to 0.28% per °C [135]. RTI was independent of the instantaneous dose rate for pre-irradiated diodes, but not for unirradiated n-type diodes. It was proposed that pre-irradiation could eliminate the instantaneous dose rate dependence of RTI, but not the instantaneous dose rate dependence of the diode response itself.

Pre-irradiation can be used to stabilise the RTI owing to:

$$\frac{d\ln\tau}{dT} \sim N_t \frac{d\tau}{dT} \tag{3.12}$$

Subsequent irradiations do not further increase RTI due the same saturating behaviour of τ with accumulated dose, and the RTI initially assessed can therefore be used for corrections at any accumulated dose.

From a clinical perspective, the variation of S with temperature is a problem potentially affecting the dosimetry when the diode is placed on the patient and is used for *in vivo* entrance dose measurements. In this case, it may take up to about 5 minutes to reach equilibrium temperature with the patient surface [138], depending on the packaging of the detector. Suitable corrections should be applied [66]. An alternative approach for stabilization of S and RTI with accumulated dose consists in the deliberate introduction of defects acting as suitable G-R centres [137], [139]. Oxygen, platinum and gold can be used for an unirradiated n-type base, leading to a final effective concentration of G-R centres with properties resembling those of a pre-irradiated p-type base.

3.2.4 Directional dependence

Silicon detectors are known to have a directional-dependent response. The angular dependence of diodes and diode arrays has been reported in several studies and explained mainly by anisotropy in materials surrounding the detector SV and detector assembly. This is because the different materials surrounding the SV generate a varying secondary electron spectrum depending on irradiation angle [101], [132].

The detector angular dependence limits its accuracy for plan verification for arc radiotherapy delivery. It can be mitigated by using an angular dependence correction methodology [132].

3.2.5 Energy dependence

The response of silicon detectors is energy dependent [99], owing to a relative increase, in silicon relative to water, of the cross-section for the photoelectric effect. At photon energies

below 200 keV, the energy mass-attenuation coefficient of silicon is up to seven times higher [140], [141].

The significant low-energy scattered-photon component in broad radiation fields explain the over-response of diodes, which can be up to 10% [2], [22], [142]. Historically, this has been addressed by using shielded diodes (also referred to as photon diodes), i.e. by encapsulating the SV with high-Z packaging to absorb low-energy photons [143], [144]. Monte Carlo analysis suggested that shielding can be responsible for a significant filtration of low-energy photons [51]: for instance, approximately 50% of photons below 100 keV are filtrated in a PTW T60016 diode. A small shielding effect can also be observed in unshielded diodes, owing to the presence of thin layers of materials in the packaging surrounding the SV proper.

Shielded and unshielded diodes are expected to have a different response, which was compared in 6 MV and 10 MV flattened photon beams [44], with shielded diodes requiring $<$ 1% correction, down to radiation fields 2 cm across.

The low-energy scattered-photon component increases with depth. However, some diodes have been reported to exhibit under-response at large depths, an effect attributed to their instantaneous dose rate dependence [61].

3.3 Use of silicon diodes for small-field dosimetry

3.3.1 Preliminary considerations

The performance of silicon detectors for small-field dosimetry can be optimized by designing SVs as small as reasonably possible relative to the smallest photon beam size of application, in order to minimize volume averaging effects and positioning inaccuracies.

Unshielded diodes, and in particular stereotactic diodes [1], [2], are better suitable for measurements in small radiation fields [28], [51], [141], [145], [146]. The low-energy scattered-photon component is significantly reduced in small fields, relative to broad fields, and unshielded diodes typically perturb less both photon and electron spectra [26], [51] and have a response which is less angularly-dependent [1]. Unshielded diodes can produce high-resolution relative OAR measurements practically identical to Monte Carlo-calculated ones in water and are suitable for use in fields $<$ 3 cm across provided appropriate field-size dependent correction factors are applied [1], [2], [26] (see section 2.2.3 page 20).

Monte Carlo simulations have been shown to be an effective tool in characterizing detector responses in small fields and their required correction factors [56], [57], [59], [61], [62], [147]. As previously introduced, these remain inconvenient to use in practice, especially for PDD,

TMR and OAR, because of the multi-dimensional factor dependencies (radiation field size, measurements depth and distance from CAX). It is recommend PDD, TMR and OAR corrections be used for an informed selection of the detector and evaluation of the results rather than for correcting measurements [59]. Most importantly, calculating correction factors by Monte Carlo simulations requires detailed knowledge of a detector construction and inaccurate information will produce inaccurate results [63].

It is possible to design a 'correction-free' detector, or one requiring a correction factor sufficiently close to unity. This can be achieved by limiting or removing high atomic-number and density components, and/or by adding low atomic-number and density components, in the packaging surrounding the SV [28], [48], [49], [64], [148]. Amount and characteristics of these modifications are intended to balance the spectral perturbations introduced by the non-water atomic number, density and I-value of the SV (and extra-cameral components). The modifications have a complex dependence on atomic number, density and I-value of SV (and extra-cameral components) materials, as well as on the considered photon-beam quality and measurement conditions [51]. It is necessary to verify that, when introduced, they are appropriate under all relevant measurement conditions [65].

3.3.2 Point detectors

The performance in small radiation fields of commercially available diodes has been assessed in various investigations.

One of those [6] considered SRT-dedicated conical collimator of diameter 5 mm to 45 mm. Measurements were performed with Gafchromic EBT2 films (Ashland Inc, USA), an SFD diode (IBA Dosimetry, Germany), a PTW 60012 diode (PTW, Germany) and a small-volume cc01 ionization chamber (IBA Dosimetry, Germany). Measurements were supported by Monte Carlo simulations. It was concluded that the two diodes were suitable for OARs measurements but required corrections in small fields.

In [149], three mini-ionization chambers (PTW 31014, PTW 31006, IBA CC01), three diodes (PTW 60018, IBA SFD and IBA PFD) and one synthetic diamond-detector (PTW 60019) were used to investigate a daisy-chain correction method as an alternative to correction factors calculated by Monte Carlo. Differences between calculated and measured OFs were, except for the IBA PFD, $< 0.5\%$ for square fields in the range from 1.5 cm to 5 cm side. For the smallest field investigated of 1 cm side, differences were within 2%. It was concluded that the investigated detectors could be used with a daisy-chain correction method to determine OFs

in water. However, measurements by the PFD diode were not suitable due to the presence of tungsten powder in the detector packaging.

The SFD diode (IBA Dosimetry, Germany), fabricated with a SV of 0.6 mm diameter, has been one of the most discussed diodes dedicated to small-field dosimetry [6]. Short-term stability and instantaneous dose rate dependence were found to be non-optimal, eventually leading to the development of the Razor diode [7]. The Razor was fabricated with a SV of the same dimensions of the SFD diode, but with superior stability, dose linearity and radiation hardness [9]. Similarly to its predecessor, it was found to require corrections when used in small fields [8]. Its over-response was found to be consistent with data for other unshielded diodes [63], [104], [147]. The Razor was investigated under irradiation with FFF beams and its was found that the flattening filter affected the correction factor by $< 1.5\%$ [8]. This result was in agreement with previous investigations [150]–[152]. A similar study [104] found no significant difference in the over-response of unshielded diodes irradiated by a 6 MV FB and FFF beams, matched to have the same $TPR20/10$ quality index, sd delivered by an Elekta linac. However, in 10 MV beams that were not matched, as is the case for the implementation of FFF beams in Varian linacs, filter removal produced a difference of up to 1.3% [150].

3.3.3 Array detectors

Commercially available 2D diode-arrays, effectively matrices of single diodes, include the MapCheck® series (SunNuclear Corporation, Melbourne, FL, USA) and the SRS profiler (SunNuclear Corporation, Melbourne, FL, USA).

The MapCheck® has proved a popular device [153], [154] [155], [156]. In its original design, it was fabricated with 445 n-type Pt-doped diode-SVs arranged on a $22\ cm \times 22\ cm$ area. Each SV had a square area of 0.8 mm side and was 20 μm thick [155]. It was shown to be useful for 2D dose mapping in a plane of the phantom perpendicular to central axis of the beam [155]–[157] and in IMRT QA. In its more recent design, called MapCHECK® 3 (Figure 7), it has 1527 SunPoint® 2 diode-SVs, 0.48 mm or $0.007\ mm^3$ each, with a 1 cm pitch in the X and Y directions, but with row spacing offset by 0.5 mm so that the effective pitch is 7.07 mm, over an area of $32\ cm \times 26\ cm$.

The SRS Profiler (Figure 8) has 125 diode-SVs distributed over four linear arrays (vertical, horizontal and two diagonals) with a pitch of 4 mm. Its performance for machine-specific QA for a CyberKnife® system was investigated and compared with those of the Octavius 1000SRS

(PTW, Germany), and the Nonius (QUART, Germany) [13]. All three devices were able to detect beam shifts with sub-millimetre accuracy.

Figure 7. A MapCHECK3. Image courtesy of SunNuclear.

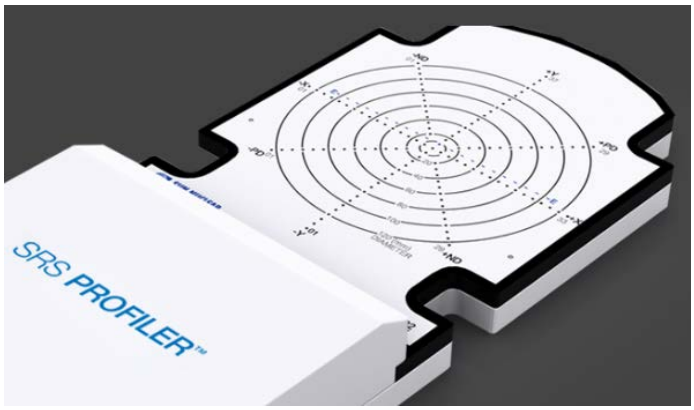

Figure 8. The SRS Profiler has 125 diode-SVs distributed over four linear arrays (vertical, horizontal and two diagonals) with a pitch of 4 mm. Image courtesy of SunNuclear.

Scaling up the number of SVs to improve spatial resolution is only possible within certain limits owing to constrains on the maximum number of channels in a read-out system. This could be partially addressed by smart arrangements of the SVs. However, the more complex the configuration of the SVs, the more difficult it becomes to relate their readings to dose in particular if the response is angularly dependent [27].

Two commercially available quasi-3D diode arrays have been commercialized so far, the Delta^4 (ScandiDos AB, Uppsala, Sweden) and the ArcCHECK (SunNuclear Corporation, Melbourne, FL, USA).

The Delta^4 (Figure 9) has 1069 cylindrical p-type diode-SVs, each with diameter 1 mm and thickness 0.05 mm, arranged on two perpendicular planes. These planes are inserted into a cylindrical PMMA phantom with diameter 22 cm and length 40 cm. The pitch of the SVs is 0.5 cm in the central 6 cm × 6 cm region of the 20 cm × 20 cm active area of each plane, and 1 cm elsewhere.

The ArcCHECK (Figure 10) has received significant attention in the literature [156], [158]–[166]. Both the prototype [159], [167] and commercial [166] versions of the device have been described. It has 1386 SunPoint® n-type diode-SVs ($0.8 \times 0.8 \times 0.03$ mm^3) arranged with a 1 cm pitch on an HeliGrid™ (Figure 10) inserted into a cylindrical PMMA phantom of 21 cm diameter and 21 cm length with a central air cavity. The central air cavity can be filled with a range of inhomogeneities inserts. These are useful, for instance, for verification of dose calculations by a TPS, which are known to be inaccurate in the presence of inhomogeneities [166], [168].

Both the Delta^4 and the ArcCHECK have their use for small-field dosimetry impaired by their limited spatial resolution [157], [169]. Furthermore, the use of these is time-consuming, incapable of tracking delivered per-fraction dose, and incapable of determining the root cause of failures [170].

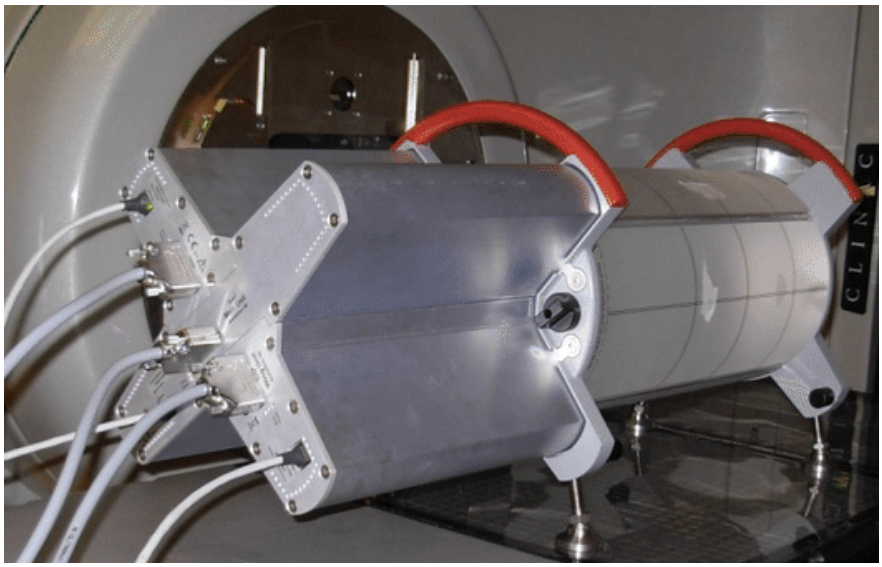

Figure 9. The Delta4 has 1069 cylindrical p-type diode-SVs arranged on two orthogonal planes.

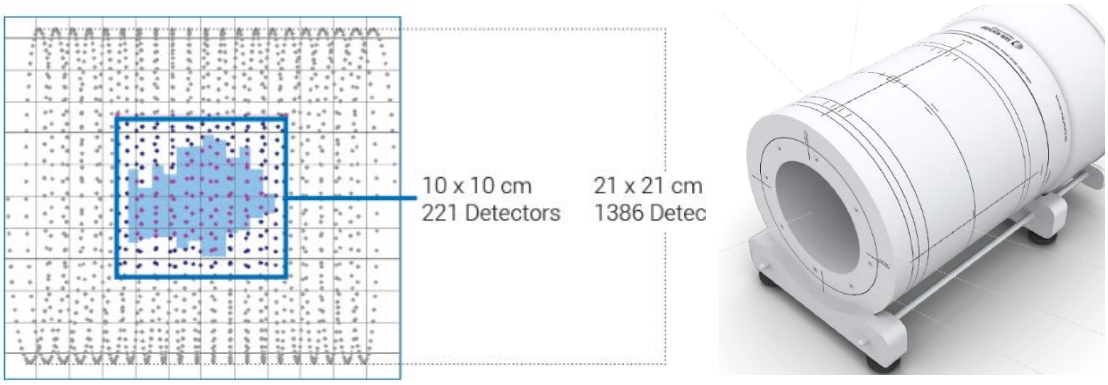

Figure 10. An ArcCHECK has diode-SVs arranged on a HeliGrid™ to increase the sampling rate and reduce overlapping and shadowing between SVs. A 10 cm × 10 cm area contains 221 SVs, equivalent to the SV density in a MapCHECK2. Image courtesy of SunNuclear.

A range of array prototypes with sub-millimetre spatial resolutions has been proposed. One such prototype was the DOSI (Figure 11) [55], [171]. It was fabricated on a monolithic high-resistivity ($1 - 10$ kΩcm) 300 µm thick n-type silicon wafer. It had 128 diode-SVs, a 250 µm pitch, a total sensitive area of 0.25×32 mm^2 and an estimated active depth of ~50 µm. Its potential for machine-specific QA was assessed by measuring PDD, OAR and OFs and using commercial devices such as diamond detector and a small PinPoint IC as benchmarks. There was an excellent agreement between measurements by DOSI and by the diamond detector. There were significant differences in OARs and OFs measured by DOSI and the IC, explained by the volume-averaging effect of the latter.

Figure 11. Picture of the 128-channel DOSI prototype dosimeter complete with its associated electronics. Image courtesy of [171].

A different group [172] has proposed the use of a silicon-diode strip detector prototype manufactured on a 500 μm thick n-type silicon wafer. It was subdivided into 16 strip-SVs, with 3.1 mm pitch, covering an active area of $50 \times 50\ mm^2$.

3.3.4 The CMRP and the quest for the ideal diode-array detector

The Dose Magnifying Glass (DMG, Figure 12) (CMRP, University of Wollongong, Australia) was a 1D silicon-diode array detector prototype based on a 0.375 mm thick p-type substrate. It had 128 diode-SVs with a 0.2 mm pitch. The device, which could be used in passive or active mode, was produced in different configurations: with a 5 kΩcm resistivity or with a 10 kΩcm resistivity substrate; with a $0.02 \times 5\ mm^2$ or $0.02 \times 2\ mm^2$ area of the SVs. Its energy-dependent response was investigated in the energy range 50 kV to 10 MV (corresponding to a range 26.8 keV – 2.97 MeV photon-equivalent energies) [173]. The DMG showed an enhanced response, up to six times, to low-energy photons with a maximum response at 75 kV nominal photon energy, owing to the increased cross-section for photoelectric effect [174]. Its angularly dependent response was reported to be 28.1% when the incident radiation beam was parallel to the detector plane [173]. It was shown that by mounting the DMG at the end of a 0.12 mm Kapton pigtail, instead of on a ceramic base, it was possible to improve its angularly dependent response by 12.8%. The instantaneous dose rate dependence of the response of the DMG could be reduced to 2% by using a low resistivity silicon substrate and pre-irradiating the device. A maximum dose rate variation of 5% for the non-pre-irradiated low-resistivity device was reported in the range 200 cGy/min to 840 cGy/min while for the pre-irradiated device (15 kGy with 1 MeV electrons) showed a variation $< 2\%$ in the range 200 cGy/min to 600 cGy/min. The linearity with accumulated dose of the DMG was excellent in the range 3.89 cGy to 311.05 cGy, while measurements of PDD showed good agreement with an IC (within 0.8%) at all points up to 20 cm depth, under irradiation with a 6 MV flattened photon beam [173]. The DMG encapsulated in a solid water holder was used for machine-specific QA with a custom-made solid water head phantom [175]. This allowed the DMG to measure non-coplanar SRT treatment deliveries. One of the SRT QA procedures required prior to delivery is the measurement of the centre of rotation (COR) and position offset of the linac. The 0.2 mm spatial resolution of the DMG allowed for assessing the COR of the linac gantry, determined from the centre of the beam profiles obtained from the 0° and 180° gantry rotation. The COR offset was defined as half the difference between the x-coordinates of the two mid points of the beam profiles. The determination of the collimator and

couch rotation was also determined with a similar procedure. The device was used for IMRT QA [173], for SRT small-field dosimetry [175] and to measure Tomotherapy binary leaf speed [176].

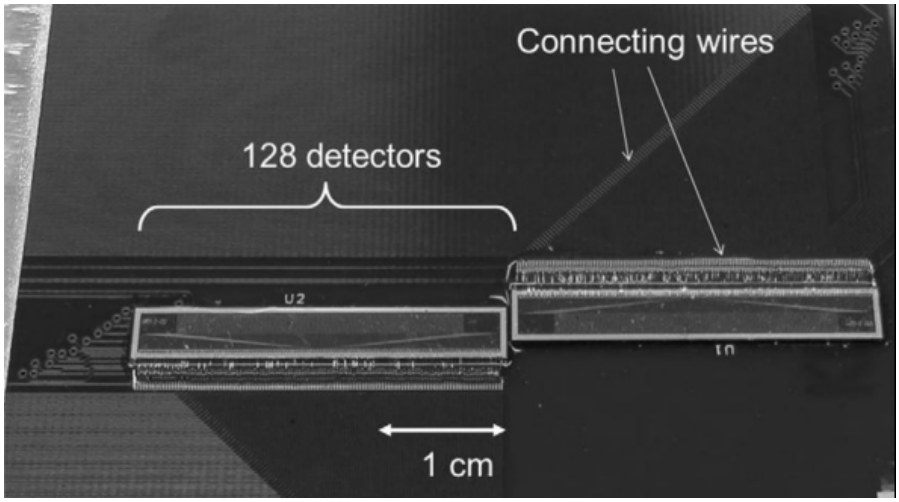

Figure 12. The DMG is a 1D diode-array detector (CMRP, University of Wollongong, Australia). In the figure, two DMGs are shown side-by-side. Image courtesy of [27].

The MP512 [116], [177] and the Duo [118] (Figure 13) (CMRP, University of Wollongong, Australia) are a 1st generation of 2D monolithic silicon-diode array detector prototypes. Based on p-type silicon substrate, they have 512 SVs. The SVs were uniformly distributed on the silicon wafer surface with a 2 mm pixel pitch in the case of the MP512 and arranged with 0.2 mm pixel pitch along 2 orthogonal linear arrays in the case of the Duo.

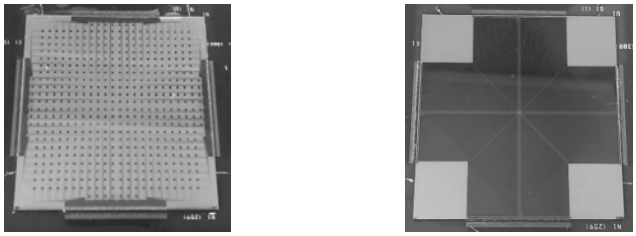

(a) (b)

Figure 13. 2D monolithic silicon-diode array detectors proposed by the CMRP for QA in MV photon beams: (a) the MP512 and (b) the Duo.

The MP512 was demonstrated to be suitable for use in phantom dosimeter for SRT QA. Its measurements were found to match well film measurements down to 1 cm side square fields, with discrepancy of 4% in the determination of OFs of beams smaller than 5 mm side square fields (all fields were jaw-defined, produced by 6 MV flattened photon beams). OARs in terms of FWHM were found to have a discrepancy of less than 1.3% when compared to films. It was suggested that a reduction in the detector pitch to less than 2 mm would improve the penumbra reconstruction accuracy at the cost of read-out electronics complexity [116]. The

MP512 was evaluated for accurate reconstruction of a dose profile with motion and with tracking of the motion. It showed excellent performance to reconstruct the dose deposition in real-time or retrospectively as a function of time for detailed analysis of the effect of motion in a specific pixel or area of interest [177]. The angular dependence of the MP512 was investigated and could be corrected for, making it a suitable candidate for arc therapy delivery QA [132].

The Duo, with a total size 5.2 cm square side, was similarly found to be suitable for small-field dosimetry. It was shown to be an accurate dosimeter for OFs, PDD and OARs measurements in radiation fields produced by 6 MV flattened photon beams, with a dose per pulse (DPP) dependence [118].

The MP512 and Duo both have pulse-by-pulse real-time acquisition, high signal stability, radiation hardness and dose linearity [178]. Nonetheless, their attractiveness for modern small-field dosimetry is impaired by the coarse spatial resolution of the MP512 and by the limited spatial characterization of the 2D dose map of the Duo.

3.4 Conclusions

None of the commercial arrays described so far would measure dose distribution in real-time with sub-millimetre resolution. These conditions would be satisfied by one of the discussed array prototypes (Duo). However, the device would offer a description of 2D dose distributions too limited to be considered informative. This is unsurprising, considering that the size of a small radiation field (be it nominally regular or irregular, defined by secondary or tertiary collimators or a combination of the two) need to be accurately verified in all possible directions. Dose gradients require detailed spatial description. Accurately assessing the effective dimensions of the radiation field of interest is relevant also when considering measurements of OFs, or PDD and TMR distributions.

To offer a more detailed and informative description of 2D dose distributions, without sacrificing the sub-millimetre spatial resolution, a 2nd generation of 2D monolithic silicon-diode array detector prototypes, identified by the name ‘Octa’, was designed incorporating its predecessors’ technology and building on acquired experience. A detailed description of this novel device is the topic of the next chapter.

4 Enter the Octa

4.1 Concept and design

Modern radiotherapy employs small radiation fields to deliver highly conformal dose distributions. Sub-millimetre accuracy in the measurement of the delivered dose map is a crucial detector requirement for quality assurance (QA) applications. However, the only commercially available devices able to satisfy this requirement are point-like detectors used with various scanning techniques [2].

A preferable solution would be a 2D array detector. In particular, 2D monolithic array detectors would optimize the spatial resolution in a large active area [115], [116]. Along with commonly characterized QA parameters, such as output factors (OFs), percentage depth dose (PDD) and tissue maximum ratio (TMR) distributions, and out-off axis ratios (OARs), thanks to their fixed geometry, these devices would allow for repeatable machine-specific QA. Examples would include the positional accuracy verification of the movable parts of a medical linear accelerator (linac), such as the leaves of a multi-leaf collimator (MLC) and the aperture of dynamic circular collimators (Iris™).

Silicon detectors based on either a n^+-p or p^+-n junction would be a great choice for monolithic arrays. Thanks to their advantages, such as the potential for manufacturing very small sensitive volumes (SVs), a stable and nearly energy independent response, good linearity with dose and real-time read-out [84], they have recently been recommend by Codes of Practice (CoP) dedicated to small-field dosimetry QA [1], [2].

The Octa (Figure 14) is a 2D monolithic silicon array detector. It was designed at the Centre of Medical Radiation Physics (CMRP, University of Wollongong, Australia), and fabricated at the SPA-BIT facility (Kiev, Ukraine).

The device is based on a p-type silicon substrate and has 512 n^+ strip-SVs. The SVs are arranged along 4 intersecting orthogonal linear arrays, oriented 45 degrees with respect to each other. The SVs have all the same area of $0.032\ mm^2$ and are of elongated rectangular shape ($0.04\ mm \times 0.80\ mm$), except for the 9 pixels in the central matrix at the intersection of the 4 arrays ($0.16\ mm \times 0.20\ mm$). The pitch is sub-millimetre, $0.3\ mm$ along the vertical and horizontal arrays and $0.43\ mm$ along the diagonals.

The device has a total area of $38.7\ mm \times 38.7\ mm$ and is covered by a $0.10\ mm$ thick layer of epoxy resin to provide a tissue equivalent protection against moisture and accidental damage. Conceived as a 2D planar dosimeter for dose measurements in solid water, the Octa

is sandwiched between two Perspex plates, each 5 mm thick and is wire bonded to a printed circuit board (PCB) for connection to a multichannel read-out data-acquisition (DAQ) system.

The peculiar layout of the SVs of the Octa gives the latter unique potentials for small-field dosimetry QA applications. Along with the OF, cross-plane, in-plane and 2 diagonal OARs are characterized simultaneously for any given radiation field, with sub-millimetre spatial resolution.

All silicon-based solid-state detectors show a field-size dependent response for measurements in small-field photon beams, due to their perturbation of the secondary electron fluence profile (see section 2.2, page 15, for further details). Therefore, correction factors, calculated either by Monte Carlo simulations or by experimental cross-checks with ideal dosimeters, need to be applied to convert the detector readings to dose [2]. Alternatively, a 'correction-free' detector, or one maintaining a correction factor close to unity, would have to be designed by adding low density media to the high density detector SVs and packaging components [64]. For 2D monolithic silicon array detectors, this could be achieved by introducing a small air gap on top of the SVs [179]. Based on these results, an air gap was introduced on top of the Octa. However, it is still necessary to verify that this modification is appropriate under any given beam quality and measurement condition [65].

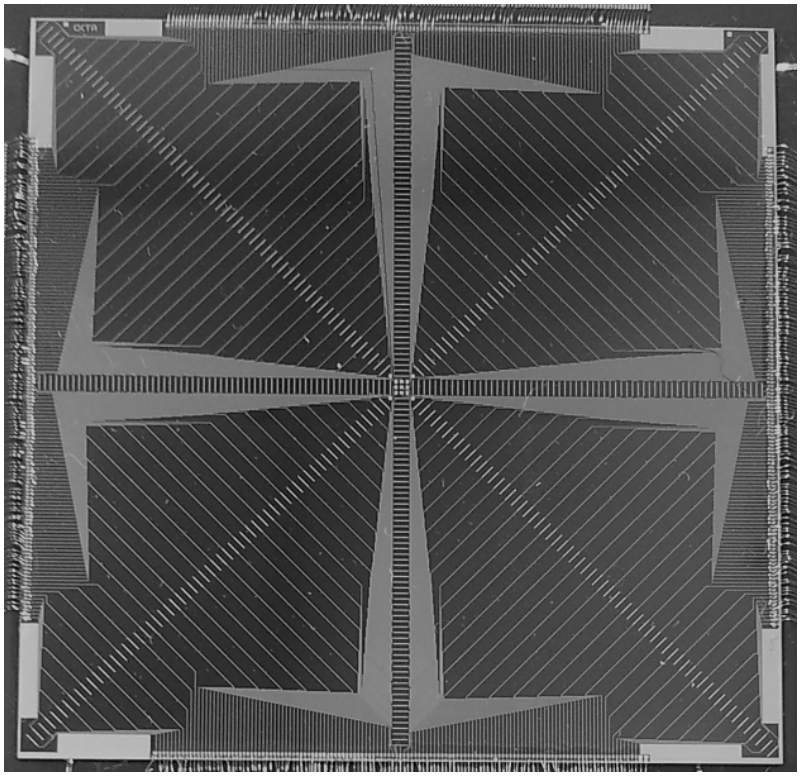

Figure 14. Snapshot of the Octa. The device is a 2D monolithic silicon array detector consisting of 512 diode-SVs operated in passive mode. They are arranged along 4 intersecting orthogonal linear arrays oriented 45 degrees with respect to each other. Each diode has a sensitive area of 0.032 mm^2, with a 0.3 mm pitch along the vertical and horizontal arrays and a 0.43 mm pitch along the 2 diagonals.

4.2 Manufacturing technology

The Octa was produced in two samples, on a bulk and on an epitaxial substrate.

The first Octa was manufactured, similarly to all monolithic devices proposed by the CMRP up to that point, on an $0.460\ \mathrm{mm}$ thick p-type substrate with resistivity $10\ \Omega\mathrm{cm}$ (bulk device). The silicon wafer was created using a Czochralski process [180]. High-purity silicon is melted into a crucible and boron dopants are added to the melt. The silicon ingot proper is grown on a rotating seed crystal which is first dipped into the melt and slowly drawn out whilst being rotated. The ingot is cut into wafers with a thickness of $0.300\ \mathrm{mm}$ to $0.500\ \mathrm{mm}$.

Individual strips creating separate p-n junctions are implanted on the wafer, spaced by a distance commonly referred to as pitch. An aluminium layer is deposited on top of each strip to create the electric contact for the read-out system.

During the implantation process of the strips, a silicon dioxide SiO_2 layer forms on top of the n^+ doped implants. The layer can accumulate positive charges attracting electrons. At the interface between silicon strip and the silicon dioxide layer this can result in an accumulation of electrons, which can short the n^+ strips. As a solution, p^+ implants referred to as guard-rings are placed between the n^+ strips. They break electron accumulation layer re-shaping the electric field of the p-n junction and preventing the n^+ shortening.

As previously discussed (see section 3.2, page 30, for further details), the Octa bulk would be affected by significant radiation damage throughout the time it is used as a dosimeter. This would result in the production of deep-energy level defects, such as interstitial and vacancy defects, and generation-recombination (G-R) centres via interaction of secondary electrons with the detector substrate crystal lattice [181], [182]. The increase in deep level defects concentration explains the decrease in the minority carrier lifetime τ_e. The result is an overall sensitivity degradation with accumulated dose [117], [133]. Radiation would also lead to the appearance of surface damage [183], with positive charge permanently trapped into the SiO_2 layer and at the Si- SiO_2 interface [184].

The Octa bulk sensitivity was stabilized by pre-irradiation [99] with a $\mathrm{Co\text{-}60}$ gamma source at the Gamma Technology Research Irradiator facility (ANSTO, Australia) in the order of $0.12\ \mathrm{MGy}$ ($12\ \mathrm{Mrad}$). Because pre-irradiation increases the concentration of deep level defects in the substrate and of charge trapped at the Si- SiO_2 interface, both contributing to an increase of the leakage current [84], [185]–[187], the device is to be operated without applying an external bias.

The second Octa was manufactured on a different, 0.035 mm thick, p-type epitaxial [188] layer with resistivity 100 Ωcm, grown onto a 0.525 mm thick heavily doped p^+ substrate with resistivity 0.001 Ωcm. The epitaxial layer is doped by adding gaseous boron compounds to the environment. As a result, oxygen diffuses into the layer. Its final concentration affects the detector properties.

As previously discussed (see section 3.2, page 30, for further details), the advantage of using a device based on an epitaxial layer is that, by choosing a layer thickness shorter than the L_e expected in the operative dose range, it is possible to fix the SVs collection area and obtain a device whose sensitivity is independent of the accumulated dose [117], [189].

4.3 Comments on the read-out system

The Octa is wire-bonded to a 0.5 mm thick PCB for connection to a multichannel read-out DAQ system. The DAQ system proper is comprised of the read-out electronics, which has been described elsewhere [190], the graphical user interface (GUI), which was coded in C++ using a Qt (Nokia) application and whose original version has been described elsewhere [191], and the firmware.

Recent updates introduced to both the firmware and the GUI are described below, after an introduction on their original implementation.

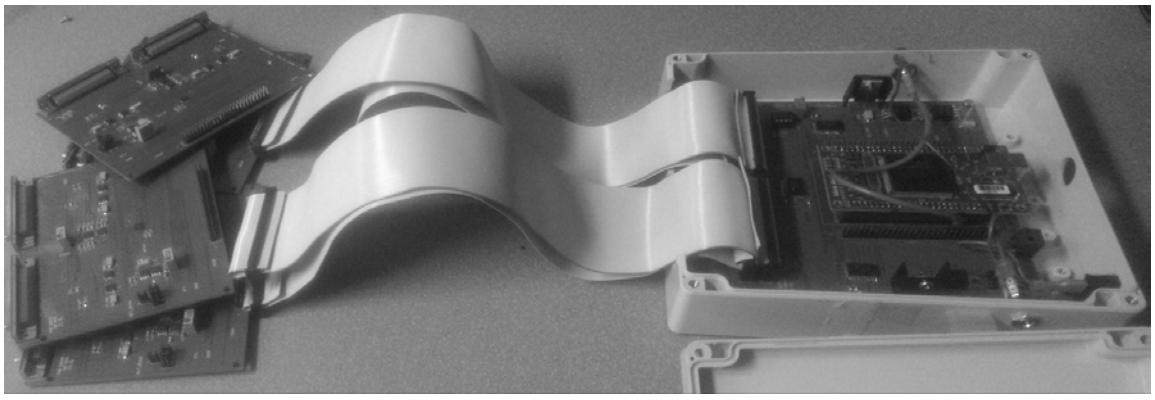

Figure 15. Snapshot of the Octa data acquisition system (DAQ). Starting from the left side, the 4 boards with 2 AFEs each. Plastic case containing the FPGA and associated circuits. Three ports are visible on the case: that for the USB link (for data transmission to/from PC), that for the power supply and that for the coaxial cable (for linac trigger signal acquisition).

The read-out electronic system (Figure 15), is based on a field-programmable gate array (FPGA) Xilinx Spartan 3, 4 analogue-to-digital converters (ADCs) and 8 commercially available analogue front-end (AFE) AFE0064 (Texas Instruments) chips [192].

The system was devised so that the Octa could be used as a dosimeter for linacs. These machines deliver a pulsed radiation beam, with a fixed repetition rate in the range from 200 Hz to 400 Hz, a parameter characteristic of each linac model [84]. The pulse is triggered by an electron gun and lasts for 3 μs to 5 μs.

The user is required to have knowledge of the electron gun trigger frequency and set it in the GUI. Parameters and commands set by the user in the GUI are read and used by the FPGA, which handles the data transfer to/from the PC through an Opal Kelly XEM3001 integration module. The FPGA handles also the synchronisation between AFEs and the linac trigger, acquiring the latter via a coaxial cable.

A firmware, which configures the FPGA and defines the input/output (I/O) addresses used for communication with the PC, must be loaded in the GUI at device turn-on.

The AFE performs two functions, 'Integration' and 'Data Read' for each pulse acquisition (see Figure 16 and Figure 17). The integration function consists of two compulsory phases, 'Reset' and 'Integration'.

The reset phase is initiated by closing the reset switch (IRST rising edge), setting each amplifier output to the reset-level. At the end of this phase, the output V is measured to get the reset sample. This phase lasts for 70 μs using a 2 MHz FPGA clock. Because the linac trigger frequency is known and constant, the reset sample is acquired during the 70 μs immediately before the expected arrival of the trigger signal. The reset phase ends with the SHR rising edge.

Starting from 30 μs before the expected linac trigger, and for the duration of the beam pulse, the charge resulting from electron-hole pairs generated in the device owing to the incident radiation is collected by a capacitor. The 30 μs offset was introduced to ensure that the beam pulse would turn on during the integration window.

At the end of this integration phase, an output sampling command triggers the simultaneous sampling of the 512 channels. The collected charge is converted into a voltage level V, corresponding to the signal sample, which is the output of the amplifier of each channel:

$$V = \frac{Q}{C} \tag{4.1}$$

The difference between signal and reset samples is then sent to the ADCs. In this way, the effects of electronic noise and leakage current are minimized. Data transfer (labelled data read in Figure 16, Figure 17) is performed during the reset phase and is triggered by the STI rising edge. This description illustrates the original working release of the firmware (Figure 18).

These firmware settings were designed so that the DAQ could work with linacs, such as the Varian Clinac® iX system and the Elekta Axesse™, which have a constant electron gun

frequency. In modern radiotherapy, novel treatment machines used to deliver small radiation fields such as the Varian TrueBeam™ STx, have an electron gun frequency which is non-constant and varies during treatment delivery depending on beam energy and dose rate. Ever more often, they are also used to deliver flattening filter free beams, which are characterized by higher instantaneous dose rates. These may result in the detector response being saturated.

To deal with these issues and allow for the DAQ to work with novel linacs, two updates where introduced to the original firmware version *Top_11_512ch*, as listed in Table 4.

A first update (*Top_512ch_15MHz*) was devised to disentangle the acquisition from the constant trigger frequency requirement. This was achieved by synchronizing the IRST rising edge with the trigger signal, with the user no longer required to set the trigger frequency in the GUI (see Figure 19). The compulsory reset phase is performed in 8.6 μs using a 15 MHz FPGA clock (the maximum allowed by the manufacturer). The INTG rising edge immediately follows the SHR rising edge. The data transfer is performed immediately at the end of the integration phase. This firmware was validated against the original version by comparing the acquisition of a 2 cm square field with a 6 MV medical linac, all other measurement conditions being equal.

A second update (*MP_512_IToffset)* was conceived to prevent the detector response from being saturated at high instantaneous dose rates. An offset, a constant parameter set by the user in the GUI and applied to each beam pulse acquisition, was introduced. The beginning of signal integration is delayed for a fixed time after the arrival of the trigger signal (see Figure 20). This results in an overall lower integrated charge.

A third update which merges the previous two firmware updates is also available.

Table 4. List of available firmware and their description.

Firmware name	Description
Top_11_512ch	Original working release
Top_512ch_15MHz	Reset procedure is performed with FPGA clock at 15 MHz
MP_512_IToffset	Offset delays start of integration window

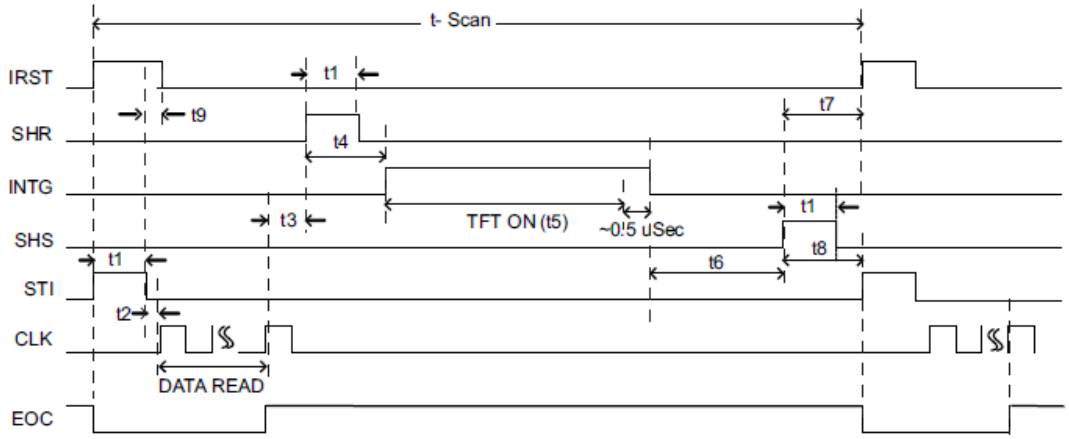

Figure 16. For each beam pulse acquisition, the FPGA performs two functions, ‘Integration’ and ‘Data Read’. Signals IRST, SHR, SHS, INTG, CLK control 'Integration Function' and STI, CLK control 'Data Read Function'. EOC is a device output and a low level on the EOC pin indicates a data read is in progress. IRST rising edge starts the ‘Reset’ phase which ends with SHR rising edge. IRST rising edge resets the integrator capacitors on rising edge of this input. STI rising edge resets the channel counter. SHR rising edge samples the 'reset' level of the integrator output. INTG filters bandwidth control for Signal sample (SHS). SHS rising edge samples 'signal' level of integrator output. STI falling edge enables data transfer. CLK device serially outputs the analog voltage from each integrator channel on every fourth rising edge of CLK [192].

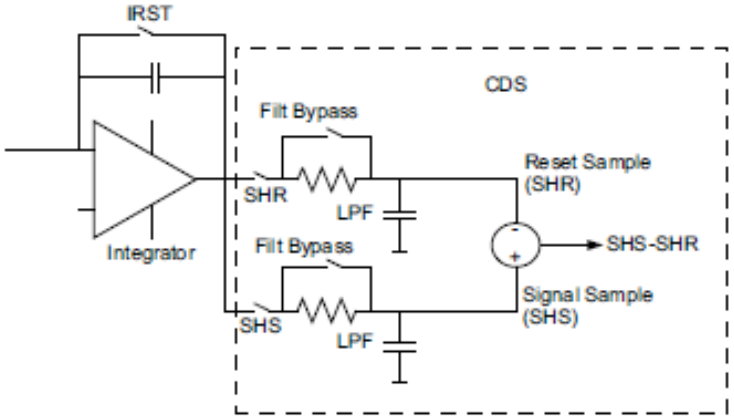

Figure 17. Each integrator has a reset (IRST) switch which resets the integrator output to the 'reset-level'. The input current is integrated while this switch is open. There are two sample and hold circuits connected to each integrator output. SHR samples integrator reset-level output and SHS samples integrator output post-integration of signal. The device subtracts the SHR sample from the SHS sample. The difference is then available as output in a differential format [192].

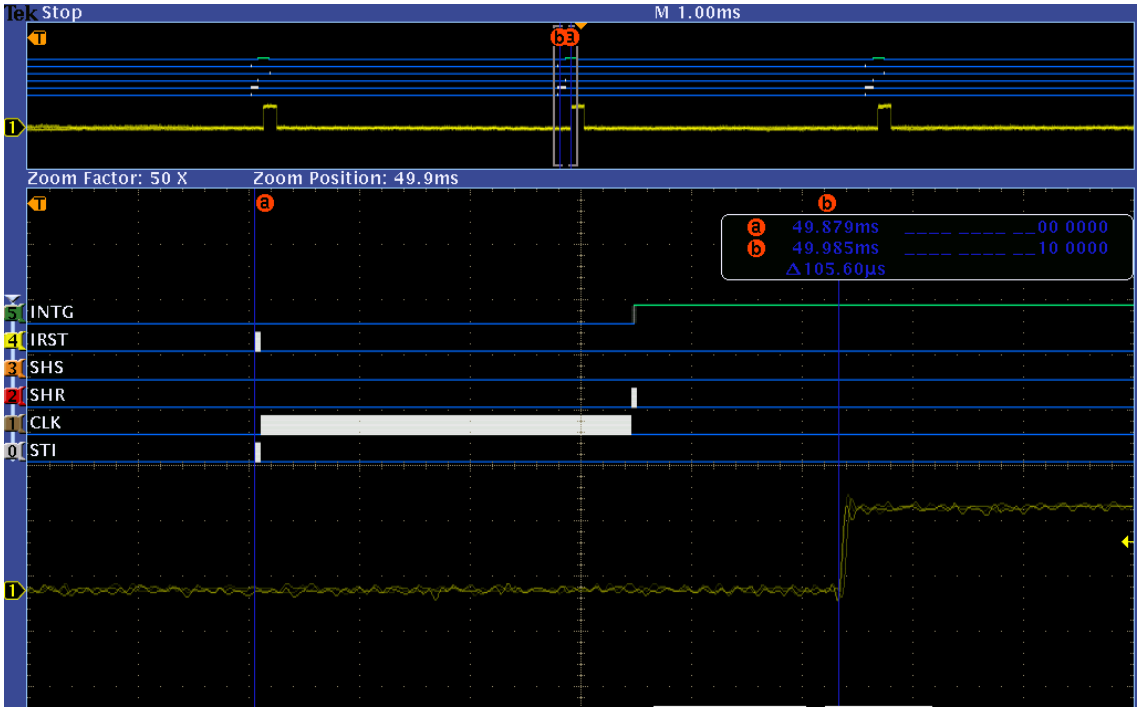

Figure 18. Original firmware settings. The reset procedure is performed in 70 µs before the expected trigger signal (fixed frequency set by the user in the GUI). Data transfer (of previous beam pulse acquisition) is carried out during the reset window. Integration (of current beam pulse) starts (INTG) 30 µs before the trigger. Yellow signal is trigger signal.

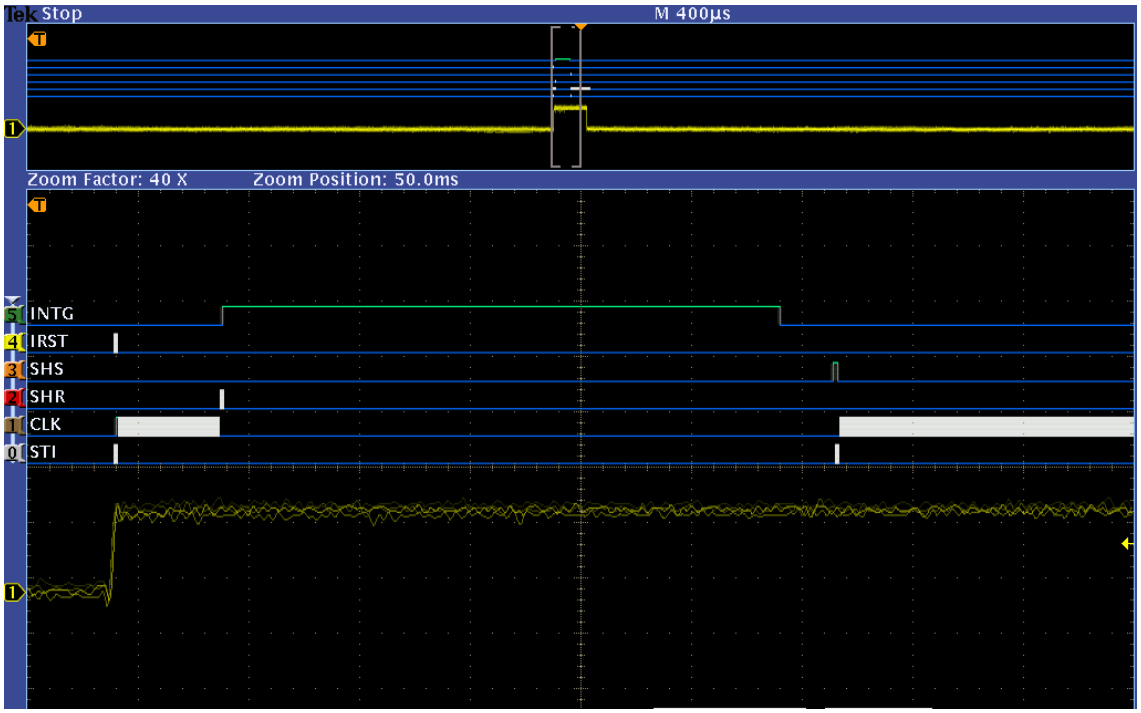

Figure 19. Firmware update 'Top_512ch_15MHz'. At trigger signal, the reset procedure is performed at 15 MHz in 8.6 µs. At its completion, integration starts (INTG). 15 MHz is the maximum clock frequency allowed by this FPGA design. Yellow signal is trigger signal.

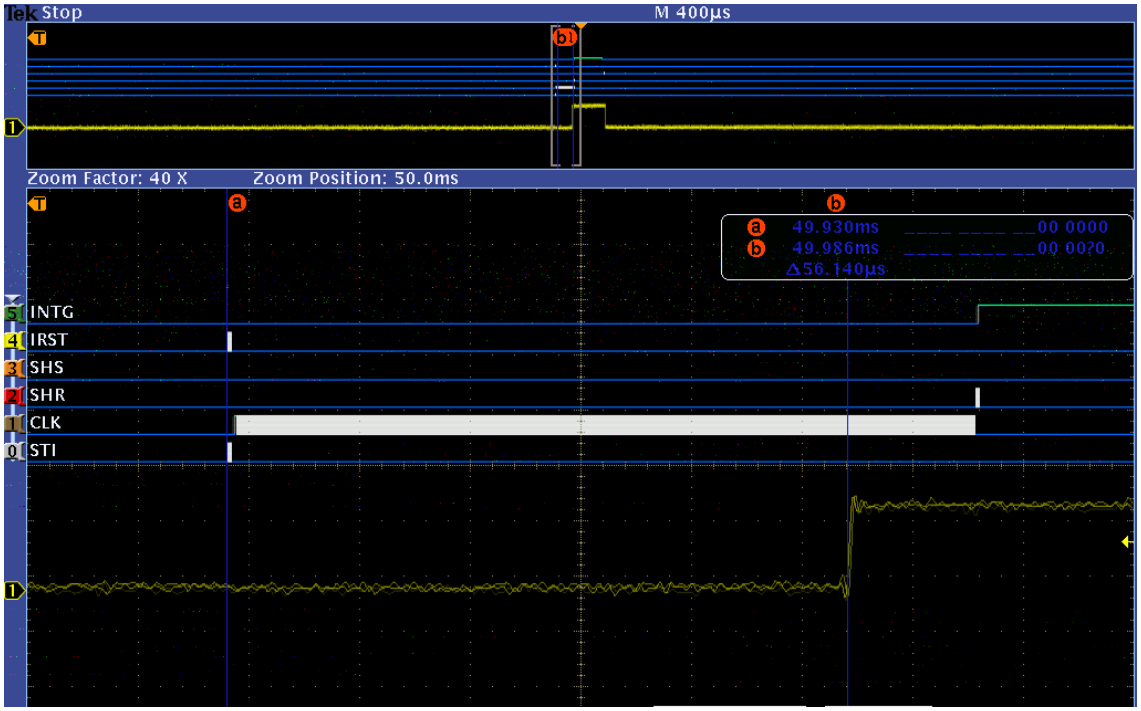

Figure 20. Firmware update 'MP_512_IToffset'. The reset procedure is performed in 70 µs before the expected trigger signal (fixed frequency set by the user in the GUI). Data transfer (of previous beam pulse acquisition) is carried out during the reset window. Integration (of current beam pulse) starts (INTG) after the trigger by a fixed user-defined time window (offset). Yellow signal is trigger signal.

4.4 A touch of Monte Carlo

4.4.1 The Geant4 application

A Monte Carlo method consists of mathematical techniques based on random number generation for sampling values of a stochastic variable, given its cumulative distribution function [193]. Monte Carlo simulations are an investigation tool used in many areas of scientific research and industrial development, and are considered the gold standard for describing particle transport within a medium [194]. Monte Carlo simulations are successfully employed in radiotherapy to retrieve quantities (particles spectra, tracks, range, interaction and number and types of secondary particles, …) which would not be easily measured in experiments or using analytical methods.

Monte Carlo simulations are not generally directly employed for clinical treatment-planning systems (TPSs) but are used instead to generate data of physical quantities (e.g. dose kernels) which will in turn constitute input values for the TPSs.

Geant4 [195], [196] is a general purpose open source Monte Carlo tool-kit for the simulation of the passage of particles through matter. It is based on a collection of C++ classes available from the Geant4 collaboration [9].

Even though initially developed for high-energy physics applications, it is currently used in different branches of physics, from space science and radiation protection to medical physics, for which it has been validated by several groups [197], [198].

For radiotherapy applications, it is employed in the clinical practice for dose verification of TPSs, to characterise and optimise novel detectors and to understand specific aspects of experimental measurements.

Simulations presented in this dissertation were performed with Geant4 version 10.00. The software ROOT (ROOT - Data Analysis Framework) was used for data analysis.

To develop a Geant4 application, the user implements their own C++ classes which inherit behaviour from custom Geant4 classes. For any given simulation, the tool-kit allows for the customization of geometry and materials involved, particles of interest, physics models and quantities to be tracked.

The *G4VUserDetectorConstruction* class defines the geometries (the solid model definition and their spatial positions) and the materials involved in the simulation, such as those of detectors, targets and all relevant volumes.

The *G4VUserPrimaryGeneratorAction* class defines the incident primary particles in terms of particle type, energy, momentum and point of origin.

The *G4VUserPhysicsList* activates the set of particle types, physics models and cross sections relevant to any given simulation. The tool-kit offers alternative physics models and it is let for the user to decide which physics approach fits the simulation requirements in terms of accuracy of the results and computing time. A detailed description of all physics models included in Geant4 is given in the relevant Physics Reference Manual from the Geant4 collaboration website. Reference physics lists are extensively and routinely validated [196]. For the scope of this work, electromagnetic interactions were described by the Geant4 *standard EM model 4*, as suggested by the collaboration [196]. In the *G4VUserPhysicsList*, there are three methods which can be implemented. The *Construct-Particle* method defines the relevant particles for the simulation, the *Construct-Process* method defines interaction models to be used, the *Set-Cuts* methods defines the cut to be applied to the particles. A particle generated with a range in the material less than the defined cut value will not be tracked and its kinetic

[9] source: http://geant4.web.cern.ch/geant4/collaboration/index.shtml

energy will be considered deposited locally. It is fundamental to appropriately set the cut based on considerations such as accuracy of results, which would require a lower cut, and constrains on computing time, which would benefit from a higher cut.

The *G4UserSteppingAction* class allows for the implementation of methods to be executed at the end of each *step*, such as the request to store a particle's information for further analysis. In a Geant4 application, a step describes the transport of a particle between two points in space. The length between the two points is chosen by a combination of transportation and physics processes and may be limited to a fixed size by the user in cases where small step lengths are desired. A *track* is a snapshot of a particle (energy, momentum, position, mass, charge, etc.) at a point along its path. A collection of *tracks* along a particle's path is called a *trajectory* [196].

4.4.2 The Octa model

The Octa (512 diode-SVs, silicon wafer, PCB board and PMMA phantom surrounding the detector), as illustrated in Figure 21 and in Figure 22, was modelled using the *G4VUserDetectorConstruction* class.

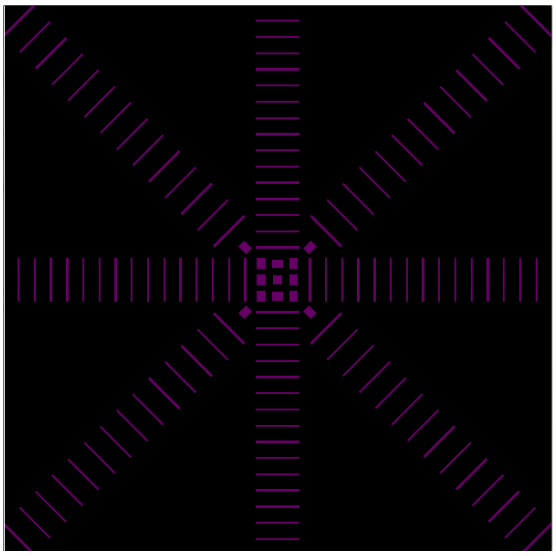

Figure 21. A snapshot of the 512 sensitive volumes (SVs) of the Octa. They are arranged along 4 linear arrays, at 45 degrees with respect to each other. The 9 SVs of the central matrix are of rectangular shape but maintain the same sensitive area of the strip-shaped SVs.

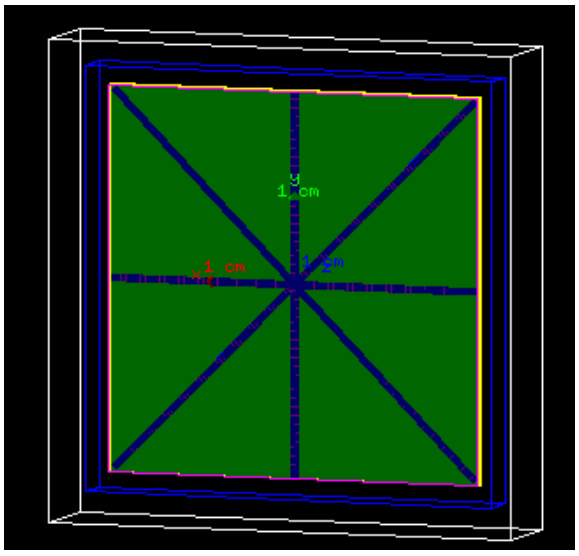

Figure 22. The Octa model implemented into the Geant4 tool-kit. The 4 linear arrays are manufactured onto a silicon wafer (green area), supported by a PCB board and enclosed into a PMMA phantom (white square-shaped). An air gap was modelled.

4.5 A touch of TCAD

4.5.1 The Sentaurus® TCAD software

Technology Computer-Aided Design (TCAD) simulations are a tool for semiconductor devices development and performance analysis. TCAD simulations discussed in this dissertation were performed using Sentaurus™ Workbench [199] within the Synopsys® (Synopsys, Inc., Mountain View, CA) framework.

The Sentaurus Structure Editor [200] is used to model a 2D TCAD device, defining the relevant geometry, materials, doping concentrations (or resistivity), doping profiles, contact regions. A TCAD device approximates a real device and continuous properties (e.g. doping profiles) are defined at a finite number of discrete points (or nodes) in space. At any point between these nodes, properties will be calculated by interpolation. The mesh can be user-defined though the declaration of a meshing strategy, which will have to be a compromise between results accuracy requiring finer meshes and simulation time constrains commanding coarser meshes.

This mesh-like grid structure of nodes is loaded into the Sentaurus Device (*Sdevice*) [201] simulation tool. In all semiconductor devices, charges (such as electrons and holes) and traps (dopants, defects, …) determine the electrostatic potential and, in turn, are themselves affected by the electrostatic potential. The electrostatic potential ϕ is solved everywhere in the device using the Poisson equation:

$$\nabla \cdot (\varepsilon \nabla \phi) = -q(p - n + N_D - N_A) - \rho_{trap} \tag{4.2}$$

where ε is the electrical permittivity, q is the electron charge, n and p are the electron and hole densities (units cm^{-3}), N_D and N_A are the donors and acceptors doping concentrations (units cm^{-3}), ρ_{trap} is the charge density contributed by traps and fixed charges.

TCAD allows charge deposition at any location in a device. For subsequent drift and diffusion processes, carrier transport is governed by the continuity equations. For a semiconductor these are described in the form of charge conservation as:

$$\begin{cases} \nabla \cdot \overrightarrow{J_n} = q\left(R_{net} + \dfrac{\partial n}{\partial t}\right) \text{ for electrons} \\ -\nabla \cdot \overrightarrow{J_p} = q\left(R_{net} + \dfrac{\partial p}{\partial t}\right) \text{ for holes} \end{cases} \tag{4.3}$$

where $\overrightarrow{J_n}$ and $\overrightarrow{J_p}$ are the current densities (units Acm^{-2}) for electrons and holes respectively, n and p are the electron and hole densities respectively, R_{net} is the net recombination rate (units s^{-1}) is the net rate of recombination by all processes. These equations are solved iteratively, starting with an initial guess of the solution. Iterations continue until the error is small enough

to satisfy predefined convergence criteria, or until a given number of user-defined iterations has been performed.

Depending on the device under investigation and the level of accuracy required, different transport models, each based on a different expression to compute the current densities, can be selected in *Sdevice*. For the simulations described in this dissertation, the *drift-diffusion* model was used. It considers the effect of thermal diffusion and the drift caused by the local electric field resulting from applied bias (if any) and electrostatic forces between carriers. It is the default carrier transport model and it is suitable for isothermal simulations of low-power density devices with long active regions.

Defects reduce charge collection by various generation–recombination processes. These are processes that exchange carriers between the conduction band and the valence band. Recombination through deep defect levels in the semiconductor energy gap is called Shockley–Read–Hall (SRH) recombination. An electron from the conduction band and a hole from the valence band combine at the trap level and their contribution to the signal is lost. The SRH lifetimes dependence on doping profiles is modelled in *Sdevice* through the Scharfetter relation.

The *Mobility* model was declared in the *Physics* section of the *Sdevice* command file to implement an SRH doping-dependent process.

Traps and fixed charges are important parameters. They may enhance recombination and increase leakage current. The SRH model depends on traps implicitly but does not model them. It is left for the user to define their concentrations and characteristics.

Traps can be fixed charge traps, which are always completely occupied; acceptor traps, which are uncharged when unoccupied and carry the charge of one electron when occupied, donor traps, which are uncharged when unoccupied and carry the charge of one hole when occupied.

The specification of trap characteristics for a material or region in the TCAD device can be done using the *Trap* model in the *Physics* section. It allows for the parametrization of the trapped charge at the interfaces and of the point defects in the substrate, specifying the energy levels, the concentration as a function of the accumulated dose and the cross-section for electrons and holes.

Radiation incident on a semiconductor device triggers the generation of electron–hole pairs in silicon. With *Sdevice*, in the *Physics* section it is possible to model the carrier generation through the *Gamma Radiation Model*. The user can define a dose rate (rad/s) and the irradiation duration.

Alternatively, a *Heavy Ion Model* can be used. The model is used to represent a minimum ionising particle (MIP) incident on the device. The charge deposited by the particle along a track, or its linear energy transfer (LET) generation density ($pairs/cm^3$), is a user-defined parameter, along with track length, incident location and direction, and lateral distribution.

Once environment variables (e.g. temperature) are set and the relevant physical models are activated (charge carrier mobility, avalanche effects, saturation of the electric field etc.), the electrical behaviour of the TCAD device is simulated by *Sdevice*. Currents, voltages and charge distributions and generations are computed at each mesh node based on the set of equations chosen to describe the carrier transport mechanisms, following the standard finite element analysis (FEA) scheme. Three main simulation types can be performed.

A voltage ramping simulation, in which the voltage applied to an electrical contact is ramped up (or down). This is used to simulate the measurement of the device I-V characteristic.

A small-signal AC analysis, in which small sinusoidal signals are super-imposed upon the direct-current bias voltage. From the device response, capacitances can be extracted. This is used to simulate the measurement of the device C-V characteristic.

A time-dependent simulation, in which the transient response of the TCAD device to incident particles is assessed. Either the *Gamma Radiation Model* or the *Heavy Ion Model* can be used.

Results simulated at each mesh node are examined by visualization with Sentaurus Visual (*Svisual*). This helps the study of field shapes and charge trajectories that are unknowable in experiment. Signals extracted from the electrodes can be displayed with the Sentaurus Inspect tool.

4.5.2 The Octa model

Using Sentaurus Structure Editor, 2D TCAD devices representative of the Octas bulk and epitaxial were created. For the latter, Figure 23 illustrates one of its n^+ electrode along with its p^+ guard ring. Figure 24 illustrates the simulated electric field for the same area.

The simulated representation of the space-charge distribution in Figure 23 shows that the depleted region is stretched outside the limits of the p-n junction due to the presence of charges in the silicon oxide layer. The depleted region depth for the Octa epitaxial was estimated to be approximately 3 μm, a value which is consistent with those reported for dosimeters based on p-n junctions operated without any external bias [117] and with values simulated for a similar epitaxial device presented in Aldosari et al. [202].

The radiation damage of the pre-irradiated Octa bulk was considered by implementing the *Trap* model. As reported in the literature, defects generated in a silicon substrate by a Co-60 gamma source can be effectively modelled by introducing interstitial C_iO_i complexes and VV divacancy centres in the substrate, as well as positive trapped charge at the interfaces with and within the silicon dioxide layers [203].

Following recommendations in Aldosari et al. [202] and references therein, a two-level radiation damage model was implemented for the silicon substrate (Table 5).

Following recommendations reported in the same references, a concentration of trapped charges at the Si-SiO_2 interfaces and within the SiO_2 layers of $C = 10^{12}\,\frac{1}{cm^2}$ and $C = 10^{7}\,\frac{1}{cm^2}$ for the pre-irradiated Octa bulk and for the Octa epitaxial respectively was considered.

The TCAD devices were validated against experimentally determined I-V and C-V characteristics, with doping concentrations and profiles tuned to fit the experimental results.

Table 5. Two-level radiation damage model. D is the dose in water in units of kGy [202].

Energy [eV]	Type of defect	Introduction rate [cm^{-1}]	Cross section [cm^{-2}]	
			Electrons	Holes
$E_v + 0.36$	C_iO_i donor	$1.826 \times 10^{12} \times D$	2.5×10^{-14}	2.5×10^{-15}
$E_c - 0.42$	$VV^{(-0)}$ acceptor	$3.040 \times 10^{12} \times D$	2.0×10^{-15}	2.0×10^{-14}

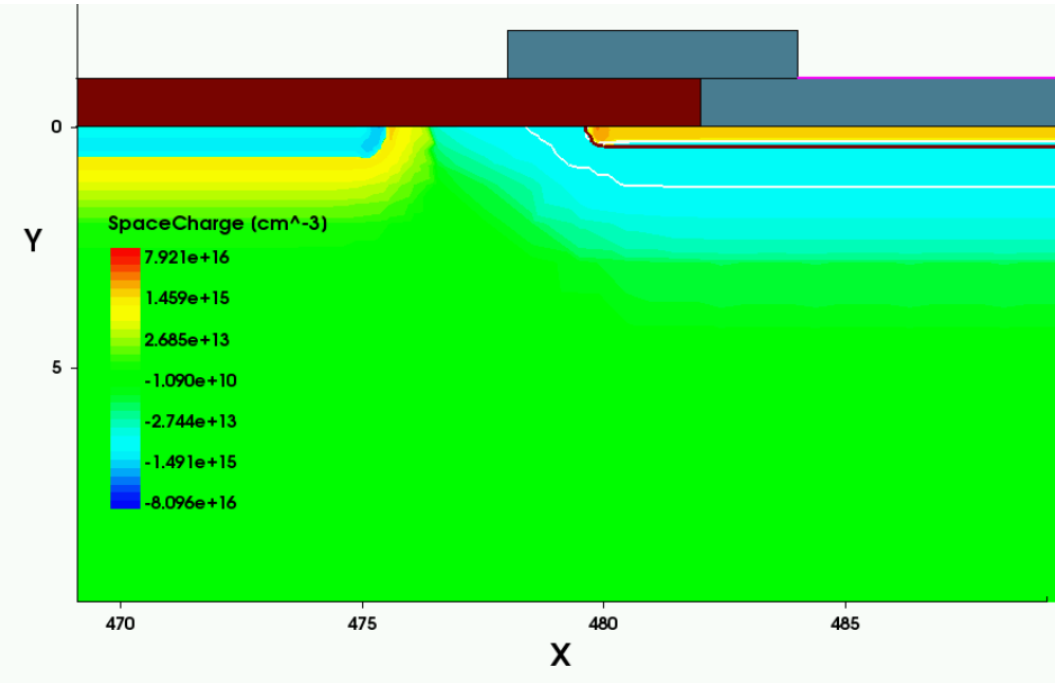

Figure 23. Simulated representation of the space-charge distribution for an epitaxial device. The depletion region is stretched outside the limits of the p-n junction due to the presence of charges in silicon oxide layer. Distances are in microns. Brown area represents the SiO_2 layer, grey areas represent the aluminium contact of the n^+ electrode. The p^+ guard ring is visible on the left.

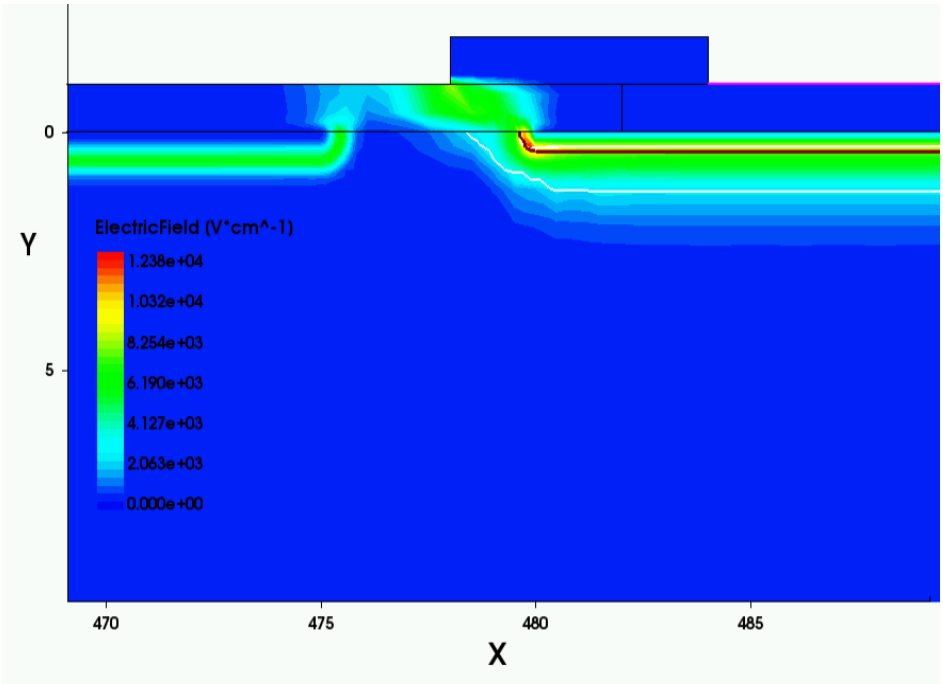

Figure 24. Simulated representation of the electric field between the n^+ electrode and its p^+ guard ring for an epitaxial device.

5 A rehearsal: first measurements with the Octa

5.1 Introduction

This chapter discusses the experimental investigations performed to characterize the Octa bulk as a small-field-dedicated dosimeter in the context of machine-specific quality assurance (QA). Measurements with the Octa, such as of off-axis ratios (OARs) and output factors (OFs), were benchmarked against commercially available dosimeters. All measurements discussed hereafter were performed in 2016.

5.2 Materials and methods

5.2.1 Dosimeters and linacs

Experimental measurements described in this study were carried out at the Illawarra Cancer Care Centre (ICCC), Wollongong, Australia, at the Peter MacCallum Cancer Centre (PMCC, Figure 25), Melbourne, Australia and at the Sir Charles Gairdner Hospital (SCGH), Nedlands, Australia using medical linear accelerators and megavoltage photon beams as in Table 6. Measurements with the Octa were benchmarked using the commercially available dosimeters in Table 7.

Table 6. Participating centers and characteristics of linacs and beam qualities used. 6 MV and 10 MV FB were flattened beams. 6 MV and 10 MV FFF were flattening filter free (FFF) beams.

Centre	Linear accelerator	Collimator	Energy [MeV]
ICCC	Clinac® iX [10]	jaws	6 MV FB
ICCC	Clinac® iX	jaws	10 MV FB
PMCC	TrueBeam™ STx [11]	jaws	6 MV FFF
PMCC	TrueBeam™ STx	jaws	10 MV FFF
SCGH	CyberKnife® M6 [12]	Iris™	6 MV FFF

[10] Varian Medical Systems, Palo Alto, CA, USA
[11] Varian Medical Systems, Palo Alto, CA, USA
[12] Accuray, Palo Alto, CA, USA

Table 7. Reference dosimeters used for benchmarking the Octa for this study.

Dosimeter	Comments	Type
EBT3 Gafhromic films [13]	EPSON expression 10000XL scanner	dosimetry films
microDiamond [14]		synthetic diamond
SRS 60018 [15]		silicon diode

5.2.2 Output factors and off-axis ratios

OFs are defined as the ratio between the detector reading at specific field size ($clin$) and that at the machine specific reference field (msr), following the formalism used by Francescon et al. [147]:

$$\mathrm{OF}_{\mathrm{det}} = \frac{\mathrm{M}^{\mathrm{f_{clin}}}}{\mathrm{M}^{\mathrm{f_{msr}}}} \tag{5.1}$$

where $\mathrm{M}^{\mathrm{f_{clin}}}$ and $\mathrm{M}^{\mathrm{f_{msr}}}$ are the corrected detector readings in the $\mathrm{f_{clin}}$ and $\mathrm{f_{msr}}$ fields respectively.

The OFs were measured at 90 cm source-to-surface distance (SSD) and 10 cm depth in solid water. Dose profiles were acquired at 90 cm SSD and 10 cm depth in solid water for measurements at ICCC, and at 100 cm SSD and 10 cm depth for measurements at PMCC, in order to follow the QA protocol in place. However, measurements with the CyberKnife® system were performed as follow: OFs and OARs were measured at 1.5 cm depth and 80 cm source-to-detector distance (SDD).

[13] Ashland Inc., USA
[14] PTW, Freiburg, Germany
[15] PTW, Freiburg, Germany

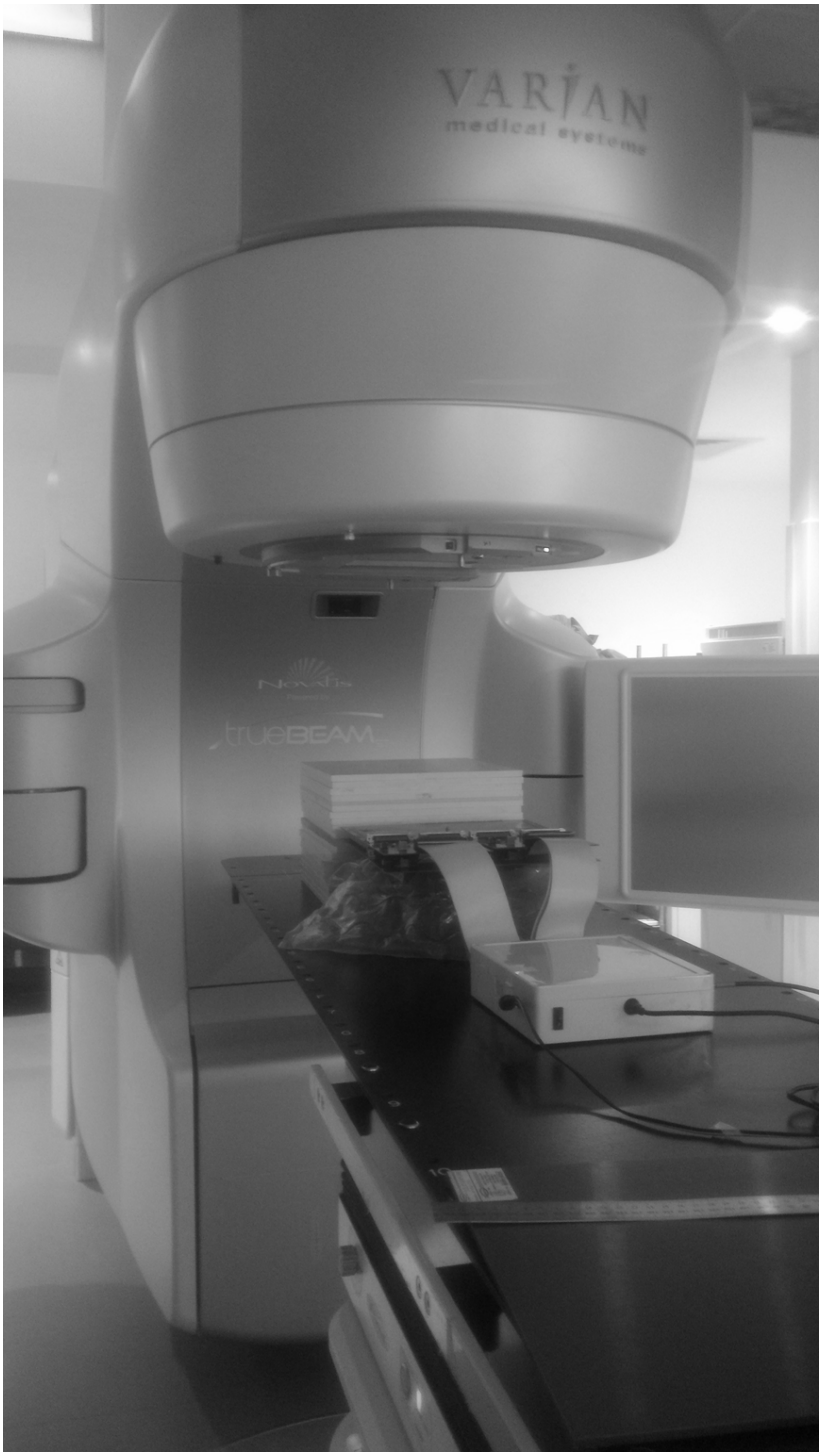

Figure 25. Experimental setup at the PMCC. The Octa was positioned on the treatment couch on top of solid water slabs (10 cm) for backscattering purposes. Additional solid water slabs were then added on top of the detector to reach required water-equivalent depths.

Prior to measurements, the Octa was aligned with respect to the beam central axis (CAX) by maximizing the response of its central pixel using the smallest available field size, a 5 mm side square field with Varian linacs and a 5 mm diameter circular field with the CyberKnife® system.

For OFs measurements, the detector reading at each field size was taken as the average response of its central pixel over 3 repetitions of the same measure followed by normalization of these averages to the average reading at the reference field size.

For OARs, the Octa reading at each field size was taken as the reading of each channel averaged over 3 repetitions of the same measure followed by normalisation of the response of each channel to the median response of the pixels within 0.5 mm of CAX.

OARs were evaluated by comparing FWHM and penumbra values, which was taken as the distance between the 80% and the 20% isodose levels. For a quantitative estimation, profiles were analysed with MATLAB (Mathworks, Inc.) using a shape preserving interpolant function.

5.2.3 EBT3 films, microdiamond detector and SRS60018 diode detector

EBT3 Gafchromic films used in this study were sandwiched between the same Perspex plates used with the Octa. Films were scanned with an EPSON expression 10000XL using a $48-$ bit RGB with a resolution of 72 dpi. All films were pre- and post-scanned six times using only the last 3 optical density maps, maintaining a consistent orientation. The film analysis method employed was the same as that used by Aldosari et al. [116].

The PTW SRS diode 60018 and the microdiamond were mounted parallel to be the beam axis and used in a water phantom. The diode was oriented vertically, measuring at the effective point of measurement of 1.3 mm from top surface. Its readings were corrected using correction factors by Francescon et al. [147].

5.2.4 Percentage differences and uncertainty estimation

In all cases, the percentage differences between the Octa readings and those for the dosimeters used as reference was presented as below:

$$\%\text{diff} = \frac{\text{Octa} - \text{dosimeter}_{\text{ref}}}{\text{dosimeter}_{\text{ref}}} \times 100 \qquad (5.2)$$

For all measurements, we defined the final reading of each one of the Octa 512 channel as the mean value over 3 repetitions of the same measure with error bars calculated as 2 standard deviations.

5.3 Results

5.3.1 Output factors

The OFs measured with the Octa are in Figure 26 for the 6 and 10 MV flattened beams.

In the proposed figures, OFs were normalized to the 30 mm side square field, the smallest available field size for which charged particle equilibrium (CPE) is still provided for all energies [104].

5.3.2 Off-axis ratios

Selected OARs measured with the Octa and with the corresponding benchmark are shown in Figure 27 to Figure 33 for all beams investigated. FWHM and penumbra values for the in-plane and cross-plane profiles are shown in Table 8 and Table 10. In the figures, profiles were aligned such that the origin lies at the coordinate corresponding to the 50% response.

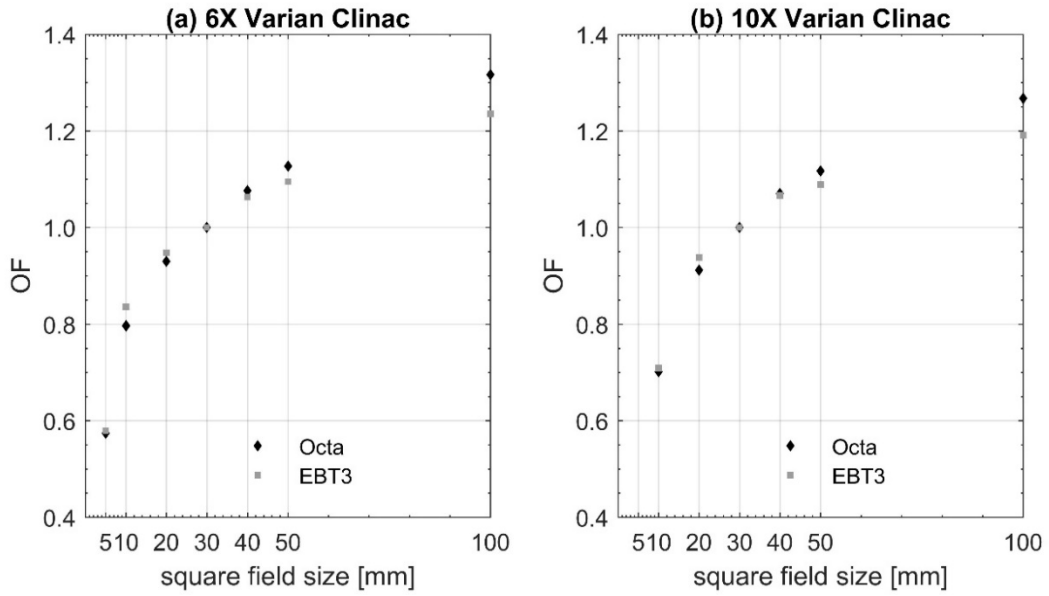

Figure 26. (a) OFs measured with the Octa and EBT3 films for a 6 MV FB for field sizes from 5 mm side square field to 100 mm side square field, normalized to 30 mm side square field. (b) OFs measured with the Octa and EBT3 films for a 10 MV FB for field sizes from 5 mm side square field to 100 mm side square field, normalized to 30 mm side square field.

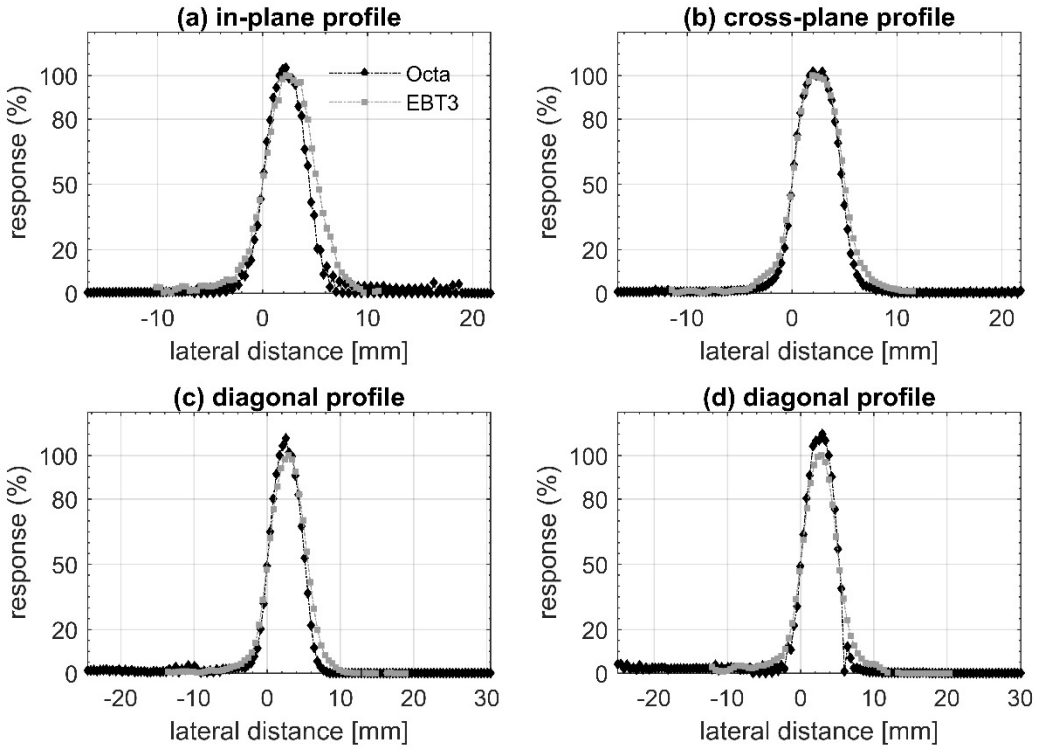

Figure 27. OARs measured with the Octa and EBT3 films for a 6 MV FB, 5 mm side square field. Profiles are aligned with respect to the 50% peak response, taken as the median value around the CAX.

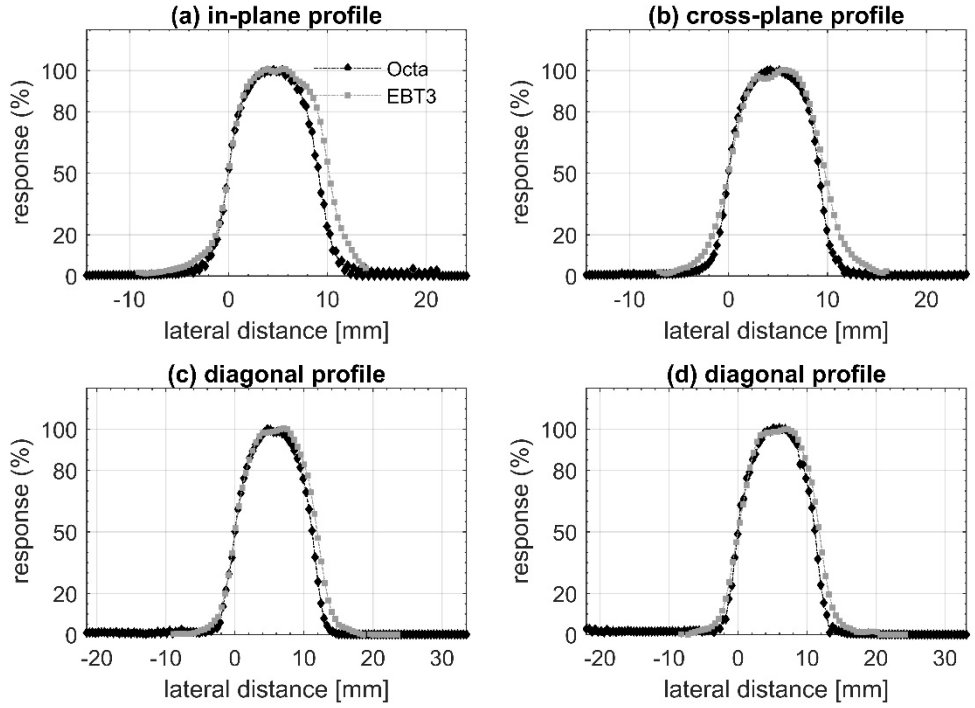

Figure 28. OARs measured with the Octa and EBT3 films for a 6 MV FB, 10 mm side square field. Profiles are aligned with respect to the 50% peak response, taken as the median value around the CAX.

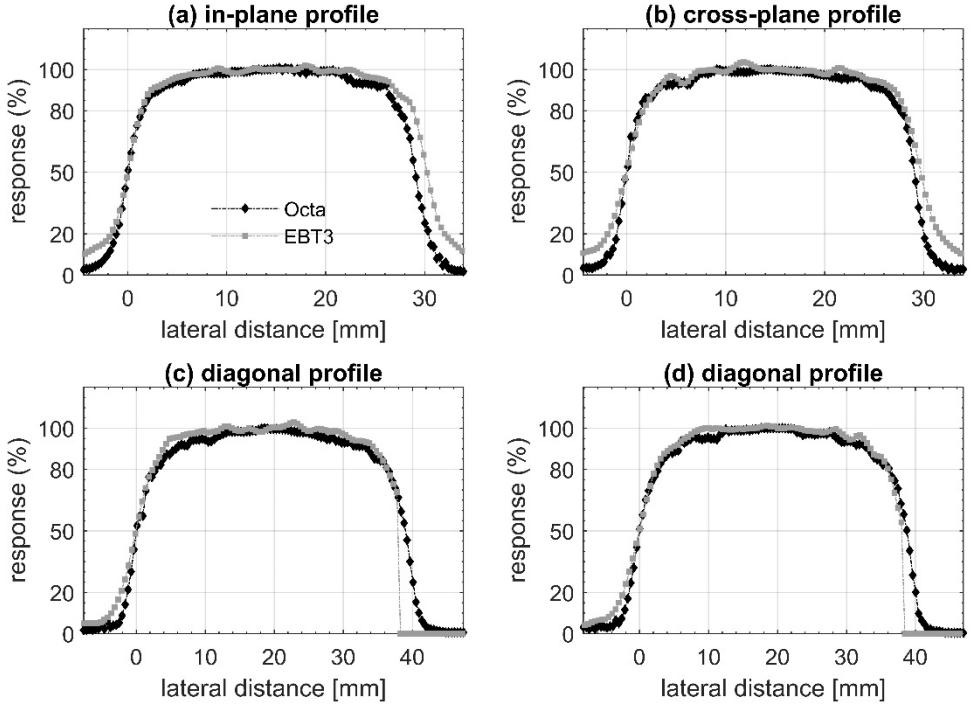

Figure 29. OARs measured with the Octa and EBT3 films for a 6 MV FB, 30 mm side square field. Profiles are aligned with respect to the 50% peak response, taken as the median value around the CAX.

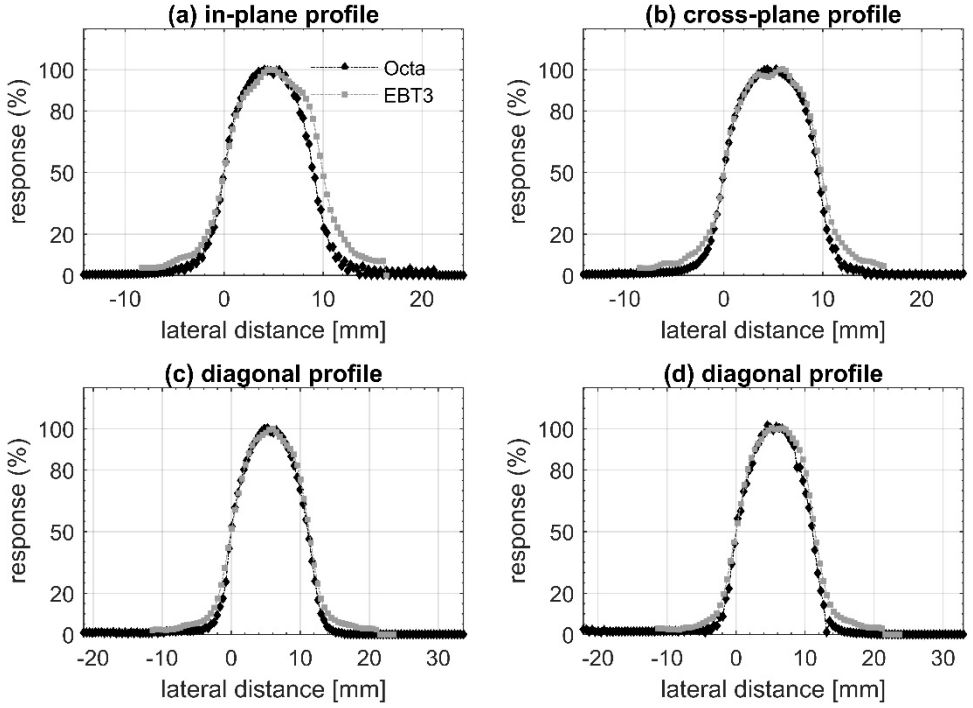

Figure 30. OARs measured with the Octa and EBT3 films for a 10 MV FB, 10 mm side square field. Profiles are aligned with respect to the 50% peak response, taken as the median value around the CAX.

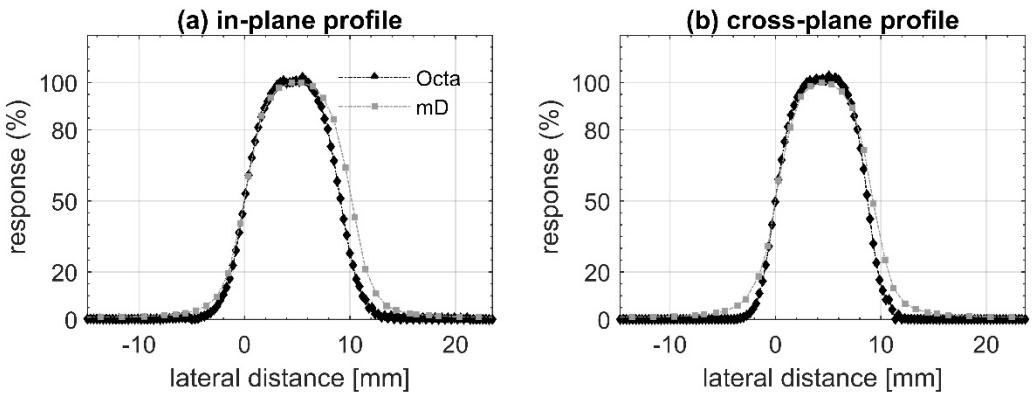

Figure 31. OARs measured with the Octa and microDiamond for a 6 MV FFF beam, 10 mm side square field, produced with a TrueBeam™ STx linac. Profiles are aligned with respect to the 50% peak response, taken as the median value around the CAX.

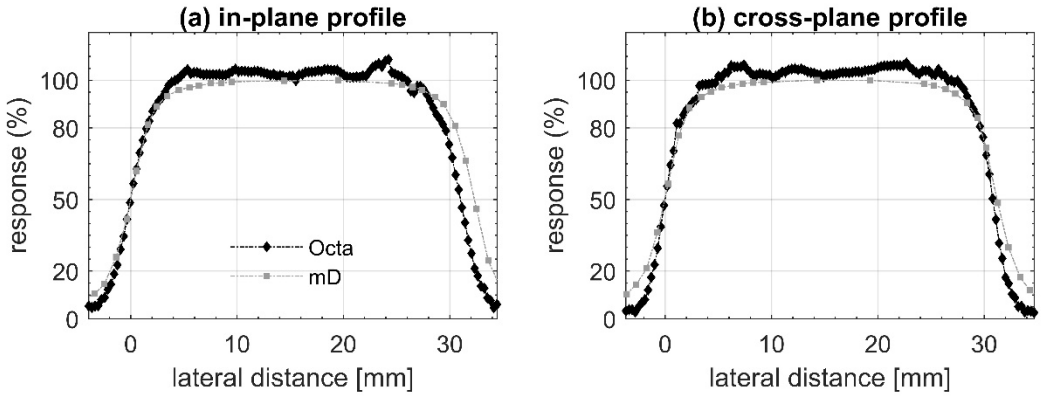

Figure 32. OARs measured with the Octa and microDiamond for a 6 MV FFF beam, 30 mm side square field, produced with a TrueBeam™ STx linac. Profiles are aligned with respect to the 50% peak response, taken as the median value around the CAX.

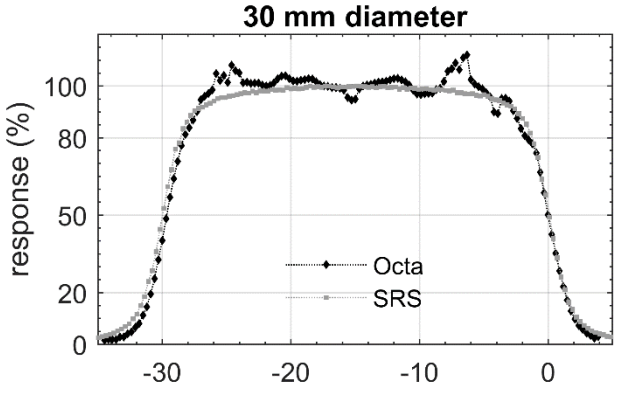

Figure 33. In-line profiles measured with the Octa. Profiles are for a radiation field collimated with the variable aperture Iris™ collimator mounted on a CyberKnife®. A 6 MV FFF beam was used. Data is benchmarked with measurements with an SRS diode and aligned to the 50% response.

Table 8. Summary of FWHM and penumbra values measured with the Octa and the reference dosimeter, for the in-plane profiles presented in Figure 27 to Figure 32.

Beam	Side of the square field [mm]	Octa		Reference		Difference	
		FWHM [mm]	Penumbra [mm]	FWHM [mm]	Penumbra [mm]	ΔFWHM (%)	ΔPenumbra [mm]
6 MV FB	5	4.5	1.6	5.3	2.2	-15.1	-0.6
6 MV FB	10	9.1	2.1	10.1	2.3	-9.9	-0.2
6 MV FB	30	29.0	2.7	30.2	3.1	-4.0	-0.4
10 MV FB	10	9.0	2.6	10.0	3.1	-10.0	-0.5
6 MV FFF	10	9.1	2.5	10.2	2.7	-10.8	-0.2
6 MV FFF	30	31.0	2.9	32.3	3.4	-4.0	-0.5

Table 9. FWHM and penumbra values measured with the Octa and the SRS diode, for the in-plane profiles in Figure 33.

Beam	Diameter of the circular field [mm]	Octa		Reference		Difference	
		FWHM [mm]	Penumbra [mm]	FWHM [mm]	Penumbra [mm]	ΔFWHM (%)	ΔPenumbra [mm]
6 MV FFF	30	29.6	3.0	29.8	2.6	-0.7	0.4

Table 10. Summary of FWHM and penumbra values measured with the Octa and the reference dosimeter, for the cross-plane profiles presented in Figure 27 to Figure 32.

Beam	Side of the square field [mm]	Octa		Reference		Difference	
		FWHM [mm]	Penumbra [mm]	FWHM [mm]	Penumbra [mm]	ΔFWHM (%)	ΔPenumbra [mm]
6 MV FB	5	4.8	1.4	5.0	1.9	-4.0	-0.5
6 MV FB	10	9.2	2.0	9.7	3.0	-5.2	-1.0
6 MV FB	30	29.1	2.4	29.7	3.6	-2.0	-1.2
10 MV FB	10	9.5	2.4	9.9	2.9	-4.0	-0.5
6 MV FFF	10	8.7	2.2	9.2	2.8	-5.4	-0.6
6 MV FFF	30	30.8	2.2	31.2	3.4	-1.3	-1.2

5.4 Discussion and conclusion

The central pixels of the Octa (0.16 mm x 0.2 mm) were small enough to measure accurately the position of CAX peak without any volume-averaging effect.

Once aligned to the CAX, OFs for the Octa were measured for both small and large radiation fields. Positioning uncertainties were therefore negligible, in stark contrast with point-like detectors for which this is a major source of error in OFs measurements.

For all beam qualities investigated, OFs for the Octa were generally accurate within 3% with respect to values measured with the reference dosimeter.

FWHM values for the Octa for in-plane, cross-plane and diagonal dose profiles were not always in agreement with respect to the reference. Small differences between nominal and effective field sizes for small jaw-defined radiation fields, due to the jaws calibration and or their positioning accuracy, are known to have a strong impact on small field measurements [204], [205]. Ideally, OARs would have to be measured at the same time with the dosimeter being evaluated and that used as reference.

Our conclusion was that the Octa bulk, thanks to its a sub-millimetre resolution along 4 linear arrays, was in principle able to provide a much more detailed characterization of the 2D dose map than that of its predecessor the MP512 and the Duo detector prototypes (see Chapter 3 for detail on these devices). However, non-uniformity in the OARs, especially in those produced in FFF beams, and discrepancies in measured OARs with respect to benchmarks suggested there was ample scope for a more detailed numerical and experimental analysis of the behaviour of the prototype. Earlier results of this analysis, which will be presented in Chapters 9 and 10, prompted a move towards the use and characterization of an alternative Octa device, this one manufactured on an epitaxial substrate (see section 4.2 for further details).

6 Characterization of the Octa as a dosimeter

This chapter, which is based on material published in **G. Biasi** *et al*, (2018) A novel high-resolution 2D silicon array detector for small field dosimetry with FFF photon beams, *Physica Medica*, 45, 117–126 [15][16], discusses the experimental investigations performed to evaluate the potential of the Octa epitaxial as a small-field-dedicated dosimeter.

Flattening filter free (FFF) beams are increasingly being considered for stereotactic radiotherapy (SRT). For the first time, the performance of a 2D monolithic silicon-diode array detector prototype, the Octa, was evaluated under 6 and 10 MV FFF beams. The dosimeter was tested also under flattened beams for comparison. All measurements discussed hereafter were performed during the first half of 2017.

6.1 Introduction

Stereotactic radiotherapy (SRT) techniques, of which stereotactic body radiation therapy (SBRT) is an example, are a form of external beam radiotherapy (EBRT). These treatments deliver high doses in just a few fractions, up to 45 Gy/fraction in the case of SBRT, using small radiation fields [24], [25].

Codes of Practice for quality assurance (QA) in the case of small field dosimetry have been only recently outlined [1], [2]. Challenges associated with this scenario are beam related, such as partial occlusion of the primary source and loss of CPE on the central axis, and detector related, relative to its dimensions with respect to the field and its perturbation effects on the particles spectra [1], [2]. These conditions, resulting in overlapping penumbrae over the detector volume, may affects its readings, thus the accuracy of the treatment planning system (TPS) in predicting dose distributions. Dosimetric inaccuracies may lead to poor outcomes for patients [2], [24].

Recently, a growing interest in rapid delivery of heterogeneous dose distributions has revived the use of flattening filter free (FFF) beams [21]. The removal of the flattening filter from the LINAC changes the profile and dosimetric characteristics of radiation beams [22]. Reported clinical benefits are mainly a result of an increased available dose rate and lower peripheral doses (PD) [23]. With higher dose per pulses and dose profiles having steeper

[16] References are combined in a single bibliography at the end of the present dissertation.

gradients, FFF beams compound all the problems associated with small field dosimetry for flattened beams and may prove challenging for dosimeters performance [22], [23].

Ideal dosimeters for SRT QA are to be water equivalent, dose-rate independent, with a good signal to noise ratio and real-time read-out [1], [2]. They should have a sufficiently small sensitive volume to avoid volume-averaging effects [2], which are related to the dose gradients over the sensitive volume [21] and can result in a different signal compared to the signal a point-like detector would measure. To date, in the absence of such an ideal dosimeter, it has been common practice to perform QA measurements with at least two types of radiation detectors and then crosscheck the results for consistency [6], often along with the use of Monte Carlo (MC) simulations. Several alternatives have been described in the literature.

EBT3 Gafchromic films have minimal energy dependence and offer high spatial resolution but not real-time readings, which are also affected by large uncertainties due to film polarization, non-uniformity, scanning and handling techniques [6]. Ionization chambers (IC) are the recognized standard for large field dosimetry but are impaired by volume-averaging effects when used for small radiation fields [1]. Diamond-based detectors have been employed for routine QA thanks to their water equivalence, energy independence and high signal to noise ratio [1], [2], but are expensive and as such not widely employed. Furthermore, they exhibit dose rate dependence, though corrections can be applied [2]. All these dosimeters are subject to central axis (CAX) alignment problems, an issue all the more relevant for small radiation fields [1].

Silicon diodes are a valuable option for small field dosimetry thanks to their large dynamic range and high sensitivity, real-time operations, well–developed manufacturing technology and high spatial resolution due to the small sensitive volumes (SVs). However, they are known to be dose rate dependent, with an increase in sensitivity with dose per pulse reported for p-type silicon diodes [137], [206].

Furthermore, correction factors need to be applied to account for beam perturbations, due to their SVs and extra-cameral components. These factors depend on detector design, treatment head design, beam quality, field size and measurement conditions [2].

It was shown that it is possible to design a ‘correction-free’ detector, though, with the addition of low density media to the high density detector components [64]. However, it must be verified that these modifications are correctly compensating whatever the beam quality and measurements conditions [65].

2D monolithic silicon diode array detectors, with either 2 mm and 3 mm pitch, have been shown to be promising as dosimeters by several groups [115], [116]. Commercially available

options based on single diodes are the ArcCHECK (Sun Nuclear Corp., Melbourne, FL) and the Delta^4 (ScandiDos AB, Uppsala, Sweden). Their spatial resolution, though, is not adequate for small field dosimetry. In fact, while with 1D monolithic detectors it is easy to decrease the pitch between silicon diodes down to 0.2 mm (CMRP DMG) [173], in the case of 2D detectors a compromise is necessary between the overall active area and the spatial resolution provided, in order to be within limitations in the number of read-out channels.

The Centre for Medical Radiation Physics (CMRP), University of Wollongong, has designed and characterized two 1st generation monolithic silicon diode array detectors for SRT QA, the MP512 [177] and the Duo [118]. In those studies, they were shown to be accurate dosimeters for output factors (OFs), percentage depth dose (PDD) and dose profile measurements under flattened beams with a dose per pulse (DPP) dependence. The angular dependence of the MP512 was investigated and could be corrected for, making it a suitable candidate for arc therapy delivery QA [132]. The rather coarse spatial resolution (2 mm) of the MP512 and the limited characterization of the 2D dose map given by the Duo, though, impair their attractiveness for contemporary small field dosimetry where sub-millimetre spatial resolution and a detailed description of the 2D dose map is paramount, especially when using FFF beams.

The Octa, a 2nd generation monolithic silicon diode array detector, incorporates its predecessors' technology and as such, it is characterized by the same signal stability, radiation hardness and dose linearity. The Octa's 512 diodes-SVs are arranged in four intersecting orthogonal linear arrays such that cross-plane, in-plane and 2 diagonal dose profiles are characterized simultaneously with sub-millimetre resolution.

This study evaluated the potential of the Octa for relative dose measurements, in particular in the challenging measurements conditions of small fields with FFF beams. Parameters commonly used by commercial TPSs, such as dose profiles, PDD curves and OFs were investigated. Results were benchmarked against those for other commercially available dosimeters. In order to have a comprehensive analysis of the Octa performance, 6 and 10 MV flattened beams were included in the study.

6.2 Materials and methods

6.2.1 The dosimeter

The Octa is a 2D monolithic silicon array detector based on SVs fabricated on a high resistivity p-type epitaxial [188], grown on top of a low resistivity p+ substrate. A thin

protective layer of epoxy covers the SVs. The 512 diodes have all the same sensitive area of $0.032\ mm^2$ and are of elongated rectangular shape ($0.04\ mm \times 0.8\ mm$), except for the 9 pixels in the central matrix at the intersection of the 4 arrays ($0.16\ mm \times 0.20\ mm$). The device has a sub-millimetre resolution with diodes having a 0.3 mm pitch along the vertical and horizontal arrays and a 0.43 mm pitch along the 2 diagonal arrays. The diodes are operated in passive mode, i.e. with no bias voltage applied, and connected to a multichannel readout electronics data acquisition (DAQ) system based on a commercially available analogue front end (AFE0064, Texas Instruments), which was previously described in detail [177], [190]. In this study, an equalization procedure [207] was used to correct for small differences in each channel response. This variability is due to a small difference in the sensitivity of each diode and the gain of its corresponding preamplifier in an application-specific integrated-circuit (ASIC).

Conceived as a 2D planar dosimeter for dose measurements in solid water, the Octa is sandwiched between two Perspex plates, each 5 mm thick. A small air gap on top of its SVs minimizes the number and size of corrections that are required to relate its readings to dose [179].

Experimental measurements described in this study were carried out at the Illawarra Cancer Care Centre, Wollongong NSW, Australia using a Varian Clinac linac (Varian Medical Systems, Palo Alto CA) and at the Peter MacCallum Cancer Centre, Melbourne VIC, Australia using a Varian TrueBeam™ STx linac (Varian Medical Systems, Palo Alto CA), as summarized in Table 11. Dosimeters used as reference are summarized in Table 12.

Table 11. Participating centres and characteristics of linacs and beam qualities used. All linacs were calibrated to deliver 1 cGy/MU at d_{max} in water at 100 cm SSD.

Centre	Linear accelerator	Collimator	Energy [MeV]
ICCC	Varian Clinac® [17]	jaws	6 MV FB
ICCC	Varian Clinac®	jaws	10 MV FB
PMCC	Varian TrueBeam™ STx [18]	jaws	6 MV FFF
PMCC	Varian TrueBeam™ STx	jaws	10 MV FFF

[17] Varian Medical Systems, Palo Alto, CA, USA
[18] Varian Medical Systems, Palo Alto, CA, USA

Table 12. Commercially available dosimeters used for benchmarking the Octa.

Dosimeter	Comments	Type
EBT3 Gafchromic films [19]	EPSON expression 10000XL scanner	dosimetry films
microDiamond [20]		synthetic diamond
CC13 [21]		ionization chamber
Farmer chamber (a) [22]	Type IBA-FC-65P	ionization chamber
Farmer chamber (b)	Type NE2571A	ionization chamber
Markus [23]	Model N23343	ionization chamber

6.2.2 Output factors and off-axis ratios

Output factors are defined as the ratio between the detector reading at specific field size ($clin$) and that at the machine specific reference field (msr), following the formalism used by Francescon et al. [147]:

$$OF_{det} = \frac{M^{f_{clin}}}{M^{f_{msr}}} \tag{6.1}$$

where $M^{f_{clin}}$ and $M^{f_{msr}}$ are the corrected detector readings in the f_{clin} and f_{msr} fields respectively.

The OFs were measured at 90 cm source to surface distance (SSD) and 10 cm depth in solid water. Dose profiles were acquired at 90 cm SSD and 10 cm depth in solid water for measurements at the Illawarra Cancer Care Centre, and at 100 cm SSD and 10 cm depth for measurements at the Peter MacCallum Cancer Centre, in order to follow the QA protocol in place.

Prior to measurements, the Octa was aligned with respect to the CAX by maximizing the response of its central pixel using the smallest available field size, a 5 mm side square field.

For OFs measurements, the detector reading at each field size was taken as the average response of its central pixel over 3 repetitions of the same measure followed by normalization of these averages to the average reading at the reference field size.

[19] Ashland Inc., USA
[20] PTW, Freiburg, Germany
[21] IBA Dosimetry GmbH, Germany
[22] IBA Dosimetry GmbH, Germany
[23] PTW, Freiburg, Germany

For dose profiles, the Octa reading at each field size was taken as the reading of each channel averaged over 3 repetitions of the same measure followed by normalisation of the response of each channel to the median response of the pixels within 0.5 mm of CAX.

Dose profiles were evaluated by comparing FWHM and penumbra values, which was taken as the distance between the 80% and the 20% isodose levels. For a quantitative estimation, profiles were analysed with MATLAB (Mathworks, Inc.) using a shape preserving interpolant function.

6.2.3 Dose per pulse dependence

The dose per pulse (DPP) dependence, which refers to the change of the detector sensitivity due to a change of dose per pulse, was studied by irradiating the Octa with a fixed number of monitor units (MU) and changing the SSD to change the dose per pulse at the detector location [116], [137].

The range of doses per pulse investigated was between a maximum of 0.977 mGy/pulse for the 10 MV FFF beam and a minimum of 0.021 mGy/pulse for the 6 MV FB (Table 13). A 10 cm side square field size was used for all SSDs and beam qualities, with measurements were carried out at 1.5 cm depth for the 6 MV FB, but at 10 cm depth for the 6 and 10 FFF beams.

The DPP sensitivity of the Octa was defined as the ratio of the charge measured by the detector to the charge measured by the ionization chamber used as the reference dosimeter, at the same SSD, i.e. for the same dose per pulse value. The DPP dependence of the Octa was then taken as its sensitivity at each dose per pulse, normalized to that at the dose per pulse at 100 cm SSD 1.5 cm depth for the 6 MV FB, and to that at 100 cm SSD 10 cm depth for the 6 and 10 MV FFF (Table 13).

The two-voltage method, which was deemed accurate in the dose per pulse range investigated [208], was used to evaluate the ion recombination correction factor to correct the Farmer ionization chamber readings in the case of 6 MV FFF and 10 MV FFF beam qualities. No correction factor was applied to the Farmer ionization chamber readings in the case of 6 MV FB [22].

Table 13. Investigation of the DPP dependence of the Octa: range of DPP used for each beam quality and reference dosimeters. For each beam quality, results were normalized to those for the reference dose per pulse indicated.

Range of DPP investigated [mGy/pulse]	Reference DPP [mGy/pulse]	Square field side [mm]	Collimator	Beam quality	Reference dosimeter
0.021 to 0.278	0.278	100	jaws	6 MV FB	Farmer chamber (b)
0.041 to 0.416	0.416	100	jaws	6 MV FFF	Farmer chamber (a)
0.079 to 0.977	0.797	100	jaws	10 MV FFF	Farmer chamber (a)

6.2.4 Percentage depth dose

CAX PDDs were measured by the Octa at 100 cm SSD, with 10 cm solid water for backscattering purposes. A 10 cm side square field size was used for all beam qualities investigated and the desired water depths were reached adding the required amount of solid water slabs on top of the detector.

The average of measurements carried out with a both a CC13 and a Markus ionization chamber under the same experimental conditions was used as reference.

For a quantitative estimation of the percentage differences between the PDDs by the Octa and those for the reference dosimeters, acquired values were analysed with MATLAB (Mathworks, Inc.) using a shape preserving interpolant function.

6.2.5 EBT3 films

The EBT3 Gafchromic films used in this study were sandwiched between Perspex plates as used for the Octa. Films were scanned with an EPSON expression 10000XL using a 48-bit RGB with a resolution of 72 dpi. All films were pre- and post-scanned six times using only the last 3 optical density maps, maintaining a consistent orientation. The film analysis method employed was the same as that used by Aldosari et al. [116].

6.2.6 Percentage differences and uncertainty estimation

In all cases, the percentage differences between the readings by the Octa and those by the dosimeters used as reference was presented as below:

$$\%\text{diff} = \frac{\text{Octa} - \text{dosimeter}_{\text{ref}}}{\text{dosimeter}_{\text{ref}}} \times 100 \qquad (6.2)$$

For all measurements, we defined the final reading of each one of the 512 channel of the Octa as the mean value over 3 repetitions of the same measure with error bars calculated as 2 standard deviations.

For the investigation of the DPP dependence, the error bars shown are the results of the error propagation of the statistical dispersion of both the Octa and the ionization chamber measurements.

6.3 Results

6.3.1 Output factors

OFs measured by the Octa are shown in Figure 34 for the 6 and 10 MV FBs, and in Figure 35 for the 6 and 10 MV FFF beams. OFs were normalized to the 30 mm side square field, the smallest available field size for which charged particle equilibrium (CPE) is still provided for all energies [104].

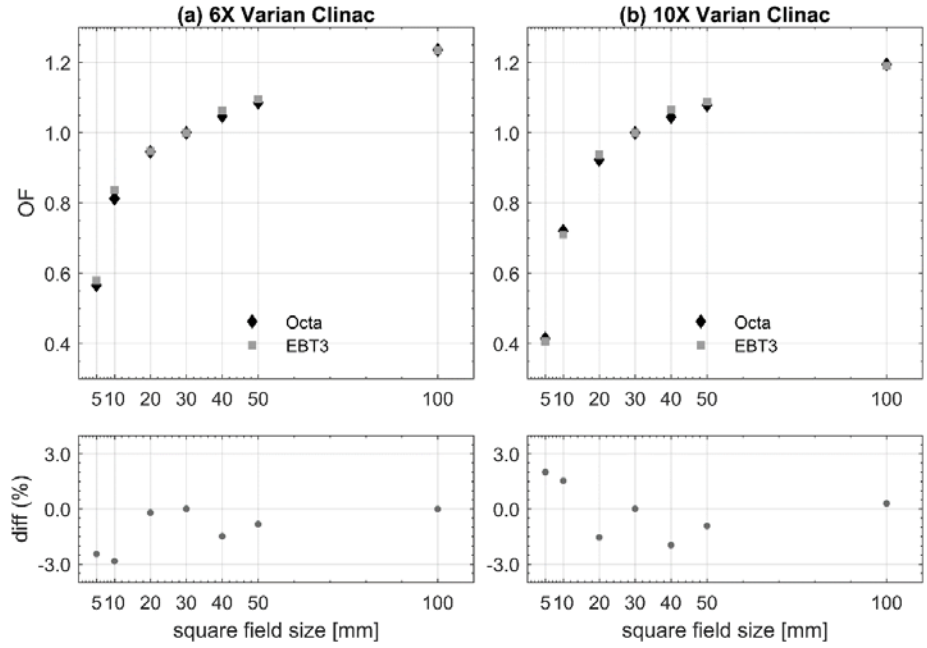

Figure 34. (a) OFs measured by the Octa and EBT3 films for a 6 MV FB for field sizes from 5 mm side square field to 100 mm side square field, normalized to 30 mm side square field. (b) OFs measured by the Octa and EBT3 films for a 10 MV FB for field sizes from 5 mm side square field to 100 mm side square field, normalized to 30 *mm* side square field. Percentage differences are shown in the lower panels.

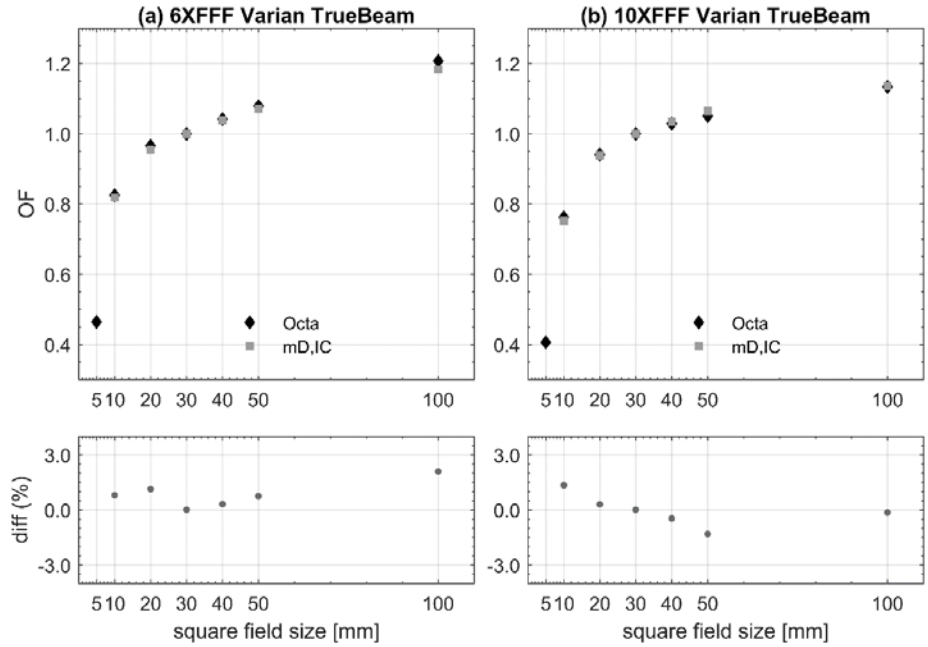

Figure 35. (a) OFs measured by the Octa and microDiamond, IC for a 6 MV FFF beam for field sizes from 5 mm side square field to 100 mm side square field, normalized to 30 mm side square field. (b) OFs measured by the Octa and microDiamond/IC for a 10 MV FFF beam for field sizes from 5 mm side square field to 100 mm side square field, normalized to 30 mm side square field. Percentage differences are shown in the lower panels. Reference data was acquired using a daisy-chain method with microDiamond (for field sizes equal and smaller than 3 cm side) and ionization chamber (for field sizes equal and larger than 3 *cm* side) and was not available for the 5 mm side square field, for both beam qualities.

6.3.2 Off-axis ratios

Selected OARs measured by the Octa are shown in Figure 36 to Figure 41 for all beam qualities investigated and with the corresponding benchmark, where available. FWHM and penumbra values for the in-plane and cross-plane profiles are shown in Table 14 and Table 15.

In the figures, profiles were aligned such that the origin lies at the coordinate corresponding to the 50% response.

Table 14. Summary of FWHM and penumbra values measured by the Octa and the reference dosimeter, for the in-plane profiles presented in Figure 36 to Figure 41.

Beam quality	Square field size [mm]	Octa (in-plane)		Reference (in-plane)		Difference	
		FWHM [mm]	Penumbra [mm]	FWHM [mm]	Penumbra [mm]	ΔFWHM (%)	ΔPenumbra [mm]
10 MV FB	5	5.1	2.2	5.4	2.2	-5.6	0.0
10 MV FB	10	9.9	3.1	10.0	3.1	-1.0	0.0
10 MV FB	30	30.2	4.0	30.4	4.0	-0.7	0.0
6 MV FFF	10	10.5	3.2	10.2	2.7	2.9	0.5
6 MV FFF	30	32.5	4.0	32.3	3.4	0.6	0.6
10 MV FFF	30	32.6	4.9	32.0	3.8	1.9	1.1

Table 15. Summary of FWHM and penumbra values measured by the Octa and the reference dosimeter, for the cross-plane profiles presented in Figure 36 to Figure 41.

Beam quality	Square field size [mm]	Octa (cross-plane)		Reference (cross-plane)		Difference	
		FWHM [mm]	Penumbra [mm]	FWHM [mm]	Penumbra [mm]	ΔFWHM (%)	ΔPenumbra [mm]
10 MV FB	5	5.1	1.9	5.2	2.0	-1.9	-0.1
10 MV FB	10	10.2	2.7	9.9	2.9	3.0	-0.2
10 MV FB	30	29.6	3.9	30.0	3.5	-1.3	0.4
6 MV FFF	10	9.1	2.6	9.2	2.8	-1.1	-0.2
6 MV FFF	30	31.3	3.3	31.2	3.4	0.0	-0.1
10 MV FFF	30	31.1	3.7	31.2	4.4	-0.3	-0.7

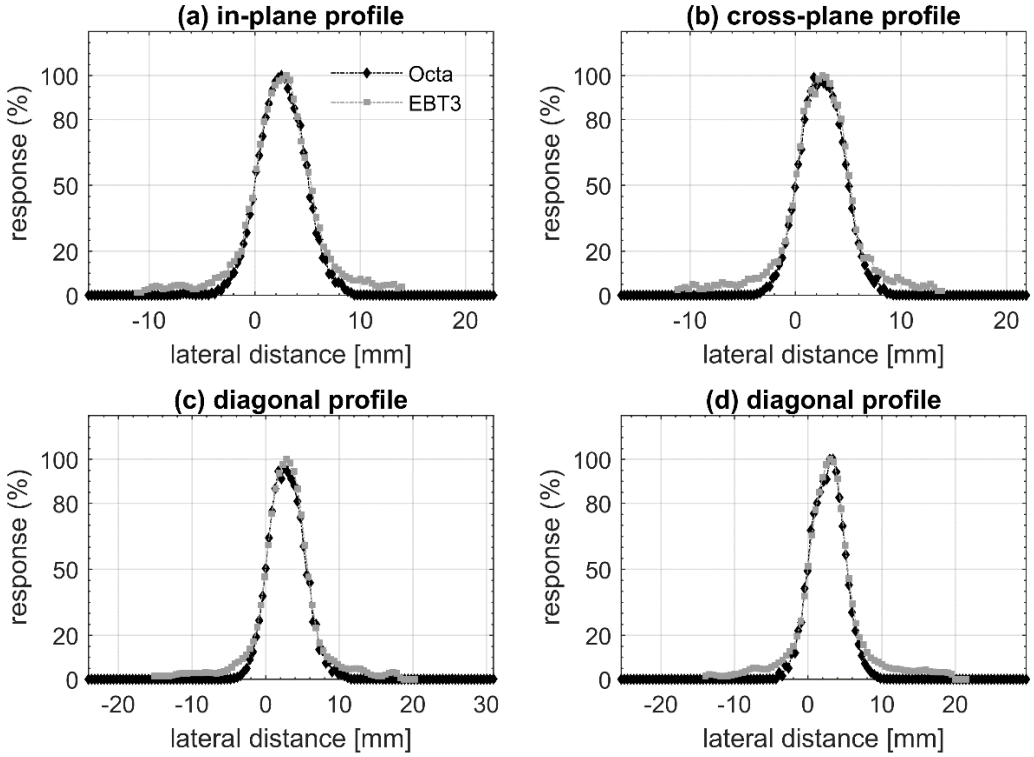

Figure 36. OARs measured by the Octa and EBT3 films for a 10 MV FB, 5 mm side square field. Profiles are aligned with respect to the 50% peak response, taken as the median value around the CAX.

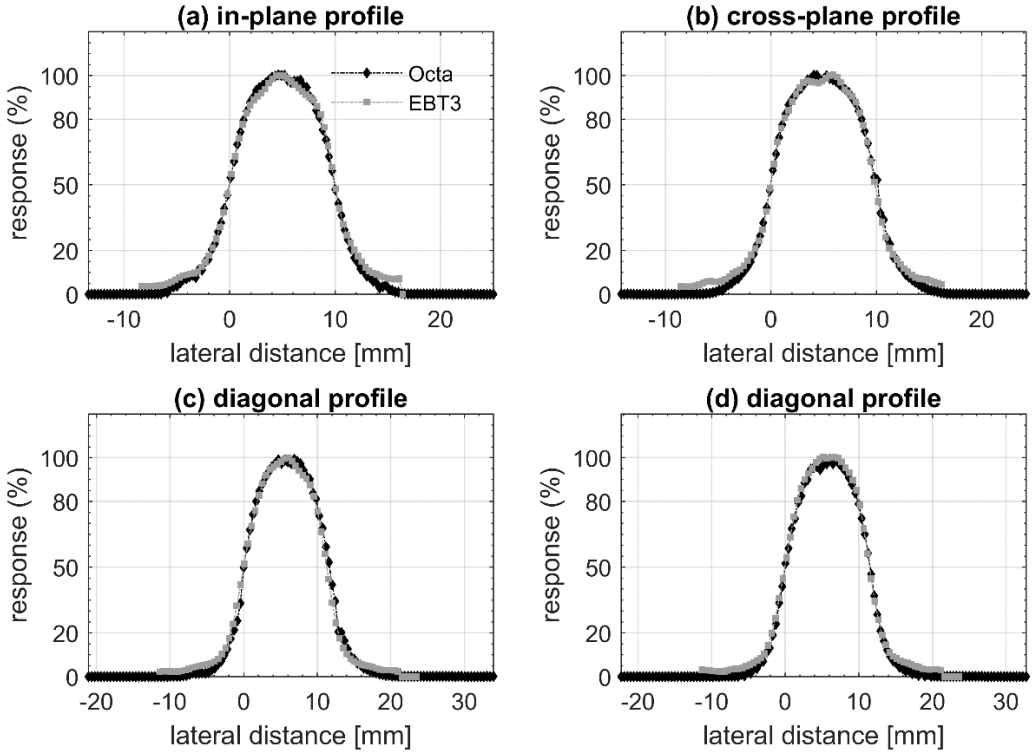

Figure 37. OARs measured by the Octa and EBT3 films for a 10 MV FB, 10 mm side square field. Profiles are aligned with respect to the 50% peak response, taken as the median value around the CAX.

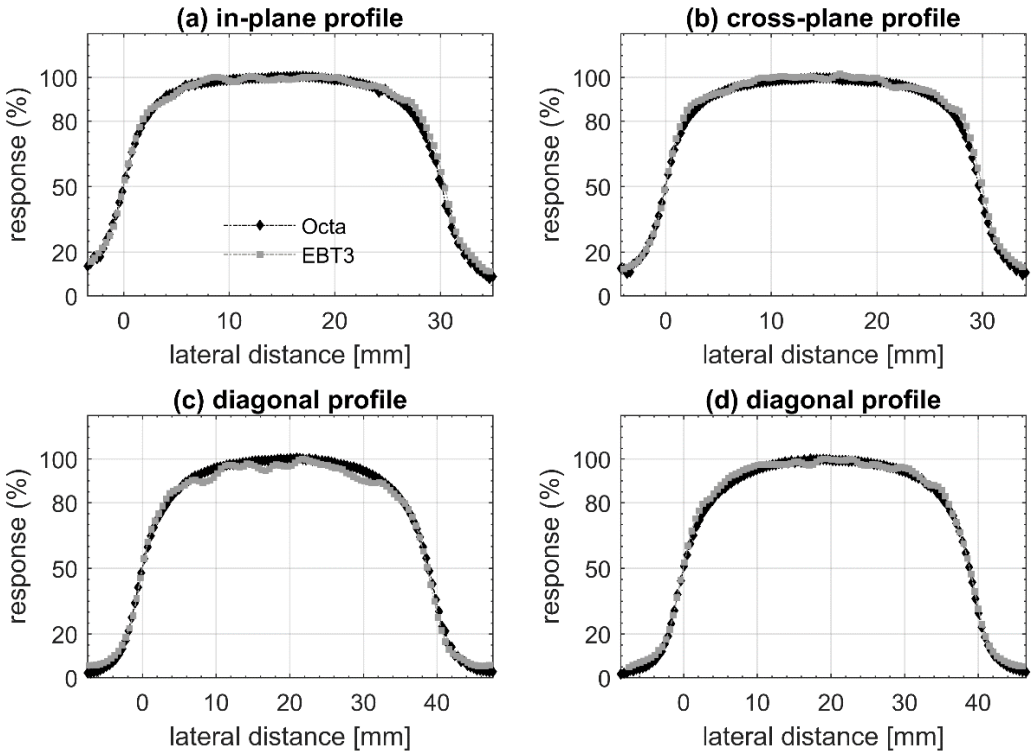

Figure 38. OARs measured with by Octa and EBT3 films for a 10 MV FB, 30 mm side square field. Profiles are aligned with respect to the 50% peak response, taken as the median value around the CAX.

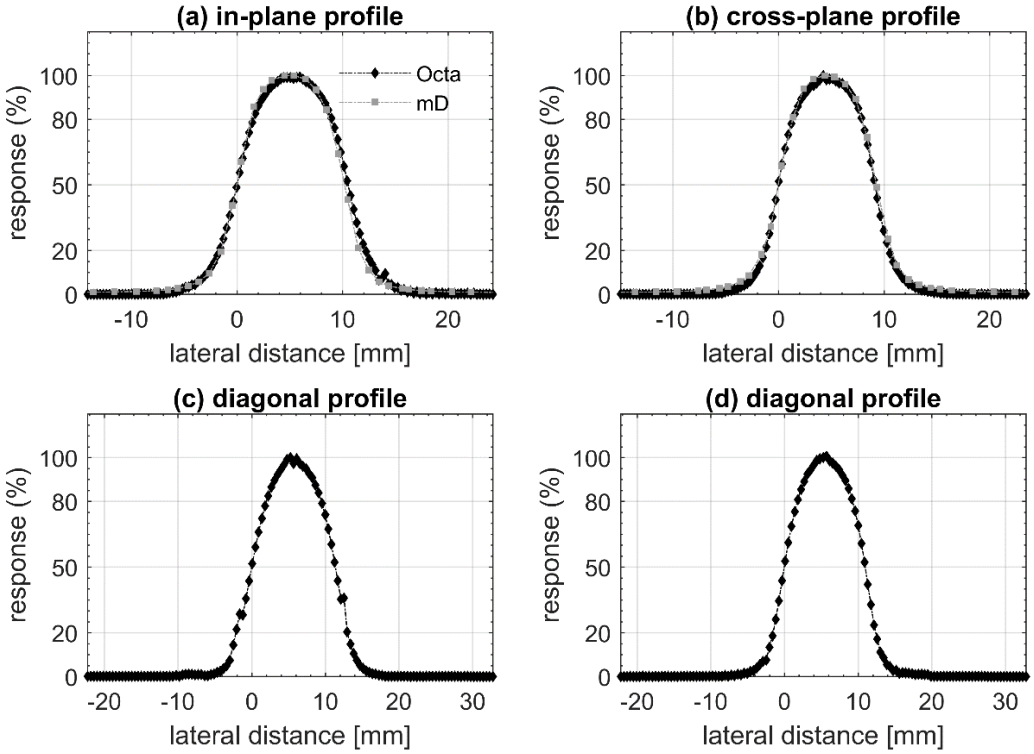

Figure 39. OARs measured by the Octa and microDiamond for a 6 MV FFF beam, 10 mm side square field. Profiles are aligned with respect to the 50% peak response, taken as the median value around the CAX. Reference data was not available for diagonal profiles.

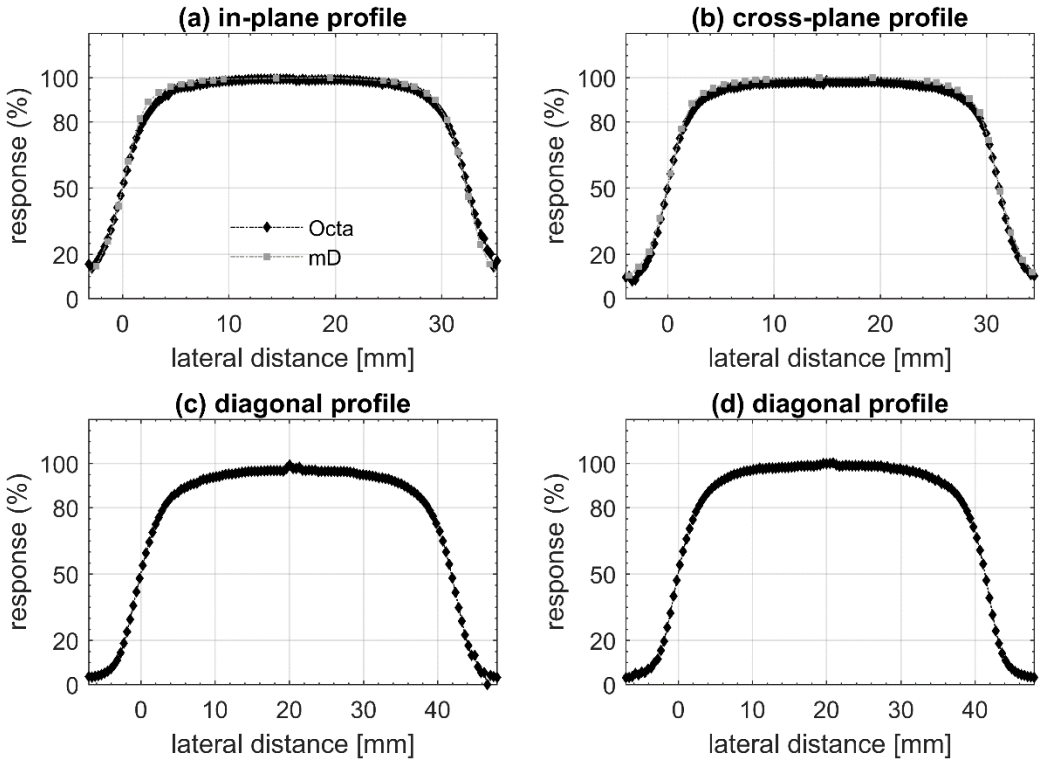

Figure 40. OARs measured by the Octa and microDiamond for a 6 MV FFF beam, 30 mm side square field. Profiles are aligned with respect to the 50% peak response, taken as the median value around the CAX. Reference data was not available for diagonal profiles.

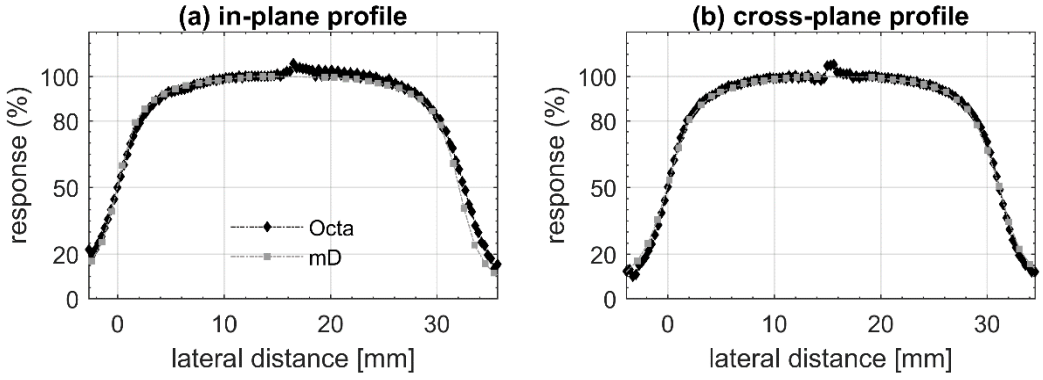

Figure 41. OARs measured by the Octa and microDiamond for a 10 MV FFF beam, 30 mm side square field. Profiles are aligned with respect to the 50% peak response, taken as the median value around the CAX.

6.3.3 Dose per pulse dependence

The results of the investigation of the DPP dependence of the Octa is shown in Figure 42 for all beam qualities investigated.

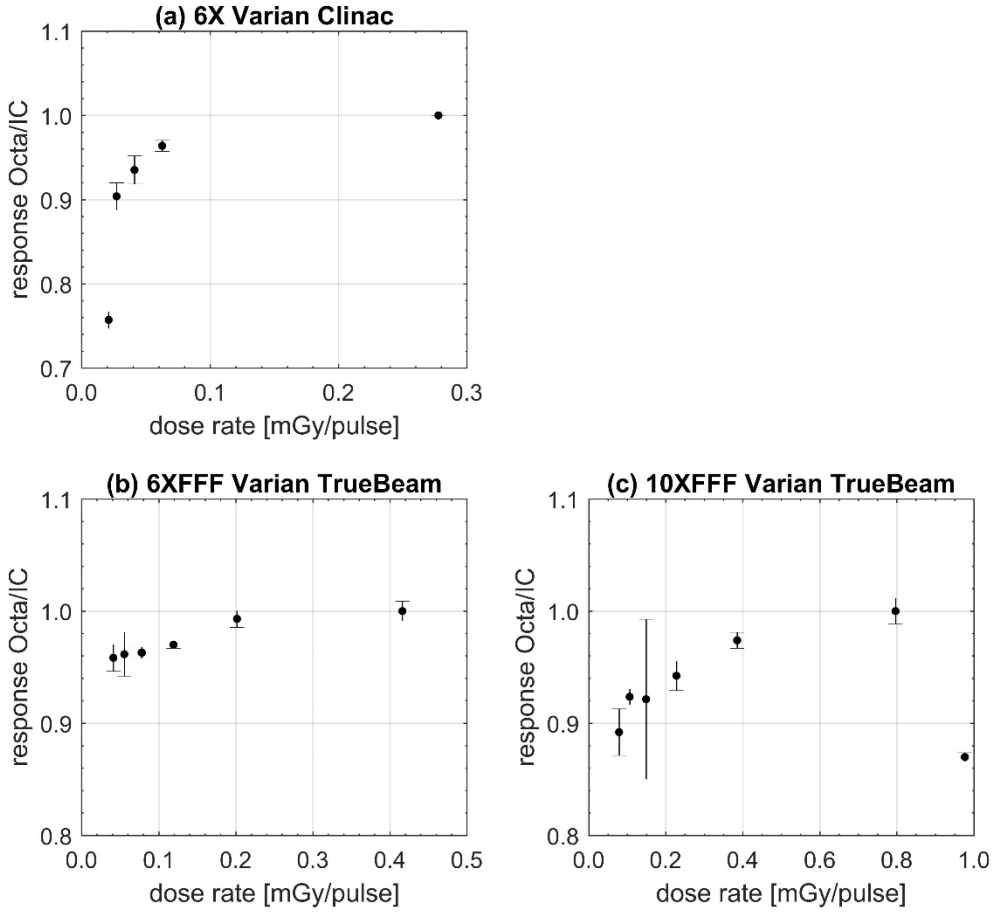

Figure 42. The Octa response measured against the ionization chamber as a function of dose per pulse. (a) DPP dependence for a 6 MV FB, with ratios normalized to the dose per pulse at 100 cm SSD 1.5 cm depth (0.278 mGy/pulse). (b) DPP dependence for a 6 MV FFF beam, with ratios normalized to the dose per pulse at 100 cm SSD 10 cm depth (0.416 mGy/pulse). (c) DPP dependence for a 10 MV FFF beam, with ratios normalized to the dose per pulse at 100 cm SSD 10 cm depth (0.797 mGy/pulse). Error bars represent the combined uncertainties.

6.3.4 Percentage depth dose

PDDs measured by the Octa are shown in Figure 43 for the 6 MV FB and in Figure 44 for the 6 and 10 MV FFF beams. Nominal depths were converted to water equivalent depths to account for the density of the Perspex plates. PDDs for the 6 MV FFF and 10 MV FFF beam qualities were measured only up to 10 cm nominal depth in solid water due to limited availability of solid water slabs at the Peter MacCallum Cancer Centre.

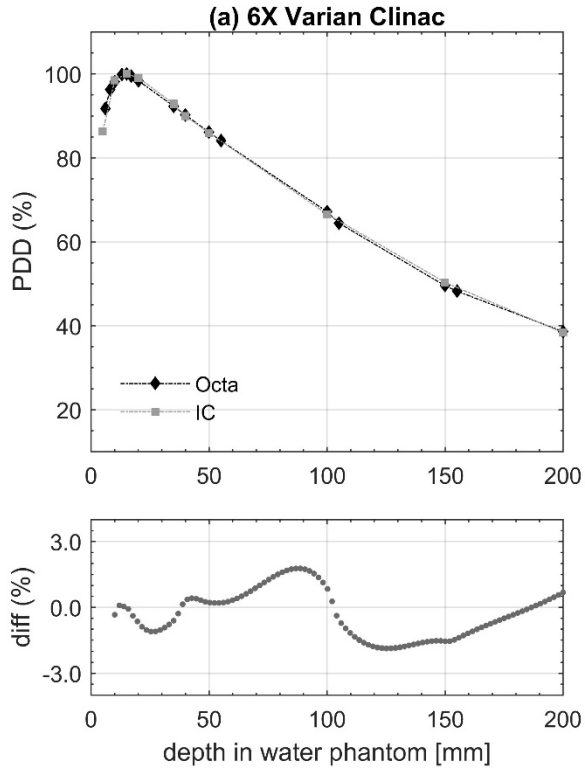

Figure 43. (a) PDD measured by the Octa and ionization chamber for a 6 MV FB, 10 cm side square field. Experimental values were analysed using a shape preserving interpolant function. Percentage differences are shown in the lower panel.

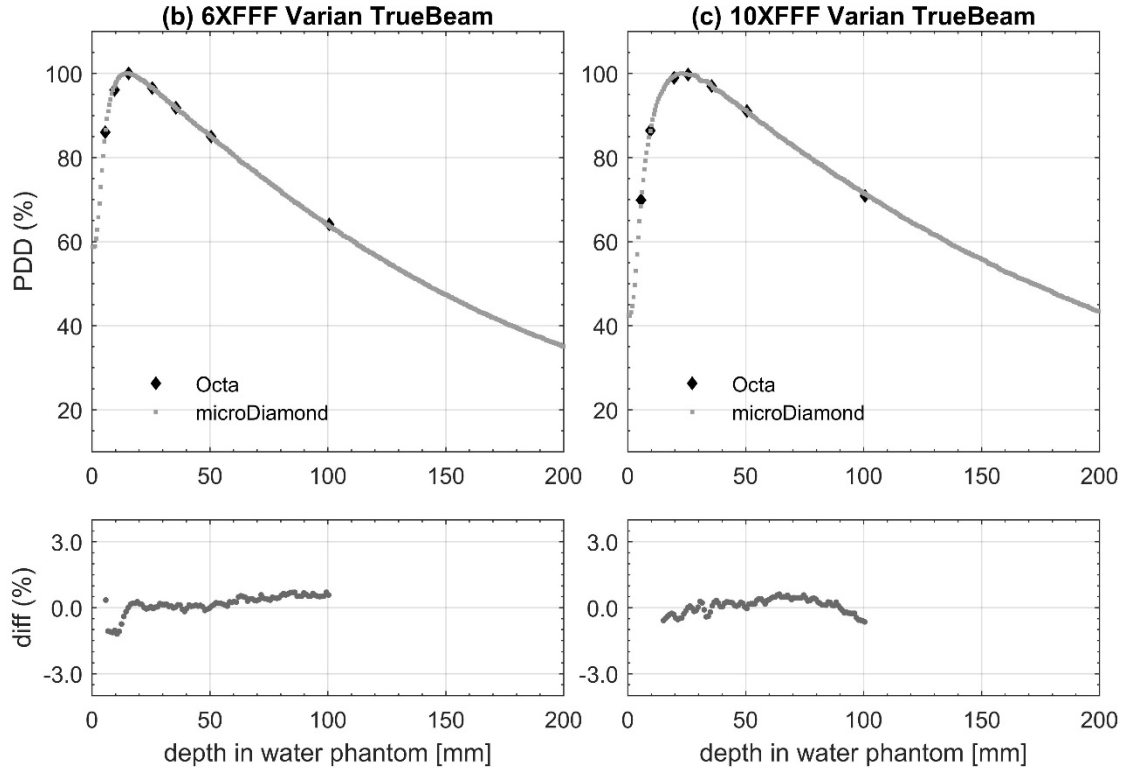

Figure 44. (a) PDD measured by the Octa and microDiamond for a 6 MV FFF beam, 10 cm side square field. (b) PDD measured by the Octa and microDiamond for a 10 MV FFF beam, 10 cm side square field. Experimental values were analysed using a shape preserving interpolant function. Percentage differences are shown in the lower panels.

6.4 Discussion

6.4.1 Output factors

The central pixels of the Octa (0.16 mm x 0.20 mm) were small enough to measure accurately the position of the central axis (CAX) peak without any volume-averaging effect. Once aligned to the CAX, OFs were measured by the Octa for both small and large radiation fields. Positioning uncertainties were therefore negligible, in stark contrast with point-like detectors for which this is a major source of error in OFs measurements.

Silicon diodes are known to over-respond to photons of low energy because of the increasing cross-section of the photoelectric effect in silicon compared to water [140] with the electron density of the extra-cameral components also playing a role.

This is exacerbated by the removal of the flattening filter from the linac, which results in most of the low-energy photons to pass through and a consequent lower average beam energy [22]. As previously reported, though, deviations in small fields correction factors for silicon diodes between flattened and FFF beams are sufficiently small (up to a maximum of $\pm$ 1.7%) to allow for their potential interchangeability on the same linac [150].

Consistently with this result, we used the same air gap to render the Octa a 'correction-free' dosimeter for OFs measurements for all beam qualities investigated. For all beam qualities investigated, OFs for the Octa were accurate within 3% with respect to values measured by reference dosimeters.

A Monte Carlo numerical correction factor would be useful for an evaluation of the extra-cameral effect for the Octa and for monolithic silicon array detectors in general but goes beyond the scope of this work.

6.4.2 Off-axis ratios

FWHM values measured by the Octa for in-plane, cross-plane and diagonal dose profiles were well within 3% with respect to the reference. Exception was the in-plane profile relative to the 5 mm side square field for the 10 MV FB, for which the percentage difference for the FWHM value was found to be 5.6%.

It should be emphasized that small differences between nominal and effective field sizes for small jaws-defined radiation fields, due to the jaws calibration and or their positioning inaccuracies, are known to have a strong impact on small field measurements [204], [205].

Ideally, dose profiles for both the dosimeter being evaluated and that used as reference would have to be measured at the same time.

6.4.3 Dose per pulse dependence

Dose per pulse measurements are often difficult as the spectral composition of a beam changes with attenuation and distance from the source (due to contamination). They are a known limitation of silicon-based dosimeters is their dependence on dose per pulse under linac irradiation.

As first reported by Rikner and Grusell [130], a decrease in sensitivity is expected with decreased dose per pulse. While at low dose per pulses the recombination centres near the band edges of the silicon are empty with part of the charge carriers generated by the ionizing radiation being lost to these traps, at high dose per pulses the fraction of these that recombine decreases and a larger portion of the signal is available to be collected [137].

The Octa was shown to have a DPP dependence in FFF beams comparable to that of other solid-state dosimeters that are considered stable, for the whole range of doses per pulse investigated.

A maximum DPP dependence of 24% at 0.021 mGy/pulse, relative to 0.278 mGy/pulse, was found and could be easily corrected for in the case of machine-specific QA applications.

At the higher dose per pulse of the 10 MV FFF beam quality, a difference in the relative response of the pixels in the central matrix of the detector was noted. Since the sensitivity of the diode is proportional to the diffusion length, which is a function of the dose rate, at high dose per pulses there may be an enhanced effect of charge sharing between neighbouring pixels. Further investigation is in order, but beyond the scope of this work.

6.4.4 Percentage depth dose

With increasing depth, silicon diodes are expected to overestimate the dose due to the increase of the relative number of low energy scattered photons for clinical photon beams, an effect which could be offset by an underestimation due to dose rate dependence [9], [42].

For the Octa, while a DPP dependence was found, discrepancies in PPDs with respect to the reference values were within 2% at all depths, for all beam qualities, in a worst-case scenario of a 10 cm side square field.

Due to a limited availability of solid water slabs at Peter MacCallum Cancer Centre, we were unable to measure PDDs beyond 10 cm depth. Based on the excellent comparison between the Octa and the ionization chamber PDDs for the 6 MV FB, though, we don't expect any relevant differences for the FFF.

6.5 Conclusions

The Octa was demonstrated to be an accurate dosimeter, with a performance comparable to that of commercially available detectors deemed suitable for small-field dosimetry, such as the EBT3 Gafchromic films and the PTW microDiamond. In contrast to those, though, the Octa allowed for the simultaneous real-time read-out of OF and OARs for cross-plane, in-plane and two diagonal directions, for any given field size.

The air gap used to render the Octa a 'correction-free' dosimeter for OFs measurements was found to be applicable to both flattened and FFF beams, in accordance to previous studies in the literature.

PDDs for all beam qualities investigated were accurate within 2%. Though a DPP dependence was found that could be corrected for, the high doses per pulse typical of FFF beams were not detrimental to the overall performance of the dosimeter.

Our conclusion was that the Octa, thanks to its a sub-millimetre pitch and 4 intersecting linear arrays, while still offering a stable and real-time readout provides a much more detailed 2D dose map characterization than that of its predecessor the MP512 and the Duo.

At the same time, the monolithic silicon array detector technology developed by the CMRP on which the Octa is based, was proved to have unique characteristics for relative dosimetry applications for a wide range of beam qualities and dose per pulses.

7 On the use of the Octa in stereotactic radiation fields

This chapter is based on material in **G. Biasi** *et al*, (2019) Today's monolithic silicon array detector for small field dosimetry: the Octa, *Journal of Physics: Conference series MMND&ITRO 2018* 1154 012002 [16][24], and presented at the 2018 MMND-ITRO Conference (Mooloolaba, Australia).

The dosimetry of small photon beams is challenging due to detector position uncertainties, dose averaging and lack of charged particle equilibrium (CPE). Currently only few, point-like detectors are suitable for measurements in this context, and none is ideal. This study reports on the dosimetry characterization of small fields collimated by fixed cones, performed with the Octa epitaxial prototype. All measurements discussed hereafter were performed during the first half of 2017.

7.1 Introduction

The challenges associated with the relative dosimetry of small photon beams, i.e. detector position uncertainties, dose averaging and lack of charged particle equilibrium, have been widely discussed in the recent literature [1], [2]. For a detector dedicated to small field dosimetry, characteristics such as a sensitive volume (SV) sufficiently small with respect to the radiation field and the ability to offer high spatial resolution measurements are considered paramount. Ideally, it would also be water equivalent and have a response which is linear with the absorbed dose, as well as be energy and dose rate independent. However, no ideal detector dedicated to small field dosimetry exists, and it is advised to use different dosimeters and cross-check the consistency of results [1], [2].

In particular, solid-state detectors are recommended by the IAEA-AAPM protocol dedicated to small field dosimetry [1], but only single 1D solid-state detectors used with various scanning techniques have been shown to offer the necessary sub-mm spatial resolution [2]. Furthermore, their readings need correction factors to account for beam perturbations that are detector design, linear accelerator (linac) treatment head design, beam quality, field size and measurement conditions dependent [51]. As a consequence, these are inconvenient to use in practice because of the multidimensional factor dependencies (field size, depth and distance) [59].

[24] References are combined in a single bibliography at the end of the present dissertation.

A ‘correction-free’ detector, i.e. one maintaining a correction factor close to unity, would be a preferable solution. This has been shown to be possible with the addition of low density media to the high density SVs components [209]. However, it would still be necessary to verify that these modifications are correctly compensating for a specific measurement condition [65].

Recently, the Centre for Medical Radiation Physics (CMRP) has developed the Octa, a 2nd generation silicon array detector dedicated to small field dosimetry which has been shown to be accurate for relative dosimetry with both flattened and flattening filter free photon beams [15] and to possess unique potentials for quality assurance for an Accuray CyberKnife system [17]. This study reports on its dosimetric characterization of small fields collimated by fixed cones attached to an Elekta Axesse™ linac.

7.2 Materials and methods

7.2.1 Experimental measurements

Experimental measurements described in this study were carried out at the Prince of Wales Hospital (Randwick, NSW, Australia), using 6 MV flattened photon beam from an Elekta Axesse™ linac with a retrofitted Agility head. Fixed conical collimators (Elekta) with nominal diameter, defined as the projection of their openings at the isocentre, between 5 mm and 50 mm were employed. Parameters commonly used by commercial treatment planning systems, such as dose profiles (DPs), percentage depth dose (PDD) and output factors (OFs) were measured with at least 2 different detectors. For the Octa, measurements were performed in solid water (Gammex RMI 457, Middleton, USA). Measurements by Gafchromic™ EBT3 films (ASHLAND) performed in solid water (Gammex RMI 457, Middleton, USA) and by a SFD diode (IBA Dosimetry) performed in water tank (Bluephantom, IBA) were added to the study to cross-check the consistency of results. EBT3 Gafchromic™ films were scanned 24 hours post irradiation with an EPSON 10000XL using a 48-bit RGB with a resolution of 72 dpi following a procedure detailed in [116]. A test to verify the gantry sag was performed by rotating the gantry at 0° and 180° and measuring the shift in the most responsive SV on the Octa.

Prior to all measurements, the Octa was aligned with respect to the machine central axis (CAX) by maximizing the response of its central pixel using the smallest available field size. OFs and DPs were measured at 90 cm source to surface distance (SSD), 10 cm depth. The accuracy of DPs was assessed by comparing FWHM and penumbra widths, defined as the distance between the 20% and 80% of the CAX dose. CAX PDD were measured with 10 cm

solid water for backscattering purposes and by adding the required amount of solid water slabs on top of the detector. For a quantitative estimation of the results, the detector readings were analysed using MATLAB (MathWorks) with a shape preserving interpolant function.

The gantry sag was assessed by measuring the coincidence/shift of the isocentres at different gantry angles. We defined the radiation isocentre as the centre of the radiation field collimated by the smallest cone available (5 mm diameter) and aligned the central sensitive volume of the Octa with that. OARs were then measured for gantry angles 0° and 180°.

7.3 Results

The central pixels of the Octa were small enough to identify the CAX position accurately without any volume-averaging effect. Figure 45 shows OFs measured by the Octa and EBT3 films for all fixed cones investigated, normalized to the biggest available field size of 50 mm diameter.

OARs measured by the Octa and EBT3 films are shown for circular fields of diameter 5 mm (Figure 46), 7.5 mm (Figure 47), 10 mm (Figure 48), 12.5 mm (Figure 49). In the proposed figures, profiles are normalized to the response at CAX and aligned such that the origin lies at the coordinate corresponding to the 50% CAX dose. Error bars[25] were within the symbol size.

CAX PDDs measured by the Octa and by the SFD diode are shown for circular fields of diameter 5 mm and 10 mm (Figure 50). Nominal depths were converted to water equivalent depths to account for the density of the Perspex plates of the Octa. Error bars were within the symbol size.

Figure 51 shows OARs measured by the Octa at different gantry angles (0°, 180°) for a 5 mm diameter circular field collimated by a fixed conical cone. In the figure, OARs are normalized to the CAX dose response at gantry angle 0°. The maximum response for OARs at gantry angle 180° is lower due to couch attenuation. Error bars were within the symbol size.

[25] Error bars were calculated as 2 standard deviations.

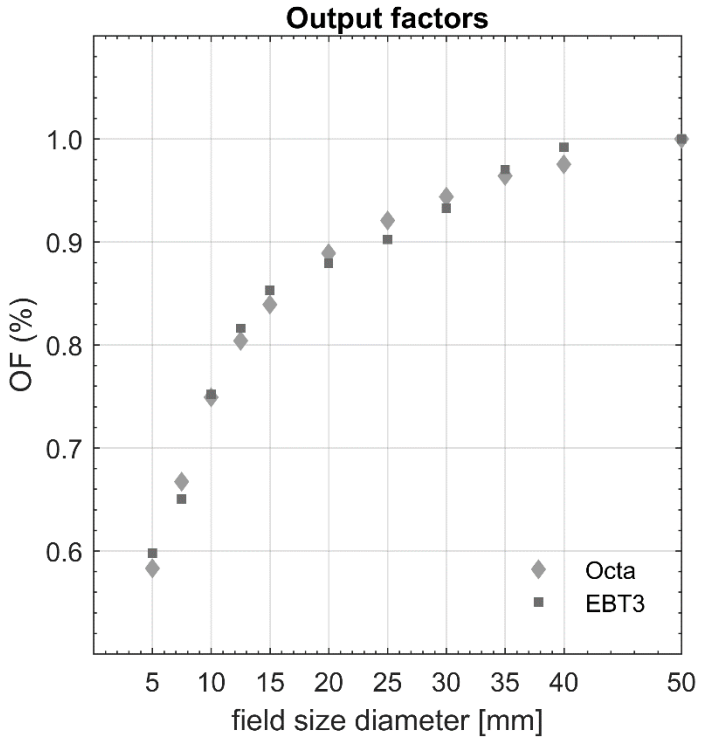

Figure 45. OFs measured by the Octa and EBT3 films for circular fields in the range between 5 mm to 50 mm diameter, collimated by fixed conical cones. OFs are shown normalized to the 50 mm diameter response.

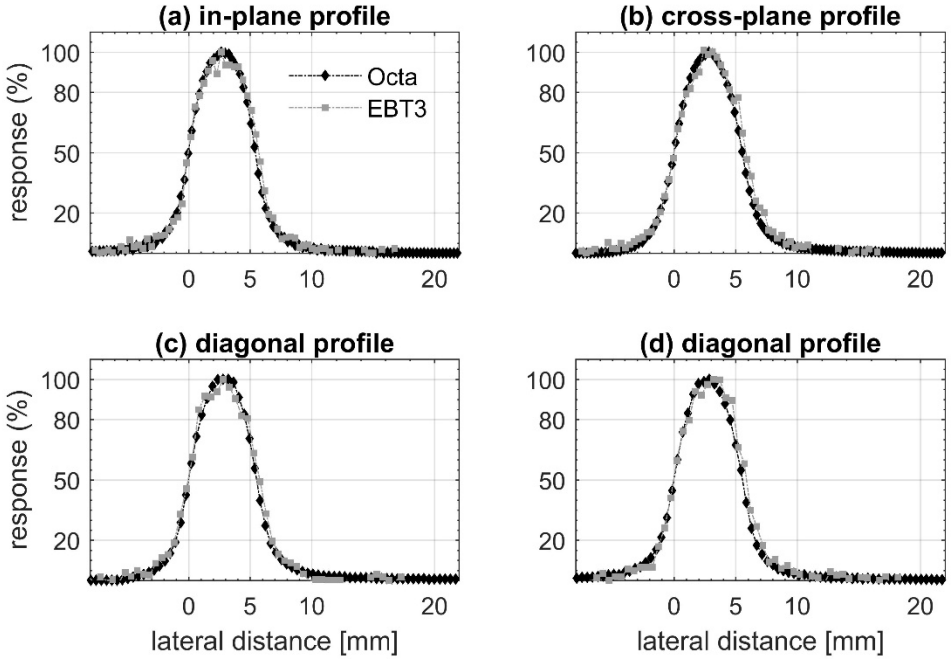

Figure 46. OARs measured by the Octa and EBT3 films for a 5 mm diameter circular field collimated by a fixed conical cone. Profiles are normalized to the CAX dose response and aligned to its 50% value.

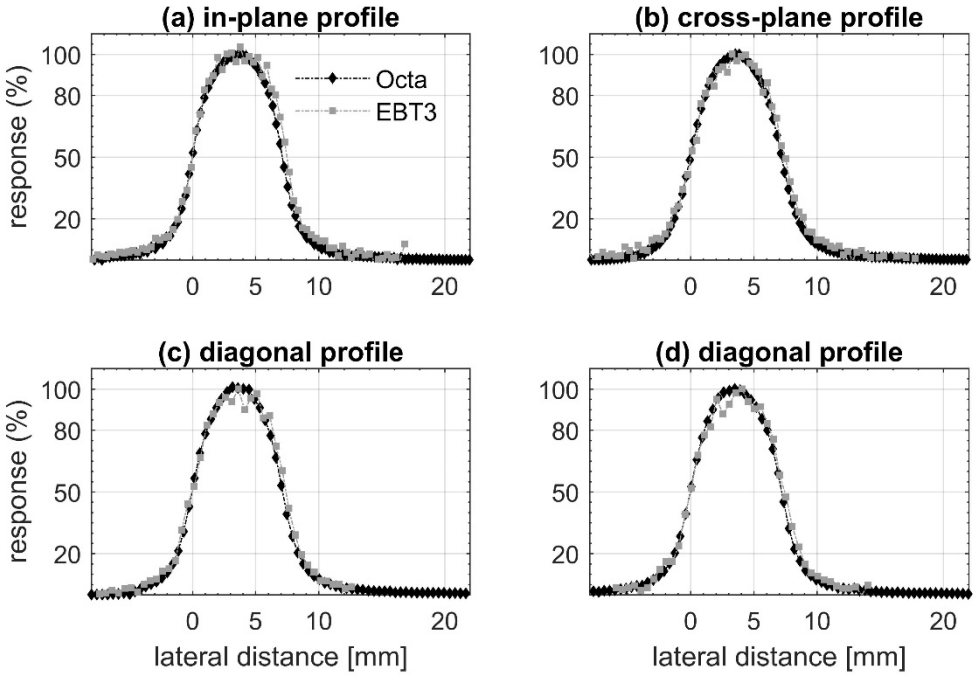

Figure 47. OARs measured by the Octa and EBT3 films for a 7.5 mm diameter circular field collimated by a fixed conical cone. Profiles are normalized to the CAX dose response and aligned to its 50% value.

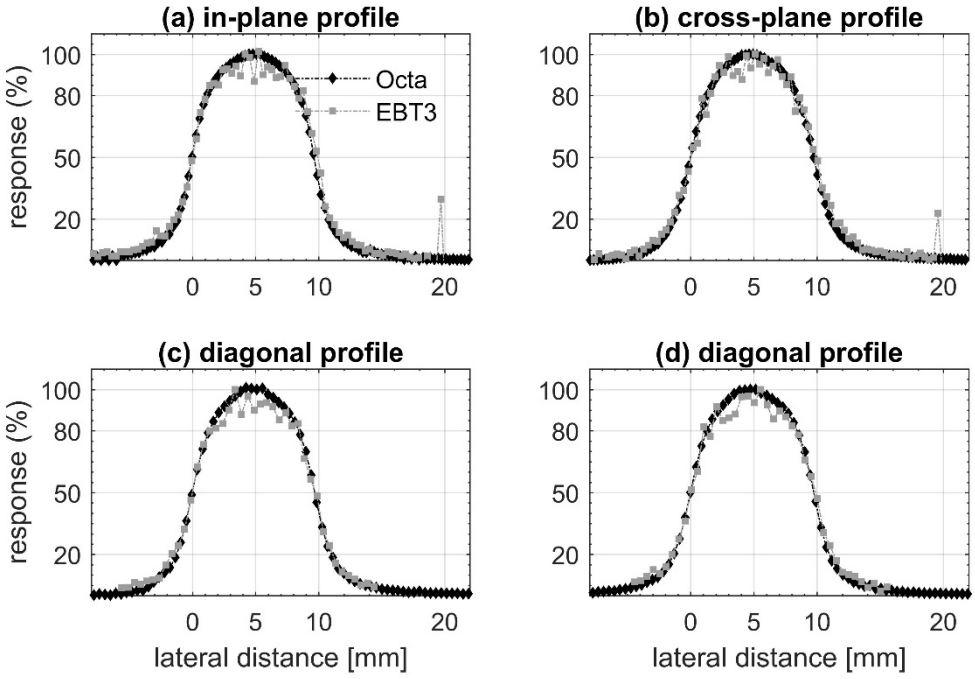

Figure 48. OARs measured by the Octa and EBT3 films for a 10 mm diameter circular field collimated by a fixed conical cone. Profiles are normalized to the CAX dose response and aligned to its 50% value.

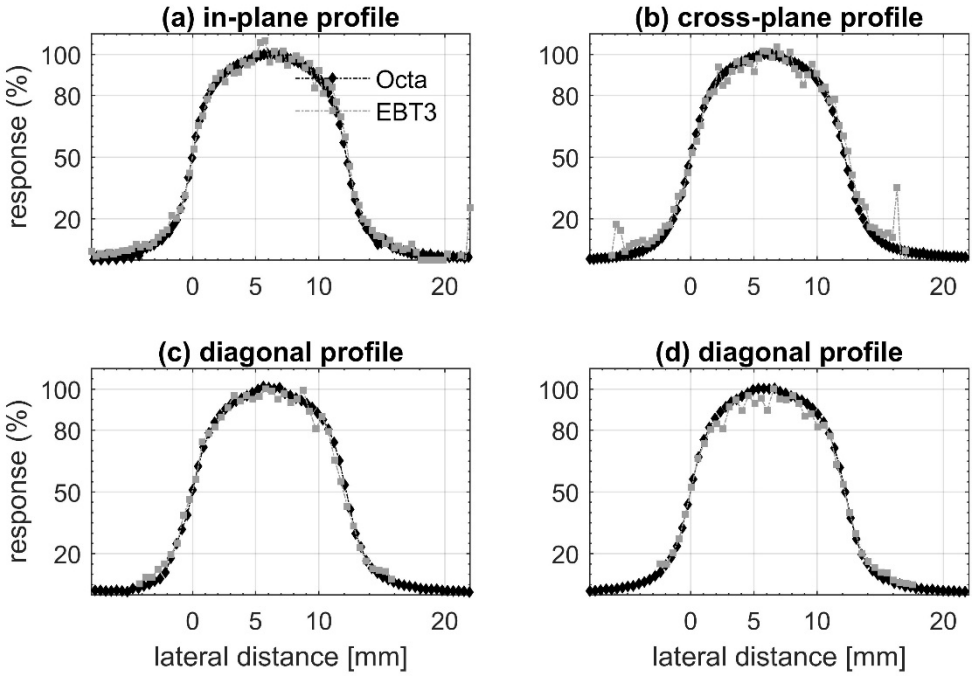

Figure 49. OARs measured by the Octa and EBT3 films for a 12.5 mm diameter circular field collimated by a fixed conical cone. Profiles are normalized to the CAX dose response and aligned to its 50% value.

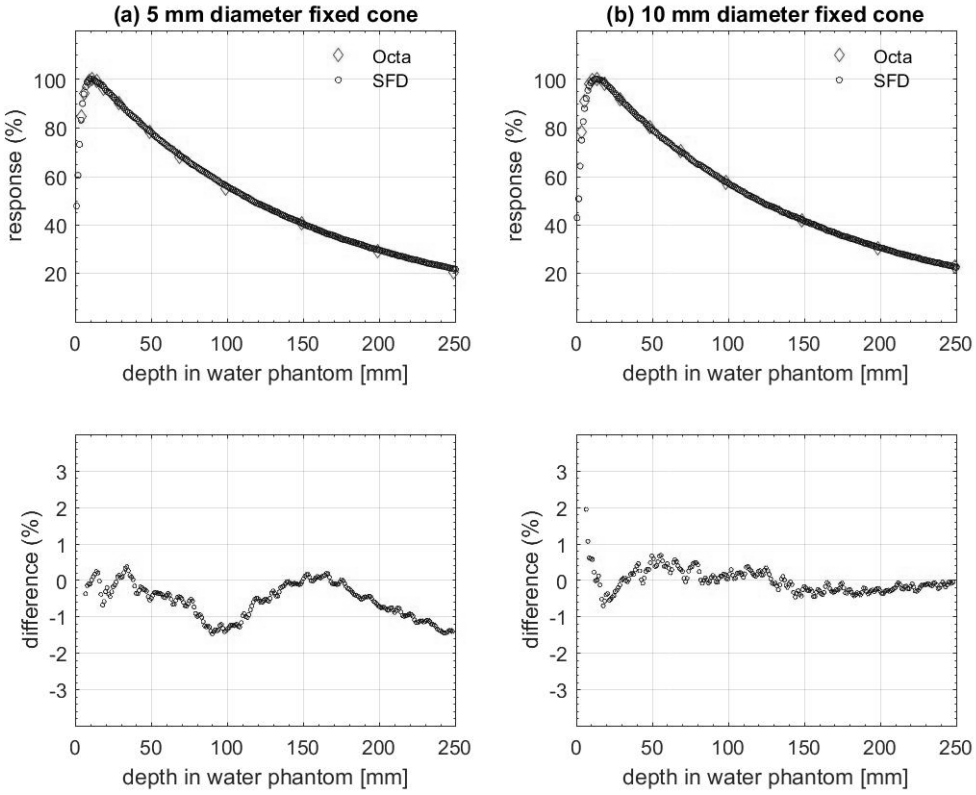

Figure 50. CAX PDDs measured by the Octa and an SFD diode for circular fields of diameter a (a) 5 mm and (b) 10 mm collimated by a fixed conical cone.

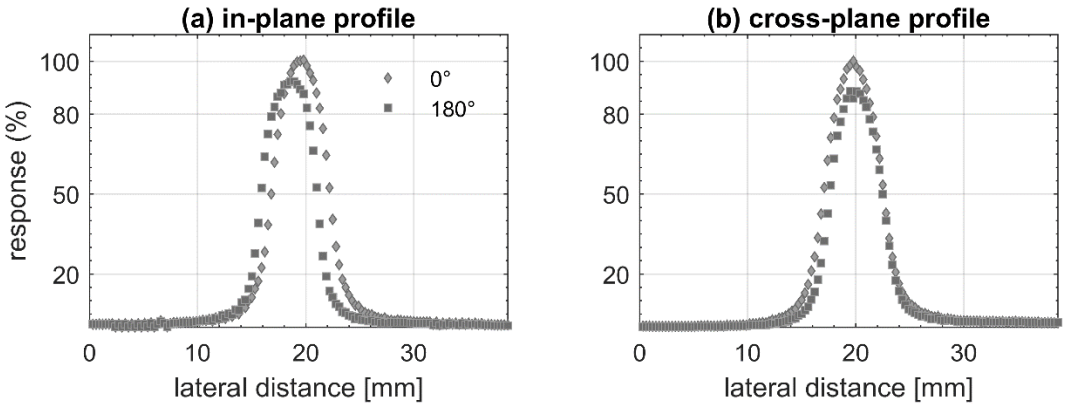

Figure 51. OARs measured by the Octa for a 5 mm diameter circular field collimated by a fixed conical cone, at different gantry angles (0°, 180°). Profiles are normalized to the CAX dose response at gantry angle 0°. Maximum response at gantry angle 180° is lower due to couch attenuation.

7.4 Discussion

7.4.1 Output factors

Dosimetry data typically measured for commissioning and verification of a TPS include OFs, PDDs and OARs. Uncertainties in the collected data seriously hinder a TPS ability to accurately predict the dose distributions [2], [24], [54]. Of all parameters, the measurement of OFs is arguably the most delicate. Since they directly impact the calculation of the number of monitor units necessary to deliver the prescribed clinical dose, it is recommended that OFs calculated by a TPS be carefully verified against measurements [2], [36], [210]. Regrettably, the measurement of an OF is highly sensitive to small changes in the size and shape of the radiation field. In a previous investigation, a difference in OF of about 10% for a 0.3 mm variation in a 5 mm cone aperture was reported [211]. In the case of fixed conical collimators, there may be variations to the nominal size being inadvertently introduced by the manufactured. For this reason, it is recommended that the TPS output be validated with beam data collected in-house and not rely on the literature.

In our study, the central sensitive volumes of the Octa (0.16 mm × 0.20 mm) were small enough to allow for an accurate alignment with the machine central axis (CAX) without any volume-averaging effect. Once aligned to the CAX, OFs were measured by the Octa for both small and large radiation fields. Alignment uncertainties were therefore negligible, in contrast with point-like detectors (such as the SFD diode), for which this is a major source of error in OFs measurements.

Silicon diodes are known to require corrections for OF measurements due to the non-water equivalence of their sensitive volumes and extra-cameral components [26], [212].

In our study, OFs measured by the Octa were accurate within 3% with respect to those measured by the water-equivalent EBT3 films, a result which supports the current 'correction-free' design of the detector for these measurement conditions [213].

7.4.2 Off-axis ratios

OARs by the Octa were overall in good agreement with measurements by the EBT3 in terms of FWHM, with discrepancies well within 3% for fields equal to or larger than 10 mm in diameter, and approximately 5% for the 5 mm and 7.5 mm field diameters. A maximum discrepancy of 6.9% or 0.4 mm was found for the in-line profile of the 5 mm cone.

Overall, penumbra widths measured by the Octa were generally in close agreement with those measured by EBT3 films, with discrepancies within 0.3 mm. The Octa measured a penumbra width of 1.8 mm for the in-plane profile and of 2.1 mm for the cross-plane profile. The elliptical shape of the electron source in Elekta linacs explains the expected small differences between in- and cross-plane penumbra width [211].

A similar dosimetry characterization of stereotactic-dedicated fixed conical collimators mounted on an Elekta Axesse™ was performed with a 2D monolithic silicon array detector called Duo [214]. The device had the same number of sensitive volumes of the Octa, only arranged along 2 orthogonal linear arrays (with a 0.2 mm pitch) instead of along 4 linear arrays (with a 0.3 mm and 0.43 mm pitch).

In that study, OARs were measured for all available cones in the range between 5 mm to 50 mm diameter. Results by the Duo were cross-checked against measurements by ETB3 films and an SFD diode. It was concluded that OARs by the Duo and by EBT3 films agreed in terms of FWHM and penumbra width (within 0.5 mm for FWHM and 0.7 mm for penumbra width). Therefore, the Duo was deemed suitable for fast small-field dosimetry.

However, since the device only produced OARs along 2 directions (cross-plane and in-plane), we propose the Octa would provide a more complete description of the dose distributions, while maintaining a sufficiently high spatial resolution for small-field dosimetry and a fast and reliable read-out.

7.4.3 Percentage depth dose

In clinical photon beams, silicon diodes are expected to show an increasing over-estimation of the dose with increasing depth owing to the growing relative number of low energy scattered photons. However, this effect could be offset by an under-estimation of the dose owing to an instantaneous dose rate dependence [9], [42], [130], [141].

For the Octa, a DPP dependence was found in previous investigations. In this study, the discrepancies in PPDs measured by the Octa with respect to measurements by the SFD diode were within 3% at all depths, for all field sizes investigated. No correction was made to account for the instantaneous dose rate dependence of the former.

7.4.4 Gantry sag test

Gantry-based linacs have three axes of rotation, one for each of the following components: the collimator, the gantry and the couch. These degree of freedom are all used in the treatment planning process to optimize the dose delivery [215]. At all times, the correct alignment between beam axis and mechanical axes impact the accuracy of the treatment delivery [216].

For linacs dedicated to stereotactic treatments, quality assurance guidelines recommend that the coincidence of radiation and mechanical isocentre be verified annually and be within a ± 1 mm tolerance from baseline [216]. However, assessing the correct alignment of the radiation beam axis and the mechanical axes of the linac is a time-consuming and complex quality assurance procedure, typically performed with EBT3 films [215].

In our study, we performed a test aimed at quantifying the gantry sag (a proxy for the alignment between beam axis and gantry axis). We found it to be within measurement accuracy (0.3 mm) in the cross-plane direction, and within 1.2 mm in the in-plane direction. The test was performed in real-time.

At the time of writing, we are not aware of any other such investigation with a 2D real-time device with a sub-mm spatial resolution.

7.5 Conclusions

Overall, the Octa was demonstrated to be an accurate ‘correction-free’ detector for small-field dosimetry with potential for the dosimetry characterization of stereotactic-dedicated collimators such as fixed cones mounted on an Elekta Axesse™ linac.

In the case of OARs, its performance was comparable with that of EBT3 films in terms of spatial accuracy, but with a real-time read-out.

PDD measurements were cross-checked against those performed by a commercially available SFD diode and deemed accurate.

It was therefore proposed that, in the case of a machine-specific quality assurance application, the Octa would reduce the measurement time needed to comply with current protocols. It would also have unique dosimetry potentials for a real-time verification of the alignment of the radiation beam and mechanical axes of a linac.

8 The CyberKnife® system and the Octa

This chapter is based on material in **G. Biasi** *et al*, (2018) CyberKnife® fixed cone and Iris™ defined small radiation fields: assessment with a high-resolution solid-state detector array, *Journal of Applied Clinical Medical Physics*, 19 (5), 547-557 [17][26], presented at the 2017 GEANT4 User Workshop (Wollongong, Australia), at the 2018 ESTRO conference [217] (Barcelona, Spain) and at the 2018 EPSM conference (Adelaide, Australia). All measurements and numerical simulations discussed hereafter were performed during the second half of 2017.

8.1 Introduction

The CyberKnife® system (Figure 52) can deliver stereotactic radiotherapy (SRT) treatments with high doses in a few fractions using small radiation fields, with sub-millimetre positional accuracy [24], [218]. The linear accelerator (linac), mounted on a robotic arm, is operated without a flattening filter and the treatment beam is shaped using fixed circular cones (Figure 53), the InCise™ multi-leaf collimator or the variable aperture Iris™ collimator (Figure 54, Figure 55) [218], [219]. The latter, allowing for the radiation field size to be varied during treatment delivery, has the potential to decrease the peripheral dose compared to fixed collimators [220] and to reduce treatment time [219]. A CyberKnife system, the first of its kind in Australia, was recently installed at the Sir Charles Gairdner Hospital (SCGH), Perth WA, with promising early clinical results [221].

Figure 52. The CyberKnife® system: radiation beams are collimated to form circular fields and delivered with sub-mm positional accuracy. An x-rays imaging system checks target positioning and correct displacement in real-time. This figure was not included in [17].

[26] References are combined in a single bibliography at the end of the present dissertation.

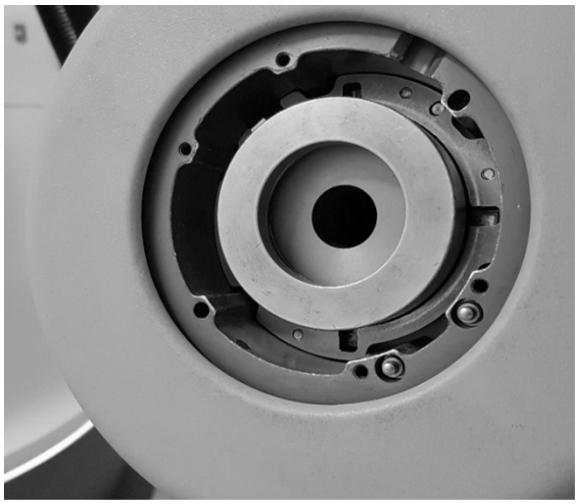

Figure 53. Snapshot of the CyberKnife® linac head with a fixed cone collimator at 40 mm diameter. This figure was not included in [17].

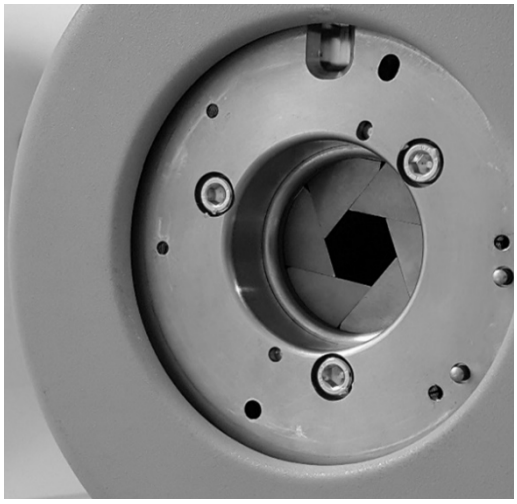

Figure 54. Snapshot of the CyberKnife® linac head with the Iris collimator at 40 mm diameter.

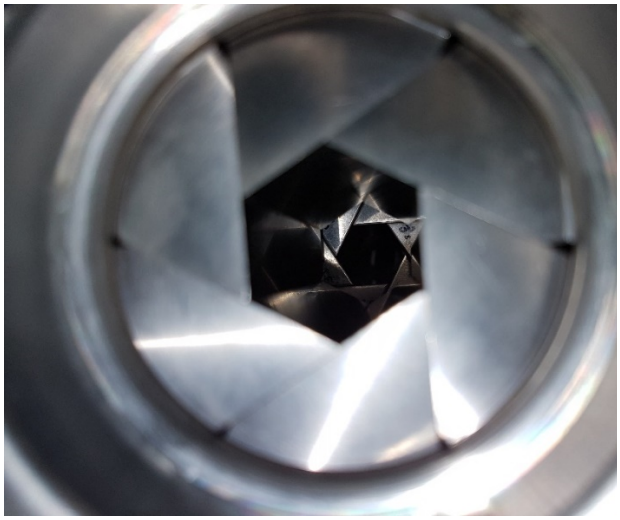

Figure 55. Snapshot of the variable aperture Iris™ collimator. By allowing for the radiation field size to be varied during treatment delivery, thus realizing an optimal treatment path, it has the potential to reduce treatment time. This figure was not included in [17].

Small-field dosimetry, known to be challenging due to volume averaging effects and a lack of charged particle equilibrium (CPE), has been extensively discussed in the literature [1], [2]. The problems associated with small-field dosimetry for flattened beams are likely to be compounded in flattening filter free (FFF) beams, given their inherently higher dose gradients, not just the penumbral region but also in the central beam, and higher doses per pulse [22], [23].

In the context of small-field SRT, the accuracy of treatment planning systems (TPSs) in predicting dose distributions can be significantly limited by uncertainties in underlying dosimetry data [24]. In particular, incorrectly measured output factors (OFs) can result in

systematic uncertainties leading to incorrect TPS-derived output [36]. This would be a major concern when a variable aperture collimator such as the Iris™ is used, for which its mechanical reproducibility would have to be verified.

Dedicated dosimeters are an essential part of a small-field-specific quality assurance (QA) protocol, which has been shown to be clinically justified [53]. These would ideally have a small water-equivalent sensitive volume (SV), allowing for high positioning accuracy, and show negligible energy, dose rate and directional dependence [55]. While commercially available detectors do not satisfy all of the above criteria, it has been common practice to perform measurements with at least two types of dosimeters to crosscheck the consistency of results [6], as recently recommended by an ICRU report [2].

For a CyberKnife® system, the dosimeter of choice for beam characterization has long been the Gafchromic film, thanks to its small energy dependence and high spatial resolution [86], [222]. Films, though, require a post-irradiation analysis process with long waiting times. Film-derived readings may be affected by large uncertainties due to batch-to-batch sensitivity variations, film polarization, non-uniformity, scanning and handling techniques [6].

Solid-state detectors have stable response, a ratio of signal in dosimeter to dose in water that is nearly energy independent in the megavoltage photon range (while calibrated at a depth in water, the same calibration can be used for other depths), high sensitivity and small SVs. Solid-state detectors thus have the potential to offer comparable performance to Gafchromic film, though with a real-time read-out. Their use is recommended by a recent IAEA-AAPM dosimetry protocol [1], but only single detectors used with various scanning techniques have been shown to offer sub-millimetre spatial resolution [2]. When used for small-field dosimetry, correction factors need to be applied to account for beam perturbations, due to their SVs and extra-cameral components. These factors depend on detector design, treatment head design, beam quality, field size and measurement conditions [2]. Monte Carlo (MC) codes are commonly used for modelling linac beam lines, and have been shown to be an effective tool in characterizing detector response in small radiation fields and their required correction factors [59]. Nevertheless, these remain inconvenient to use in practice, especially for percentage depth dose (PDD), tissue maximum ratio (TMR) and dose profile (DP) measurements because of the multidimensional factor dependencies (field size, depth and distance) [59]. Most importantly, corrections factors from MC simulations require knowledge of the detector construction and deficiencies in information provided by vendors, or manufacturing variability,

will lead to inaccurate results [63]. A preferable solution would be to design a 'correction-free' detector, or one maintaining a correction factor close to unity. This has been shown to be possible with the addition of low density media to the high density detector components [64]. However, it would still be necessary to verify that these modifications are appropriate under all beam quality and measurement conditions [65].

The Octa is a 2nd generation monolithic silicon-diode array detector designed by the Centre for Medical Radiation Physics (CMRP), University of Wollongong. Its 512 diodes are arranged in four intersecting orthogonal linear arrays such that OF, cross-plane, in-plane and 2 diagonal DPs are characterized simultaneously with a sub-millimetre resolution, for any given field size. The Octa was previously characterized as an accurate detector for relative dosimetry under irradiation with both flattened and FFF beams, for small radiation fields as defined with photon jaws [15]. In the present study, the potential of the Octa for beam characterization in the particular case of small radiation fields for SRT treatments with the CyberKnife® system was evaluated.

8.2 Materials and methods

8.2.1 The Octa detector

The Octa is a 2D monolithic silicon array detector based on SVs fabricated on a high resistivity p-type epitaxial layer [188], grown on top of a low resistivity p+ substrate. A thin protective layer of epoxy covers the SVs. The 512 diodes each have a sensitive area of 0.032 mm^2. The device has a sub-millimetre resolution with diodes having a 0.3 mm pitch along the vertical and horizontal arrays and 0.43 mm pitch along the 2 diagonal arrays. The diodes are operated in passive mode and are connected to a multichannel readout electronics data acquisition (DAQ) system based on a commercially available analogue front end (AFE0064, Texas Instruments), which was previously described in detail [177], [190]. An equalization procedure [207] is used to correct for small differences in each channel response. The Octa is sandwiched between two Perspex plates, each 5 mm thick, with a small air gap on top of its SVs to minimize the number and size of corrections that are required to relate its readings to dose [179].

8.2.2 Experimental measurements

Experimental measurements described in this study were carried out at the Sir Charles Gairdner Hospital (SCGH), Perth, WA, Australia, with an Accuray CyberKnife M6 linac. IBA solid water slabs type RW3 were used to reach the required measurement depths (Figure 56).

Measurements by the Octa were compared with those made using a PTW SRS diode 60018 mounted parallel to beam axis in an IBA 3D water-phantom. The diode was oriented vertically, measuring at the effective point of measurement of 1.3 mm from top surface. Its readings were corrected using the correction factors by Francescon et al. [147].

Figure 56. Experimental setup at the SCGH. The Octa detector was set on the treatment couch on top of 10 cm solid water for backscattering purposes. Solid water slabs were then added on top of the detector to reach the water equivalent depth required for each measurement. This figure was not included in [17].

8.2.3 Output factors and off-axis ratios

In this study, output factors were defined as the ratio between the detector reading at a specific field size ($clin$) and that at the machine specific reference field (msr), following the formalism used by Francescon et al. [147]:

$$OF_{det} = \frac{M^{f_{clin}}}{M^{f_{msr}}} \tag{8.1}$$

where $M^{f_{clin}}$ and $M^{f_{msr}}$ are the corrected detector readings in the f_{clin} and f_{msr} fields respectively. For the CyberKnife® system, the reference field was taken as that given by the 60 mm diameter collimator.

The OFs and OARs were measured by the Octa at 15 mm depth in solid water, 800 mm source to detector distance (SDD). Prior to the measurements, the Octa was aligned with respect to the treatment machine central axis (CAX) by maximizing the response of its central pixel using the smallest available field size (5 mm diameter). Once aligned, for any given field size, OF and OARs (in-plane, cross-plane and 2 diagonals) were measured simultaneously.

For OF measurements, the detector reading at each field size was taken as the average response of its central pixel over 3 repetitions of the same measure. This was followed by normalization of these averages to the average reading at the reference field size.

For OAR measurements, the Octa reading at each field size was taken as the reading of each channel averaged over 3 repetitions of the same measure followed by normalisation of the response of each channel to the median response of the pixels within 0.5 mm of the CAX. For a quantitative estimation of the FWHM and penumbra width, all profiles were analysed with MATLAB (Mathworks®) using a shape preserving interpolant function. Penumbra width was taken as the distance between the 80% and the 20% isodose levels.

Following the approach recommended by the vendor [219], and as requested by the CyberKnife® system TPS, for any given field size OARs were measured at different angles with respect to the in-plane direction. For the fixed cones, the representative equivalent circular profile was then taken as the average of the profiles measured at 0° and 90°, while for the Iris™ it was taken as the average of the profiles measured at 0°, 15°, 90° and 105°, to sample the underlying collimator asymmetry. For both OFs and OARs measurements, circular field sizes investigated were 5, 7.5, 10, 15, 20, 25, 30, 60 mm diameter for the fixed cones and 5, 7.5, 10, 12.5, 15, 20, 25, 30, 60 mm diameter for the Iris™. Field sizes were defined at 800 mm from the linac target.

8.2.4 Percentage depth dose and tissue maximum ratio

CAX PDDs were measured by the Octa at 800 mm source to surface distance (SSD) with 10 cm solid water for backscattering purposes, reaching the desired water by adding the required amount of solid water slabs on top of the detector. A 60 mm diameter circular field size was investigated for a fixed cone and the Iris™. SSD was maintained by moving the linac head.

CAX TMRs were measured by the Octa at 800 mm SDD with 10 cm solid water for backscattering purposes, reaching the desired water by adding the required amount of solid water slabs on top of the detector. 5 and 60 mm diameter circular fields were investigated for fixed cones and the Iris™. SDD was maintained by moving the linac head.

Nominal solid water depths were converted to water equivalent depths including accounting for the density of Perspex plates. For a quantitative estimation of the percentage differences, measured values were analysed with MATLAB using a shape preserving interpolant function.

8.2.5 Monte Carlo calculations

Calculations with Geant4 (GEometry ANd Tracking 4) [196], a general purpose MC tool-kit for the simulation of the passage of particles through matter which has been validated for medical applications by different groups [197], [198], were added to the study to support the experimental characterization of the detector response.

The International Atomic Energy Agency (IAEA) phase space (PHSP) files containing the detailed description (position, direction, kinetic energy, statistical weight, type) of the particles scored at the exit of the Iris™ collimator, for a CyberKnife® linac, were downloaded from the online repository (http://www-nds.iaea.org/phsp/phsp.htmlx).

The PHSP files, previously validated by Francescon et al. [56], were read by a Geant4 application purposely developed in-house for this study using a C++ class adapted from a previous work by Cortés-Giraldo [223].

The PHSP files were in this way used as the primary generator in the Geant4 application in order to simulate the irradiation of a solid water phantom.

The solid water was modelled as the IBA type RW3, to match that used for the experimental measurements with the Octa. The GEANT4 *Standard EM physics list option 4* was used in this study, with production cuts set to 0.1 mm for electrons and photons in the phantom.

8.3 Results

8.3.1 Output factors

The OFs for the Octa, SRS diode and MC calculations are shown in Figure 57, along with percentage differences in the lower panels. MC calculated OFs were taken as the dose deposited in a voxel of solid water whose dimensions were those of the central SV of the Octa detector. When measuring OFs, the central pixels of the Octa were small enough to identify the CAX position accurately without any volume-averaging effect. Error bars, calculated as 3 standard deviations, did not exceed the symbol size for both experimental measurements and MC calculated results.

8.3.2 Off-axis ratios

Representative equivalent circular profiles for the Octa and SRS diode are shown in Figure 58 for fixed cones and in Figure 59 for Iris™ collimated radiation fields. In Figure 60, equivalent profiles measured by the Octa for fixed cones are compared to those measured for the Iris™, for the same nominal field size. In Figure 61 in-plane non-averaged profiles measured by the Octa are compared before and after a reset of the Iris™, defined as setting the aperture of the collimator to the desired size, followed by its complete closure and then a re-set of the aperture to the desired size.

Profiles are shown in the figures aligned such that the origin lies at the coordinate corresponding to the 50% response. Error bars, calculated as 3 standard deviations, did not exceed the symbol size. FWHM and penumbra values are shown in Table 16 for fixed cones and in Table 17 for the Iris™.

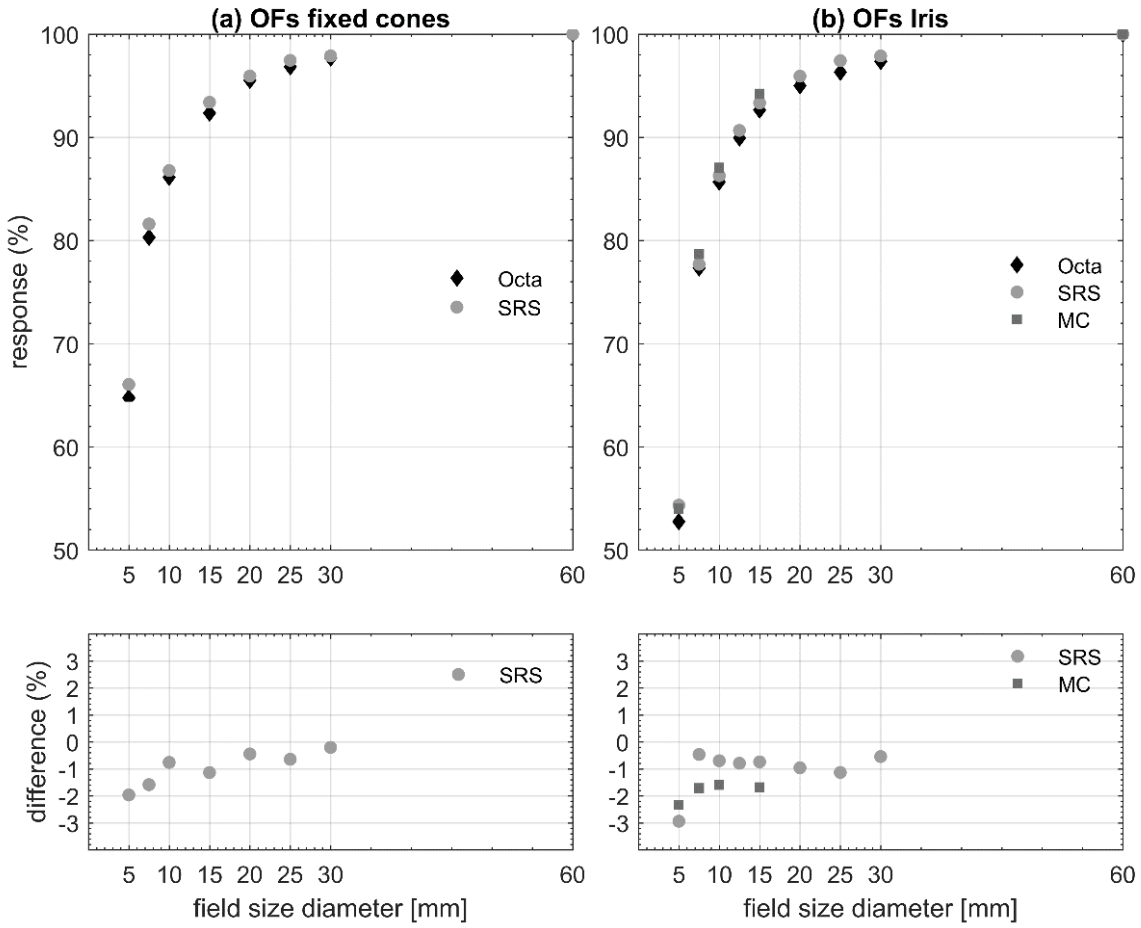

Figure 57. (a) OFs measured by the Octa and SRS diode, with percentage differences with respect the SRS diode, for fixed cones. (b) OFs measured by the Octa and SRS diode, and MC calculated OFs in solid water, for the Iris™. Percentage differences are for the Octa with respect to the SRS diode and for the Octa with respect to MC OFs, respectively.

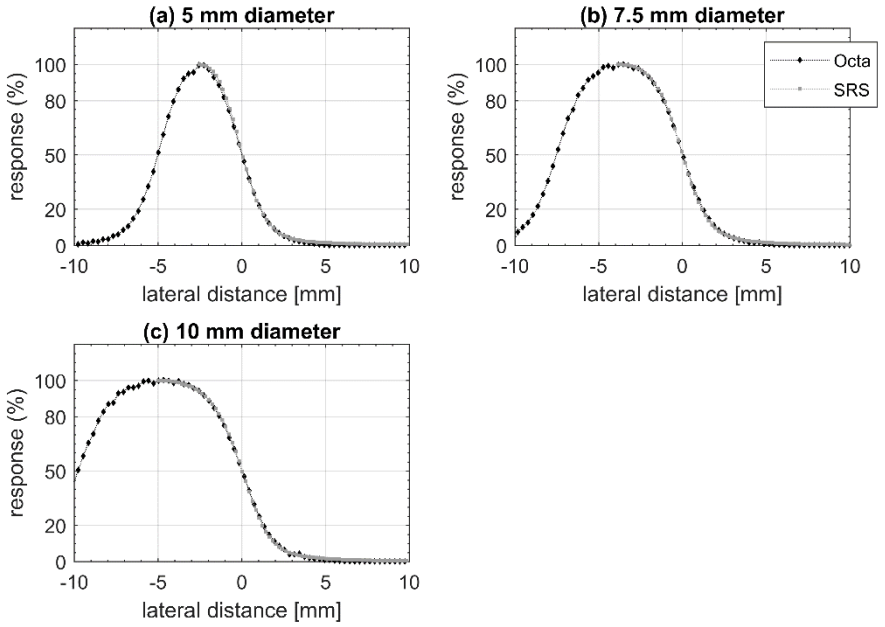

Figure 58. In-plane and cross-plane averaged OARs measured by the Octa and SRS diode for (a) 5 mm, (b) 7.5 mm and (c) 10 mm diameter circular field sizes collimated with fixed cones. Profiles are aligned to the 50% response.

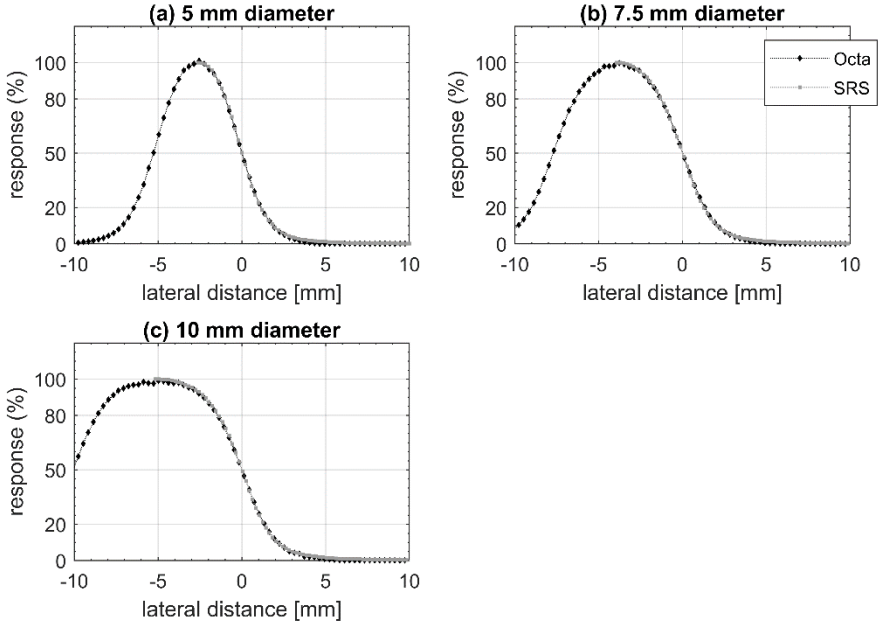

Figure 59. In-plane, cross-plane, 15° and 105° degrees averaged OARs measured by the Octa and SRS diode for (a) 5 mm, (b) 7.5 mm and (c) 10 mm diameter circular field sizes collimated with the Iris™. Profiles are aligned to the 50% response.

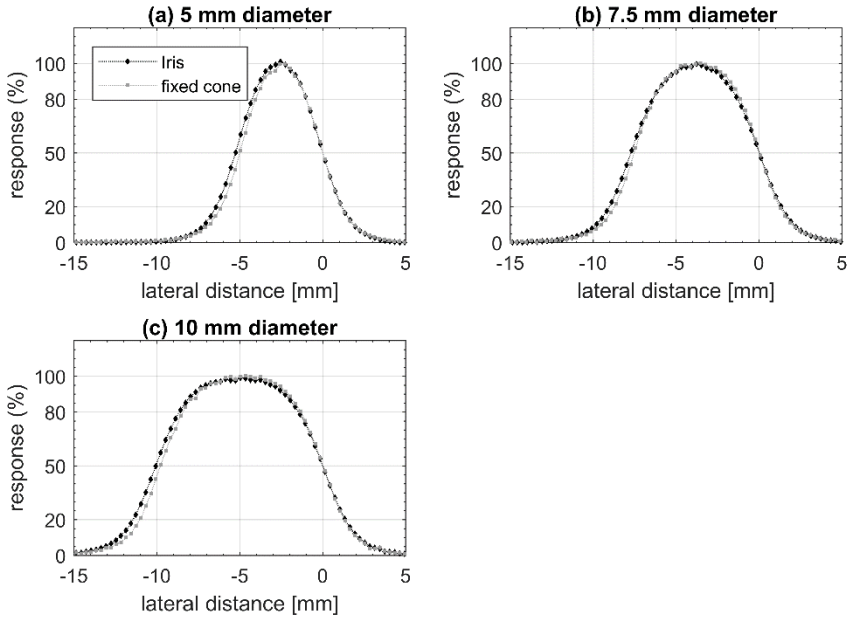

Figure 60. Representative equivalent OARs measured by the Octa for (a) 5 mm, (b) 7.5 mm and (c) 10 mm diameter circular field sizes collimated with fixed cones and the Iris™. Profiles are aligned to the 50% response.

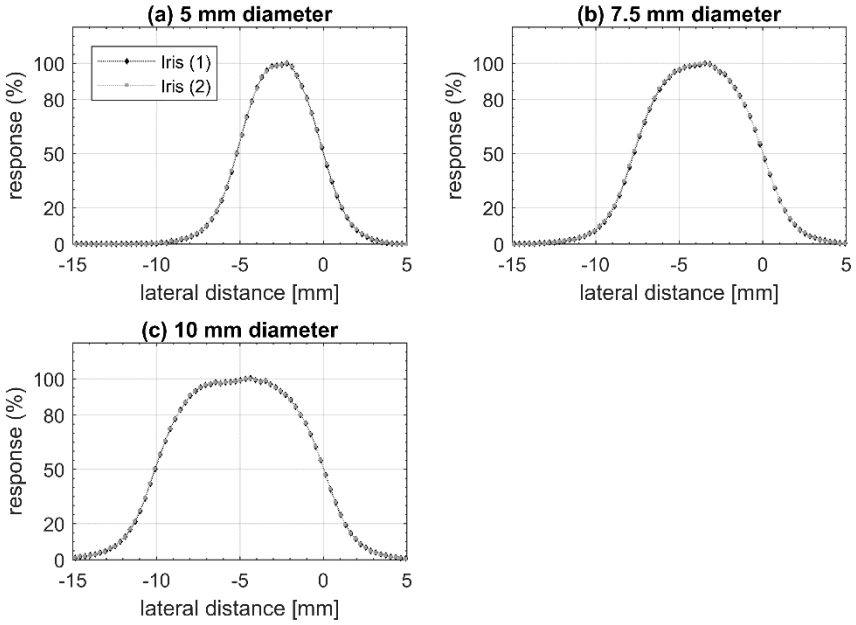

Figure 61. In-plane OARs measured by the Octa before (1) and after (2) a reset of the Iris™ collimator, for (a) 5 mm, (b) 7.5 mm and (c) 10 mm diameter circular field sizes. Profiles are aligned to the 50% response. In the OAR relative to the 10 mm diameter, a small asymmetry attributed to the non –perfect uniformity of the detector response could be appreciated.

Table 16. Summary of FWHM and penumbra values measured by the Octa and the SRS diode for radiation fields defined by fixed cones. Values refer to representative equivalent profiles measured at 15 mm depth, 800 mm SDD.

Field size	Octa		SRS diode		Difference	
diameter	FWHM	Penumbra	FWHM	Penumbra	ΔFWHM	ΔPenumbra
[mm]	[mm]	[mm]	[mm]	[mm]	[%]	[mm]
5	5.0	2.1	5.0	2.0	0.0	0.1
7.5	7.5	2.4	7.7	2.2	-2.6	0.2
10	9.8	2.6	9.9	2.5	-1.0	0.1

Table 17. Summary of FWHM and penumbra values measured by the Octa and the SRS diode for radiation fields defined by the Iris™. Values refer to representative equivalent profiles measured at 15 mm depth, 800 mm SDD.

Field size	Octa		SRS diode		Difference	
diameter	FWHM	Penumbra	FWHM	Penumbra	ΔFWHM	ΔPenumbra
[mm]	[mm]	[mm]	[mm]	[mm]	[%]	[mm]
5	5.2	2.1	5.2	2.1	0.0	0.0
7.5	7.7	2.7	7.8	2.5	-1.3	0.2
10	10.0	2.8	10.3	2.7	-2.9	0.1

8.3.3 Percentage depth dose and tissue maximum ratio

Figure 62 shows the depth doses measured by the Octa in solid water, the SRS diode in water tank and MC calculated in solid water for the 60 mm diameter Iris™. Figure 63 shows the TMRs measured by the Octa in solid water and SRS diode in water tank for the 5 mm and the 60 mm diameter fixed cones. Figure 64 shows analogous results for Iris™ collimated field sizes, with the addition of MC calculated dose depositions. For all results, percentage differences for the Octa with respect to the benchmarks are shown in the lower panels of the corresponding figure.

Error bars, calculated as 3 standard deviations, did not exceed the symbol size for both experimental measurements and MC calculated results.

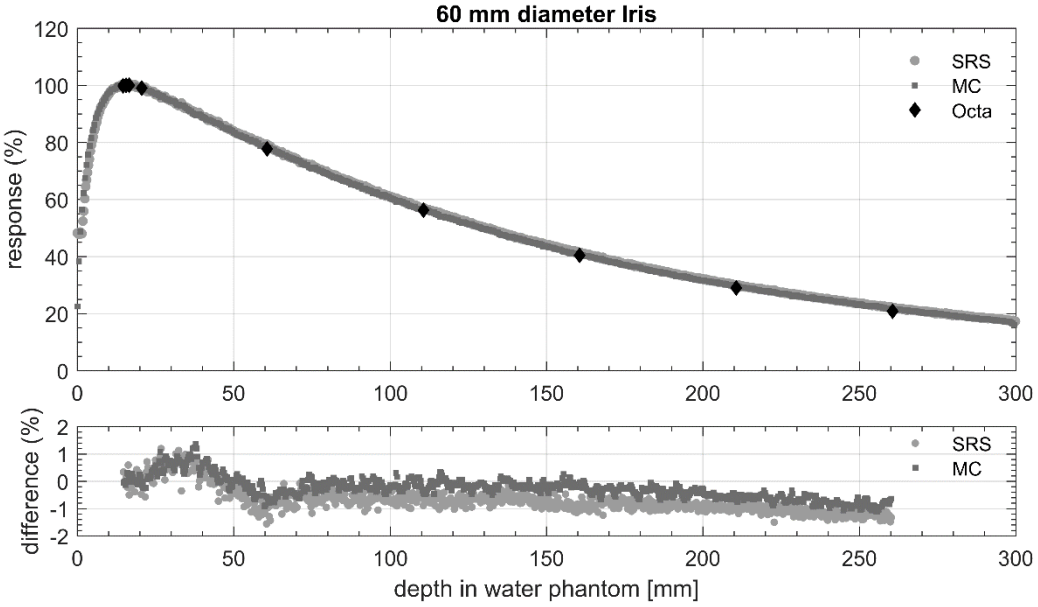

Figure 62. PDDs measured by the SRS diode in water and by the Octa in solid water, along with PDD simulated with MC in solid water (type RW3), for 60 mm diameter Iris™. Percentage differences are for the Octa with respect to SRS diode and MC, respectively.

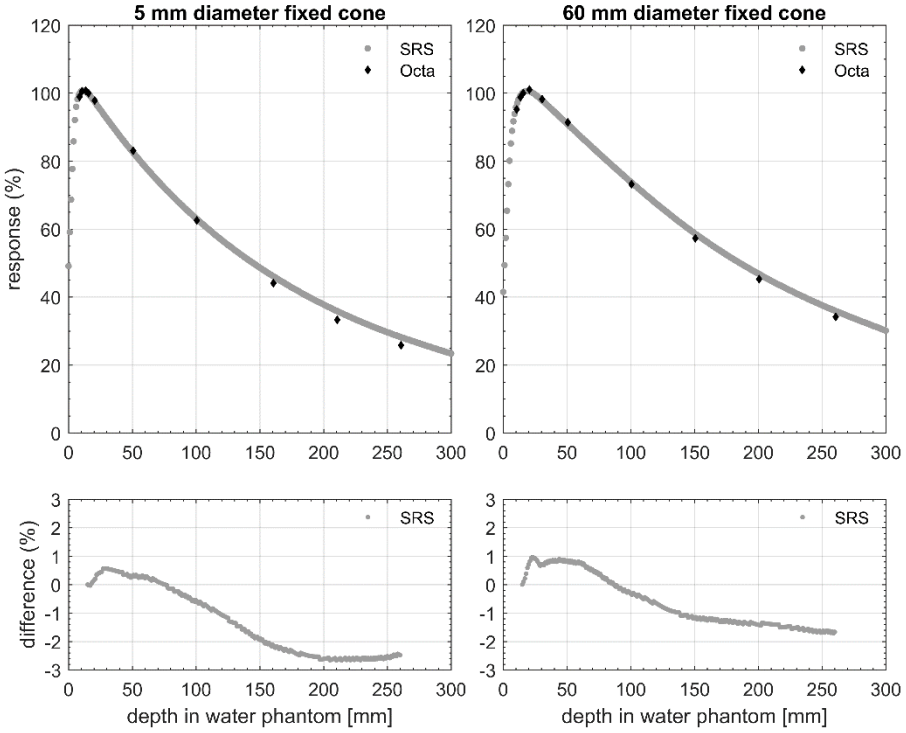

Figure 63. TMRs measured by the Octa in a solid water (type RW3) and SRS diode in water, for 5 and 60 mm diameter fixed cone. Percentage differences are for the Octa with respect to SRS diode.

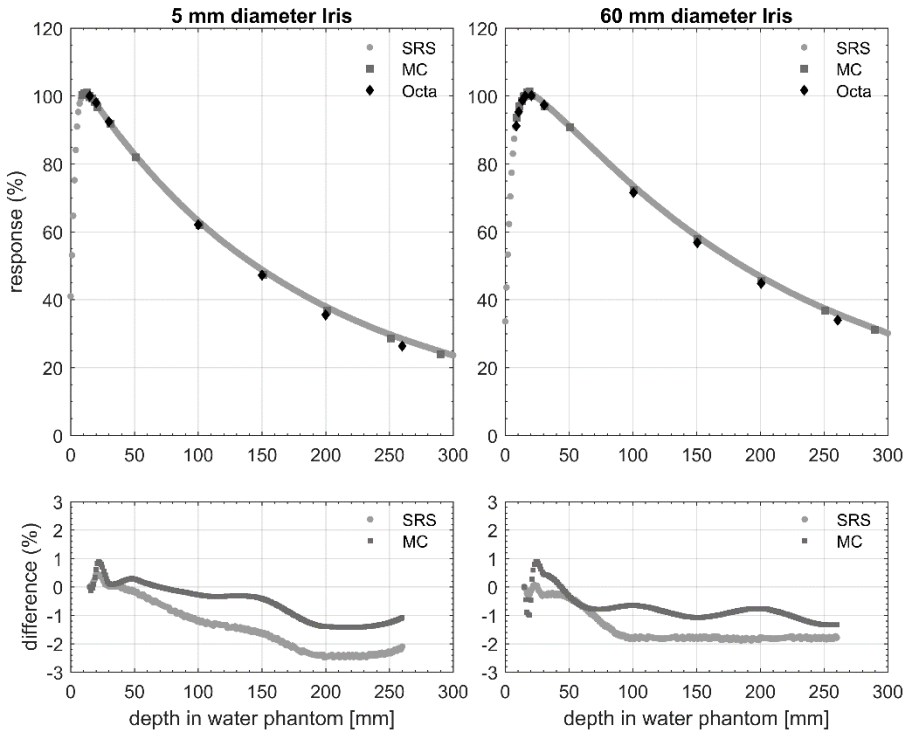

Figure 64. TMRs measured by SRS diode in water and by the Octa in solid water, along with MC simulated values in solid water, for 5 and 60 mm diameter Iris™. Percentage differences are for the Octa with respect to SRS diode and MC, respectively.

8.4 Discussion

8.4.1 Output factors

Silicon diodes are known to require corrections for output factor measurements due to the electron spectra being perturbed in silicon with respect to water, an effect that increases with decreasing field size. This perturbation has been attributed to the atomic number, mean excitation energy (*I-value*) and density of silicon SVs being different from that of water, with the non-silicon extra-cameral components of the detector playing a non-negligible role [51], [224]. FFF beams, which have a lower average beam energy than corresponding flattened beams [22], may require a different correction factor.

In this study, the Octa OFs were accurate within 3% with respect to the SRS diode for both fixed cones and the Iris™, with a maximum discrepancy of 2.9% found for the 5 mm diameter Iris™. Discrepancies for the Octa with respect to the expected MC simulated OFs in solid water were well within 2%, except for the 5 mm circular field size for which it was 2.3%.

This conclusion supports the current ‘correction-free’ design of the detector for the 6XFFF beam quality with a CyberKnife® linac. Thanks to the negligible beam quality variations among the different CyberKnife® linacs, even of different generations [225], we expect this

result to extend to all CyberKnife® systems currently in operation. Nevertheless, the results show a small but systematic under-response by the Octa, suggesting that a small adjustment of the air cavity may reduce the discrepancy further.

OFs for the two smallest apertures, 5 mm and 7.5 mm diameter, were lower for the Iris™ than for the fixed cones. This result has already been reported in the literature and was attributed to the increased length of the Iris™ leading to a difference in the head scatter component [226]. After a reset of the Iris™, OFs were accurate within measurement error, an indication of the robust mechanical properties of the collimator. Ideally, this would have to be a long-term test.

8.4.2 Off-axis ratios

Small irregularities in the profiles measured by the Octa are due the applied equalization procedure not being able to completely correct for the non-uniform sensitivity of the 512 diodes.

Overall, FWHM values for the Octa for in-plane, cross-plane and diagonal OARs were well within 3% with respect to the SRS diode values. In particular, for the fixed cones, a maximum discrepancy of 2.6% in FWHM was found for the 7.5 mm diameter field, with differences in penumbra within 0.2 mm for all fields investigated. For the Iris™, a maximum discrepancy of 2.9% in FWHM was found for the 10 mm diameter aperture, with differences in penumbra within 0.2 mm for all apertures investigated.

When comparing equivalent profiles measured by the Octa for fixed cones against those measured for the Iris™, all discrepancies were within the spatial resolution of the device of 0.3 mm. In particular, with OARs analysed with MATLAB using a shape preserving interpolant function, a maximum difference of 4% in FWHM was found for the 5 mm aperture (0.2 mm), along with a 2.7% difference for the 7.5 mm aperture (0.2 mm) and 2% difference for the 10 mm aperture (0.2 mm). Penumbra values were accurate within 0.2 mm. These results, which were supported by equivalent SRS diode measurements, were consistent with those of a previous investigation in which FWHM and penumbra values for fixed cones and the Iris™ were found to be in substantial agreement, with a maximum discrepancy of 0.2 mm in penumbra width for the 5 mm diameter [227]. By the vendor's technical specifications, the average penumbra for the Iris™ is expected to be larger by 0.2 to 0.6 mm than that for the equivalent fixed cone and to increase with field size, a consequence of the stepwise approximation of a divergent collimator shape because of the increase in transmission

penumbra [219]. To our knowledge, no other inter-comparison between Iris™ and fixed cones collimator dose profiles exists in the literature.

The Iris™ collimator is designed to achieve an aperture reproducibility of 0.2 mm at 800 mm SDD [219], with the current recommendation (Accuray Physics Essentials Guide 2012, P/N 1023868-ENG A) for QA suggesting monthly film measurements of all 12 field sizes. Non-equivalent OARs reproducibility after a reset of the Iris™ aperture were found to be accurate within 2% for all profiles, with a maximum discrepancy of 1.9% for the 5 mm diameter in-plane profile (< 0.1 mm) and of 1% for the 10 mm diameter in plane and cross-plane profiles. Discrepancies in penumbra values were not appreciable.

8.4.3 Percentage depth dose and tissue maximum ratio

For silicon detectors, a decrease in sensitivity is expected with decreased dose per pulse [130]. To some extent, this effect could be offset by an overestimate of the dose due to the increase of the relative number of low energy scattered photons with increasing depth [9], [42], [141]. While a DPP dependence was found in a previous characterization of the Octa [15], in this study discrepancies in PDD with respect to the SRS diode and the calculated MC values in solid water were within 2% at all depths. For these measurements, no corrections were made for dose rate response variations.

By definition, in TMR measurements the field sizes remain constant with depth and thus the correction factor needed for the Octa remains unchanged related to the change of field dimensions. This is reflected in the TMR plots, where a dose rate dependence becomes apparent leading to a clear under-response of the Octa beyond 10 cm depth. Nevertheless, TMRs measured by the Octa were in agreement within 3% at all depths with respect to the SRS diode, for both 5 mm and 60 mm circular field diameters with fixed cones. Comparable agreement was found with respect to the SRS diode and MC simulations in solid water for the 5 mm and 60 mm diameter with the Iris™.

8.4.4 General observations on the measurements by the Octa

The CyberKnife® used for the present study was not equipped with an InCise™ multi-leaf collimator. However, based on our results, we believe the features of the Octa would be well suited to QA for this device.

Allowing for the simultaneous acquisition of dose profiles at 0°, 45°, 90° and 135°, and of those at 15° and 105° upon rotation, the Octa would greatly reduce the measurement time

needed to comply with the vendor's QA protocol, potentially allowing for a more robust implementation of the requirements when including OARs along directions not currently considered. In our study, OFs and OARs for all field sizes investigated were measured by the Octa in less than 10 minutes for the Iris™ collimator and in approximately 20 minutes for the fixed cones. PDD measurements were performed in approximately 25 minutes for both PDD and TMR, for each field size.

8.4.5 Commercially available detectors and the Octa

Examples of commercially available detector array recently proposed for machine-specific CyberKnife® QA are the Octavius 1000SRS (PTW, Germany), the SRS-Profiler (SunNuclear, USA), the Nonius (QUART, Germany) and the ArcCHECK (SunNuclear, USA).

The Octavius 1000SRS is a 2D array of 977 ionization chambers. SVs have a pitch of 2.5 mm in the square central area of 5 cm side, and a 5 mm pitch outside. In a recent characterization of the device [14], differences between OFs measurements by the 1000SRS, a synthetic diamond (TM60019, PTW) and a small-field diode (ETM60017, PTW), were approximately 3.0% for a 5 mm collimator and 1.5% for a 7.5 mm collimator, in agreement with previous investigations [147]. The size of the SVs ($2.3 \times 2.3 \times 0.5\ mm^3$) would be responsible for the 3% under-response for the 5 mm collimator owing to volume-averaging effect [14]. The array sensitivity was investigated by introducing beam shifts by moving the robot with 0.1 mm steps (for the 5, 35, 60 mm diameter fields). The shifts were detected with sub-mm accuracy [14].

In a different study, the 1000SRS, the SRS-Profiler (125 diodes arranged in a star-like fashion with 4.0 mm resolution) and the Nonius (diodes arranged in a linear array with 2.8 mm resolution), were all able to detect beam shifts with sub-mm accuracy [13]. When compared to the other 2 tested devices, however, the performance of the 1000SRS was found to be superior, comparable to EBT3 films in terms of accuracy and sensitivity, and more user-friendly.

The ArcCHECK is a 3D cylindrical array of 1386 diodes ($0.8 \times 0.8 \times 0.03\ mm^3$) with 10 mm pitch. The EDGE diodes response, a similar version of the ArcCHECK's diodes, was investigated [228] in CyberKnife® small-fields. OFs agreed with MC calculations and measurements by benchmark detectors within 1% for field sizes larger than 10 mm diameter. Differences were between 3.6% and 5.1% for cones with diameter < 10 mm. The ArcCHECK was recently investigated for commissioning of a Multiplan® Monte Carlo dose calculation algorithm [229]. It was found that while the ArcCHECK addresses some of the small-field

dosimetry challenges (its diodes have real-time response, high sensitivity and sub-mm lateral size of the SVs), the measurement of field sizes with diameter inferior or equal to the SVs pitch should be considered with care.

When considering machine-specific QA applications for the smallest field sizes offered by a CyberKnife® (5, 7.5 and 10 mm diameter), the 1000SRS is probably the most obvious choice. The Octa array offers a comparable performance for OFs measurements, without the volume averaging effect of the former, with a superior nominal spatial resolution for OAR measurements and most importantly pulse-per-pulse real-time acquisition.

8.5 Conclusions

In this work, the Octa detector has been investigated for the dosimetry of small radiation fields as used in SRT with the CyberKnife® system. For any given field size, the Octa allowed for the simultaneous real-time read-out of OFs and dose profiles for cross-plane, in-plane and two diagonal directions. PDD and TMRs were accurate within 3% with respect to both SRS diode and MC simulations, for all field sizes investigated. The Octa was used for a real-time high-spatial resolution verification of the Iris™ variable aperture reproducibility in terms of FWHM and penumbra values of the dose profiles, as well as OFs. The Iris™ reproducibility was found to be within the vendor's technical specifications.

Overall, the Octa was shown to be a 'correction-free' dosimeter for routine QA for a CyberKnife® system, offering a reliable real-time read-out along with unique properties for dosimetry verification, such as a long-term stability evaluation of the Iris™ collimator.

8.6 Appendix: A Monte Carlo investigation on the Octa

8.6.1 The Geant4 application

The results of the Geant4 application developed to read the IAEA PHSP files containing the description of the particles at the exit plane of the Iris™ collimator were cross-checked against experimental data measured by the SRS diode at the Sir Charles Gairdner Hospital. A selection of these confirmations is presented and discussed hereafter. For all Geant4 calculations, the Standard EM physics list option 4 was used, with production cuts set to 0.01 mm for electrons and photons in the water and solid water phantoms. Error bars, calculated as 2 standard deviations, did not exceed the symbols size.

Figure 65, Figure 66 and Figure 67 show a 2D cross-sectional view of the energy deposition in a water phantom in the plane perpendicular to the primary photon beam direction, for a circular field size of diameter 5, 7.5 and 10 mm respectively. Collecting volumes for the energy deposition were set at $0.3 \times 0.3 \times 0.06$ mm^3. The 2D plane was set at 15 mm depth, 800 mm SDD.

Figure 68 shows CAX TMRs measured at 800 mm SDD by the SRS diode and calculated by the GEANT4 application in water, for a 5 mm diameter Iris™. Figure 69 shows CAX PDDs at 800 mm SSD measured by the SRS diode and calculated by the GEANT4 application in water, for a 60 mm diameter Iris™. For the same collimator aperture, Figure 70 shows CAX PDDs at 800 mm SSD calculated by the GEANT4 application in water and in solid water (modelled as the IBA type RW3; composition 98% polystyrene + 2% TiO_2, 1.045 g/cm^3).

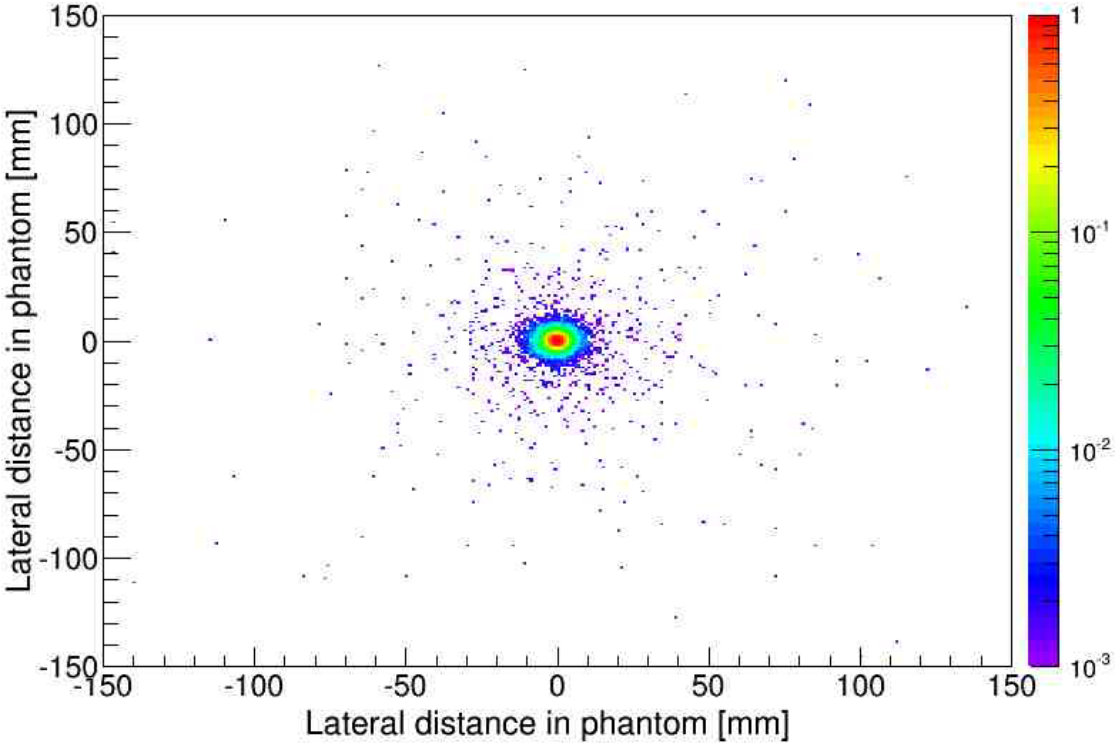

Figure 65. Cross-sectional view in the plane perpendicular to the photon beam direction of the energy deposition in a water phantom at 15 mm depth, 800 mm SDD for a circular field size of diameter 5 mm.

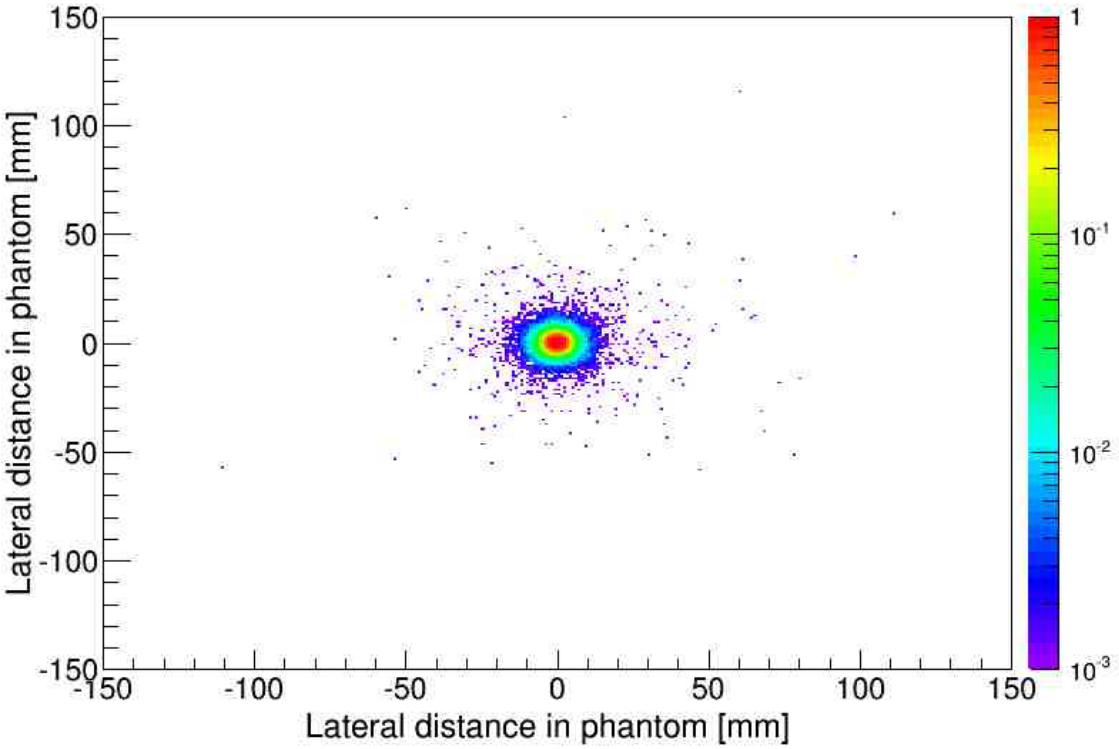

Figure 66. Cross-sectional view in the plane perpendicular to the photon beam direction of the energy deposition in a water phantom at 15 mm depth, 800 mm SDD for a circular field size of diameter 7.5 mm.

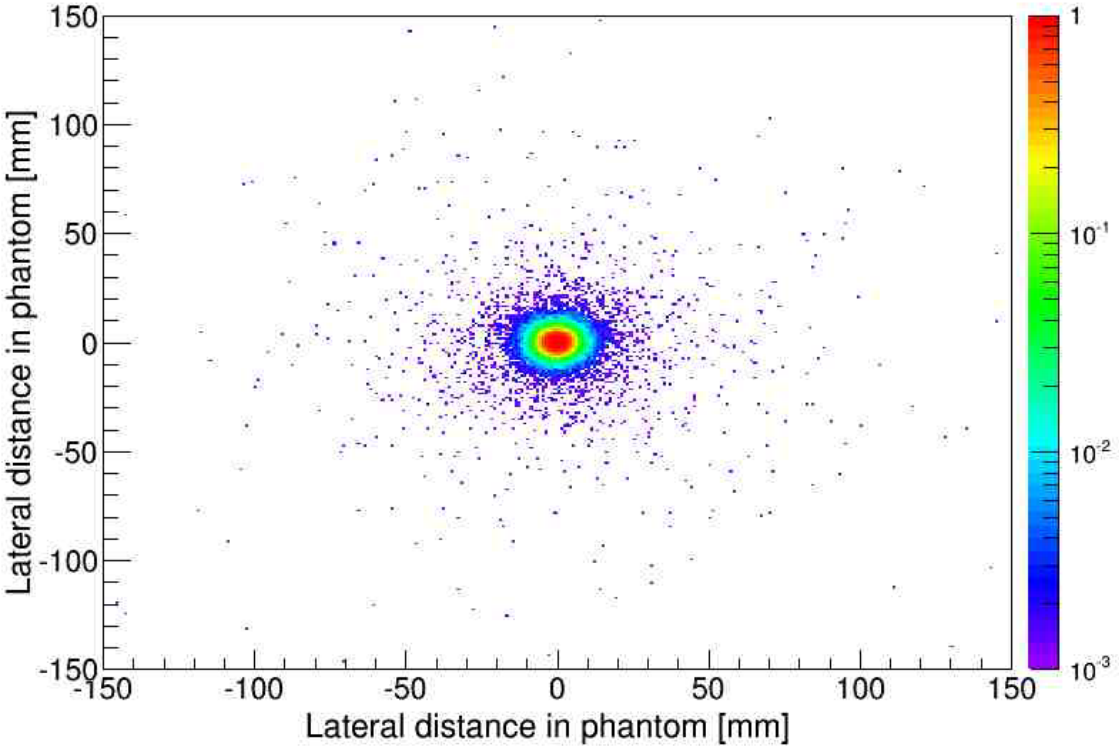

Figure 67. Cross-sectional view in the plane perpendicular to the photon beam direction of the energy deposition in a water phantom at 15 mm depth, 800 mm SDD for a circular field size of diameter 10 mm.

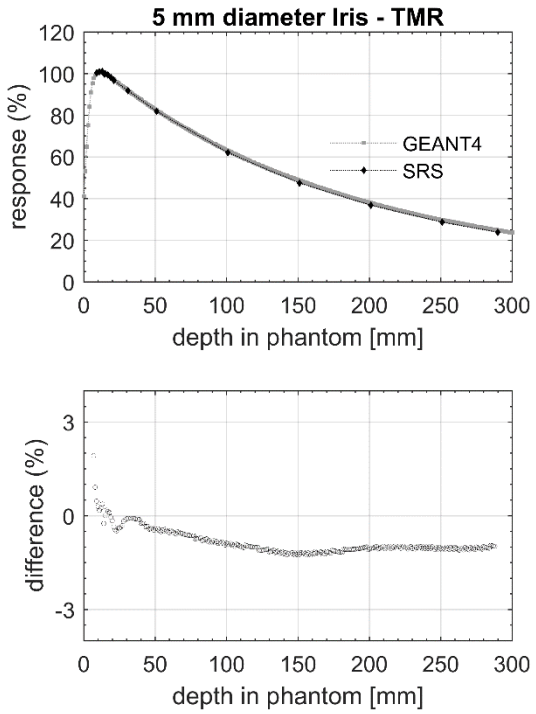

Figure 68. CAX TMRs measured by the SRS diode and calculated by the Geant4 application in water, for a 5 mm diameter Iris™. Percentage differences, shown in the lower panel, suggest the application is accurate in reproducing the experimental measurements.

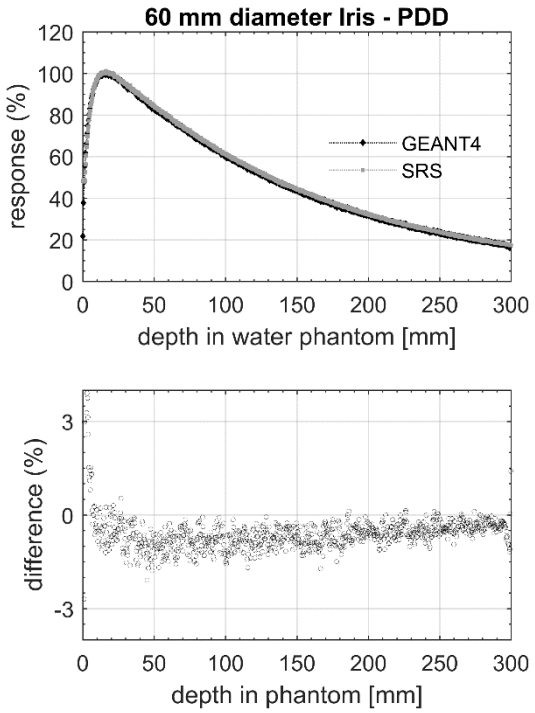

Figure 69. CAX PDDs measured by the SRS diode and calculated by the Geant4 application in water, for a 60 mm diameter Iris™. Percentage differences, shown in the lower panel, suggest the application is accurate in reproducing the experimental measurements.

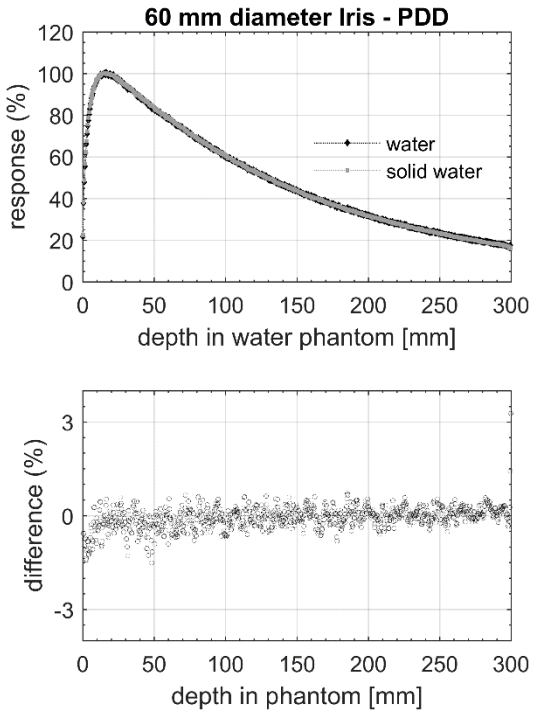

Figure 70. CAX PDDs calculated by the GEANT4 application in water and in solid water (type RW3), for a 60 mm diameter Iris™. Percentage differences are shown in the lower panel. This result confirm that relative dose measurements performed in solid water phantoms (as for the Octa experimental measurements throughout this chapter) can be cross-checked with measurements performed in water tank by another detector (as for the SRS diode).

These results suggest that the Geant4 application is accurate in reproducing the SRS diode experimental data and could be used for further investigations of the behaviour of the Octa detector under irradiation with a 6 MV FFF beam delivered by a CyberKnife® linac.

8.6.2 Extra-cameral components and the air gap

Diode detectors dedicated to measurements in small radiation fields command the use of correction factors to relate their readings to dose. This is because both the silicon SVs and the surrounding packaging, the latter sometimes referred to as extra-cameral components, perturb the photon and electron fluences with respect to water. In the case of the Octa, though, a small air gap on top of its SVs makes it a detector requiring a correction factor close to unity, for a wide range of beam qualities [15].

MC calculations have been previously used for investigations of the behaviour of a detector and the effect of its extra-cameral components in small-field measurements, but only in the case of point-like detectors [51], [65]. This study deals with a similar investigation, but considers a 2D monolithic detector, the Octa, and its specific extra-cameral components: a protective epoxy layer and a PCB board that provides electronic connections to the read-out system (Figure 71). Its Geant4 model was described in section 4.4.2, page 53. The primary photon beam was given by the Geant4 application discussed in the previous section.

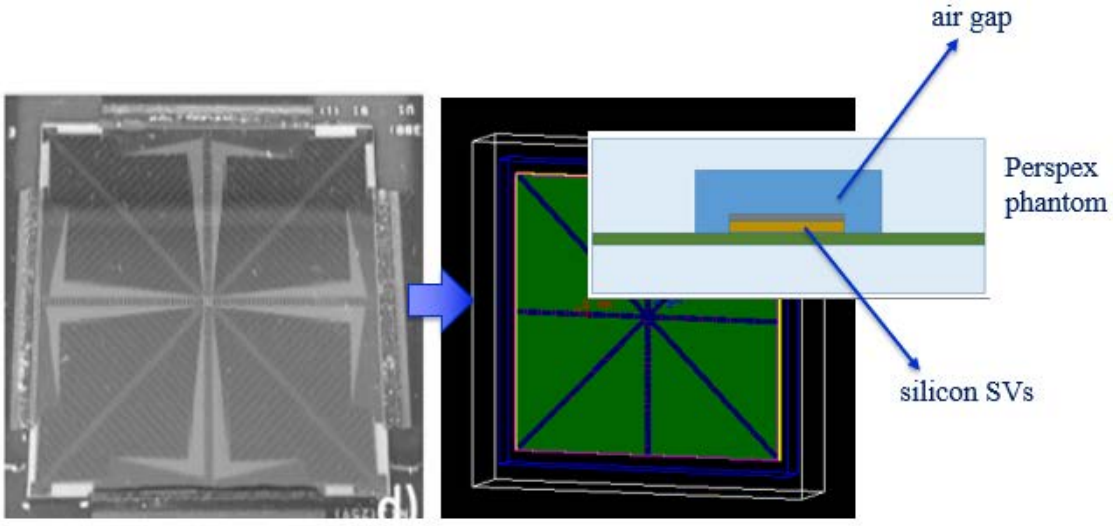

Figure 71. A visual description of the Octa detector (left), the Geant4 Octa model (right) and a cross-section illustrating the Octa packaging: silicon SVs (brown layer), PCB board for read-out connections (green layer), protective epoxy layer on top of the SVs (grey layer), air gap (dark blue) and surrounding Perspex phantom (light blue).

Output factors were defined as the ratio between the Geant4-calculated energy deposition (ED) scored in a SV of the Octa at a specific field size ($clin$) and that at the machine specific reference field (msr) [147]:

$$\mathrm{OF} = \frac{\mathrm{ED}^{\mathrm{f_{clin}}}}{\mathrm{ED}^{\mathrm{f_{msr}}}} \tag{8.2}$$

where $\mathrm{ED}^{\mathrm{f_{clin}}}$ and $\mathrm{ED}^{\mathrm{f_{msr}}}$ are the energy depositions scored in the $\mathrm{f_{clin}}$ and $\mathrm{f_{msr}}$ fields respectively. The reference field was taken as that given by the 60 mm diameter Iris™. The model of the Octa was placed at 15 mm depth in solid water, 800 mm SDD.

As a first step, an investigation into the effect of the thickness of the protective epoxy layer on OFs measurements was performed by calculating the ED scored in the central SV of the Octa for a range of thicknesses.

Results (Figure 72) show that 150 µm is the value which most accurately reproduce experimental measurements of OFs (represented by 'Octa' in the figure). All other conditions being equal, increasing the thickness of the epoxy layer leads to a relative over-response of the SVs at small fields, although the difference seems appreciable only for values above 250 µm.

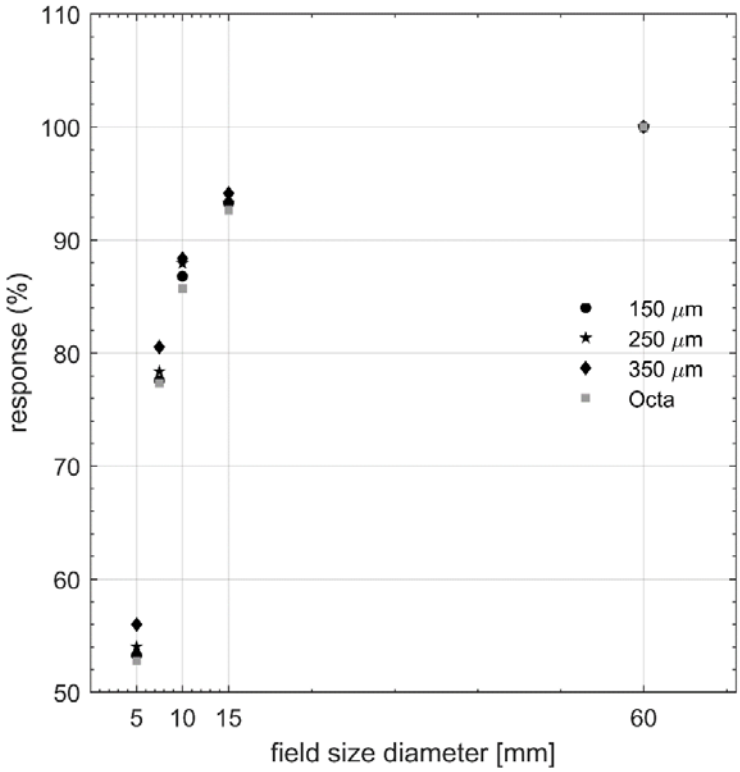

Figure 72. OFs: effect of the epoxy layer thickness. Shown are the Geant4-calculated OFs scored in the central SV of the Octa, for 3 different thicknesses (150 µm, 250 µm, 350 µm). 'Octa' values refer to the experimental OFs measurement by the Octa.

Secondly, an investigation into the effect of the thickness of the air gap on OFs measurements was performed by calculating the ED scored in the central SV of the Octa for a range of thicknesses close (but not equal) to the one used for the experimental device (1.2 mm, 1.5 mm, 1.8 mm).

Results (Figure 73) show that the air gap, i.e. the amount of compensation to be introduced to balance the perturbations due to SVs and other packaging materials, requires a careful fine-tuning, especially for measurements at the smallest fields.

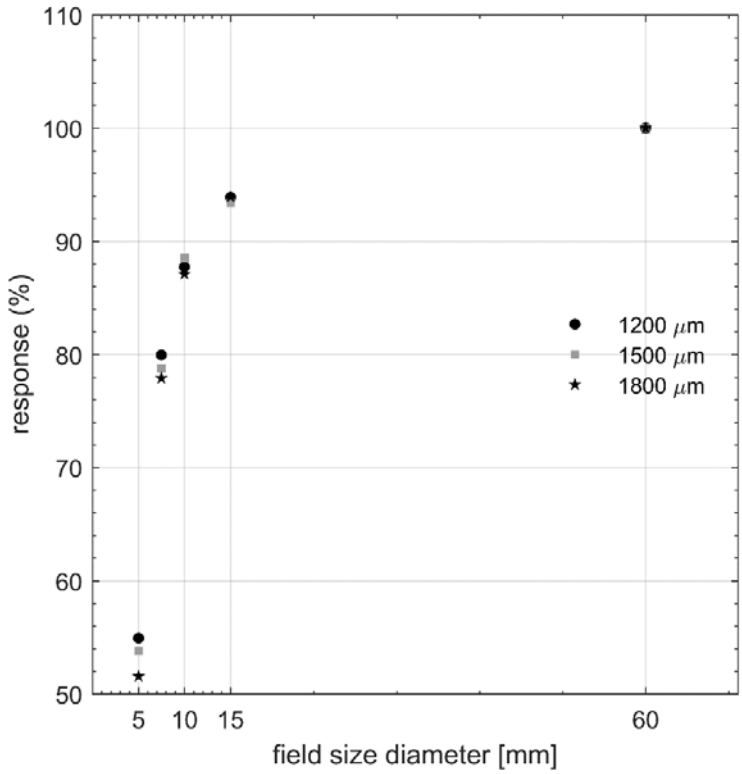

Figure 73. OFs: effect of the air gap thickness. Shown are the Geant4-calculated OFs scored in the central SV of the Octa, for 3 different air gaps (1.2 mm, 1.5 mm, 1.8 mm).

A third investigation into the effect of the different extra-cameral components on OFs measurements was performed by calculating the ED scored in the central SV of the Octa for a range of cases: the absorbed dose in the bare (i.e. with no surrounding packaging) SV filled with solid water, the absorbed dose in the bare SV filled with silicon, the absorbed dose in the silicon-SV with surrounding packaging (PCB board, protective epoxy layer) and the absorbed dose in the silicon-SV in the fully-modelled detector (with packaging and air gap).

In previous similar investigations it was found that, on top of those introduced by silicon SVs, significant perturbations were caused by extra-cameral components of atomic number Z, density and *I-value* different than those of water, and that the degree of the introduced

perturbation was a function of the radiation field size with respect to that of the detector [51], [147].

In the case of the Octa, results (Figure 74) suggest that the effect of the extra-cameral components on OF measurements is obvious for the smallest fields, i.e. ≤ 10 mm diameter. As expected, the performance of the Octa could be improved by adding a small air gap (in the proposed figure, of thickness equal to that used for the experimental device and different from the values investigated in Figure 73). It is important to reiterate that the required amount of this compensation is also a function of the beam quality and measurement conditions [51].

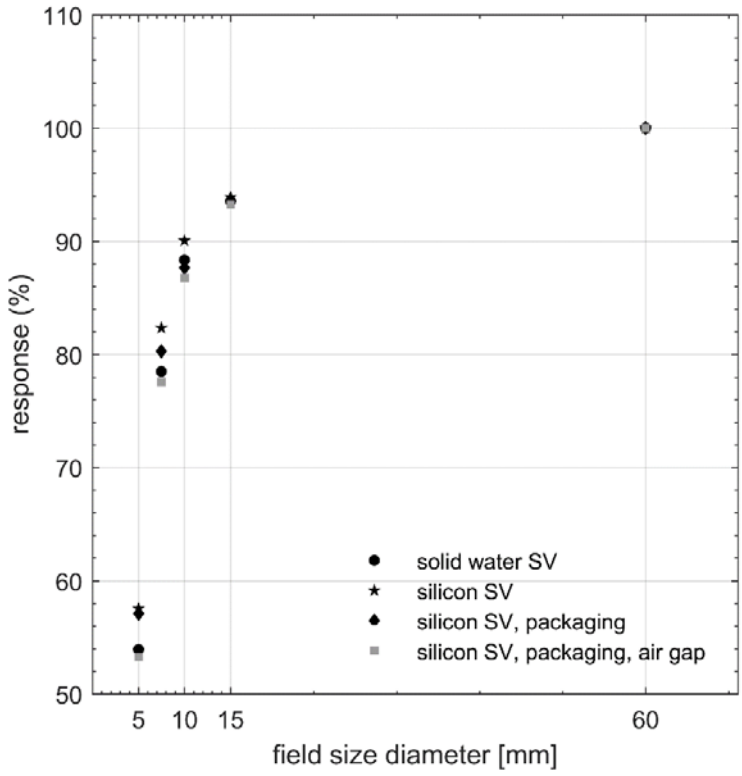

Figure 74. OFs: effect of the extra-cameral components. Shown are the Geant4-calculated OFs in the central SV of the Octa.

In-line, cross-line and 2 diagonal OARs experimentally measured by the Octa and calculated by the Geant4 application, with ED scored in the SVs of the model of the Octa, are shown in Figure 75 for a 7.5 mm diameter Iris™ and in Figure 76 for a 10 mm diameter Iris™. TMRs measured by the Octa and calculated by the Geant4 application, with ED scored in the central SV of the model of the Octa, are shown in Figure 77 for a 5 mm diameter Iris™. These results suggest the model of the Octa is accurate and could potentially be used to anticipate the results of future experimental measurements, for example by investigating that the air gap

thickness is optimized for any given beam quality and measurement condition, a step which is recommended in the literature [65].

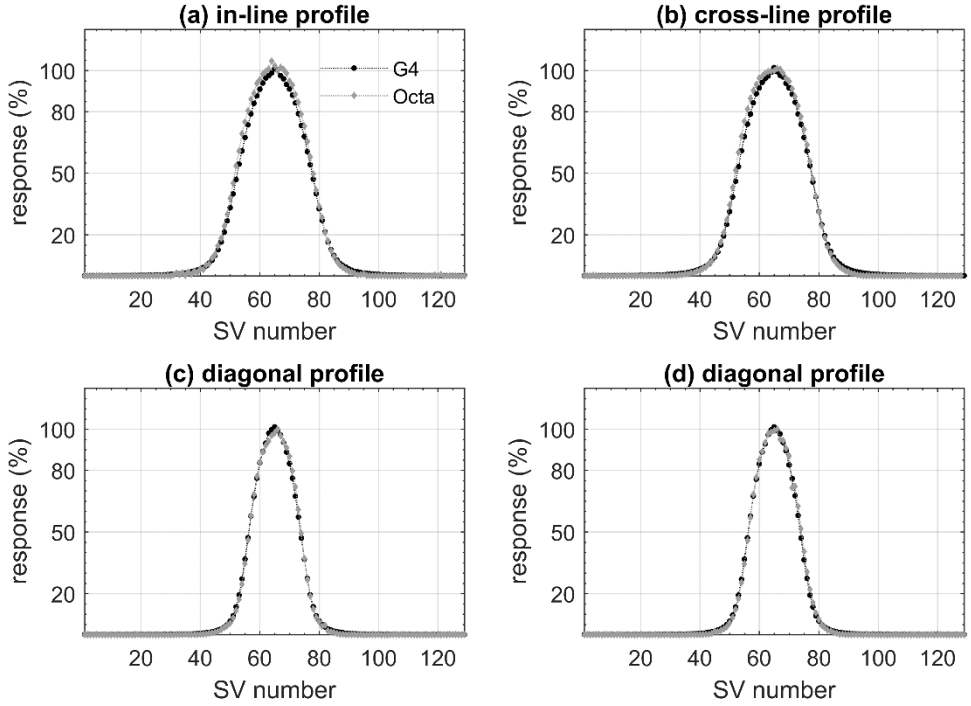

Figure 75. 7.5 mm Iris™ circular field. In- and cross-line and 2 diagonal OARs experimentally measured by the Octa and Geant4-calculated ED scored in the SVs of the Octa ('G4').

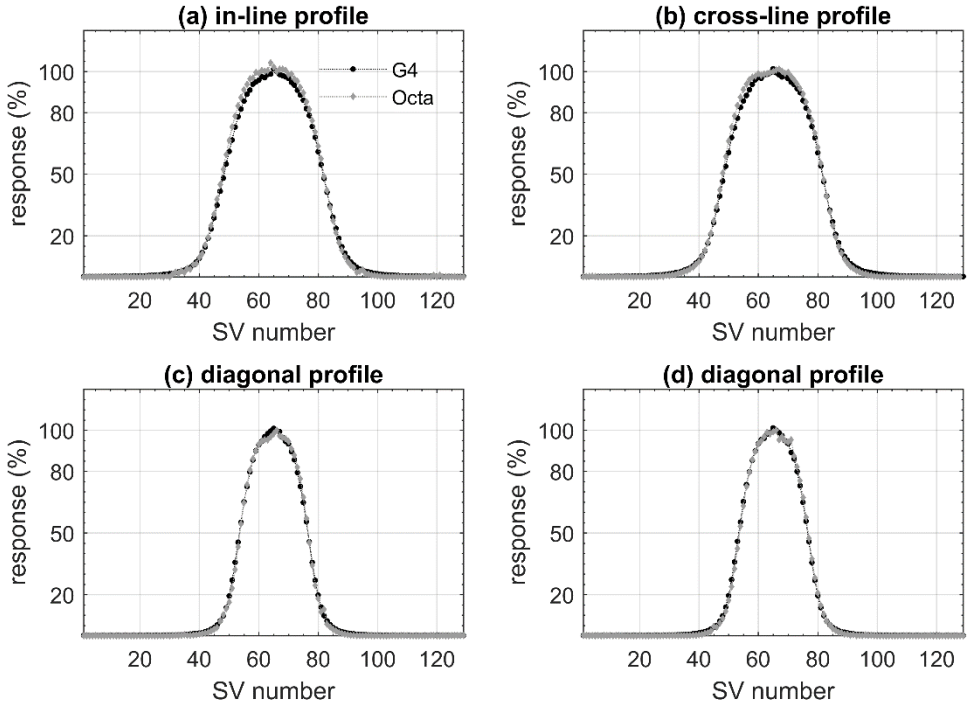

Figure 76. 10 mm Iris™ circular field. In- and cross-line and 2 diagonal OARs experimentally measured by the Octa and Geant4-calculated ED scored in the SVs of Octa ('G4').

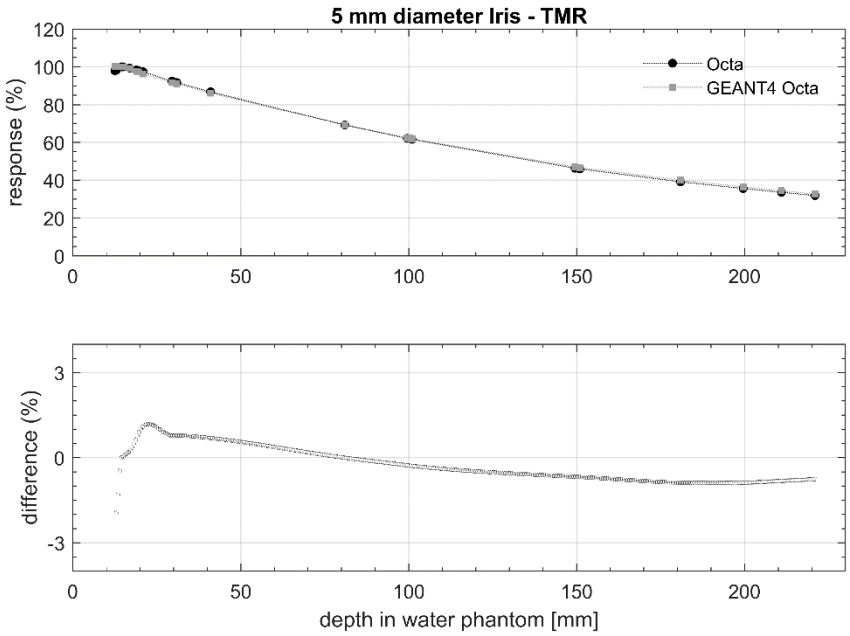

Figure 77. 5 mm Iris™ circular field. TMRs experimentally measured by the Octa and Geant4-calculated ED scored in the central SV of the Octa. Percentage differences are shown in the lower panel.

8.6.3 Conclusions

A Geant4 application was developed to read the International Atomic Energy Agency (IAEA) phase space (PHSP) files containing the description of the particles scored at the exit plane of the Iris™ collimator. Its output was cross-checked against experimental data measured by the SRS diode at the Sir Charles Gairdner Hospital.

A Geant4 model of the Octa was used to investigate the behaviour of the detector and the effect of its SVs and extra-cameral components in small-field measurements. It was confirmed that their perturbation of the photon and electron fluences, resulting from their being non-water equivalent, could be offset by adding a small air gap. This result is consistent with OFs experimental measurements (section 8.3.1, page 104). Finally, by comparing OARs and TMRs experimentally measured by the Octa and calculated by the Geant4 application as ED scored in the SVs of the model of the Octa, it was suggested that the latter was accurate enough to anticipate the result of future experimental measurements and possibly be used for optimizing the air gap for any given beam quality and measurement condition.

9 On monolithic silicon array detectors for small-field photon beam dosimetry

This chapter is based on material in **G. Biasi** *et al*, (2018) On monolithic silicon array detectors for small-field photon beam dosimetry, *IEEE Transaction on Nuclear Science*, 65 (9), 2640-2649 [18][27] and presented at the 2018 IEEE NSS-MIC Conference (Sydney, Australia). Measurements and numerical investigations discussed hereafter were performed during 2016, 2017 and first half of 2018.

9.1 Introduction

Contemporary x-ray radiotherapy employs small radiation fields (< 3 cm side) to deliver highly conformal dose distributions to the target. To avoid dosimetric inaccuracies in the quality assurance (QA) process, which may cause poor patients outcomes [2], [24], sub-millimetre spatial resolution in the measurement of the delivered dose map is a crucial detector requirement. Currently, the only commercially available options able to satisfy this requirement are point detectors used with various scanning techniques [2].

A preferable solution would be a suitable 2D detector. In particular, 2D monolithic silicon arrays can be fabricated of relatively large area while optimizing the spatial resolution with small sensitive volumes (SVs) [115]–[118]. They would offer advantages in terms of QA applications. Along with commonly characterized parameters, such as output factors (OFs), percentage depth dose (PDD) and tissue maximum ratio (TMR) distributions, and out off-axis ratios (OARs), their fixed geometry would allow for accurate reproducible machine-specific QA. Examples would include the positional accuracy verification of the movable parts of a medical linear accelerator (linac), such as the leaves of a multi-leaf collimator (MLC) and the aperture of dynamic circular collimators (Iris™).

Silicon detectors based on either n^+-p or p^+-n junctions would be a sensible choice for monolithic arrays. Their advantages include the potential for manufacturing very small SVs, a stable and near energy-independent response in megavoltage (MV) photon fields, good dose linearity and real-time read-out [84]. They have recently been recommended by Codes of Practice for small-field dosimetry QA [1], [2].

[27] References are combined in a single bibliography at the end of the present dissertation.

2D monolithic silicon arrays are manufactured on doped wafers, which are then implanted to create pixels (radiation SVs). The substrate of choice has long been a p-type low-resistivity wafer in order to improve the linearity with the dose rate [117].

Unfortunately, these devices are affected by significant radiation damage, resulting in the production of deep level defects, such as interstitial and vacancy defects, and generation-recombination (G-R) centres via interaction of secondary electrons with the detector substrate [181], [182]. G-R centres capture excess minority carriers and facilitate recombination with majority carriers [124], [129], [137]. Because each defect introduces its own energy level and thus contributes to the overall recombination efficiency, the lifetime τ of minority charge carriers, i.e. the average time the excess minority carrier needs to recombine, depends on the overall defect structure in the substrate. Other than the relative contribution of each defect energy level, the minority lifetime τ depends on the injection level and temperature [84]. In the general form, its complex expression is based on Reed–Shockley recombination theory [84].

As a first approximation, the variation of defect concentration explains the variation of the minority carrier lifetime, i.e. the average time the excess minority carrier needs to recombine, which for a p-type substrate can be expressed as [117], [127], [133]:

$$\tau_e = \frac{1}{\sigma_e \nu_{th} N_t} \tag{9.1}$$

with σ_e the cross-section for capture of electrons, ν_{th} their thermal velocity in the lattice at a specific temperature and N_t the defect concentration in the substrate. As the radiation-induced defects increase with accumulated dose, τ_e decreases. This is reflected in the minority carrier diffusion length through:

$$L_e = \sqrt{D_e \tau_e} \tag{9.2}$$

where D_e is the minority carrier diffusion constant. The sensitivity per unit area of a thick silicon device is directly proportional to its minority carrier diffusion length L_e [117]:

$$S \propto L_e \tag{9.3}$$

Therefore, a decrease in the minority carrier lifetime τ_e leads to a sensitivity degradation with accumulated dose [117], [133].

Pre-irradiation of the device up to 10 kGy, while reducing the sensitivity, allows for its stabilization [99]. This is explained by the saturating behaviour of τ with accumulated dose [84]. In order to counter the increase of dark current due to pre-irradiation [84], [187], a device can be operated without applying an external bias, i.e. in ‘passive’ mode. In this case, the depleted region is only a few microns thick, its thickness a function of the built-in potential

[202], and the current generated by radiation is controlled by the diffusion current of the excess minority carriers [124].

More recently, it has been shown that it is possible to achieve a constant sensitivity almost independent of the accumulated dose by fixing the SV in two directions: laterally, by using guard-rings, and in depth, by growing onto a highly conductive substrate an epitaxial layer whose thickness is shorter than the L_e expected in the operative dose range [117], [189]. It was demonstrated that, for an epitaxial device with a thickness of $50\ \mu m$ grown on a Czochralski (Cz) substrate, if:

$$L_e \geq W, r \tag{9.4}$$

with W the epitaxial layer thickness and r the guard ring-SV distance, the active volume V did not change significantly even at the highest accumulated dose, resulting in a stable sensitivity [117], [189].

The Centre for Medical Radiation Physics (CMRP), University of Wollongong, has designed and characterized two generations of 2D monolithic silicon array devices. The 1st generation (MP512 and Duo [116], [118], [177]) was fabricated on a bulk p-type silicon substrate and featured 512 SVs. In the case of the MP512 the SVs were uniformly distributed on the silicon wafer surface with a $2\ mm$ pitch, whereas for the Duo they were arranged with $200\ \mu m$ pitch along 2 linear orthogonal arrays.

Whilst the MP512 and the Duo performed excellently under flattened beam (FB) irradiation in terms of OFs, OARs, PDD distribution, with a small dose per pulse (DPP) dependence [116], [118], [177], their applicability for small-field dosimetry was impaired by the coarse spatial resolution of the MP512 and by the limited spatial characterization of the 2D dose map offered by the Duo.

Thus, a new 2nd generation device 'Octa' has been developed. It was shown that the peculiar layout of the SVs of the Octa has unique potentials for small-field dosimetry, providing a more detailed 2D dose map characterization without sacrificing the necessary spatial resolution. It allows for the simultaneous measurement of OF, cross-plane, in-plane and 2 diagonal OARs for any given radiation field, with sub-millimetre resolution. [15], [17].

The Octa was produced in two versions, on a bulk and on an epitaxial substrate. We report on their numerical modelling and experimental characterization discussing the effects of resistivity and defects concentration profiles across their large-area monolithic silicon wafers

in terms of response linearity with dose, response uniformity and charge-collection efficiency (CCE). Their performance is assessed with respect to small-field dosimetry for medical QA applications.

9.2 Materials and methods

9.2.1 The Octa

The Octa is a 2D monolithic silicon array detector based on a p-type silicon substrate. Its 512 ion-implanted n^+ SVs are arranged along 4 intersecting orthogonal linear arrays, oriented 45 degrees with respect to each other. The SVs have all the same area ($0.032\ mm^2$) and are of elongated rectangular shape ($40\ \mu m \times 800\ \mu m$), except for the 9 SVs in the central matrix at the intersection of the arrays ($160\ \mu m \times 200\ \mu m$).

As a requirement of the SVs ion-implantation planar-technology and for silicon surface passivation, a silicon dioxide SiO_2 layer is formed on top of the silicon wafer. The layer accumulates positive charges attracting electrons. The accumulation of electrons at the interfaces between the layer and the SVs may short the latter. Non-isolated implants may be detrimental to the 2D spatial resolution of the device. As a solution, p^+ stop areas are implanted in between the n^+ SVs. These re-shapes the electric field of the SVs n^+-p junctions, cutting into the accumulation layer and preventing the shortening.

The SVs pitch is sub-millimetre, $300\ \mu m$ along the vertical and horizontal arrays and $430\ \mu m$ along the diagonal arrays.

The device has a total area of $38.7\ mm \times 38.7\ mm$ and is covered by a $100\ \mu m$ thick layer of epoxy resin to provide a tissue equivalent protection against moisture and accidental damage. Conceived for dose measurements in solid water, it is sandwiched between two Perspex plates, each $5\ mm$ thick.

The Octa is wire bonded to a $200\ \mu m$ thick printed circuit board (PCB) for connection to a multichannel read-out data-acquisition (DAQ) system, which is based on a commercially available analogue front-end (AFE0064, Texas Instruments), which was described in detail elsewhere [177], [190].

The first version of the Octa was manufactured (SPA-BIT, Kiev, Ukraine) on a $460\ \mu m$ bulk p-type substrate (resistivity $10\ \Omega cm$). The silicon wafer was created using a Czochralski process [180]. The bulk Octa sensitivity was stabilized by pre-irradiation [99] with a Co-60

gamma source at the Gamma Technology Research Irradiator (GATRI) facility at the Australian Nuclear Science and Technology Organisation (ANSTO) in the order of 12 Mrad.

The second version of the Octa was manufactured (SPA-BIT, Kiev, Ukraine) on a 35 μm p-type epitaxial [188] layer (resistivity 100 Ωcm), grown onto a 525 μm thick heavily doped silicon substrate with resistivity 0.001 Ωcm.

The topology in both bulk and epitaxial versions was the same.

9.2.2 Radiation damage and electrical characterization

A current–voltage I-V characterization is a standard test to determine the baseline leakage current and assess the uniformity of the diodes response. In this study, reverse current voltage I-V characteristics measurements were performed using an automatic Semiconductor Measurement Unit (SMU) 237 from Keithley, at a constant laboratory temperature of 24°C. The diodes reverse bias was investigated in the range from 0 V to 100 V. The bias was applied to the backside contact.

A capacitance-voltage (C-V) characterization is a test aimed at determining the device full depletion voltage. In this study, measurements were performed with a bridge capacitance meter Boonton 7200, at a constant laboratory temperature of 24°C. The diodes bias was investigated in the range from 0 V to 20 V.

For both I-V and C-V characterizations, measurements were carried out for one SV at a time, randomly located on the silicon wafer. Neighbouring SVs were not grounded during measurements. The effect of this on the magnitude of the collected currents was neglected for the scope of this discussion.

9.2.3 Linearity

A characterization of the linearity of the bulk Octa response was performed by irradiating the device at 1.5 cm depth in a water equivalent phantom at 100 cm surface-to-source distance (SSD) with a 20 cm side square flat field with a 6 MV flattened beam (FB) delivered by a medical linear accelerator. In these conditions, at 1.5 cm depth, 1 MU delivered by the accelerator corresponds to 1 cGy. The response linearity was investigated in the range of 50 MU to 500 MU.

The linearity of the epitaxial Octa response was performed using the same experimental settings, but with the device at 10 cm depth in the phantom, owing to different availability of solid water slabs at that time.

9.2.4 Uniformity

Ideally, the response of the Octa 512 diodes would be uniform when the device is irradiated in a flat field. However, this is not the case, owing to unavoidable non-uniformity of the original silicon wafer and possible variations involved in the fabrication processes. A key issue is the presence of defects within the silicon material, intrinsic or due to radiation induced damage. Differences in their local concentration lead to variances in the electric field distribution and charge trapping/recombination process.

Understanding of this change in the electrostatic and charge collection behaviour of the device is especially relevant when operating the device in passive mode.

Other factors affecting a diode response are the parasitic capacitance associated with different length of the connecting leads to each SV and variation in preamplifiers gain in multichannel read-out system , which can vary within 0.1% to 0.5% of the dynamic range [192].

The non-uniformity of the integral response can be addressed with an equalization procedure requiring the irradiation of the device with a flat radiation field and then the application of the corresponding equalization factors.

The Octa was irradiated at 10 cm depth 90 cm SSD in a water equivalent phantom with a 20 cm side square flat field with a 6 MV FB delivered by a medical linear accelerator. An equalization factor for each diode was obtained by normalizing each channel response X_i to the average response of all channels $\langle X \rangle$ to the flat field. The equalization factor was defined as:

$$F_i = \frac{X_i}{\langle X \rangle} \tag{9.5}$$

The equalized response $X_{eq,i}$ of each diode was then:

$$X_{eq,i} = \frac{X_i}{F_i} \tag{9.6}$$

The uniformity $X_{\%}$ of the 512 diodes response was calculated as:

$$X_{\%} = \frac{X_{eq} - \langle X \rangle}{\langle X \rangle} \times 100 \tag{9.7}$$

9.2.5 Simulation models of the Octa

Technology computer-aided design (TCAD) is a simulation tool for semiconductor devices modelling and performance analysis. TCAD simulations were performed using Sentaurus™ Workbench [199] within the Synopsys® (Synopsys, Inc., Mountain View, CA) framework.

The Sentaurus TCAD software solves the Poisson and carrier continuity equations using finite element methods on a discretised mesh, user-defined and optimized for any given geometry. This mesh-like grid structure of nodes is loaded into the Sentaurus Device (*Sdevice*) [201] simulation tool.

Depending on the device under investigation and the level of accuracy required, different transport models, each based on a different expression to compute the current densities, can be selected in *Sdevice*. The *drift-diffusion* model, which considers the effect of thermal diffusion and the drift caused by the local electric field resulting from applied bias (if any) and electrostatic forces between carriers, was used.

Defects in the substrate reduce charge collection by various generation–recombination processes. Recombination through deep defect levels in the semiconductor energy gap is modelled using the Shockley–Read–Hall (SRH) recombination theory. The SRH lifetimes dependence on doping profiles is modelled in *Sdevice* through the Scharfetter relation [201].

The *Trap* model in the *Physics* section of the *Sdevice* command file allows for the parametrization of the trapped charge at the interfaces and of the point defects in the substrate, specifying the energy levels, the concentration as a function of the accumulated dose and the cross-section for electrons and holes.

Radiation incident on a semiconductor triggers the generation of electron–hole pairs (ehp). In the *Physics* section of the *Sdevice* command file it is possible to model the carrier generation through the *Gamma Radiation Model*. The user can define a dose rate ($\mathrm{rad/s}$) and the irradiation duration. Alternatively, a *Heavy Ion Model* can be used. The model is used to represent a minimum ionising particle (MIP) incident on the device. The charge deposited by the particle along a track, or its linear energy transfer (LET) generation density ($\mathrm{ehp/cm^3}$), is a user-defined parameter, along with track length, incident location and direction, and lateral distribution. A detailed descriptions of these models can be found in the Sentaurus-Device User Guide and references therein [201].

Using the Sentaurus Structure Editor (SDE) [200], 2D TCAD devices representative of the bulk and epitaxial Octa were created. For both devices, the considered SV was 40 µm wide. Other parameters (pitch and number of modelled SVs per single device) were variable in the simulations.

The radiation damage of the pre-irradiated bulk Octa was considered by implementing the *Trap* model. As reported in the literature, defects generated in a silicon substrate by a Co-60 gamma source can be effectively modelled by introducing interstitial $\mathrm{C_iO_i}$ complexes and

VV divacancy centres in the substrate, as well as positive trapped charge at the interfaces with and within the silicon dioxide layers [203].

Following recommendations in Aldosari et al. [202] and references therein, a two-level radiation damage model was implemented for the silicon substrate (see Table 18). Following recommendations reported in the same references, a concentration of trapped charges at the Si-SiO_2 interfaces and within the SiO_2 layers of $C = 10^{12}\text{cm}^{-2}$ and $C = 10^{7}\text{cm}^{-2}$ for the pre-irradiated bulk Octa and for the epitaxial Octa respectively was considered. The concentration saturates between $1.5 \times 10^{12}\text{cm}^{-2}$ and $3.5 \times 10^{12}\text{cm}^{-2}$ [230].

The *Mobility* model was declared in the *Physics* section of the *Sdevice* command file to implement a SRH doping-dependent process.

The TCAD devices were validated against experimentally determined I-V and C-V characteristics, with doping concentrations and profiles tuned to fit the experimental results. Avalanche models available to simulate the breakdown voltage were not considered for the scope of this discussion.

The *Heavy Ion Model* and the *Gamma Radiation Model* were used to investigate the CCE in the Octa's SVs as a function of pitch and substrate parameters, at zero bias.

In a first scenario, the MIP simulated with the *Heavy Ion Model* had a normal incidence on the device with a continuous charge distribution generation of $80\ \text{ehp}/\mu\text{m}$. The CCE was defined as:

$$\text{CCE}(\%) = \frac{Q_{j,x}}{Q_{j,x=0}} \times 100 \tag{9.8}$$

$Q_{x=0}$ is the charge collected by the SV j, taken as the integrated current, when the MIP hits at its centre; $Q_{j,x}$ is the charge collected by the same SV when the MIP hits at a distance x from its centre. The Octa was modelled with 5 SVs and j was the middle SV.

In a second scenario, using the *Gamma Radiation Model*, the dose rate was of $4.2 \times 10^4\ \text{rad/s}$ for a $5\ \mu\text{s}$ duration, representative of a typical medical linac measurement condition. The CCE was defined as:

$$\text{CCE}(\%) = \frac{Q_{j,5p}}{Q_{j,1p}} \times 100 \tag{9.9}$$

$Q_{j,5p}$ is the charge collected by the SV j, taken as the integrated current, when the simulated device has 5 SVs and j is the middle one; $Q_{j,1p}$ is the charge collected by the same SV, when the simulated device is the same as the previous one, but has only the one SV.

Table 18. Two-level radiation damage model. D is the dose in water in units of kGy [202].

Energy [eV]	Type of defect	Introduction rate [cm^{-1}]	Cross section [cm^{-2}]	
			Electrons	Holes
$E_v + 0.36$	C_iO_i donor	$1.826 \times 10^{12} \times D$	2.5×10^{-14}	2.5×10^{-15}
$E_c - 0.42$	$VV^{(-0)}$ acceptor	$3.040 \times 10^{12} \times D$	2.0×10^{-15}	2.0×10^{-14}

9.2.6 Clinical application

As a clinical application, we considered the measurement of out of axis ratios (OARs). Experimental measurements described in this study were performed at the Sir Charles Gairdner Hospital (SCGH), Nedlands, WA, Australia.

The Octa was irradiated with a 6 MV flattening filter free (FFF) beam using an Accuray CyberKnife® M6 linear accelerator (Accuray, Palo Alto, CA). Radiation field sizes were defined using a dynamic circular collimator called Iris™ (Accuray, Palo Alto, CA).

OARs were measured by the Octa on top of a 10 cm solid water slab for backscattering purposes, at 1.5 cm depth and 80 cm source-to-detector distance (SDD). IBA solid water slabs type RW3 were used. The initial experimental setup is shown in Figure 78, with the Octa set on the treatment couch.

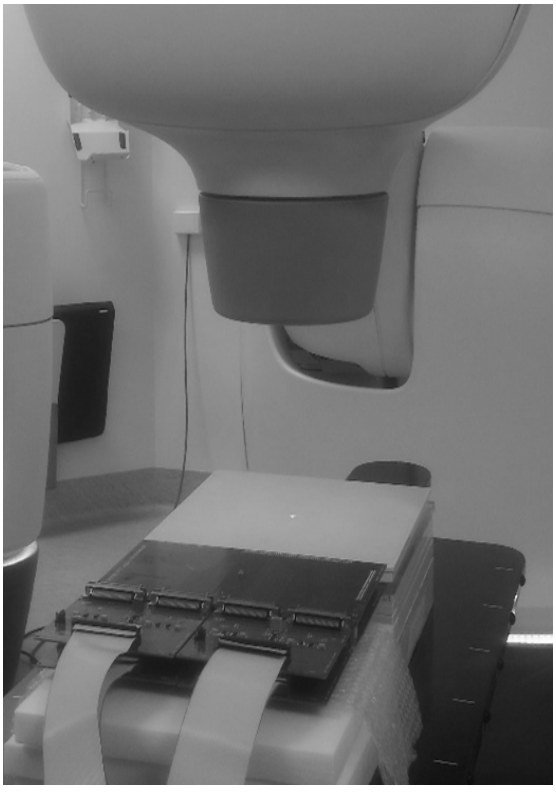

Figure 78. Experimental setup at the SCGH. The Octa detector was set on the treatment couch on top of 10 cm solid water for backscattering purposes. Solid water slabs were then added on top of the detector to reach the water equivalent depth required for each measurement.

Prior to the measurements, the Octa was aligned with respect to the treatment machine central axis (CAX) by maximizing the response of its central SV using the smallest available field size (5 mm diameter). Once aligned, for any given field size, OARs (in-line, cross-line and 2 diagonals) were measured simultaneously. The readings of the Octa at each field size were taken as the reading of each channel averaged over 3 repetitions of the same measure followed by normalisation of the response of each channel to the median response of the SVs within 0.5 mm of the CAX. For each profile, estimates were made of the full width at half-maximum (FWHM) and the penumbra width (taken as the distance between the 80% and the 20% isodose levels).

Measurements by the Octa were compared with those made using a PTW SRS diode 60018 mounted parallel to the axis in an IBA 3D water-phantom. The diode was oriented vertically, measuring at the effective point of measurement of 1.3 mm from top surface. Its readings were corrected using the correction factors by Francescon et al. [147].

9.3 Results and discussion

9.3.1 Radiation damage and electrical characterization

The simulated space-charge distribution (Figure 79) for one of the Octa n^+ electrodes (SV), along with its p^+ stop, shows that the depleted region is stretched outside the limits of the junction area due to the presence of charges in the silicon oxide layer (dark brown in the picture), however do not spread inside of the p^+ stop area .

The depleted region depth for the Octa epitaxial under zero bias was estimated to be approximately between 1 μm and 2 μm, which is consistent with those reported for dosimeters based on p-n junctions operated without any external bias [117] along with values simulated for a similar epitaxial device presented by Aldosari et al, 2013 [202].

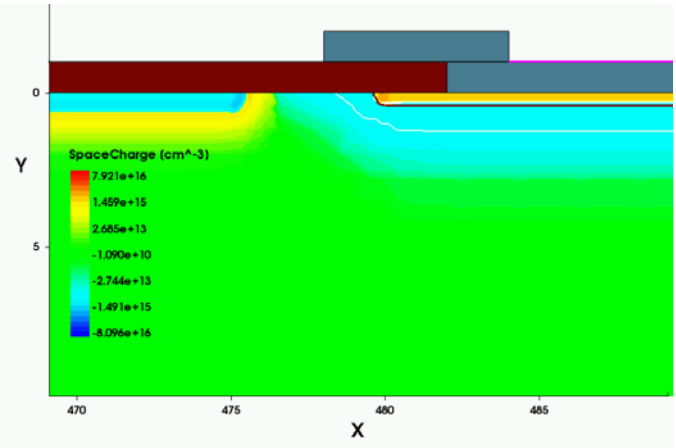

Figure 79. Simulated representation of the space-charge distribution for an epitaxial Octa. The depletion region (white line) is stretched outside the limits of the n^+-p junction (brown line) due to the presence of charges in the SiO_2 layer (brown area). Grey areas represent the aluminum contact of the n^+ electrode (SV). The p^+ stop area is visible on the left. Distances are in microns.

The leakage current I_{leak} is related to the applied voltage V across the device through [203]:

$$I_{leak} \propto W \propto \sqrt{V} \quad \text{for} \quad V \leq V_{dep} \tag{9.10}$$

with W the thickness of the depleted region.

The fact that the depletion is not only under the SVs but is spread laterally (because of their small size) explains the deviation of the experimental measurements from the ideal behaviour.

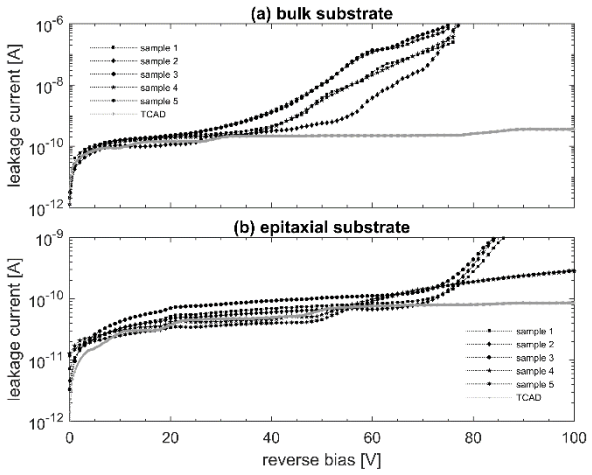

Figure 80. Family of experimental I-V characteristics from a few sample diodes (SVs) of the (a) bulk and (b) epitaxial Octa, along with the simulated characteristic.

The leakage current is also proportional to [203]:

$$I_{leak} \propto \frac{W}{\tau_g} \tag{9.11}$$

with τ_g the generation lifetime, i.e. the time it takes on average to generate an electron-hole pair, a parameter which is inversely proportional to the impurity density and the capture cross-section for electrons and holes but is in general not equal to the recombination lifetime [127].

Therefore, variations in the values of the I-V characteristics among diodes (SVs) on the same device are, in part, explained by their specific position within the silicon wafer and heterogeneous distribution of defects and doping concentration.

The variation of I_{leak} as a function of accumulated dose, which would reflect the increasing concentration of radiation-induced defects in the silicon and Si- SiO_2 interfaces, has previously been characterized for similar bulk and epitaxial substrates elsewhere [178], [202].

When considering the I-V characterization of the TCAD model, an area factor was introduced to normalize the I_{leak} so that the model had the same volume of the experimental device.

Simulated I-V characteristics of a single SV, in a device modelled with 5 SVs, were found to follow those of an ideal junction and fit within the range of the experimental measurements, for both the bulk and epitaxial Octa (Figure 80).

The capacitance C of the junction is given by [133]:

$$C = \frac{\varepsilon_0 \varepsilon_{Si}}{W} = \sqrt{\frac{q\varepsilon_0 \varepsilon_{Si} N_{eff}}{2(V_{bl} - V)}} \tag{9.12}$$

with W the width of the depleted region, ε_0 is the permittivity of free space, ε_{Si} is the dielectric constant of silicon, V_{bl} is the junction built-in potential, V is the applied reverse bias, N_{eff} the doping concentration. By increasing the applied bias across the device, the capacitance C decreases as [203]:

$$C \propto \frac{1}{\sqrt{V}} \tag{9.13}$$

up to when full depletion is reached, which was not reached in our study due to the low resistivity values of the considered silicon. V_{depl} is the applied reverse bias, at which the entire detector volume is depleted of free charge carriers. At that point, applying any higher voltages would not change the depletion depth, hence the measured capacitance.

For small SVs, though, lateral depletion is very pronounced, and capacitance decreases even after full depletion.

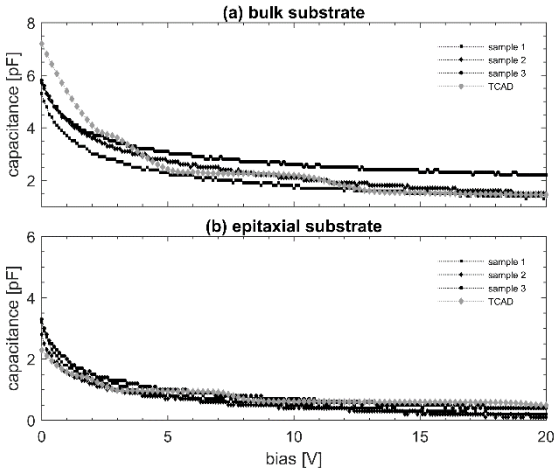

Figure 81. Family of experimental C-V characteristics from a few sample diodes (SVs) of the (a) bulk and (b) epitaxial Octa, along with the simulated characteristic.

When considering the C-V characterization of the TCAD model, an area factor was introduced to normalize the capacitance so that the model had the same volume of the experimental device.

Simulated C-V characteristics of a single SV, in a device modelled with 5 SVs, were found to fit within the range of the experimental measurements, for both the bulk and epitaxial Octa (Figure 81).

The device packaging, though, which is not accounted for in the simulations, results in an increase in the real device total capacitance. This discrepancy value was subtracted from the experimental characteristics for the entire range of bias measured.

The simulated devices were found to reproduce experimental I-V and C-V characterizations when modelled with a resistivity of 4 Ωcm and 40 Ωcm for the bulk and epitaxial Octa respectively.

9.3.2 Linearity

In terms of response linearity with delivered dose, the bulk Octa results are, as expected, consistent with those of similar bulk devices previously characterized, such as the MP512 [191] and the Duo [178]. Figure 82 shows that the epitaxial Octa demonstrated an equally good linear response. In both figures, error bars, calculated as 2 standard deviations, did not exceed the symbol size.

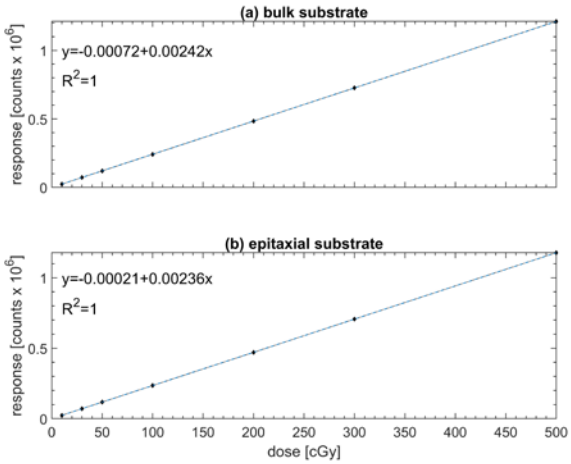

Figure 82. Linearity response of (a) bulk and (b) epitaxial Octa. The regression coefficient R2 is 1 in both cases.

9.3.3 Uniformity

When irradiated in a flat field, the epitaxial Octa demonstrated a more uniform response than its bulk counterpart (Figure 83, Figure 84)[28].

Since the same data acquisition system was used for both detectors, this result is mainly explained by the much better uniformity and quality of the epitaxial silicon wafer in terms of resistivity and recombination properties.

For the epitaxial device, the diodes along the diagonal arrays were found to be slightly more sensitive than those along the vertical and horizontal arrays (Figure 83).

This over-response, due to the SVs larger collection area allowed by their greater pitch, is addressed by applying the equalization factors.

Based on previous radiation damage studies [178], it is estimated that the sensitivity of the bulk Octa has been reduced by approximately 55% as a consequence of its pre-irradiation. Conversely, the sensitivity of the epitaxial Octa, which was not pre-irradiated, could be expected to increase, albeit slightly, with future exposure to irradiation as a consequence of continuous clinical testing [202].

[28] Flat field irradiation was repeated 3 times. In the Appendix of the present Chapter, Table 20 shows the response of the 129 diodes along the vertical array of the Octa epitaxial, for each measurement; mean value and 2 standard deviations of the sample. Reported results are representative of all diodes on the Octa epitaxial; diodes on the Octa bulk had standard deviations of the same magnitude. In Figure 83, error bars, calculated as 2 standard deviations, did not exceed the symbol size.

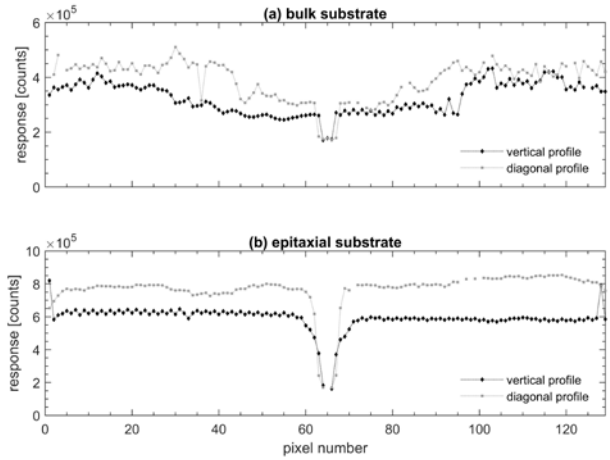

Figure 83. Response to a flat field, with no equalization applied, of the diodes along the vertical (300 µm pitch) and diagonal (430 µm pitch) arrays of the (a) bulk and (b) epitaxial Octa.

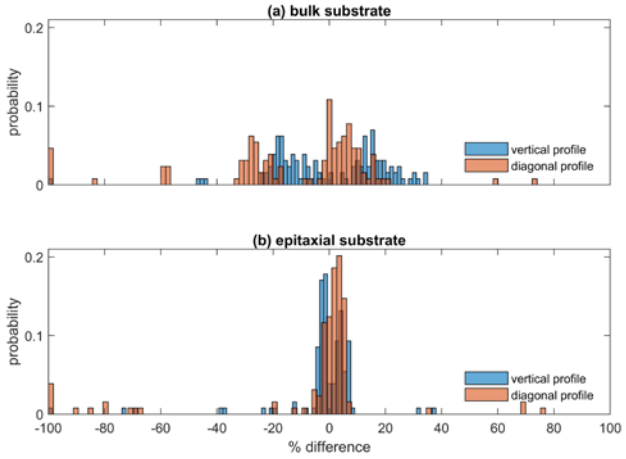

Figure 84. Statistical distribution of the SVs response to a flat field, with no equalization applied, for the (a) bulk and (b) epitaxial Octa.

9.3.4 Charge collection efficiency and spatial resolution

According to TCAD simulations performed using the Heavy Ion Model (Figure 85), for a bulk Octa CCE becomes negligible ($< 0.5\%$) approximately at 60 µm from the SV centre.

For an epitaxial Octa, CCE was 2.75% at a distance of 300 µm from the SV centre, for the 300 µm pitch, and $< 1\%$ at a distance of 430 µm for the 430 µm pitch.

The difference in CCE between the Octas is mainly explained by the τ_e of the epitaxial substrate being greater than that for the pre-irradiated bulk substrate, allowing the p-n junction to collect charge over a greater lateral distance with respect to the SV centre.

By considering the distance at which the CCE is 50%, the 430 µm-epitaxial configuration could be used to estimate that the L_e for this substrate is approximately 90 µm. It is proposed that for the pre-irradiated bulk device L_e is between 20 µm and 40 µm.

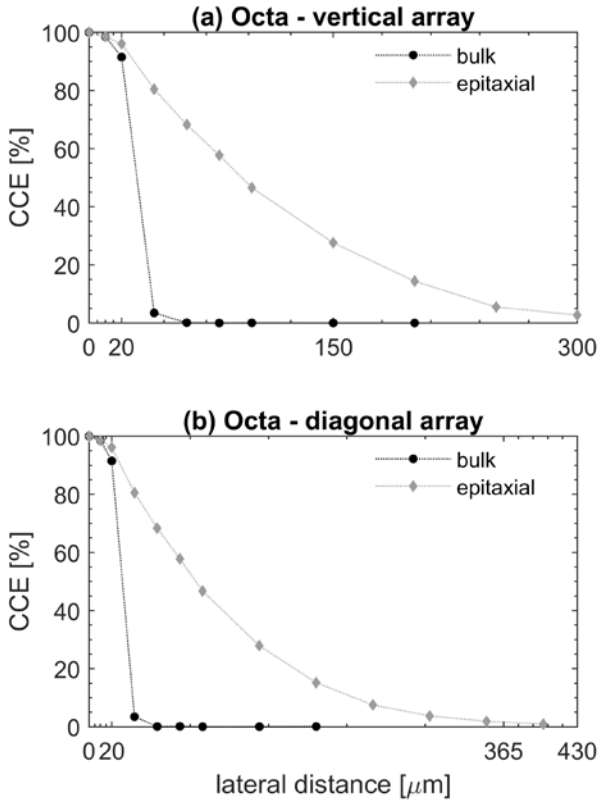

Figure 85. Simulated CCE as a function of the lateral distance from the SV center, for a SV (a) in a 300 µm pitch configuration and (b) in a 430 µm pitch configuration, for the pre-irradiated bulk Octa and for the epitaxial Octa.

According to TCAD simulations performed using the *Gamma Radiation Model*, CCE dependence on the SVs' pitch is negligible for the pre-irradiated bulk Octa (Figure 86), whereas it is appreciable for the epitaxial Octa (Figure 87). In this case, the simulated CCE was 50.24% for a 200 µm pitch, 68.19% for a 300 µm and 83.34% for a 430 µm pitch.

The SVs of the epitaxial Octa collect more charge when in a 430 µm pitch configuration as compared to a 300 µm pitch configuration. Remarkably, TCAD simulations show 18% increase (Figure 87) which is in close agreement with the findings of experimental measurements which showed on average 24% increase (Figure 83).

A CCE different from 100%, though, does not mean that the device spatial resolution is affected. Its deterioration would depend on a non-linear charge sharing between neighbouring SVs due to the presence of dose gradients. Experimental characterizations of small beam profiles on MV linear medical accelerators performed by the epitaxial Octa indicates that this is not the case. Both a 300 µm pitch configuration and a 430 µm pitch configuration were shown to be suitable for high spatial resolution dose mapping [15], [17].

The CCE was also found to depend on the epitaxial layer resistivity (Figure 88), with a saturating behaviour below 0.5 Ωcm, in the case of the 300 µm pitch configuration. Decreasing the silicon resistivity would improve the SVs CCE, at the cost of decreased device sensitivity.

Defining a minimum value of acceptable resistivity for the silicon on which the Octa is based, however, would require a complex theoretical and experimental evaluation on the impact this would have on the whole system composed of radiation detector proper and read-out electronics. This assessment was beyond the scope of this work.

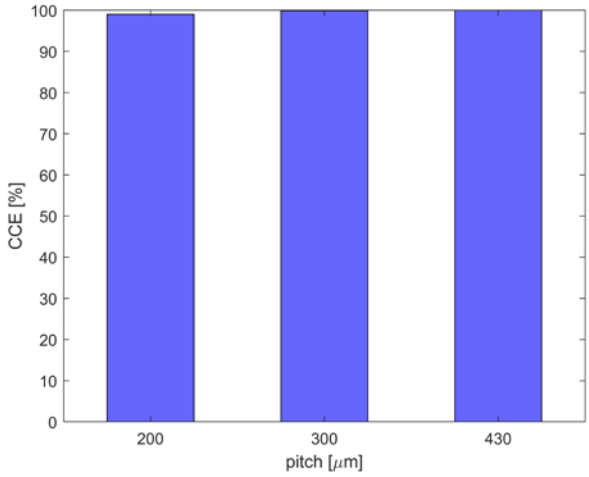

Figure 86. Simulated CCE as a function of the SVs' pitch for the pre-irradiated bulk Octa, in the case of a resistivity of 4 Ωcm.

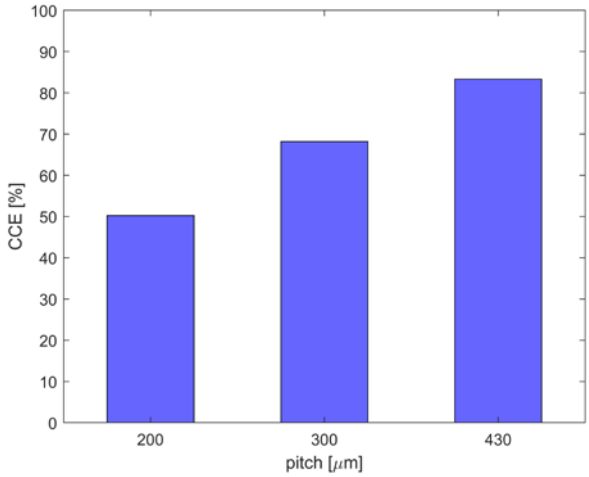

Figure 87. Simulated CCE as a function of the SVs' pitch for the epitaxial Octa, in the case of an epitaxial layer resistivity of 40 Ωcm.

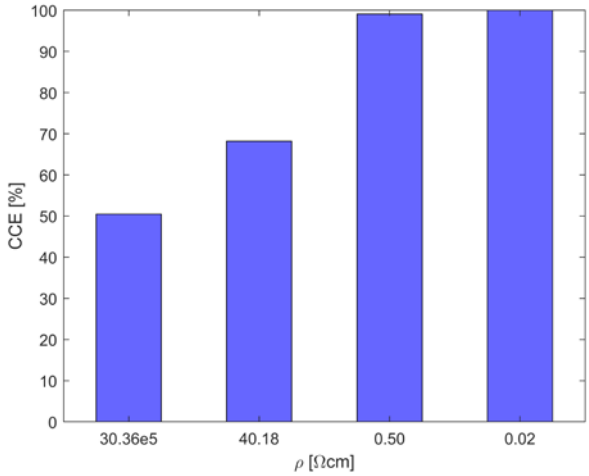

Figure 88. Simulated CCE as a function of the epitaxial layer doping for the 300 µm pitch configuration.

9.3.5 Clinical application

A reliable sub-millimetre spatial-resolution of the 2D dose map in terms of FWHM and penumbra width was demonstrated for both Octas, with results consistent with respect to SRS diode measurements (Table 19).

The in-line profiles for a 3 cm side circular field measured by the bulk and epitaxial Octas are shown in Figure 89 a) and b) respectively. The full study of the epitaxial Octa as a QA tool for the CyberKnife® linear accelerator is reported elsewhere [17].

Typically, for any given dose measurement, equalization factors from a flat-field acquisition using the same beam quality and the same linear accelerator would have to be applied.

When using the Octa for CyberKnife® QA applications, though, this would be impossible, as the linac is operated only in flattening filter free (FFF) modality and cannot produce flat fields. In this case, a different linac with flattened beam (FB) modality would need to be used for the flat-field acquisition followed by equalization. Critically, the two linacs would be operating at different instantaneous dose rates.

Other than the obvious technical convenience, the reason for using the same linac was to avoid issues arising from the τ_e dependence on instantaneous the dose rate [124], [137], which affects the sensitivity of the silicon device. But τ_e is mainly a function of the defects in the substrate, which have been reported in the literature to be arranged in concentric rings across a bulk silicon wafer [133], as a consequence of the manufacturing process. A variation in the local defects concentration results in a sensitivity variation, as a function of the instantaneous dose rate, across the wafer. In other words, recombination properties may be affected by non-uniformities (Figure 83) in a bulk wafer when using different dose rates. In the case presented,

the device irradiation was performed with different dose rates for the flat field and for the field to be equalized, and a ring-shaped non-uniformity resulted in the equalized dose profiles for the bulk device (Figure 89). The over-response in a ring of diameter approximately 2 cm is apparent in the figure and relates the non-uniformities in (Figure 83).

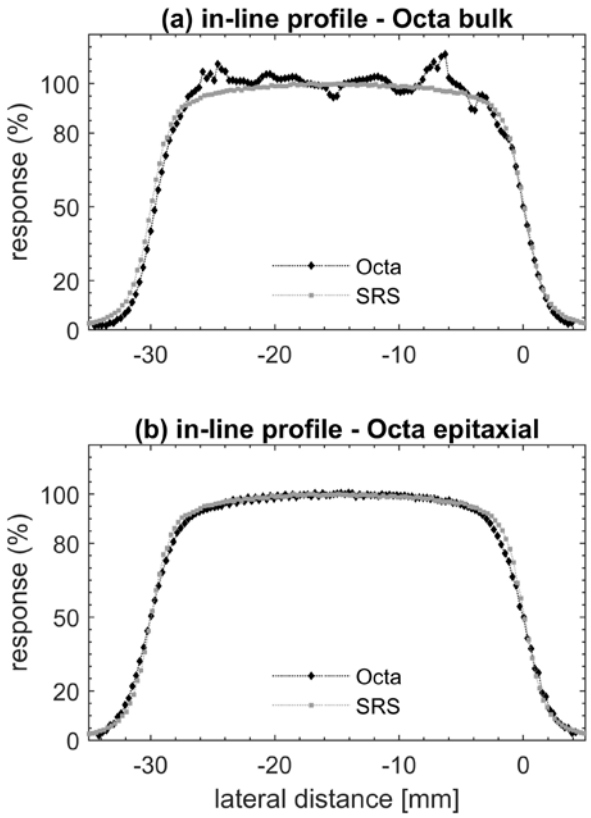

Figure 89. In-line profiles measured by the Octa (a) bulk and (b) an epitaxial substrate. Profiles are for a radiation field collimated with the variable aperture Iris collimator mounted on a CyberKnife®® M6. A 6 MV FFF beam quality was used. Data is benchmarked with measurements by a SRS diode and aligned to the 50% response.

Table 19. FWHM and penumbra width as measured by the Octas. Differences are with respect to measurements performed by an SRS diode in the same experimental settings.

	FWHM [cm]	Penumbra [cm]	ΔFWHM [%]	ΔPenumbra [cm]
Octa (bulk)	2.96	0.30	-0.7	0.04
Octa (epitaxial)	3.00	0.33	0.7	0.07
SRS diode	2.98	0.26	-	-

On the other hand, for the epitaxial Octa, a much more homogenous distribution of concentration across the epitaxial layer and fewer intrinsic defects, owing to an improved manufacturing process, grants a much more uniform response (Figure 83). Therefore, the equalized inline dose profile in Figure 89 measured by the epitaxial Octa is as smooth as that measured by the SRS diode.

9.4 Conclusions

The Octa, a 2D monolithic silicon array detector dedicated to small-field dosimetry, was produced in two samples, on a bulk and on an epitaxial substrate. Their performance was investigated by experimental measurements and TCAD based numerical simulations in terms of response linearity with dose, response uniformity and charge-collection efficiency (CCE). Results were compared and discussed with respect to small-field dosimetry for medical quality assurance (QA) applications.

TCAD simulations of a minimum ionizing particle (MIP) through the device using the Heavy Ion Model were demonstrated to be a good tool for characterization of the charge collection efficiency (CCE) of a monolithic array detector. The simulated CCE distribution could be used to optimize the pitch and the SVs' layout across the silicon wafer based on the estimated minority carrier diffusion length.

We are not aware of any other study in the literature of the CCE characterization for a monolithic array detector using the Gamma Radiation Model. This was shown to be an invaluable tool for investigating how the detector performance is affected by parameters such the SVs pitch, the silicon resistivity and traps concentration. This methodology provides a means of optimising future devices prior to fabrication.

For a bulk pre-irradiated device, with a sufficiently small L_e, the SVs pitch does not affect their CCE, owing to the charge collection being confined to the geometrical size of the SVs themselves.

For an epitaxial device, if $L_e \geq W, r$, radiation hardness is preserved, and the device does not require pre-irradiation. However, with a comparably higher L_e, the SVs pitch affects their CCE. The charge collection is less confined to the SV and there is a significant lateral diffusion of charge. This could be in principle be addressed by decreasing the silicon resistivity, at the cost of a reduced sensitivity. Nonetheless, even in the presence of a sub-optimal CCE, the detector nominal spatial resolution is expected to be preserved, as supported by previous experimental clinical measurements of the 2D dose map.

Experimentally, both Octas showed good linearity with dose and a non-uniform response across the whole arrays that could easily be corrected for by applying an equalization procedure. Unfortunately, in the case of modern radiotherapy applications with flattening filter free (FFF) beam irradiations, this was demonstrated to be a workable solution only in the case of a device manufactured with a uniform profile in terms of resistivity and recombination properties, i.e. for the epitaxial Octa.

9.5 Appendix

The Octa epitaxial was irradiated 3 times at 10 cm depth 90 cm SSD in a water equivalent phantom with a 20 cm side square flat field with a 6 MV FB delivered by a medical linear accelerator; Table 20 shows the response to the flat field of the 129 pixels (diodes) along the vertical array, with no equalization applied, the mean over the 3 measurements and 2 standard deviations of the sample. These results are representative of all 512 diodes on the Octa epitaxial; diodes on the Octa bulk had standard deviations of the same magnitude.

Table 20. Response [unit: counts] of the 129 pixels (diodes) along the vertical array of the Octa epitaxial; 3 repetitions of the same measurement, mean over the 3 measurements and 2 standard deviations of the sample.

Pixel number	Measurement 1	Measurement 2	Measurement 3	Mean	2 Standard deviations
1	8.2E+05	8.2E+05	8.2E+05	8.2E+05	5.4E+03
2	5.8E+05	5.8E+05	5.8E+05	5.8E+05	4.3E+03
3	6.1E+05	6.1E+05	6.1E+05	6.1E+05	2.7E+03
4	6.2E+05	6.2E+05	6.2E+05	6.2E+05	1.4E+02
5	6.4E+05	6.4E+05	6.4E+05	6.4E+05	1.2E+03
6	6.2E+05	6.2E+05	6.2E+05	6.2E+05	3.3E+02
7	6.4E+05	6.4E+05	6.5E+05	6.4E+05	6.7E+03
8	6.1E+05	6.1E+05	6.1E+05	6.1E+05	1.9E+02
9	6.4E+05	6.4E+05	6.4E+05	6.4E+05	2.2E+03
10	6.2E+05	6.2E+05	6.2E+05	6.2E+05	8.2E+02
11	6.4E+05	6.4E+05	6.4E+05	6.4E+05	6.4E+03
12	6.2E+05	6.2E+05	6.2E+05	6.2E+05	5.6E+02
13	6.3E+05	6.3E+05	6.4E+05	6.4E+05	6.1E+03
14	6.2E+05	6.2E+05	6.2E+05	6.2E+05	4.8E+02
15	6.4E+05	6.4E+05	6.4E+05	6.4E+05	4.2E+03
16	6.2E+05	6.2E+05	6.2E+05	6.2E+05	2.3E+02
17	6.4E+05	6.4E+05	6.4E+05	6.4E+05	3.1E+03
18	6.2E+05	6.2E+05	6.2E+05	6.2E+05	3.5E+02
19	6.4E+05	6.4E+05	6.5E+05	6.4E+05	5.5E+03
20	6.2E+05	6.2E+05	6.2E+05	6.2E+05	6.1E+00
21	6.4E+05	6.4E+05	6.5E+05	6.4E+05	5.8E+03
22	6.2E+05	6.2E+05	6.2E+05	6.2E+05	3.4E+02

23	6.4E+05	6.4E+05	6.4E+05	6.4E+05	2.9E+03
24	6.2E+05	6.2E+05	6.2E+05	6.2E+05	3.5E+02
25	6.3E+05	6.4E+05	6.3E+05	6.3E+05	6.8E+03
26	6.2E+05	6.2E+05	6.2E+05	6.2E+05	2.9E+02
27	6.3E+05	6.4E+05	6.3E+05	6.3E+05	3.5E+03
28	6.2E+05	6.2E+05	6.2E+05	6.2E+05	4.7E+02
29	6.4E+05	6.4E+05	6.4E+05	6.4E+05	2.3E+03
30	6.1E+05	6.1E+05	6.1E+05	6.1E+05	1.8E+02
31	6.5E+05	6.5E+05	6.5E+05	6.5E+05	1.8E+03
32	6.2E+05	6.2E+05	6.2E+05	6.2E+05	3.2E+02
33	5.9E+05	5.9E+05	5.9E+05	5.9E+05	4.0E+03
34	6.2E+05	6.2E+05	6.2E+05	6.2E+05	1.2E+02
35	6.3E+05	6.4E+05	6.4E+05	6.4E+05	5.4E+03
36	6.2E+05	6.2E+05	6.2E+05	6.2E+05	1.3E+02
37	6.3E+05	6.4E+05	6.4E+05	6.3E+05	5.0E+03
38	6.2E+05	6.2E+05	6.2E+05	6.2E+05	6.0E+02
39	6.3E+05	6.3E+05	6.3E+05	6.3E+05	2.8E+03
40	6.2E+05	6.1E+05	6.2E+05	6.2E+05	3.8E+02
41	6.3E+05	6.3E+05	6.4E+05	6.3E+05	6.9E+03
42	6.2E+05	6.2E+05	6.2E+05	6.2E+05	3.8E+02
43	6.3E+05	6.3E+05	6.3E+05	6.3E+05	2.7E+03
44	6.2E+05	6.2E+05	6.2E+05	6.2E+05	7.8E+01
45	6.3E+05	6.3E+05	6.3E+05	6.3E+05	5.9E+02
46	6.1E+05	6.1E+05	6.1E+05	6.1E+05	2.6E+02
47	6.2E+05	6.3E+05	6.3E+05	6.3E+05	7.9E+03
48	6.1E+05	6.1E+05	6.1E+05	6.1E+05	5.1E+02
49	6.3E+05	6.3E+05	6.3E+05	6.3E+05	4.7E+03
50	6.1E+05	6.1E+05	6.1E+05	6.1E+05	3.0E+02
51	6.2E+05	6.2E+05	6.2E+05	6.2E+05	2.7E+03
52	6.1E+05	6.1E+05	6.1E+05	6.1E+05	4.2E+02
53	6.2E+05	6.2E+05	6.2E+05	6.2E+05	2.7E+03
54	6.1E+05	6.1E+05	6.1E+05	6.1E+05	4.3E+02

55	6.2E+05	6.2E+05	6.3E+05	6.2E+05	3.3E+03
56	6.0E+05	6.0E+05	6.0E+05	6.0E+05	9.5E+01
57	6.1E+05	6.2E+05	6.2E+05	6.2E+05	5.6E+03
58	6.0E+05	6.0E+05	6.0E+05	6.0E+05	1.9E+02
59	5.9E+05	6.0E+05	6.0E+05	5.9E+05	5.0E+03
60	5.5E+05	5.5E+05	5.5E+05	5.5E+05	2.2E+02
61	5.2E+05	5.2E+05	5.2E+05	5.2E+05	4.0E+03
62	4.7E+05	4.7E+05	4.7E+05	4.7E+05	2.2E+02
63	3.8E+05	3.8E+05	3.8E+05	3.8E+05	3.9E+02
64	1.8E+05	1.8E+05	1.8E+05	1.8E+05	3.8E+03
65	1.7E+05	1.7E+05	1.7E+05	1.7E+05	1.8E+03
66	1.6E+05	1.6E+05	1.6E+05	1.6E+05	3.0E+02
67	3.7E+05	3.7E+05	3.7E+05	3.7E+05	2.1E+02
68	4.6E+05	4.6E+05	4.6E+05	4.6E+05	4.5E+02
69	4.8E+05	4.8E+05	4.8E+05	4.8E+05	4.9E+02
70	5.2E+05	5.2E+05	5.2E+05	5.2E+05	6.8E+02
71	5.7E+05	5.7E+05	5.7E+05	5.7E+05	1.4E+02
72	5.8E+05	5.8E+05	5.8E+05	5.8E+05	3.2E+02
73	5.9E+05	5.9E+05	5.9E+05	5.9E+05	2.5E+02
74	5.8E+05	5.8E+05	5.8E+05	5.8E+05	7.5E+02
75	6.0E+05	6.0E+05	6.0E+05	6.0E+05	2.4E+02
76	5.9E+05	5.9E+05	5.9E+05	5.9E+05	4.4E+02
77	6.0E+05	6.0E+05	6.0E+05	6.0E+05	1.7E+02
78	5.8E+05	5.8E+05	5.8E+05	5.8E+05	4.3E+02
79	5.9E+05	5.9E+05	5.9E+05	5.9E+05	7.3E+01
80	5.8E+05	5.8E+05	5.8E+05	5.8E+05	7.2E+01
81	5.9E+05	5.9E+05	5.9E+05	5.9E+05	4.7E+02
82	5.8E+05	5.8E+05	5.8E+05	5.8E+05	3.6E+02
83	5.9E+05	5.9E+05	5.9E+05	5.9E+05	4.1E+02
84	5.9E+05	5.9E+05	5.9E+05	5.9E+05	4.0E+02
85	5.9E+05	5.9E+05	5.9E+05	5.9E+05	4.9E+02
86	5.8E+05	5.8E+05	5.8E+05	5.8E+05	1.1E+02

87	5.9E+05	5.9E+05	5.9E+05	5.9E+05	6.3E+02
88	5.8E+05	5.8E+05	5.8E+05	5.8E+05	3.5E+02
89	5.9E+05	5.9E+05	5.9E+05	5.9E+05	7.5E+02
90	5.8E+05	5.9E+05	5.9E+05	5.9E+05	4.5E+02
91	5.9E+05	5.9E+05	5.9E+05	5.9E+05	2.4E+02
92	5.8E+05	5.8E+05	5.8E+05	5.8E+05	3.0E+02
93	5.9E+05	5.9E+05	5.9E+05	5.9E+05	6.7E+02
94	5.8E+05	5.8E+05	5.8E+05	5.8E+05	3.5E+02
95	5.9E+05	5.9E+05	5.9E+05	5.9E+05	9.4E+01
96	5.8E+05	5.8E+05	5.8E+05	5.8E+05	3.6E+02
97	5.9E+05	5.9E+05	5.9E+05	5.9E+05	3.5E+02
98	5.8E+05	5.8E+05	5.8E+05	5.8E+05	6.0E+02
99	5.9E+05	5.9E+05	5.9E+05	5.9E+05	5.6E+01
100	5.8E+05	5.8E+05	5.8E+05	5.8E+05	4.4E+02
101	5.8E+05	5.8E+05	5.8E+05	5.8E+05	3.9E+02
102	5.7E+05	5.7E+05	5.7E+05	5.7E+05	2.7E+02
103	5.8E+05	5.8E+05	5.8E+05	5.8E+05	4.7E+01
104	5.7E+05	5.7E+05	5.7E+05	5.7E+05	5.2E+02
105	5.8E+05	5.8E+05	5.8E+05	5.8E+05	2.9E+02
106	5.8E+05	5.8E+05	5.8E+05	5.8E+05	4.1E+02
107	5.9E+05	5.9E+05	5.9E+05	5.9E+05	2.3E+02
108	5.9E+05	5.9E+05	5.9E+05	5.9E+05	3.5E+02
109	5.9E+05	5.9E+05	5.9E+05	5.9E+05	3.8E+02
110	6.0E+05	6.0E+05	6.0E+05	6.0E+05	2.9E+02
111	5.9E+05	5.9E+05	5.9E+05	5.9E+05	4.2E+02
112	5.9E+05	5.9E+05	5.9E+05	5.9E+05	2.7E+02
113	5.9E+05	5.9E+05	5.9E+05	5.9E+05	2.3E+02
114	5.8E+05	5.8E+05	5.8E+05	5.8E+05	1.5E+02
115	5.9E+05	5.9E+05	5.9E+05	5.9E+05	3.4E+02
116	5.7E+05	5.8E+05	5.8E+05	5.8E+05	2.3E+02
117	5.8E+05	5.8E+05	5.8E+05	5.8E+05	3.6E+02
118	5.7E+05	5.7E+05	5.7E+05	5.7E+05	5.6E+02

119	5.9E+05	5.9E+05	5.9E+05	5.9E+05	3.0E+02
120	5.8E+05	5.8E+05	5.8E+05	5.8E+05	1.7E+02
121	5.8E+05	5.8E+05	5.8E+05	5.8E+05	3.6E+02
122	5.7E+05	5.7E+05	5.7E+05	5.7E+05	2.5E+02
123	5.8E+05	5.8E+05	5.8E+05	5.8E+05	1.7E+02
124	5.8E+05	5.8E+05	5.8E+05	5.8E+05	3.0E+02
125	5.9E+05	5.9E+05	5.9E+05	5.9E+05	9.0E+02
126	5.8E+05	5.8E+05	5.8E+05	5.8E+05	3.3E+02
127	5.9E+05	5.9E+05	5.9E+05	5.9E+05	4.6E+02
128	7.9E+05	7.9E+05	7.9E+05	7.9E+05	1.0E+03
129	5.8E+05	5.9E+05	5.9E+05	5.9E+05	2.1E+02

10 On the instantaneous dose rate and angular dependence of monolithic silicon array detectors

This chapter is based on material in **G. Biasi** *et al*, (2019) On the instantaneous dose rate and angular dependence of monolithic silicon array detectors, *IEEE Transaction on Nuclear Science*, 66 (1), 519-527 [19][29]. Measurements and numerical investigations discussed hereafter were performed during 2016, 2017 and first half of 2018.

10.1 Introduction

Small radiation fields ($\leq$ 10 mm across[30]) characterized by steep dose gradients are used in dynamic modulated arc x-ray radiotherapy to deliver highly conformal and precisely modulated dose distributions [2], [231].

The clinical quality of a treatment depends on the correct use of the treatment planning system, whose accuracy, in turn, relies on dosimetric data measured at a treatment unit, such as a medical linear accelerator (linac) [2], [210], [232]. These typically include output factors (OFs), percentage depth doses (PDDs) and off-axis ratios (OARs) [2]. Uncertainties in data collected during machine-specific quality assurance (QA) hinder error-free dose calculations by the treatment planning system [2], [24], [54].

Correct patient-specific QA has a pivotal role in ensuring that the delivered dose distributions match those calculated by the treatment planning system [231]. Both point-dose measurements by point detectors and dose distribution measurements by 2D detectors are generally considered [12]. In the case of 2D measurements in small radiation fields, the efficacy of patient-specific QA is determined by the spatial resolution of the detector [233].

Measurements in small radiation fields present challenges which have been discussed in the literature [27], [37], [48] and addressed by recent Codes of Practice [1], [2]. These are related to the radiation beam (partial occlusion of the primary source, loss of charged particle equilibrium on the beam central axis), and related to the detector in use, specifically to its dimensions with respect to the radiation field and the perturbation effects it introduces on the photon and electron spectra if non-water equivalent.

[29] References are combined in a single bibliography at the end of the present dissertation.
[30] Fields $\leq$ 10 mm across are also referred to as very small fields [235].

In contemporary radiotherapy, the use of flattening filter free (FFF) photon beams, as opposed to once-widespread flattened beams, is increasingly common. Owing to their higher dose gradients, not just the penumbral but also in the beam central axis region, higher instantaneous dose rate and absence of filtration of low energy photons, their use is likely to compound the challenges specific to the dosimetry of small radiation fields [22], [23].

Against this background, the IAEA-AAPM code of practice recommends the use of solid-state detectors [1]. These, easily fabricated with sensitive volumes (SVs) significantly smaller than the radiation fields in which they will operate, offer advantages such as a stable and nearly energy-independent response in megavoltage photon beams, good linearity with accumulated dose, high specific sensitivity, and real-time read-out [1], [2]. Solid-state detectors can also been arranged in arrays to provide a 2D measurement of the dose distributions [117], [171], [172]. The pitch of their SVs would have to be sub-millimetre to resolve the steep dose gradients typical of small radiation fields.

Unfortunately, to correctly relate their readings to dose, solid-state detectors require correction factors accounting for their response being angular-dependent, instantaneous dose rate dependent and field-size dependent [1], [2], [26], [30], [124].

The 'Octa' is a novel 2nd generation 2D monolithic silicon-diode array detector offering a sub-millimetre real-time characterization of the dose map with negligible field-size dependence [15], [17].

The Octa was produced in two versions, based on a bulk and on an epitaxial substrate respectively. In a previous work [18], their performance was investigated by experimental and numerical characterization in terms of response linearity with accumulated dose, response uniformity across the arrays and charge-collection efficiency of the SVs. It was demonstrated that, for a bulk pre-irradiated device with a sufficiently small minority carrier diffusion length L_e, the pitch of the SVs did not affect their charge-collection efficiency, owing to the process being confined to the geometrical size of the SVs themselves. For an epitaxial device, if $L_e \geq W$, W the thickness of the epitaxial layer, it was found that pre-irradiation was not required for response stabilisation. With the L_e relatively higher, though, the charge-collection efficiency of the SVs in the array detector was affected by their pitch. Even in the presence of a sub-optimal charge-collection efficiency, the detector nominal sub-millimetre resolution was preserved [15], [17].

In the same study [18] it was shown that both the Octas had good linearity with accumulated dose and a non-uniform response across the arrays that could be corrected for by applying an equalization procedure with a flat-field irradiation. For contemporary radiotherapy with FFF beams, this was demonstrated to be a workable solution only in the case of a device manufactured with a uniform profile in terms of resistivity and defects concentration.

The instantaneous dose rate dependence [124], [128], [129], [137] and the angular-dependent response [101] have been discussed extensively in the literature for single silicon diodes. To the best knowledge of the authors, in the case of monolithic silicon-diode array detectors, only limited experimental data have been published, mostly on detectors fabricated on bulk p-type silicon substrates [115], [116], [118], [132], [157], such as the MP512 and the Duo (CMRP, University of Wollongong, Australia). Their 512 diode-SVs were arranged on the wafer surface uniformly and with a 2 mm pitch for the MP512 and along 2 linear arrays with a 0.2 mm pitch for the Duo.

We report on the experimental characterization of the two versions of the Octa, assessing their potential for machine-specific QA and patient-specific QA applications. Their performance is compared and discussed in terms of their instantaneous dose rate and angular dependent response in the context of small radiation fields delivered with modulated arc radiotherapy techniques.

10.2 Materials and methods

10.2.1 The Octa

The Octa was manufactured onto a p-type silicon substrate. Its 512 diode-SVs are based on n^+ ion-implants of area 0.032 mm^2, arranged with a pitch of 300 μm along the vertical and horizontal arrays and 430 μm along the diagonals.

The Octa bulk is based on a Czochralski [180] silicon wafer substrate with resistivity of 10 Ωcm. It was pre-irradiated with a Co-60 gamma source to stabilize its sensitivity [99]. On the other hand, the Octa epitaxial [188] (resistivity of 100 Ωcm) was not pre-irradiated. Both devices have the same topology.

The Octa is operated in passive mode (no external bias applied) and the data acquisition system was described elsewhere [15], [190].

10.2.2 The instantaneous dose rate dependence

The instantaneous dose rate dependence, or dose per pulse dependence, of the Octa was investigated by irradiating the detector with a fixed number of monitor units (MU) and changing the source-to-surface distance (SSD) to change the dose per pulse at the detector location [116], [137].

The Octa bulk was irradiated by a 6 MV flattened beam delivered with a Varian Clinac® iX linac at the Illawarra Cancer Care Centre (Wollongong, Australia). The Octa epitaxial was irradiated by a 6 MV flattened beam delivered with a Varian Clinac® iX linac at the Illawarra Cancer Care Centre, and by 6 MV and 10 MV flattening filter free (FFF) beams delivered with a Varian TrueBeam™ STx linac at the Peter MacCallum Cancer Care Centre (Melbourne, Australia).

Linacs (Table 20) were calibrated to deliver 1 cGy/MU at d_{max} in water at 100 cm SSD.

Table 21. DPP dependence of the Octa: linac, beam quality, pulse frequency and average dose rate used.

linac	Beam quality	Pulse frequency [Hz]	Dose rate [MU/min]
Clinac iX®	6 MV	360	600
TrueBeam™ STx	6 MV FFF	360	1400
TrueBeam™ STx	10 MV FFF	180	1200

The DPP dependence was investigated in the range 0.021 mGy/pulse to 0.278 mGy/pulse in the case of the Octa bulk and 0.021 mGy/pulse to 0.977mGy/pulse in the case of the Octa epitaxial (Table 21). Measurements were performed with the detector placed in a solid water phantom at 1.5 cm depth in the case of the 6 MV flattened beam, and at 10 cm depth in the case of the 6 MV FFF and 10 MV FFF beams. A 10 cm side square field, jaws-defined, was used in all cases.

For each SV of the Octa, its sensitivity at any given SSD was defined as the ratio:

$$S_{SSD} = \frac{Q}{Q_{IC}} \tag{10.1}$$

with Q the charge collected by the SV and Q_{IC} the charge collected by the ionization chamber used as reference (Table 22), at the same SSD (i.e. for the same DPP). The DPP dependence of the SV was then defined as:

$$DPP_{dep} = \frac{S_{SSD}}{S_{ref}} \tag{10.2}$$

with S_{SSD} the sensitivity of the SV at any given DPP and S_{ref} that at the reference DPP (Table 21).

The ion-recombination correction factor, calculated with a two-voltage method, was applied to correct the readings of the Farmer ionization chamber in the case of 6 MV FFF and 10 MV FFF beams [208]. No correction factor was necessary for the readings of the Farmer ionization chamber in the case of a 6 MV flattened beam [22].

Table 22. DPP dependence of the Octa: range of DPP investigated and reference DPP for each beam quality investigated.

Range of instantaneous doses investigated [mGy/pulse]	Reference [mGy/pulse]	Beam quality
0.021 to 0.278	0.278	6 MV
0.041 to 0.416	0.416	6 MV FFF
0.079 to 0.977	0.797	10 MV FFF

Table 23. DPP dependence of the Octa: reference dosimeters used for each beam quality investigated.

Beam quality	Reference dosimeter	Vendor
6 MV FFF & 10 MV FFF	Farmer chamber IBA-FC-65P	IBA Dosimetry GmbH, (Germany)
6 MV	Farmer chamber NE2571A	IBA Dosimetry GmbH, (Germany)
6 MV	Markus N23343	PTW (Freiburg, Germany)

10.2.3 Angular dependence

The characterization of the angular-dependent response of the Octa was performed with the detector firmly lodged into a DosePoint (DosePoint GmBH, Germany) RT-smartIMRT RW3-based phantom (Figure 90). The central SV of the Octa was aligned to the machine isocentre.

To avoid irradiating through the treatment couch, the phantom was rotated by 90° with respect to the orientation in Figure 90. The linac gantry starting angle, corresponding to a radiation-beam incidence angle of 0°, was then set at −90°. The radiation-beam incidence angle was changed in the range 0° to 180° in 15° steps, irradiating the Octa at each step. Measurements were performed for square fields of size 10 mm, 20 mm and 100 mm side, jaws-defined, using 6 MV and 10 MV flattened beam by a Varian Clinac iX linac at the Illawarra Cancer Care Centre.

The angular-dependent relative response of the SVs of the Octa was defined as the ratio of their response at any given radiation-beam incidence angle i (S_i) to that at angle 0° (S_0), i.e. when the incidence radiation beam was perpendicular to the 2D plane of the detector:

$$S_{AD} = \frac{S_i}{S_0} \tag{10.3}$$

Only SVs along the vertical linear array, i.e. those for which the source-to-detector distance (SDD) was not a function of the radiation-beam incidence angle, were considered.

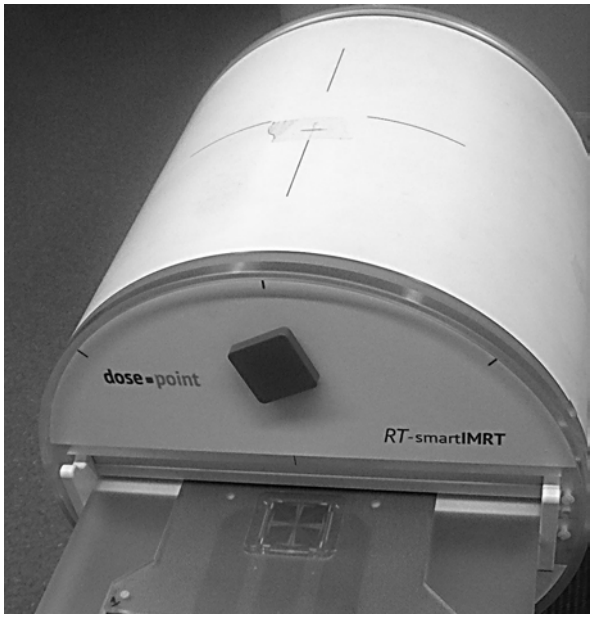

Figure 90. Snapshot of the Octa detector lodged into the RW3-based DosePoint RT-smartIMRT phantom.

10.3 Results and discussion

10.3.1 Theory

The dose D is delivered by medical linacs in pulses which last for 2 μs to 6 μs and have a repetition frequency in the range 180 Hz to 400 Hz [84], [129]. The dose in a single pulse determines the rate of charge generated in silicon G [124]:

$$G = gD \tag{10.4}$$

where $g = 4.2 \times 10^{13}\ e-h\ pairs/cGy/cm^3$ is the generation constant for silicon under ionizing radiation [125].

Silicon diode detectors are based on p-n junctions. The incident ionizing radiation generates electron–hole pairs, and the minority excess carriers (electrons on the p side and holes on the n side) are, when operating in passive mode, swept across the p-n junction by the built-in potential. This is of the order of $10^3\ V/cm$. However, only excess minority carriers

within one diffusion length (L_n for electrons on the p side, L_p for holes on the n side) reach the junction and are collected by the electrode [84], [124].

The sensitivity of a p-type diode, under the assumption of low-injection conditions, i.e. when the excess minority carrier concentration Δn is relatively small compared to the equilibrium majority carrier concentration p_0 ($\Delta n/p_0 \ll 1$), is then written as [124]:

$$S \propto L_n \equiv \sqrt{D_n \tau} \tag{10.5}$$

with D_n the diffusion length and $\tau = \tau_n$, the minority carrier lifetime. The latter, for a p-type diode, can be written as [117], [124]:

$$\tau_n = \frac{1}{\sigma_e v_{th} N_t} \tag{10.6}$$

with v_{th} the thermal velocity of electrons, σ_e the cross section of electron capture on the recombination level, N_t the concentration of recombination centres. This is explained by considering that excess minority carriers can recombine with majority carriers if captured by generation-recombination (G-R) centres [129]. These are either impurity atoms or crystal defects, the latter generated by thermal or mechanical stress during the fabrication process or as a consequence of irradiation by high-energy particles [124], [128]. As a result, a minority carrier lifetime will depend on the concentration N_t of the G-R centres, which can be considered as constant for successive beam pulses by a linac, and on their capture cross section σ_e for the minority carriers [129].

There may be also other processes, distinct from the G-R centres, which are involved in the excess minority carrier recombination [99], [128], [129]. For example, shallow traps close to either the conduction or the valence band can capture charge. The magnitude of their effect will depend on their lifetime [129].

At any rate, the fraction of excess minority carriers generated in a single pulse that recombine with majority carriers also depends on Δn itself, i.e. on the injection level [117], [129]. This is because while at low DPP the G-R centres are mostly empty, and a fraction of the excess minority carrier is captured and recombines, as the DPP increases the centres are filled. Eventually, as they approach saturation, the fraction of excess minority carriers recombining decreases and a larger fraction is available for collection by the electrode [124], [129].

Therefore, for small-deviations from a low-injection condition, as in the case of radiation delivered by a linac, the time-scale on which recombination happens can be re-written as [117], [124]:

$$\tau \approx \tau_n \left(1 + \frac{(\tau_p + \tau_n)}{\tau_n} \times \frac{\Delta n}{p_0}\right) \tag{10.7}$$

The detector sensitivity $S \propto \sqrt{D_n \tau}$ will therefore depend on the DPP as a result.

By considering the above relationship it is apparent that it is possible to reduce the DPP dependence of the diode sensitivity by decreasing the resistivity of the diode substrate (p_0 is inversely proportional to the resistivity [137]), or reducing the minority carrier lifetime (τ_n, in this case) [117], [128].

10.3.2 Instantaneous dose rate dependence

The DPP_{dep} of SVs with a pitch of 300 µm and 430 µm is shown in Figure 91 for the Octa bulk irradiated by a 6 MV flattened beam, and in Figure 92, Figure 93 and Figure 94 for the Octa epitaxial irradiated by a 6 MV flattened beam, 6 MV FFF and 10 MV FFF beam respectively. In each case, the DPP_{dep} shown is the average over that of 5 SVs, chosen close to the centre of the detector, with error bars calculated as 2 standard deviations.

The pre-irradiated Octa bulk had a maximum DPP_{dep} close to 85% at 0.021 mGy/pulse relative to 0.278 mGy/pulse.

A 1st generation of 2D monolithic silicon array detectors fabricated on analogous pre-irradiated bulk p-type silicon substrate was previously characterized. It was reported that a MP512 irradiated by a 6 MV flattened beam showed a maximum DPP_{dep} of approximately 5% in the range 0.009 mGy/pulse to 0.34 mGy/pulse with respect to 0.278 mGy/pulse [116]. A Duo irradiated by a 6 MV flattened beam showed a maximum DPP_{dep} within 23% at 0.021 mGy/pulse with respect to 0.278 mGy/pulse [118].

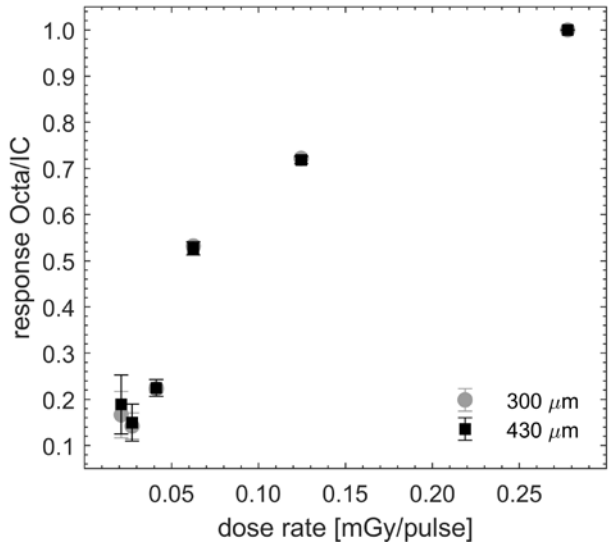

Figure 91. Octa bulk irradiated by a 6 MV flattened beam: average DPP_{dep} of 5 SVs with a pitch of 300 µm and of 430 µm. Ratios were normalized to the value at 100 cm SSD 1.5 cm depth (0.278 mGy/pulse).

The DPP_{dep} of the Octa bulk must be put into context of the results of those investigations. The quality of its substrate, in terms of uniformity of the resistivity profile and defects concentration, is not representative of a typical good-quality bulk substrate. However, its specificities allow for appreciating the importance of defects concentration, intrinsic and introduced because of radiation-induced damage, on the overall performance of a device.

It has been reported that defects introduced as a consequence of the manufacturing process are arranged in concentric rings across a bulk silicon wafer [133]. Differences in the local concentration of defects cause variations in the electric field profile and charge trapping and recombination processes. This results in an overall non-uniform minority carrier lifetime τ_n, i.e. a non-uniform sensitivity of the SVs across the wafer, at any given DPP. Since the τ_n is also a function of the DPP, the sensitivity of the SVs will also change as a function of that (Figure 95).

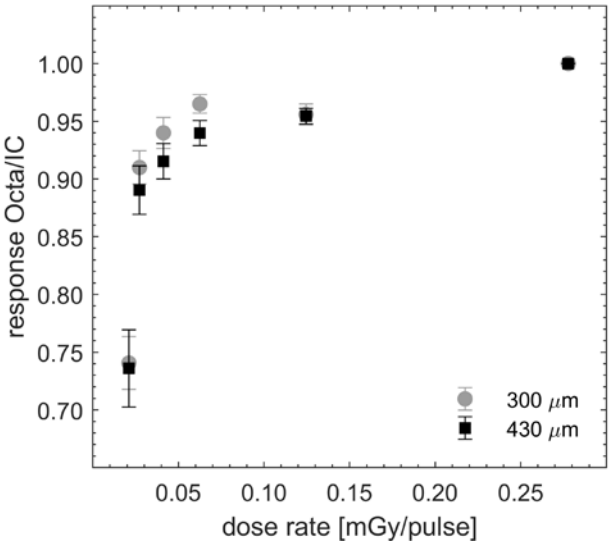

Figure 92. Octa epitaxial irradiated by a 6 MV flattened beam: average DPP_{dep} of 5 SVs with a pitch of 300 µm and of 430 µm. Ratios were normalized to the value at 100 cm SSD 1.5 cm depth (0.278 mGy/pulse).

In a 6 MV flattened beam, the non-preirradiated Octa epitaxial had a maximum DPP_{dep} of $25.94 \pm 2.29\%$ when considering SVs with a 300 µm pitch and of $26.41 \pm 3.35\%$ when considering SVs with a 430 µm pitch, at 0.021 mGy/pulse relative to 0.278 mGy/pulse. This results is in close agreement with that of the investigation performed for a pre-irradiated Duo bulk [118].

The DPP_{dep} of the Octa epitaxial was investigated also in the case of FFF beams, which are of increasingly clinical interest for the rapid treatment delivery of heterogeneous dose distributions [21]. Along with an increased DPP (a 10 MV FFF beam delivered with a Varian TrueBeam™ STx has a DPP approximately 4 times higher than that for the 10 MV flattened

beam), FFF beams have a significantly different energy spectrum and a lower average beam energy [22]. This is explained by the fact that the flattening filter, which was historically introduced to provide a nearly-uniform dose distribution over the treatment area, has a beam hardening effect removing low-energy photons (below 1 MeV), almost completely on the beam central axis and less so towards the field edges [22].

In a 6 MV FFF beam, the Octa epitaxial had a maximum DPP_{dep} of $3.09 \pm 1.61\%$ at 0.078 mGy/pulse relative to 0.406 mGy/pulse when considering SVs with a 300 µm pitch. It was of $4.74 \pm 1.16\%$ at 0.041 mGy/pulse relative to 0.406 mGy/pulse when considering SVs with a 430 µm pitch. In a 10 MV FFF beam, the Octa epitaxial had a maximum DPP_{dep} of $11.07 \pm 2.37\%$ when considering SVs with a 300 µm pitch and of $10.55 \pm 1.01\%$ when considering SVs with a 430 µm pitch, at 0.079 mGy/pulse relative to 0.797 mGy/pulse.

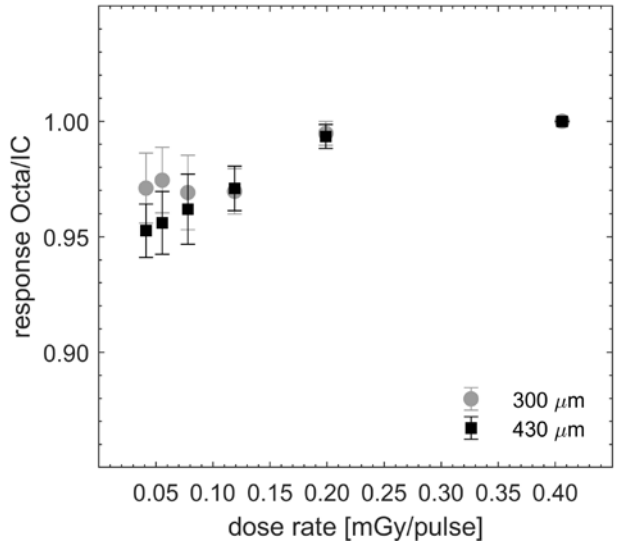

Figure 93. Octa epitaxial irradiated by a 6 MV FFF beam: average DPP_{dep} of 5 SVs with a pitch of 300 µm or of 430 µm. Ratios were normalized to the value at 100 cm SSD 10 cm depth (0.416 mGy/pulse).

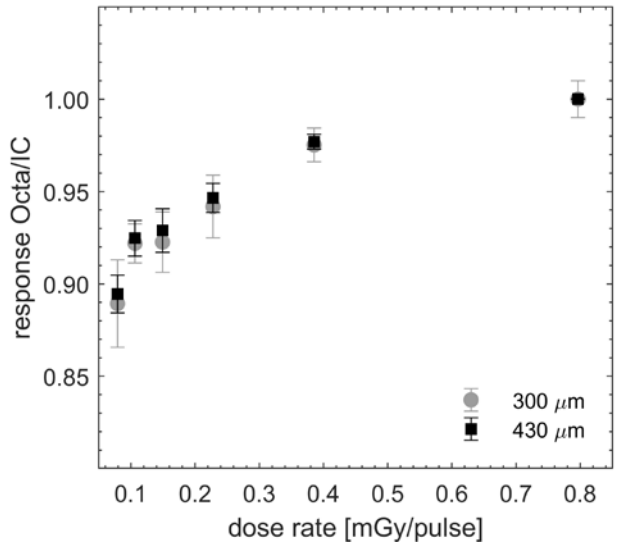

Figure 94. Octa epitaxial irradiated by a 10 MV FFF beam: average DPP_{dep} of 5 SVs with a pitch of 300 µm and of 430 µm. Ratios were normalized to the value at 100 cm SSD 10 cm depth (0.797 mGy/pulse).

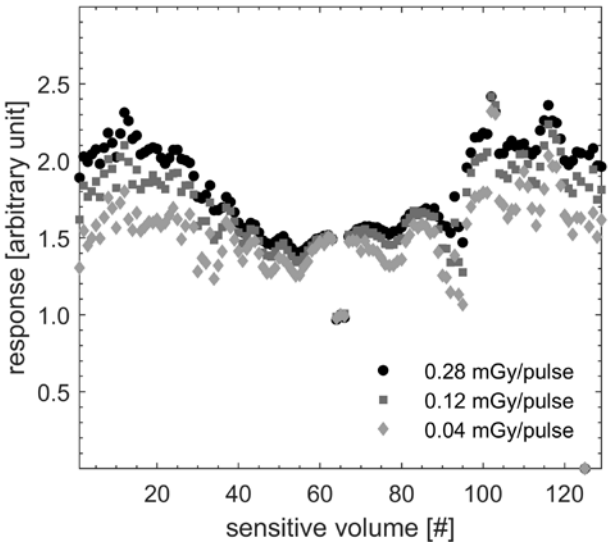

Figure 95. Octa bulk irradiated by 6 MV flattened beam: response to a flat field, with no equalization applied, of the 129 SVs along the vertical array (300 µm pitch), for 3 different DPP. Response is normalized to the response of the central SV at each DPP.

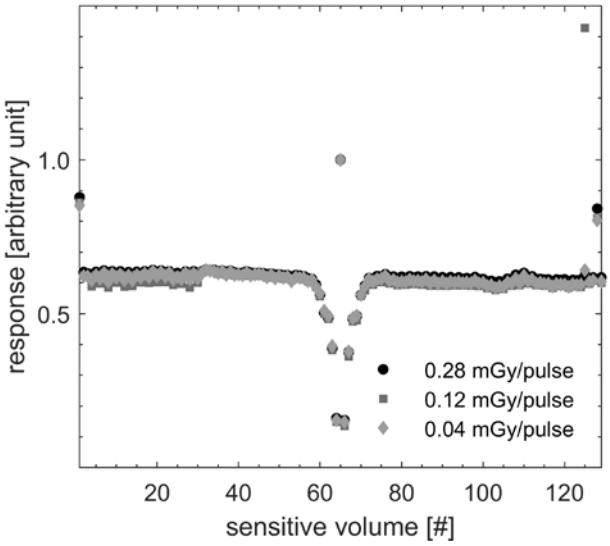

Figure 96. Octa epitaxial irradiated by 6 MV flattened beam: response to a flat field, with no equalization applied, of the 129 SVs along the vertical array (300 µm pitch), for 3 different DPP. Response is normalized to the response of the central SV at each DPP.

It is observed that the Octa epitaxial has a less pronounced DPP_{dep} in the case of FFF delivery with respect to flattened beam delivery (Figure 92, Figure 93). This is explained by considering the photon-energy dependent response of a silicon detector. The dose to silicon increases with decreasing photon energy, for the same dose to water. The dose to silicon was higher for the 6 MV FFF than for the 6 MV flattened beam delivery, owing to the intrinsically softer photon energy spectrum of the former and the measurements being performed at the 10 cm and 1.5 cm depth respectively. The comparably larger decrease in the relative response found for the 10 MV FFF (Figure 94), compared to the 6 MV FFF, is explained by the wider range of DPP values and the higher DPP value with respect to which normalization was performed, other than the harder photon energy spectrum.

For all DPP and beam qualities investigated, there was no apparent difference in DPP_{dep} between SVs in a 300 μm and a 430 μm pitch configuration.

In the context of QA applications for x-ray radiotherapy, the DPP varies with depth in a water phantom, or due to introduction of beam attenuators [124]. If FFF beams are used, DPP varies across a beam profile also in the beam central axis region [22]. These effects may seriously affect the accuracy of a measurement and needs to be considered. When considering measurements for machine-specific QA, the DPP_{dep} of the Octa epitaxial would call for a correction in the case, for instance, of PDD measurements [15].

In the case of patient-specific QA, the modulation during arc delivery applies to the average dose rate not the dose per pulse. The average dose to water delivered by a linac is of the order of $4\ Gy/min$ at d_{max} as set in units of MU/min at the treatment console. This is much different than the DPP to water under which the detector is operated, which is of the order of $10^2\ Gy/s$ [84], [129]. The Octa was shown to have a good linearity with accumulated dose [18].

It is proposed that, while possible to produce a pre-irradiated bulk device with a DPP_{dep} comparable to that of a non-preirradiated epitaxial device of higher resistivity, when considering 2D monolithic devices of approximately $5 \times 5\ cm^2$, it would be easier to produce a substrate with uniform and reproducible properties by using epitaxial technology and avoiding pre-irradiation. This can be appreciated in Figure 96 when compared to Figure 95.

10.3.3 Angular dependence

The angular-dependent response of the Octa bulk irradiated by a 6 MV flattened beam is shown in Figure 97. That of the Octa epitaxial irradiated by a 6 MV flattened beam is in Figure 98 and then in Figure 99 for a 10 MV flattened beam. In each case, the angular-dependent response shown is the average over that of 5 SVs, chosen along the vertical array and close to the centre of the detector. Error bars, calculated as 2 standard deviations, do not exceed the symbol size.

The angular-dependent response of a detector array is explained mainly by anisotropy in materials surrounding the SVs and in the detector assembly. Different materials and packaging arrangements will perturb, with respect to water, the particles spectra (primary photons and secondary electrons) in different ways as a function of the irradiation angle [157].

We first consider the results relative to the square radiation field of 100 mm side only.

For the Octa bulk, the relative response, normalized to the response at radiation beam incidence angle 0°, was found to decrease down to a minimum of 70% in the case of a 6 MV flattened beam. For the Octa epitaxial, the relative response, normalized to the response at radiation beam incidence angle 0°, was found to decrease down to minima of 77% and 80% in the case of a 6 MV flattened beam and of a 10 MV flattened beam respectively. In all cases, minima were reached at incidence angle 90°, i.e. when the beam direction was parallel to the 2D detector plane.

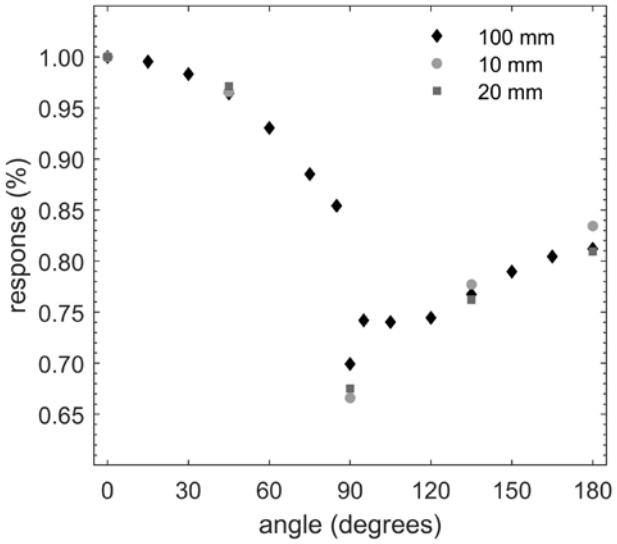

Figure 97. Response averaged over 5 central SVs of the Octa bulk irradiated by a 6 MV flattened beam as a function of the radiation-beam incidence angle. Results are shown for square radiation fields of 10 mm, 20 mm and 100 mm side.

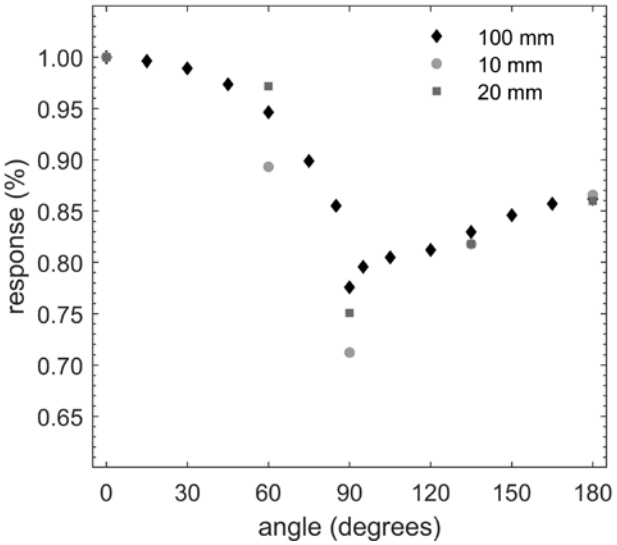

Figure 98. Response averaged over 5 central SVs of the Octa epitaxial irradiated by a 6 MV flattened beam as a function of the radiation-beam incidence angle. Results are shown for square radiation fields of 10 mm, 20 mm and 100 mm side.

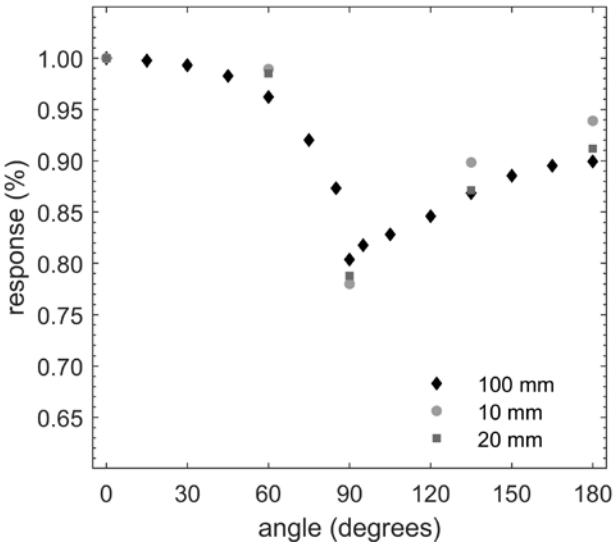

Figure 99. Response averaged over 5 central SVs of the Octa epitaxial irradiated by a 10 MV flattened beam as a function of the radiation-beam incidence angle. Results are shown for square radiation fields of 10 mm, 20 mm and 100 mm side.

The surface of the silicon wafer onto which the SVs of the Octa are implanted was set as facing the incoming radiation beam at angle 0°. Between 0° and 90°, results are explained by the radiation beam attenuation increasing with the increasing incidence angle. The amount of silicon that the beam had to traverse before reaching the SVs was maximized at angle 90°. Between 90° and 180°, an equivalent but opposite trend is seen, owing to decreasing attenuation towards 180°. The lower relative values found in this second range are explained by the higher attenuation caused by the thick silicon supporting wafer on the back of the SVs and the thin PCB board on which detector is wire-bonded. The latter, which provides electronic connections to the read-out system, is attached at the back of the former.

The materials surrounding the SVs introduce perturbations to the particle spectra, and their angular distribution, which are beam quality-dependent [26]. This results in differences in the angular-dependent response, as seen by comparing the case of a 10 MV flattened beam (Figure 99) with the case of a 6 MV flattened beam (Figure 98).

The results for the Octa epitaxial are in substantial agreement with those of a previous independent investigation on the angular-dependent response of a different 2D monolithic silicon array detector, a pre-irradiated MP512 bulk [132]. It was reported that minima were 81.5% and 84.5% in the relative response for a 6 MV flattened beam and a 10 MV flattened beam respectively. Minima were reached between 90° and 95°.

Considering the results for the 6 MV flattened beam (Figure 97, Figure 98), the relative response of the Octa bulk was in close agreement with that of the Octa epitaxial in the range 0° to 85°, but in disagreement in the range 90° to 180°. Other factors may be in play, such as

slight differences in the packaging, detector thickness and the pronounced DPP_{dep} of the Octa bulk.

Other than of the beam quality (i.e. photon spectrum), the secondary electron spectrum is a function of the size of the radiation field. The materials surrounding the SVs introduce a field-size dependent perturbation related to the field-size dependent secondary electron spectrum [51]. The field-size dependence of the angular response can be appreciated in Figure 97 to Figure 99. An analogous result was reported for the MP512 bulk [132]. The relative response is slightly decreasing with decreasing field size at 90°. For the central SVs, this is explained by the increasing partial contribution to the perturbation of the secondary electron spectrum by surrounding silicon.

It is worth considering that the Octa was originally designed for measurements at radiation-beam incident angle 0°. For that measurement condition, its response was rendered field-size independent by introducing a modification to the detector design, i.e. adding an air gap on top of its SV [15].

Any angular-dependent response hinders the use of a detector for patient-specific QA, e.g. for plan verification in the case of arc radiotherapy. However, it was shown that the problem can be mitigated by using an angular-dependent correction methodology [132], [234]. The key to this method is knowledge about the radiation-beam incidence angle at any time, for instance by using an inclinometer, and the application of an appropriate correction factor for that angle. Alternatively, the detector may be lodged into a rotating phantom, so that its 2D active surface is always perpendicular to the incoming beam.

In principle, our recommendation is that correction factors to account for the angular-dependent response of a 2D monolithic silicon array detector be measured for each device being used, for each field size and beam quality.

It is proposed that a device based on a pre-irradiated bulk substrate would show an angular-dependent response comparable to that of a device based on an epitaxial substrate, provided they share the same packaging components and the same thickness of the substrate.

In a future work, Monte Carlo numerical simulations will be used for evaluating the partial effects of each component and material surrounding the SVs on the composite field-size angular-dependent response.

10.4 Conclusions

The Octa, a 2D monolithic silicon-diode array detector dedicated to small-field high spatial resolution dosimetry, was produced in two versions, on a bulk and on an epitaxial substrate. Their performance was discussed in the context of quality assurance applications in small radiation fields delivered with modulated arc radiotherapy.

The observed radial non-uniformity of the response of the Octa bulk, and its hypothesised dependence on instantaneous dose rate, was related to non-uniform radial profiles in terms of resistivity and defects concentration across the large-area monolithic silicon wafer. Based on this and previous investigations [18], this non-linear spread-out of the instantaneous dose rate-dependent response of the sensitive volumes would be difficult to correct for by applying an equalization procedure. A quantitative analysis of the effect was outside the scope of the present study and will be considered in the future.

For a large-area monolithic array detector, it was highlighted that both anisotropy in the silicon surrounding each sensitive volume and asymmetry in the detector packaging result in a strong angular-dependent response which is slightly field-size and beam-quality dependent. However, a previous study has shown that this could be corrected for in real-time [234]. It also does not detract from the main advantages of the Octa detector technology with respect to present commercial devices, namely a high temporal and sub-mm spatial resolution.

For any device proposed for use in clinical applications, it is important to identify the parameters that influence its quality as well as those that affect detectors reproducibility in the same batch. Based on our and previous investigations [15], [116], [118], both a bulk and an epitaxial substrate would potentially be suitable candidates for a large-area 2D monolithic silicon-diode array detector. However, epitaxial technology would be preferable in terms of achievable uniformity [18] and thanks to previously demonstrated radiation hardness [202].

11 Contributions and recommendations

11.1 The Octa prototype: design and test

The aim of the project described in the present dissertation was the design and test of a detector prototype dedicated to small-field dosimetry in megavoltage photon beams.

The selection process of the type of device (in due course, a solid-state one with a real-time read-out was chosen) and of its peculiar design (512 sensitive volumes-SVs distributed along 4 linear arrays in a star-like shape with a sub-millimetre pitch, with an air gap on top of its SVs to minimize the number and size of corrections required to relate its readings to dose) was informed by an analysis of:

- the requirements of the medical physics community as outlined in internationally accepted Codes of Practice (CoP) (section 2.2.2, page 18)
- the currently available commercial dosimeters, their potentials and limitations (section 2.3, page 23)
- prototypes previously proposed and characterized by the scientific community (section 3.3.2, page 35 and section 3.3.3, page 36)
- the previous experience the Centre for Medical Radiation Physics (CMRP) had on solid-state dosimeter prototypes (section 3.3.4, page 40); constrains related to the data acquisition system in terms of maximum number of SVs with simultaneous read-out
- informal discussions with members of the medical physics community.

Eventually, the process led to the 'Octa' prototype. Its design, manufacturing characteristics and read-out system were described, respectively, in section 4.1 (page 43), section 4.2 (page 45) and section 4.3 (page 46). The Octa was produced on two different silicon substrates: a bulk one, similarly to all previous devices proposed by the CMRP up to that time, and an epitaxial substrate.

Measurements (experimental) were planned to characterize the response of the Octa bulk and of the Octa epitaxial. Numerical simulations were added to those plans whenever possible and relevant to support measurements and inform discussions on results. The prototypes were modelled with a Geant4 (GEometry ANd Tracking 4) Monte Carlo application (section 4.4, page 51) and a TCAD (Technology Computer-Aided Design) software (section 4.5, page 54).

11.2 The Octa prototype: results

The first, preliminary, measurements with the Octa (Octa manufactured on a bulk silicon substrate) in small static fields produced with flattened and flattening-filter free (FFF) megavoltage photon beams were described in chapter 5 (page 59). That chapter discussed a few of the limitations (further discussed in chapter 9, page 124 and chapter 10, page 149) related to the manufacturing process of that prototype. Those preliminary results eventually led to the use of the second sample of the Octa prototype (Octa manufactured on an epitaxial silicon substrate) for all remaining planned measurements.

The performance of the Octa epitaxial as a dosimeter dedicated to measurements in small radiation fields was assessed in flattened and FFF megavoltage photon beams produced by the most common medical linear accelerators (linacs) used by the modern medical physics community:

- a Varian Clinac iX® and a Varian TrueBeam STx™ (chapter 6, page 69): first assessment of the performance of a 2D monolithic silicon-diode array detector in FFF beams
- an Elekta Axesse™ (chapter 7, page 87): first use of a 2D monolithic silicon-diode array detector for dosimetric characterization of stereotactic-dedicated fixed cone collimators
- an Accuray CyberKnife® (chapter 8, page 97): first use of a 2D monolithic silicon-diode array detector for CyberKnife® QA.

Analysis and discussions of the results of those measurements led to the following conclusions about the Octa epitaxial:

- thanks to its 512 SVs arranged along 4 linear arrays with a sub-millimetre pitch, it provided a much more detailed characterization of 2D dose maps than that of its predecessor the MP512 and the Duo prototypes, while still offering the same stable and real-time read-out
- its dosimetric performance was comparable, in terms of spatial resolution, to that of commercially available small-field dosimeters, such as 2D EBT3 Gafchromic films and point-like devices such as the PTW microdiamond and the PTW SRS diode. In contrast to those, though, the Octa had real-time read-out and simultaneous characterization of output factor (OF) and cross-plane, in-plane and 2 diagonal off-axis ratios (OARs), in any given radiation field

- its measurements were not affected by any appreciable volume-averaging effect. Positioning procedure to align the detector central SV to the central axis (CAX) of the radiation field was straightforward
- the air gap used to render it 'correction-free' for OF measurements was found to be applicable to both flattened and FFF beams, in accordance to similar results in the literature
- notwithstanding a dose per pulse (DPP) dependence, that could in principle be corrected for, percentage depth dose (PDD) and tissue maximum ratio (TMR) measurements were accurate with respect to selected benchmarks for all beam qualities investigated, at all depths up to 300 mm in solid water
- the relatively high doses per pulse typical of FFF beams were not detrimental to its performance.

Based on those results, it was proposed that, in the case of a machine-specific QA, the Octa would reduce the measurement time needed to comply with current protocols. It would also have unique dosimetry potentials for real-time high-spatial resolution verifications of:

- the alignment of the radiation beam and of mechanical axes of a linac
- the reproducibility of the positioning of stereotactic-dedicated fixed cone collimators
- the long-term mechanical reproducibility of movable parts in the collimator system of a linac, such as jaws and the multi-leaf collimator (MLC)
- the long-term mechanical reproducibility of the variable aperture of the Iris™ collimator in terms of OF and FWHM and penumbra values of OARs.

In the present dissertation, the assessment of the performance of the Octa epitaxial was limited by the linacs, and associated collimators and commercial devices used for QA, made available for research purposes within the Australian medical physics community. For example, the CyberKnife® used was not, at that time, equipped with an InCise™ multi-leaf collimator (MLC).

11.3 Recommendations

Finally, for any proposed novel dosimeter, it is important to identify parameters that influence its quality and those that affect its reproducibility within the same production batch. Chapter 9 (page 124) and chapter 10 (page 149) used measurements (experimental) and

numerical simulations to assess the performance of the Octa bulk and of the Octa epitaxial in terms of their:

- response linearity with dose
- response uniformity over the arrays
- charge-collection efficiency (CCE)
- angularly-dependent response
- instantaneous dose rate dependence.

An analysis of the findings of that assessment showed that:

- TCAD simulations of a minimum ionizing particle (MIP) through the device were useful to characterize the CCE of a 2D monolithic diode-array detector. Simulated CCE distributions can inform an estimation of the minority carrier diffusion length. The present methodology can be used to optimize the layout of the SVs, and their pitch across the silicon wafer, of future prototypes prior to fabrication
- TCAD simulations with the *Gamma Radiation Model* were useful to investigate how the performance of a monolithic diode-array detector is affected by parameters such the pitch of its SVs, the silicon resistivity and traps concentration. Again, the present methodology can be used to optimize the layout of the SVs, and their pitch across the silicon wafer, of future prototypes prior to fabrication
- in a bulk pre-irradiated device with a sufficiently small minority carrier diffusion length (L_e, if p-type substrate), the pitch of the SVs did not affect their CCE
- in an epitaxial device, if $L_e \geq W, r$, W the epitaxial layer thickness and r the guard ring-SV distance, the device was radiation hard and did not require pre-irradiation for sensitivity stabilization. The pitch of the SVs affected their CCE. Even in the presence of a sub-optimal CCE, the nominal spatial resolution of the detector was preserved
- both the Octa bulk and the Octa epitaxial had a response linear with dose
- both the Octa bulk and the Octa epitaxial had a non-uniform response across the arrays. A suitable equalization procedure could be applied, in the case of modern radiotherapy applications with FFF beams, only for the device manufactured with a uniform profile in terms of resistivity and recombination properties (Octa epitaxial).

Elaborating further on the last finding, it was advanced that:

- the observed radial non-uniformity of the response of the SVs of the Octa bulk, and its hypothesised dependence on the instantaneous dose rate, was related to the presence of non-uniform radial profiles (in terms of resistivity and defects concentration) across its large-area monolithic silicon wafer
- the successful application of an equalization procedure to correct the non-uniform response of the SVs of the Octa bulk was prevented by their non-linear instantaneous dose rate dependence.

It was also highlighted that:

- both anisotropy in the silicon surrounding each SV and asymmetry in the detector packaging resulted in a strong angularly-dependent response which is slightly field-size and beam-quality dependent. This could be corrected for in real-time.

Both bulk and epitaxial substrates would be suitable candidates for large-area 2D monolithic silicon-diode array detectors. An epitaxial device would however be preferable owing to improved uniformity in the response of its SVs and radiation hardness of its substrate.

11.4 Conclusions

The present work demonstrated that the Octa prototype, in the context of currently available QA devices, and specifically of available solid-state array ones, was a significant step forward in terms of offered temporal resolution (pulse-by-pulse real-time acquisition) and spatial resolution (sub-millimetre measurements). Its clever design would provide the medical physicist working in the clinic with an innovative tool able to acquire whole 2D dose distributions in small radiation fields, with minimal corrections required to relate the detector readings to dose, in real time and with sub-millimetre accuracy. The Octa prototype would effectively have potential for streamlining existing QA procedures.

Bibliography

[1] IAEA, "Technical Reports Series No. 483 - Dosimetry of Small Static Fields Used in External Beam Radiotherapy An International Code of Practice for Reference and Relative Dose Determination," 2017.

[2] ICRU, "Report 91," *J. Int. Comm. Radiat. Units Meas.*, vol. 14, no. 2, pp. 1–160, 2017.

[3] N. Garnier *et al.*, "Detectors assessment for stereotactic radiosurgery with cones," *J. Appl. Clin. Med. Phys.*, vol. 19, no. 6, pp. 88–98, Nov. 2018.

[4] G. Reggiori *et al.*, "Use of PTW-microDiamond for relative dosimetry of unflattened photon beams," *Phys. Medica*, vol. 38, pp. 45–53, 2017.

[5] V. De Coste *et al.*, "Is the PTW 60019 microDiamond a suitable candidate for small field reference dosimetry?," *Phys. Med. Biol.*, vol. 62, no. 17, pp. 7036–7055, Aug. 2017.

[6] M. Tyler *et al.*, "Characterization of small-field stereotactic radiosurgery beams with modern detectors," *Phys. Med. Biol.*, vol. 58, no. 21, pp. 7595–7608, 2013.

[7] S. Derreumaux *et al.*, "SU-E-T-163: Characterization of the Response of Active Detectors and Passive Dosemeters Used for Dose Measurement in Small Photon Beams," *Med. Phys.*, vol. 38, no. 6Part12, pp. 3523–3523, Jun. 2011.

[8] P. Z. Y. Liu *et al.*, "Small field correction factors for the IBA Razor," *Phys. Medica*, vol. 32, no. 8, pp. 1025–1029, 2016.

[9] G. Reggiori *et al.*, "Characterization of a new unshielded diode for small field dosimetry under flattening filter free beams," *Phys. Medica*, vol. 32, no. 2, pp. 408–413, 2016.

[10] S. Devic, N. Tomic, and D. Lewis, "Reference radiochromic film dosimetry: Review of technical aspects," *Phys. Medica*, vol. 32, no. 4, pp. 541–556, 2016.

[11] A. L. Palmer, D. A. Bradley, and A. Nisbet, "Evaluation and mitigation of potential errors in radiochromic film dosimetry due to film curvature at scanning," *J. Appl. Clin. Med. Phys.*, vol. 16, no. 2, pp. 425–431, 2015.

[12] N. Wen *et al.*, "Precise film dosimetry for stereotactic radiosurgery and stereotactic body radiotherapy quality assurance using Gafchromic^{TM} EBT3 films," *Radiat. Oncol.*, vol. 11, no. 1, pp. 1–11, 2016.

[13] B. Loutfi-krauss, M. Damme, T. S. Stelljes, and M. K. H. Chan, "Usability and accuracy of high-resolution detectors for daily quality assurance for robotic radiosurgery," *Curr. Dir. Biomed. Eng.*, vol. 3, no. 2, pp. 277–280, 2017.

[14] O. Blanck *et al.*, "High resolution ion chamber array delivery quality assurance for robotic radiosurgery: Commissioning and validation," *Phys. Medica*, vol. 32, no. 6, pp. 838–846, 2016.

[15] G. Biasi *et al.*, "A novel high-resolution 2D silicon array detector for small field dosimetry with FFF photon beams," *Phys. Medica*, vol. 45, pp. 117–126, Jan. 2018.

[16] G. Biasi *et al.*, "Today's monolithic silicon array detector for small field dosimetry: the Octa," *J. Phys. Conf. Ser.*, vol. 1154, p. 012002, Jan. 2019.

[17] G. Biasi *et al.*, "CyberKnife ® fixed cone and Iris^{TM} defined small radiation fields: Assessment with a high-resolution solid-state detector array," *J. Appl. Clin. Med. Phys.*, vol. 19, no. 5, pp. 547–557, Sep. 2018.

[18] G. Biasi *et al.*, "On Monolithic Silicon Array Detectors for Small-Field Photon Beam Dosimetry," *IEEE Trans. Nucl. Sci.*, vol. 65, no. 9, pp. 2640–2649, Sep. 2018.

[19] G. Biasi *et al.*, "On the Instantaneous Dose Rate and Angular Dependence of Monolithic Silicon Array Detectors," *IEEE Trans. Nucl. Sci.*, vol. 66, no. 1, pp. 519–527, Jan. 2019.

[20] E. B. Podgorsak, *Compendium to Radiation Physics for Medical Physicists*. Springer, 2014.

[21] H. Bagheri *et al.*, "An overview on small-field dosimetry in photon beam radiotherapy: Developments and challenges," *J. Cancer Res. Ther.*, vol. 13, no. 2, p. 175, 2017.

[22] G. Budgell *et al.*, "IPEM topical report 1: Guidance on implementing flattening filter free (FFF) radiotherapy," *Phys. Med. Biol.*, vol. 61, no. 23, pp. 8360–8394, Dec. 2016.

[23] E. L. Covington, T. A. Ritter, J. M. Moran, A. M. Owrangi, and J. I. Prisciandaro, "Technical Report: Evaluation of peripheral dose for flattening filter free photon beams," *Med. Phys.*, vol. 43, no. 8, pp. 4789–4796, 2016.

[24] M. L. Taylor, T. Kron, and R. D. Franich, "A contemporary review of stereotactic radiotherapy: inherent dosimetric complexities and the potential for detriment," *Acta Oncol. (Madr).*, vol. 50, no. 4, pp. 483–508, 2011.

[25] M. Van Vulpen and L. Wang, "Within the next five years, adaptive hypofractionation will become the most common form of radiotherapy," *Med. Phys.*, vol. 43, no. 7, pp. 3941–3944, 2016.

[26] P. Andreo, "The physics of small megavoltage photon beam dosimetry," *Radiother. Oncol.*, vol. 126, no. 2, pp. 205–213, Feb. 2018.

[27] T. Kron, J. Lehmann, and P. B. Greer, "Dosimetry of ionising radiation in modern radiation oncology," *Phys. Med. Biol.*, vol. 61, no. 14, pp. R167–R205, Jul. 2016.

[28] A. J. D. Scott, S. Kumar, A. E. Nahum, and J. D. Fenwick, "Characterizing the

influcence of detector density on dosimeter response in non-equilibrium small photon fields," *Phys. Med. Biol.*, vol. 58, no. 9, pp. 2901–2923, 2012.

[29] G. G. Steel, *Basic Clinical Radiobiology*, Third Edit. London, 2002.

[30] P. Andreo, D. T. Burns, A. E. Nahum, J. Seuntjens, and F. H. Attix, *Fundamentals of Ionizing Radiation Dosimetry*. John Wiley & Sons, 2017.

[31] M. McEwen *et al.*, "Addendum to the AAPM's TG-51 protocol for clinical reference dosimetry of high-energy photon beams," *Med. Phys.*, vol. 41, no. 4, p. 041501, Mar. 2014.

[32] IAEA, "Absorbed Dose Determination in External Beam Radiotherapy: An International Code of Practice for Dosimetry Based on Standards of Absorbed Dose to Water; Technical Reports Series No. 398," 398, 2000.

[33] IAEA, *Technical Reports Series No. 430 - Commissioning and Quality Assurance of Computerized Planning Systems for Radiation Treatment of Cancer*. 2004.

[34] B. Fraass *et al.*, "AAPM Radiation Therapy Committee TG-53 - Radiation Treatment Planning Dosimetry Verification," *Med. Phys.*, vol. 25, no. 10, pp. 1773–1829, 1998.

[35] J. B. Smilowitz *et al.*, "AAPM Medical Physics Practice Guideline 5.a.: Commissioning and QA of Treatment Planning Dose Calculations - Megavoltage Photon and Electron Beams," *J. Appl. Clin. Med. Phys.*, vol. 16, no. 5, 2015.

[36] G. Azangwe *et al.*, "Detector to detector corrections: A comprehensive experimental study of detector specific correction factors for beam output measurements for small radiotherapy beams," *Med. Phys.*, vol. 41, no. 7, p. 072103, 2014.

[37] R. Alfonso *et al.*, "A new formalism for reference dosimetry of small and nonstandard fields," *Med. Phys.*, vol. 35, no. 11, pp. 5179–5186, 2008.

[38] S. Derreumaux *et al.*, "Lessons from recent accidents in radiation therapy in France," *Radiat. Prot. Dosimetry*, vol. 131, no. 1, pp. 130–135, Aug. 2008.

[39] ICRP (International Commission on Radiological Protection) Publication 112, *A report of preventing accidental exposures from new external beam radiation therapy technologies.*, vol. 39, no. 4. Pergamom Press, Elsevier, 2009.

[40] I. J. Das, G. X. Ding, and A. Ahnesjö, "Small fields: Nonequilibrium radiation dosimetry," *Med. Phys.*, vol. 35, no. 1, pp. 206–215, 2008.

[41] IPEM, *Small Field MV Photon Dosimetry*. 2010.

[42] X. R. Zhu, J. J. Allen, J. Shi, and W. E. Simon, "Total scatter factors and tissue maximum ratios for small radiosurgery fields: comparison of diode detectors, a parallel-plate ion chamber, and radiographic film.," *Med. Phys.*, vol. 27, no. 3, pp. 472–477, 2000.

[43] F. Sánchez-Doblado *et al.*, "Ionization chamber dosimetry of small photon fields: A Monte Carlo study on stopping-power ratios for radiosurgery and IMRT beams," *Phys. Med. Biol.*, vol. 48, no. 14, pp. 2081–2099, 2003.

[44] O. A. Sauer and J. Wilbert, "Measurement of output factors for small photon beams," *Med. Phys.*, vol. 34, no. 6, pp. 1983–1988, 2007.

[45] T. C. Zhu, "Small Field: dosimetry in electron disequilibrium region," *J. Phys. Conf. Ser.*, vol. 250, p. 012056, 2010.

[46] H. Bouchard, J. Seuntjens, and H. Palmans, "On charged particle equilibrium violation in external photon fields," *Med. Phys.*, vol. 39, no. 3, pp. 1473–1480, 2012.

[47] J. D. Fenwick, S. Kumar, A. J. D. Scott, and A. E. Nahum, "Using cavity theory to describe the dependence on detector density of dosimeter response in non-equilibrium small fields," *Phys. Med. Biol.*, vol. 58, no. 9, pp. 2901–2923, 2013.

[48] H. Bouchard, J. Seuntjens, S. Duane, Y. Kamio, and H. Palmans, "Detector dose response in megavoltage small photon beams. I. Theoretical concepts," *Med. Phys.*, vol. 42, no. 10, pp. 6033–6047, 2015.

[49] H. Bouchard, J. Seuntjens, S. Duane, Y. Kamio, and H. Palmans, "Detector dose response in megavoltage small photon beams. II. Pencil beam perturbation effects," *Med. Phys.*, vol. 42, no. 10, pp. 6033–6047, 2015.

[50] I. J. Das, J. Morales, and P. Francescon, "Small field dosimetry: What have we learnt?," *AIP Conf. Proc.*, vol. 1747, pp. 0–10, 2016.

[51] H. Benmakhlouf and P. Andreo, "Spectral distribution of particle fluence in small field detectors and its implication on small field dosimetry," *Med. Phys.*, vol. 44, no. 2, 2017.

[52] G. X. Ding, D. M. Duggan, and C. W. Coffey, "Commissioning stereotactic radiosurgery beams using both experimental and theoretical methods," *Phys. Med. Biol.*, vol. 51, no. 10, pp. 2549–2566, 2006.

[53] T. Kairn, P. Charles, S. B. Crowe, and J. V. Trapp, "Effects of inaccurate small field dose measurements on calculated treatment doses," *Australas. Phys. Eng. Sci. Med.*, vol. 39, no. 3, pp. 747–753, 2016.

[54] A. Fogliata *et al.*, "Evaluation of the dose calculation accuracy for small fields defined by jaw or MLC for AAA and Acuros XB algorithms," *Med. Phys.*, vol. 43, no. 10, pp. 5685–5694, Sep. 2016.

[55] E. Pappas *et al.*, "Small SRS photon field profile dosimetry performed using a PinPoint air ion chamber, a diamond detector, a novel silicon-diode array (DOSI), and polymer gel dosimetry. Analysis and intercomparison," *Med. Phys.*, vol. 35, no. 10, pp. 4640–

4648, 2008.

[56] P. Francescon, S. Cora, and C. Cavedon, “Total scatter factors of small beams: A multidetector and Monte Carlo study,” *Med. Phys.*, vol. 35, no. 2, pp. 504–513, 2008.

[57] P. Francescon, S. Cora, and N. Satariano, “Calculation of k Q clin, Q msr f clin, f msr for several small detectors and for two linear accelerators using Monte Carlo simulations,” *Med. Phys.*, vol. 38, no. 12, pp. 6513–6527, 2011.

[58] H. Benmakhlouf, J. Sempau, and P. Andreo, “Output correction factors for nine small field detectors in 6 MV radiation therapy photon beams: A PENELOPE monte carlo study,” *Med. Phys.*, vol. 41, no. 4, p. 041711, 2014.

[59] P. Francescon, W. Kilby, J. M. Noll, L. Masi, N. Satariano, and S. Russo, “Monte Carlo simulated corrections for beam commissioning measurements with circular and MLC shaped fields on the CyberKnife M6 System: A study including diode, microchamber, point scintillator, and synthetic microdiamond detectors,” *Phys. Med. Biol.*, vol. 62, no. 3, pp. 1076–1095, Feb. 2017.

[60] P. Andreo, H. Palmans, M. Marteinsdóttir, H. Benmakhlouf, and Å. Carlsson-Tedgren, “On the Monte Carlo simulation of small-field micro-diamond detectors for megavoltage photon dosimetry,” *Phys. Med. Biol.*, vol. 61, no. 1, pp. L1–L10, 2015.

[61] P. Francescon, S. Beddar, N. Satariano, and I. J. Das, “Variation of kQclin, Qmsr fclin,fmsr for the small-field dosimetric parameters percentage depth dose, tissue-maximum ratio, and off-axis ratio,” *Med. Phys.*, vol. 41, no. 10, p. 101708, 2014.

[62] P. Francescon, W. Kilby, and N. Satariano, “Monte Carlo simulated correction factors for output factor measurement with the CyberKnife system—results for new detectors and correction factor dependence on measurement distance and detector orientation,” *Phys. Med. Biol.*, vol. 59, no. 6, pp. N11–N17, Mar. 2014.

[63] D. J. O’Brien, L. León-Vintró, and B. McClean, “Small field detector correction factors kQ clin, Q msrf clin, f msrfor silicon-diode and diamond detectors with circular 6 MV fields derived using both empirical and numerical methods,” *Med. Phys.*, vol. 43, no. 1, p. 411, 2016.

[64] P. H. Charles *et al.*, “Monte Carlo-based diode design for correction-less small field dosimetry,” *Phys. Med. Biol.*, vol. 58, no. 13, pp. 4501–4512, 2013.

[65] J. A. Conger, “Training leaders for the twenty-first century,” *Hum. Resour. Manag. Rev.*, vol. 3, no. 3, pp. 203–218, Jun. 1993.

[66] J. Seco, B. Clasie, and M. Partridge, “Review on the characteristics of radiation detectors for dosimetry and imaging,” *Phys. Med. Biol.*, vol. 59, no. 20, pp. R303–R347, 2014.

[67] A. Ralston, P. Liu, K. Warrener, D. McKenzie, and N. Suchowerska, “Small field diode correction factors derived using an air core fibre optic scintillation dosimeter and EBT2 film,” *Phys. Med. Biol.*, vol. 57, no. 9, pp. 2587–2602, 2012.

[68] D. Létourneau, J. Pouliot, and R. Roy, “Miniature scintillating detector for small field radiation therapy,” *Med. Phys.*, vol. 26, no. 12, pp. 2555–2561, Dec. 1999.

[69] L. Archambault, A. S. Beddar, L. Gingras, F. Lacroix, R. Roy, and L. Beaulieu, “Water-equivalent dosimeter array for small-field external beam radiotherapy,” *Med. Phys.*, vol. 34, no. 5, pp. 1583–1592, Apr. 2007.

[70] A. S. Beddar, T. R. Mackie, and F. H. Attix, “Water-equivalent plastic scintillation detectors for high-energy beam dosimetry: II. Properties and measurements,” *Phys. Med. Biol.*, vol. 37, no. 10, pp. 1901–1913, Oct. 1992.

[71] A. S. Beddar, T. R. Mackie, and F. H. Attix, “Water-equivalent plastic scintillation detectors for high-energy beam dosimetry: I. Physical characteristics and theoretical considerations,” *Phys. Med. Biol.*, vol. 37, no. 10, pp. 1883–1900, Oct. 1992.

[72] D. Flühs, M. Heintz, F. Indenkämpen, C. Wieczorek, H. Kolanoski, and U. Quast, “Direct reading measurement of absorbed dose with plastic scintillators - The general concept and applications to ophthalmic plaque dosimetry,” *Med. Phys.*, vol. 23, no. 3, pp. 427–434, Mar. 1996.

[73] M. A. Clift, R. A. Sutton, and D. V. Webb, “Dealing with Cerenkov radiation generated in organic scintillator dosimeters by bremsstrahlung beams,” *Phys. Med. Biol.*, vol. 45, no. 5, pp. 1165–1182, May 2000.

[74] P. Carrasco *et al.*, “Characterization of the Exradin W1 scintillator for use in radiotherapy,” *Med. Phys.*, vol. 42, no. 1, pp. 297–304, Dec. 2014.

[75] L. Archambault, A. S. Beddar, L. Gingras, R. Roy, and L. Beaulieu, “Measurement accuracy and Cerenkov removal for high performance, high spatial resolution scintillation dosimetry,” *Med. Phys.*, vol. 33, no. 1, pp. 128–135, Dec. 2005.

[76] J. Lambert, Y. Yin, D. R. McKenzie, S. Law, and N. Suchowerska, “Cerenkov-free scintillation dosimetry in external beam radiotherapy with an air core light guide,” *Phys. Med. Biol.*, vol. 53, no. 11, pp. 3071–3080, Jun. 2008.

[77] S. Devic, N. Tomic, C. G. Soares, and E. B. Podgorsak, “Optimizing the dynamic range extension of a radiochromic film dosimetry system,” *Med. Phys.*, vol. 36, no. 2, pp. 429–437, 2009.

[78] J. C. Gore and Y. S. Kang, “Measurement of radiation dose distributions by nuclear magnetic resonance (NMR) imaging,” *Phys. Med. Biol.*, vol. 29, no. 10, pp. 1189–1197,

Oct. 1984.

[79] C. Baldock *et al.*, "Polymer gel dosimetry," *Phys. Med. Biol.*, vol. 55, no. 5, pp. R1–R63, Mar. 2010.

[80] O. Senkesen, E. Tezcanli, B. Buyuksarac, and I. Ozbay, "Comparison of 3D dose distributions for HDR192Ir brachytherapy sources with normoxic polymer gel dosimetry and treatment planning system," *Med. Dosim.*, vol. 39, no. 3, pp. 266–271, 2014.

[81] Y. De Deene, C. Claeys, and C. De Wagter, "Three dimensional radiation dosimetry in lung-equivalent regions by use of a radiation sensitive gel foam: Principles," *J. Phys. Conf. Ser.*, vol. 56, no. 1, pp. 256–258, Jun. 2006.

[82] U. J. Yeo, M. L. Taylor, L. Dunn, T. Kron, R. L. Smith, and R. D. Franich, "A novel methodology for 3D deformable dosimetry," *Med. Phys.*, vol. 39, no. 4, pp. 2203–2213, Apr. 2012.

[83] T. Kairn *et al.*, "Can a commercial gel dosimetry system be used to verify stereotactic spinal radiotherapy treatment dose distributions?," *J. Phys. Conf. Ser.*, vol. 847, no. 1, p. 012071, May 2017.

[84] A. B. Rosenfeld, "Electronic dosimetry in radiation therapy," *Radiat. Meas.*, vol. 41, pp. S134–S153, Dec. 2007.

[85] A. B. Rosenfeld, A. Rosenfeld, T. Kron, F. d'Errico, and M. Moscovitch, "Advanced Semiconductor Dosimetry in Radiation Therapy," in *AIP Conference Proceedings*, 2011, vol. 1345, no. 48, pp. 48–74.

[86] S. Dieterich and G. W. Sherouse, "Experimental comparison of seven commercial dosimetry diodes for measurement of stereotactic radiosurgery cone factors," *Med. Phys.*, vol. 38, no. 7, pp. 4166–4173, 2011.

[87] P. Papaconstadopoulos, F. Tessier, and J. Seuntjens, "On the correction, perturbation and modification of small field detectors in relative dosimetry," *Phys. Med. Biol.*, vol. 59, no. 19, pp. 5937–5952, 2014.

[88] I. Ciancaglioni *et al.*, "Dosimetric characterization of a synthetic single crystal diamond detector in clinical radiation therapy small photon beams," *Med. Phys.*, vol. 39, no. 7Part1, pp. 4493–4501, Jul. 2012.

[89] F. Marsolat *et al.*, "A new single crystal diamond dosimeter for small beam: Comparison with different commercial active detectors," *Phys. Med. Biol.*, vol. 58, no. 21, pp. 7647–7660, Nov. 2013.

[90] A. Ralston, M. Tyler, P. Liu, D. McKenzie, and N. Suchowerska, "Over-response of

synthetic microDiamond detectors in small radiation fields," *Phys. Med. Biol.*, vol. 59, no. 19, pp. 5873–5881, Oct. 2014.

[91] W. U. Laub and T. Wong, "The volume effect of detectors in the dosimetry of small fields used in IMRT," *Med. Phys.*, vol. 30, no. 3, pp. 341–347, Feb. 2003.

[92] M. Le Roy *et al.*, "Assessment of small volume ionization chambers as reference dosimeters in high-energy photon beams," *Phys. Med. Biol.*, vol. 56, no. 17, pp. 5637–5650, Sep. 2011.

[93] S. Agostinelli, S. Garelli, M. Piergentili, and F. Foppiano, "Response to high-energy photons of PTW31014 PinPoint ion chamber with a central aluminum electrode," *Med. Phys.*, vol. 35, no. 7Part1, pp. 3293–3301, Jun. 2008.

[94] L. B. Leybovich, A. Sethi, and N. Dogan, "Comparison of ionization chambers of various volumes for IMRT absolute dose verification," *Med. Phys.*, vol. 30, no. 2, pp. 119–123, Jan. 2003.

[95] J. Andersson, F. J. Kaiser, F. Gómez, O. Jäkel, J. Pardo-Montero, and H. Tölli, "A comparison of different experimental methods for general recombination correction for liquid ionization chambers," *Phys. Med. Biol.*, vol. 57, no. 21, pp. 7161–7175, Nov. 2012.

[96] J. Pardo-Montero and F. Gómez, "Determining charge collection efficiency in parallel-plate liquid ionization chambers," *Phys. Med. Biol.*, vol. 54, no. 12, pp. 3677–3689, Jun. 2009.

[97] E. Chung, S. Davis, and J. Seuntjens, "TU-A-BRB-09: Ion Recombination in a Liquid-Filled Ionization Chamber in High-Energy Photon Beams," *Med. Phys.*, vol. 39, no. 6Part22, pp. 3887–3887, Jun. 2012.

[98] F. Gómez, D. González-Castaño, P. Díaz-Botana, and J. Pardo-Montero, "Study of the PTW microLion chamber temperature dependence," *Phys. Med. Biol.*, vol. 59, no. 11, pp. 2705–2712, Jun. 2014.

[99] G. Rikner and E. Grusell, "General specifications for silicon semiconductors for use in radiation dosimetry," *Phys. Med. Biol.*, vol. 32, no. 9, pp. 1109–1117, 1987.

[100] B. Nilsson, B. I. Rudén, and B. Sorcini, "Characteristics of silicon diodes as patient dosemeters in external radiation therapy," *Radiother. Oncol.*, vol. 11, no. 3, pp. 279–288, Mar. 1988.

[101] P. A. Jursinic, "Angular dependence of dose sensitivity of surface diodes," *Med. Phys.*, vol. 36, no. 6, 2009.

[102] R. Ramani, S. Russell, and P. O'Brien, "Clinical dosimetry using mosfets," *Int. J.*

Radiat. Oncol., vol. 37, no. 4, pp. 959–964, Mar. 1997.

[103] P. W. Hoban, M. Heydarian, W. A. Beckham, and A. H. Beddoe, "Dose rate dependence of a PTW diamond detector in the dosimetry of a 6 MV photon beam," *Phys. Med. Biol.*, vol. 39, no. 8, pp. 1219–1229, Aug. 1994.

[104] W. Lechner, H. Palmans, L. Sölkner, P. Grochowska, and D. Georg, "Detector comparison for small field output factor measurements in flattening filter free photon beams," *Radiother. Oncol.*, vol. 109, no. 3, pp. 356–360, 2013.

[105] T. Kron, "Thermoluminescence dosimetry and its applications in medicine--Part 1: Physics, materials and equipment.," *Australas. Phys. Eng. Sci. Med.*, vol. 17, no. 4, pp. 175–99, Dec. 1994.

[106] S. W. S. McKeever, "New millennium frontiers of luminescence dosimetry.," *Radiat. Prot. Dosimetry*, vol. 100, no. 1–4, pp. 27–32, 2002.

[107] E. G. Yukihara and S. W. S. McKeever, "Optically stimulated luminescence (OSL) dosimetry in medicine," *Phys. Med. Biol.*, vol. 53, no. 20, pp. R351–R379, Oct. 2008.

[108] R. J. Watts, "Evaluation of a diode detector array for use as a linear accelerator QC device," *Med. Phys.*, vol. 25, no. 2, pp. 247–250, 1998.

[109] T. C. Zhu, L. Ding, C. R. Liu, J. R. Palta, W. E. Simon, and J. Shi, "Performance evaluation of a diode array for enhanced dynamic wedge dosimetry," *Med. Phys.*, vol. 24, no. 7, pp. 1173–1180, 1997.

[110] C. Martens, C. De Wagter, and W. De Neve, "The value of the LA48 linear ion chamber array for characterization of intensity-modulated beams," *Phys. Med. Biol.*, vol. 46, no. 4, pp. 1131–1148, Apr. 2001.

[111] P. A. Jursinic, "Characterization of optically stimulated luminescent dosimeters, OSLDs, for clinical dosimetric measurements," *Med. Phys.*, vol. 34, no. 12, pp. 4594–4604, 2007.

[112] C. Fiorino, C. Uleri, G. M. Cattaneo, and R. Calandrino, "On-line exit dose profile measurements by a diode linear array," *Phys. Med. Biol.*, vol. 41, pp. 1291–1304, 1996.

[113] D. M. Wells, P. J. Picco, and W. Ansbacher, "Electron energy constancy verification using a double-wedge phantom.," *J. Appl. Clin. Med. Phys.*, vol. 4, no. 3, pp. 204–208, 2003.

[114] M. Essers, L. Van Battum, and B. J. M. Heijmen, "A linear diode array (JFD-5) for match line in vivo dosimetry in photon and electron beams; evaluation for a chest wall irradiation technique," *Radiother. Oncol.*, vol. 61, no. 2, pp. 185–192, 2001.

[115] F. Bisello *et al.*, "Development of silicon monolithic arrays for dosimetry in external

beam radiotherapy," *Nucl. Instruments Methods Phys. Res. Sect. A Accel. Spectrometers, Detect. Assoc. Equip.*, vol. 796, pp. 85–88, 2015.

[116] A. H. Aldosari *et al.*, "A two dimensional silicon detectors array for quality assurance in stereotactic radiotherapy: MagicPlate-512," *Med. Phys.*, vol. 41, no. 9, 2014.

[117] M. Bruzzi, "Novel silicon devices for radiation therapy monitoring," *Nucl. Instruments Methods Phys. Res. Sect. A Accel. Spectrometers, Detect. Assoc. Equip.*, vol. 809, pp. 105–112, Feb. 2016.

[118] K. Al Shukaili *et al.*, "A 2D silicon detector array for quality assurance in small field dosimetry: DUO," *Med. Phys.*, vol. 44, no. 2, pp. 628–636, Feb. 2017.

[119] P. Naseri, N. Suchowerska, and D. R. McKenzie, "Scintillation dosimeter arrays using air core light guides: simulation and experiment," *Phys. Med. Biol.*, vol. 55, no. 12, pp. 3401–3415, Jun. 2010.

[120] R. P. Parker, "Semiconductor Nuclear Radiation Detectors," *Phys. Med. Biol.*, vol. 15, no. 4, pp. 605–620, 1970.

[121] K. R. Hogstrom and P. R. Almond, "Review of electron beam therapy physics," *Phys. Med. Biol.*, vol. 51, no. 13, 2006.

[122] J. F. Williamson, "Brachytherapy technology and physics practice since 1950: A half-century of progress," *Phys. Med. Biol.*, vol. 51, no. 13, 2006.

[123] R. Hill, B. Healy, L. Holloway, Z. Kuncic, D. Thwaites, and C. Baldock, "Advances in kilovoltage x-ray beam dosimetry," *Phys. Med. Biol.*, vol. 59, no. 6, pp. R183–R231, 2014.

[124] J. Shi, W. E. Simon, and T. C. Zhu, "Modeling the instantaneous dose rate dependence of radiation diode detectors," *Med. Phys.*, vol. 30, no. 9, 2003.

[125] G. C. Messenger and M. S. Ash, *The Effects of Radiation on Electronic Systems*. New York: Van Nostrand Reinhold Company Inc., 1986.

[126] J. L. Wirth and S. C. Rogers, "The transient response of transistors and diodes to ionizing radiation," *IEEE Trans. Nucl. Sci.*, vol. NS-11, no. 5, pp. 24–38, Nov. 1964.

[127] O. Armantier and O. Richard, "Exchanges of Cost Information in the Airline Industry," *RAND J. Econ.*, vol. 34, no. 3, p. 461, 2003.

[128] E. Grusell and G. Rikner, "Linearity with dose rate of low resistivity p-type silicon semiconductor detectors," *Phys. Med. Biol.*, vol. 38, no. 6, pp. 785–792, 1993.

[129] P. A. Jursinic, "Dependence of diode sensitivity on the pulse rate of delivered radiation," *Med. Phys.*, vol. 40, no. 2, 2013.

[130] G. Rikner and E. Grusell, "Effects of radiation damage on the silicon lattice," *Phys. Med.*

Biol., vol. 1261, no. 28, pp. 1261–1267, 1983.

[131] A. S. Saini and T. C. Zhu, "Temperature dependence of commercially available diode detectors," *Med. Phys.*, vol. 29, no. 4, pp. 622–630, Mar. 2002.

[132] N. Stansook *et al.*, "Technical Note: Angular dependence of a 2D monolithic silicon diode array for small field dosimetry," *Med. Phys.*, vol. 44, no. 8, pp. 4313–4321, 2017.

[133] S. M. Sze and K. K. Ng, *Physics of Semiconductor Devices*, 3rd ed. John Wiley & Sons, 2007.

[134] P. A. Jursinic, "Implementation of an in-vivo diode dosimetry program and changes in diode characteristics over 4-years clinical history," *Med. Phys.*, vol. 28, no. 8, pp. 1718–1726, 2001.

[135] D. Marre and G. Marinello, "Comparison of p-type commercial electron diodes for in-vivo dosimetry," *Med. Phys.*, vol. 31, no. 1, pp. 50–56, 2004.

[136] E. Grusell and G. Rikner, "Radiation damage induced dose rate non-linearity in an n-type silicon detector," *Acta Oncol. (Madr).*, vol. 23, no. 6, pp. 465–469, 1984.

[137] A. S. Saini and T. C. Zhu, "Dose rate and SDD dependence of commercially available diode detectors," *Med. Phys.*, vol. 31, no. 4, pp. 914–924, 2004.

[138] K. T. Welsh and L. E. Reinstein, "The thermal characteristics of different diodes on in vivo patient dosimetry," *Med. Phys.*, vol. 28, no. 5, pp. 844–849, 2001.

[139] R. L. Dixon and K. E. Ekstrand, "Gold and platinum doped radiation resistant silicon diode detectors," *Radiat. Prot. Dosimetry*, vol. 17, no. July, pp. 527–530, 1986.

[140] I. Griessbach, M. Lapp, J. Bohsung, G. Gademann, and D. Harder, "Dosimetric characteristics of a new unshielded silicon diode and its application in clinical photon and electron beams," *Med. Phys.*, vol. 32, no. 12, pp. 3750–3754, 2005.

[141] K. Eklund and A. Ahnesjö, "Modeling silicon diode energy response factors for use in therapeutic photon beams," *Phys. Med. Biol.*, vol. 54, no. 20, pp. 6135–6150, Oct. 2009.

[142] Z. Yin, R. P. Hugtenburg, and A. H. Beddoe, "Response corrections for solid-state detectors in megavoltage photon dosimetry," *Phys. Med. Biol.*, vol. 49, no. 16, pp. 3691–3702, 2004.

[143] K. Eklund, "Modeling Silicon Diode Dose Response in Radiotherapy Fields using Fluence Pencil Kernels," Uppsala Universitet, 2010.

[144] G. Rikner and E. Grusell, "Selective shielding of a p-si detector for quality independence," *Acta Oncol. (Madr).*, vol. 24, no. 1, pp. 65–69, 1985.

[145] K. Eklund and A. Ahnesjö, "Spectral perturbations from silicon diode detector encapsulation and shielding in photon fields.," *Med. Phys.*, vol. 37, no. 11, pp. 6055–

6060, 2010.

[146] A. J. D. Scott, A. E. Nahum, and J. D. Fenwick, “Monte Carlo modeling of small photon fields: Quantifying the impact of focal spot size on source occlusion and output factors, and exploring miniphantom design for small-field measurements,” *Med. Phys.*, vol. 36, no. 7, pp. 3132–3144, 2009.

[147] P. Francescon, W. Kilby, N. Satariano, and S. Cora, “Monte Carlo simulated correction factors for machine specific reference field dose calibration and output factor measurement using fixed and iris collimators on the CyberKnife system,” *Phys. Med. Biol.*, vol. 57, no. 12, pp. 3741–3758, Jun. 2012.

[148] T. S. a Underwood, H. C. Winter, M. a Hill, and J. D. Fenwick, “Mass-density compensation can improve the performance of a range of different detectors under non-equilibrium conditions,” *Phys. Med. Biol.*, vol. 58, pp. 8295–310, 2013.

[149] J. M. Lárraga-Gutiérrez, “Experimental determination of field factors for small radiotherapy beams using the daisy chain correction method,” *Phys. Med. Biol.*, vol. 60, no. 15, pp. 5813–5831, 2015.

[150] M. K. Tyler, P. Z. Y. Liu, C. Lee, D. R. McKenzie, and N. Suchowerska, “Small field detector correction factors: Effects of the flattening filter for Elekta and Varian linear accelerators,” *J. Appl. Clin. Med. Phys.*, vol. 17, no. 3, pp. 223–235, 2016.

[151] S. Tanny, N. Sperling, and E. I. Parsai, “Correction factor measurements for multiple detectors used in small field dosimetry on the Varian Edge radiosurgery system,” *Med. Phys.*, vol. 42, no. 9, pp. 5370–5376, 2015.

[152] T. S. A. Underwood, B. C. Rowland, R. Ferrand, and L. Vieillevigne, “Application of the Exradin W1 scintillator to determine Ediode 60017 and microDiamond 60019 correction factors for relative dosimetry within small MV and FFF fields,” *Phys. Med. Biol.*, vol. 60, no. 17, pp. 6669–6683, 2015.

[153] G. A. Ezzell *et al.*, “IMRT commissioning: Multiple institution planning and dosimetry comparisons, a report from AAPM Task Group 119,” *Med. Phys.*, vol. 36, no. 11, pp. 5359–5373, 2009.

[154] B. E. Nelms and J. A. Simon, “A survey on IMRT QA analysis,” *J. Appl. Clin. Med. Phys.*, vol. 8, no. 3, pp. 76–90, 2007.

[155] P. A. Jursinic and B. E. Nelms, “A 2-D diode array and analysis software for verification of intensity modulated radiation therapy delivery,” *Med. Phys.*, vol. 30, no. 5, pp. 870–879, 2003.

[156] D. Létourneau, M. Gulam, D. Di Yan, M. Oldham, and J. W. Wong, “Evaluation of a

2D diode array for IMRT quality assurance," *Radiother. Oncol.*, vol. 70, no. 2, pp. 199–206, 2004.

[157] P. A. Jursinic, R. Sharma, and J. Reuter, "MapCHECK used for rotational IMRT measurements: Step-and-shoot, Tomotherapy, RapidArc," *Med. Phys.*, vol. 37, no. 6, pp. 2837–2846, 2010.

[158] G. Li *et al.*, "Evaluation of the ArcCHECK QA system for IMRT and VMAT verification," *Phys. Medica*, vol. 29, no. 3, pp. 295–303, May 2013.

[159] G. Yan, B. Lu, J. Kozelka, C. Liu, and J. G. Li, "Calibration of a novel four-dimensional diode array," *Med. Phys.*, vol. 37, no. 1, pp. 108–115, Dec. 2009.

[160] V. Feygelman, G. G. Zhang, C. Stevens, and B. E. Nelms, "Evaluation of a new VMAT QA device, or the 'X' and 'O' array geometries.," *J. Appl. Clin. Med. Phys.*, vol. 12, no. 2, p. 3346, 2011.

[161] L. Coleman and C. Skourou, "Sensitivity of volumetric modulated arc therapy patient specific QA results to multileaf collimator errors and correlation to dose volume histogram based metrics," *Med. Phys.*, vol. 40, no. 11, 2013.

[162] M. Hussein, P. Rowshanfarzad, M. A. Ebert, A. Nisbet, and C. H. Clark, "A comparison of the gamma index analysis in various commercial IMRT/VMAT QA systems," *Radiother. Oncol.*, vol. 109, no. 3, pp. 370–376, 2013.

[163] A. L. Petoukhova, J. Van Egmond, M. G. C. Eenink, R. G. J. Wiggenraad, and J. P. C. Van Santvoort, "The ArcCHECK diode array for dosimetric verification of HybridArc," *Phys. Med. Biol.*, vol. 56, no. 16, pp. 5411–5428, Aug. 2011.

[164] Q. Wang, J. Dai, and K. Zhang, "A novel method for routine quality assurance of volumetric-modulated arc therapy," *Med. Phys.*, vol. 40, no. 10, p. 101712, 2013.

[165] V. Chaswal, M. Weldon, N. Gupta, A. Chakravarti, and Y. Rong, "Commissioning and comprehensive evaluation of the ArcCHECK cylindrical diode array for VMAT pretreatment delivery QA," *J. Appl. Clin. Med. Phys.*, vol. 15, no. 4, pp. 212–225, 2014.

[166] J. Kozelka, J. Robinson, B. Nelms, G. Zhang, D. Savitskij, and V. Feygelman, "Optimizing the accuracy of a helical diode array dosimeter: A comprehensive calibration methodology coupled with a novel virtual inclinometer," *Med. Phys.*, vol. 38, no. 9, pp. 5021–5032, 2011.

[167] D. Létourneau, J. Publicover, J. Kozelka, D. J. Moseley, and D. A. Jaffray, "Novel dosimetric phantom for quality assurance of volumetric modulated arc therapy," *Med. Phys.*, vol. 36, no. 5, pp. 1813–1821, 2009.

[168] D. Robinson, "Inhomogeneity correction and the analytic anisotropic algorithm," *J.*

Appl. Clin. Med. Phys., vol. 9, no. 2, pp. 112–122, 2008.

[169] B. Poppe, A. Djouguela, A. Blechschmidt, K. Willborn, A. Ruhmann, and D. Harder, "Spatial resolution of 2D ionization chamber arrays for IMRT dose verification: single-detector size and sampling step width," *Phys. Med. Biol.*, vol. 52, no. 10, pp. 2921–2935, 2007.

[170] C. W. Stanhope *et al.*, "Evaluation of machine log files/MC-based treatment planning and delivery QA as compared to ArcCHECK QA," *Med. Phys.*, vol. 45, no. 7, pp. 2864–2874, 2018.

[171] S. Manolopoulos *et al.*, "Small field measurements with a novel silicon position sensitive diode array," *Phys. Med. Biol.*, vol. 54, no. 3, pp. 485–495, 2009.

[172] A. Bocci *et al.*, "Silicon strip detector for a novel 2D dosimetric method for radiotherapy treatment verification," *Nucl. Instruments Methods Phys. Res. Sect. A Accel. Spectrometers, Detect. Assoc. Equip.*, vol. 673, pp. 98–106, 2012.

[173] J. H. D. Wong *et al.*, "A silicon strip detector dose magnifying glass for IMRT dosimetry," *Med. Phys.*, vol. 37, no. 2, pp. 427–439, Jan. 2010.

[174] P. Meyer, R. Regal, M. Jung, P. Siffert, L. Mertz, and A. Constantinesco, "Feasibility of a semiconductor dosimeter to monitor skin dose in interventional radiology," *Med. Phys.*, vol. 28, no. 10, pp. 2002–2006, 2001.

[175] J. H. D. Wong *et al.*, "The use of a silicon strip detector dose magnifying glass in stereotactic radiotherapy QA and dosimetry," *Med. Phys.*, vol. 38, no. 3, pp. 1226–1238, Feb. 2011.

[176] J. H. D. Wong *et al.*, "Independent quality assurance of a helical tomotherapy machine using the dose magnifying glass," *Med. Phys.*, vol. 38, no. 4, pp. 2256–2264, 2011.

[177] M. Petasecca *et al.*, "MagicPlate-512: A 2D silicon detector array for quality assurance of stereotactic motion adaptive radiotherapy," *Med. Phys.*, vol. 42, no. 6, pp. 2992–3004, 2015.

[178] C. S. Porumb *et al.*, "Characterisation of Silicon Diode Arrays for Dosimetry in External Beam Radiation Therapy," *IEEE Trans. Nucl. Sci.*, vol. 63, no. 3, pp. 1808–1817, 2016.

[179] K. Utitsarn *et al.*, "Optimisation of output factor measurements using the Magic Plate 512 silicon dosimeter array in small megavoltage photon fields," in *Journal of Physics: Conference Series*, 2017, vol. 777.

[180] J. Czochralski, "Ein neues Verfahren zur Messung der Kristallisationsgeschwindigheit der Metalle," *Zeitschrift Fur Phys. Chemie*, vol. 92, no. 1, pp. 219–221, Jan. 1918.

[181] P. C. Lee, W. F. Kuo, and F. C. Chang, "In situ compatibilization of PBT/ABS blends

through reactive copolymers," *Polymer (Guildf).*, vol. 35, no. 26, pp. 5641–5650, 1994.

[182] M. Bruzzi, "Radiation damage in silicon detectors for high-energy physics experiments," *IEEE Trans. Nucl. Sci.*, vol. 48, no. 4 I, pp. 960–971, 2001.

[183] E. Borchi and M. Bruzzi, "Radiation-Damage in Silicon Detectors," *Riv. Del Nuovo Cim.*, vol. 17, no. 11, pp. 1–63, 1994.

[184] J. R. Schwank, M. R. Shaneyfelt, and D. M. Fleetwood, "Radiation Effects in MOS Oxides," *IEEE Trans. Nucl. Sci.*, vol. 34, no. 4, pp. 1833–1853, 2008.

[185] E. Grusell and G. Rikner, "Evaluation of temperature effects in p-type silicon detectors," *Phys. Med. Biol.*, vol. 31, no. 5, pp. 527–534, 1986.

[186] M. Moll *et al.*, "Development of radiation tolerant semiconductor detectors for the Super-LHC," *Nucl. Instruments Methods Phys. Res. Sect. A Accel. Spectrometers, Detect. Assoc. Equip.*, vol. 546, no. 1–2, pp. 99–107, 2005.

[187] M. Moll, E. Fretwurst, M. Kuhnke, and G. Lindström, "Relation between microscopic defects and macroscopic changes in silicon detector properties after hadron irradiation," *Nucl. Instruments Methods Phys. Res. Sect. B Beam Interact. with Mater. Atoms*, vol. 186, no. 1–4, pp. 100–110, 2002.

[188] S. M. Sze and K. K. Ng, *Physics of Semiconductor Devices*, 3rd ed. Hoboken, NJ, USA: John Wiley & Sons, Inc., 2006.

[189] M. Bruzzi *et al.*, "Epitaxial silicon devices for dosimetry applications," *Appl. Phys. Lett.*, vol. 90, no. 17, pp. 17–19, 2007.

[190] I. Fuduli *et al.*, "Multichannel Data Acquisition System comparison for Quality Assurance in external beam radiation therapy," *Radiat. Meas.*, vol. 71, pp. 338–341, 2014.

[191] C. S. Porumb, "Development of a multi-detector quality assurance instrument for intensity modulated radiotherapy," University of Wollongong, 2016.

[192] "Texas Instrument - Channel Analog Front End for Digital X-Ray Detector," *Datasheet available from http://www. ti. com/lit/ds/slas672/slas672. pdf*, no. September. 2009.

[193] H. H. Rossi and M. Zaider, *Microdosimetry and its applications*. Springer, 1996.

[194] H. Paganetti, *Proton therapy physics*. IOP Publishing, 2017.

[195] J. Allison *et al.*, "Geant4 developments and applications," *IEEE Trans. Nucl. Sci.*, vol. 53, no. 1, pp. 270–278, 2006.

[196] J. Allison *et al.*, "Recent developments in GEANT4," *Nucl. Instruments Methods Phys. Res. Sect. A Accel. Spectrometers, Detect. Assoc. Equip.*, vol. 835, pp. 186–225, 2016.

[197] S. Larsson, R. Svensson, I. Gudowska, V. N. Ivanchenko, and A. Brahme, "Radiation

transport calculations for 50 MV photon therapy beam using the Monte Carlo code GEANT4," *Radiat. Prot. Dosimetry*, vol. 115, no. 1–4, pp. 503–507, 2005.

[198] B. A. Faddegon *et al.*, "Benchmarking of Monte Carlo simulation of bremsstrahlung from thick targets at radiotherapy energies," *Med. Phys.*, vol. 35, no. 10, pp. 4308–4317, 2008.

[199] Synopsys, "Sentaurus Workbench User Guide," no. March. p. 188, 2007.

[200] Synopsys, "Sentaurus Structure Editor User Guide." 2006.

[201] Synopsys, "Sentaurus Device User Guide." 2013.

[202] A. H. Aldosari *et al.*, "Characterization of an innovative p-type epitaxial diode for dosimetry in modern external beam radiotherapy," *IEEE Trans. Nucl. Sci.*, vol. 60, no. 6, pp. 4705–4712, 2013.

[203] M. Moll, "Radiation Damage in Silicon Particle Detectors," Universität Hamburg, 1999.

[204] G. Cranmer-Sargison, S. Weston, N. P. Sidhu, and D. I. Thwaites, "Experimental small field 6 MV output ratio analysis for various diode detector and accelerator combinations," *Radiother. Oncol.*, vol. 100, no. 3, pp. 429–435, 2011.

[205] A. Fogliata *et al.*, "Definition of parameters for quality assurance of flattening filter free (FFF) photon beams in radiation therapy," *Med. Phys.*, vol. 39, no. 10, pp. 6455–6464, 2012.

[206] A. Djouguela *et al.*, "Dosimetric characteristics of an unshielded p-type Si diode: linearity, photon energy dependence and spatial resolution," *Z. Med. Phys.*, vol. 18, no. 4, pp. 301–306, Dec. 2008.

[207] J. H. D. Wong *et al.*, "Characterization of a novel two dimensional diode array the 'magic plate' as a radiation detector for radiation therapy treatment," *Med. Phys.*, vol. 39, no. 5, pp. 2544–2558, 2012.

[208] R. F. Laitano, A. S. Guerra, M. Pimpinella, C. Caporali, and A. Petrucci, "Charge collection efficiency in ionization chambers exposed to electron beams with high dose per pulse," *Phys. Med. Biol.*, vol. 51, no. 24, pp. 6419–6436, 2006.

[209] P. H. Charles *et al.*, "Design and experimental testing of air slab caps which convert commercial electron diodes into dual purpose, correction-free diodes for small field dosimetry," *Med. Phys.*, vol. 41, no. 10, p. 101701, 2014.

[210] W. Lechner *et al.*, "A multinational audit of small field output factors calculated by treatment planning systems used in radiotherapy," *Phys. Imaging Radiat. Oncol.*, vol. 5, no. February, pp. 58–63, 2018.

[211] E. Borzov, A. Nevelsky, R. Bar-Deroma, and I. Orion, "Dosimetric characterization of

Elekta stereotactic cones," *J. Appl. Clin. Med. Phys.*, vol. 19, no. 1, pp. 194–203, 2018.

[212] H. K. Looe, B. Delfs, D. Poppinga, P. Jiang, D. Harder, and B. Poppe, "The 'cutting away' of potential secondary electron tracks explains the effects of beam size and detector wall density in small-field photon dosimetry," *Phys. Med. Biol.*, vol. 63, no. 1, p. 015001, Dec. 2018.

[213] P. H. Halvorsen *et al.*, "AAPM-RSS Medical Physics Practice Guideline 9.a. for SRS-SBRT," *J. Appl. Clin. Med. Phys.*, vol. 18, no. 5, pp. 10–21, 2017.

[214] K. Al Shukaili *et al.*, "Characterization of ELEKTA SRS cone collimator using high spatial resolution monolithic silicon detector array," *J. Appl. Clin. Med. Phys.*, vol. 19, no. 4, pp. 114–124, 2018.

[215] D. Létourneau, H. Keller, N. Becker, M. N. Amin, B. Norrlinger, and D. A. Jaffray, "Quality control methods for linear accelerator radiation and mechanical axes alignment," *Med. Phys.*, vol. 45, no. 6, pp. 2388–2398, 2018.

[216] E. E. Klein *et al.*, "Task group 142 report: Quality assurance of medical acceleratorsa," *Med. Phys.*, vol. 36, no. 9, pp. 4197–4212, 2009.

[217] G. Biasi, M. Petasecca, S. Guatelli, T. Kron, and A. Rosenfeld, "EP-1720: A silicon diode array detector for small field dosimetry with flattening filter free beams," *Radiother. Oncol.*, vol. 127, no. ESTRO 37 Abstract book, pp. S919–S920, Apr. 2018.

[218] W. Kilby, J. R. Dooley, G. Kuduvalli, S. Sayeh, and C. R. Maurer, "The CyberKnife® Robotic Radiosurgery System in 2010," *Technol. Cancer Res. Treat.*, vol. 9, no. 5, pp. 433–452, Oct. 2010.

[219] G. G. Echner *et al.*, "The design, physical properties and clinical utility of an iris collimator for robotic radiosurgery," *Phys. Med. Biol.*, vol. 54, no. 18, pp. 5359–5380, Sep. 2009.

[220] N. Delaby *et al.*, "CyberKnife® M6™: Peripheral dose evaluation for brain treatments," *Phys. Medica*, vol. 37, pp. 88–96, May 2017.

[221] A. Dixit *et al.*, "First Australian experience of treating localised prostate cancer patients with CyberKnife stereotactic radiotherapy: early PSA response, acute toxicity and quality of life," *J. Med. Radiat. Sci.*, vol. 64, no. 3, pp. 180–187, Sep. 2017.

[222] O. Blanck *et al.*, "Film-based delivery quality assurance for robotic radiosurgery: Commissioning and validation," *Phys. Medica*, vol. 31, no. 5, pp. 476–483, Jul. 2015.

[223] M. A. Cortés-Giraldo, J. M. Quesada, M. I. Gallardo, and R. Capote, "An implementation to read and write IAEA phase-space files in GEANT4-based simulations," *Int. J. Radiat. Biol.*, vol. 88, no. 1–2, pp. 200–208, 2012.

[224] P. Andreo and H. Benmakhlouf, “Role of the density, density effect and mean excitation energy in solid-state detectors for small photon fields,” *Phys. Med. Biol.*, vol. 62, no. 4, pp. 1518–1532, 2017.

[225] L. Masi *et al.*, “CyberKnife beam output factor measurements: A multi-site and multi-detector study,” *Phys. Medica*, vol. 32, no. 12, pp. 1637–1643, 2016.

[226] E. Pantelis *et al.*, “On the output factor measurements of the CyberKnife iris collimator small fields: Experimental determination of the kQclin, Qmsrfclin, f msrcorrection factors for microchamber and diode detectors,” *Med. Phys.*, vol. 39, no. 8, pp. 4875–4885, 2012.

[227] J.-H. Lan, S.-S. Guo, C.-C. Yao, and T.-F. Lee, “Physical Characteristics of Fixed and Dynamics Collimator for Cyberknife M6,” in *2016 3rd International Conference on Green Technology and Sustainable Development (GTSD)*, 2016, pp. 1–4.

[228] C. Bassinet *et al.*, “Small fields output factors measurements and correction factors determination for several detectors for a CyberKnife® and linear accelerators equipped with microMLC and circular cones.,” *Med. Phys.*, vol. 40, no. 7, p. 071725, 2013.

[229] D. Dechambre *et al.*, “Commissioning Monte Carlo algorithm for robotic radiosurgery using cylindrical 3D-array with variable density inserts,” *Phys. Medica*, vol. 33, pp. 152–158, Jan. 2017.

[230] J. Schwandt, E. Fretwurst, E. Garutti, R. Klanner, and I. Kopsalis, “Surface effects in segmented silicon sensors,” *Nucl. Instruments Methods Phys. Res. Sect. A Accel. Spectrometers, Detect. Assoc. Equip.*, vol. 845, pp. 159–163, 2017.

[231] S. H. Benedict *et al.*, “Stereotactic body radiation therapy: The report of AAPM Task Group 101,” *Med. Phys.*, vol. 37, no. 8, pp. 4078–4101, 2010.

[232] J. E. Villarreal-Barajas, “COMP report: CPQR technical quality control guidelines for treatment planning systems,” *J. Appl. Clin. Med. Phys.*, vol. 19, no. 2, pp. 35–38, 2018.

[233] A. Bruschi, M. Esposito, S. Pini, A. Ghirelli, G. Zatelli, and S. Russo, “How the detector resolution affects the clinical significance of SBRT pre-treatment quality assurance results,” *Phys. Medica*, vol. 49, pp. 129–134, 2018.

[234] M. Duncan *et al.*, “Real-time high spatial resolution dose verification in stereotactic motion adaptive arc radiotherapy,” *J. Appl. Clin. Med. Phys.*, vol. 19, no. 4, pp. 173–184, 2018.

[235] P. H. Charles *et al.*, “A practical and theoretical definition of very small field size for radiotherapy output factor measurements,” *Med. Phys.*, vol. 41, no. 4, p. 041707, 2014.